A Study of the Multihadronic Properties of Photon-Photon Interactions

S. J. Lumsdon

Department of Physics & Astronomy
University of Glasgow

Submitted for the degree of Ph.D at the University of Glasgow,
November 1990

ProQuest LLC.
789 East Eisenhower Parkway
P.O. Box 1346
Ann Arbor, MI 48106 – 1346

Abstract

The analysis described in this thesis concerns the study of hadron production in photon-photon interactions. The data analysed were taken with the CELLO detector on the PETRA storage ring at the DESY physics institute in Hamburg during 1986. During this time the machine operated with a centre of mass energy of 35 GeV and the total recorded integrated luminosity amounted to 86 pb^{-1}. The data studied was split into three Q^2 (where the Q^2 is the invariant mass of the virtual photon) regions in the range $0 < Q^2 < 30$ GeV^2 consisting of untagged events (with two undetected scattered beam leptons assumed to have been contained in the beam-pipe producing two nearly real photons) and single tagged events (where one beam lepton remain undetected producing a nearly real photon and one detected scattered beam lepton producing a highly virtual photon). Two tagging regions were used. Forward tags were detected in lead-glass scintillators close to the beam axis ($55 < \theta < 80$ mr) and endcap tags were detected in the lead-liquid argon endcaps ($150 < \theta < 360$ mr). The events were required to have ≥ 4 charged tracks and constrained to the hadronic mass W_{VIS} region $4 \leq W_{VIS} \leq 9$ GeV. This produced three data samples, 15610 untagged events with $\langle Q^2 \rangle \sim 0.1$ GeV^2, 371 forward tagged events with $\langle Q^2 \rangle \sim 1.0$ GeV^2 and 302 endcap tagged events with $\langle Q^2 \rangle \sim 12.7$ GeV^2.

The data was compared to an incoherent sum of the quark parton model (QPM) and a soft hadronic term described by a generalised vector dominance model (GVDM). It was found that this gives reasonable overall agreement with the data. The overall numbers of events and their Q^2 dependence was found to be in good agreement with an incoherent sum of QPM and a soft hadronic model whose W, Q^2 dependence was best modelled by the GVDM ansatz. A jet analysis of the data showed it to be dominated by a two-jet component which was well modelled by the QPM + GVDM term. An excess of events at medium and high jet p_t's was observed in the low Q^2 data. The inclusion of a phasespace component, or rescaling the QPM component provided a good description of this excess. The thrust of the high jet p_t events was described neither by the inclusion of a phasespace term (which underestimates the thrust), nor by scaling the QPM term (which overestimates the thrust). However, a good description of the thrust of high jet p_t events was provided by the addition of a multijet term to GVDM + QPM.

Preface

This thesis describes the study of multihadronic photon-photon interactions carried out using data from the CELLO detector at the PETRA e^+e^- storage ring situated at DESY, Hamburg. Multihadronic photon-photon data was studied over a wide Q^2 range. The general characteristics of the data were found to be well described by an incoherent sum of a pointlike component and a soft hadronic component. An excess of events was observed at low Q^2. The origin of this excess is discussed.

The results obtained in this thesis depend directly or indirectly on the work of many people, although the physics analysis is the individual work of the author.

No part of the work referred to in this thesis has been submitted in support of an application for another degree or qualification in this or any other university or institution of learning.

Acknowledgements

Firstly I would like to thank Peter Bussey and Ian Skillicorn for all the direction and advice they gave me in the last three years. This thesis would not have been possible without their kind help and assistance.

Many thanks also go to Denis Hendry who shed a lot of blood sweat and tears trying to get Monte-Carlo programs to work and to Stan, Butrus, Andy, Owen and the rest of the group for putting up with me. I would also like to thank the Glasgow University Physics Department and everyone in it who have helped me during the last three years and made my stay so pleasurable.

During my numerous visits to Hamburg I received a great deal of welcome assistance from the F14 group who provided me with enormous quantities of help and advice which were so valuable. I would especially like to thank Michael Feindt, Jan Hendrik Peters, Oliver Podobrin and Joannes Ahme who put up with all my silly questions.

I would like to thank the Science and Engineering Research Council who provided the financial assistance and some fruitful trips abroad. I would also like to thank the DESY directorate for their kind hospitality during my visits and the DESY Rechenzentrum for the excellent computing services provided.

Many thanks must go to Bernadette, Mary and Brian who provided the friendliest computing service I can imagine and for all their kind help and encouragement, and to Catherine for keeping me on the straight and narrow. Alan Flavell and David Martin also managed to totally baffle me on the subject of computers.

Finally, thanks to my parents for all the love, help and support they have given me during my studies.

Oh and last but not least to Tennents...

Contents

Abstract I

Preface II

Acknowledgements III

Table of Contents IV

Chapter 1 The Theory of Photon-Photon Physics.

1.1 Introduction. 1
1.2 The Basic Notation for $e^+e^-\rightarrow e^+e^-X$. 2
1.3 Characteristics of Photon-Photon Reactions. 4
1.4 Tagging. 6
1.5 The Exact Photon-Photon Cross-Section Formalism. 7
1.6 Equivalent Photon Approximations. 10
1.7 The Production of Hadrons from Photon-Photon Collisions. 12
1.8 The Vector Meson Dominance Model. 13
1.9 The GLM Model. 16
1.10 The Quark Parton Model. 17
1.11 Higher Order Processes. 19
1.12 Background Processes. 22

Chapter 2 Review of Previous Experimental Results.

2.1 Introduction. 24
2.2 The Photon Structure Function. 25
2.3 The Total Hadronic Cross-Section. 27
2.4 Jet Production in Photon-Photon Interactions. 30

Chapter 3 Experimental Apparatus.

3.1 PETRA 34
3.2 CELLO An Introduction. 35
3.3 The Central Tracking Chamber. 36
3.3.1 The Proportional Wire Chambers. 36
3.3.2 The Cylindrical Drift Chambers. 36

3.3.3 The Beam Pipe Chambers. 37
3.3.4 The Endcap Proportional Chambers. 37
3.3.5 The Superconducting Coil. 37
3.4 The Lead-Liquid Argon Calorimetry. 38
3.5 The Muon Chambers. 39
3.6 The Forward Detector. 40
3.7 The Hole Tagger. 40
3.8 The CELLO Trigger. 41
3.8.1 The Charged Trigger. 41
3.8.2 The Neutral Trigger. 43
3.9 The Data Aquisition System. 44

Chapter 4 Data Selection and Software.
4.1 The Filter. 45
4.2 OFFRAM 46
4.2.1 CELPAT 47
4.2.2 CLGEOM 47
4.2.3 ECCPAT 48
4.2.4 GLOFIT 48
4.2.5 LATRAK 48
4.2.6 MUCH 49
4.3 Data Selection. 49
4.4 VIOLA 50

Chapter 5 Monte-Carlo Methods and Models.
5.1 Introduction. 52
5.2 A Short Note on Cross-Sections and Luminosities. 53
5.3 The QPM Generator. 54
5.4 The VDM Generator. 57
5.5 The Phasespace Generator. 58
5.6 The Multijet Generators. 59
5.7 Backgrounds. 59
5.7.1 Multihadronic Annihilation. 59
5.7.2 Tau Production. 61
5.8 The Detector Simulation. 61
5.9 The Charged Trigger Simulation. 63
5.10 The Filter Program. 64

Chapter 6 Calibrations and Backgrounds.

6.1 Introduction. 65
6.2 The Calibration of the Forward and Endcap Tags. 65
6.3 Barrel Tags. 68
6.4 Backgrounds. 69
6.5 Beam Gas/Pipe Background. 71
6.6 $e^+e^- \rightarrow e^+e^-\tau^+\tau^-$ 73
6.7 The Inelastic Compton Effect and C = −1 Final States. 73
6.8 The Background and Final Event Samples. 74

Chapter 7 The General Characteristics of the Data.

7.1 Introduction. 76
7.2 A Comparison of the Data with an Incoherent Sum of QPM and a Soft Hadronic Component. 77
7.3 The General Characteristics of the Data. 79
7.4 The Q^2 Dependence of the Hadronic Component. 81
7.5 The Inclusive Particle p_t and Angular Distributions. 83
7.6 Conclusions. 84

Chapter 8 A Jet Analysis of Hadronic Photon-Photon Data.

8.1 Introduction. 85
8.2 Methods of Jet Analysis. 86
8.3 Jet Production in MC Models and the Effects of Detector Acceptance on Jet Reconstruction. 89
8.4 Evidence of Jet Production in the Data. 92
8.5 The Jet p_t and Angular Distributions of the Data. 93
8.6 Discrepancies in the low Q^2 Data. 94
8.7 An Additional Term to the GVDM + QPM Ansatz. 95
8.8 A Fit to the Jet p_t Distribution. 96
8.9 The $R_{\gamma\gamma}$ Distributions. 99
8.10 Conclusions. 100

Chapter 9 Summary and Conclusions. 102

The CELLO Collaboration. 105

References 107

Chapter 1

The Theory Of Photon-Photon Interactions.

1.1 Introduction

The classical Maxwell theory of light does not allow photons to interact with one another. They simply pass through each other as a superposition of two waves. However, the theory of Quantum Electrodynamics (QED) predicts the interaction of one photon with another. QED allows photons to couple to the charge of a fermion. Photons still cannot interact directly with one another but a photon can produce a pair of charged fermions. The other photon can then interact via the charge on one of these fermions. The Feynman diagram for the simplest form of photon-photon scattering is through the fermion box diagram (Fig 1.1). In order to study photon-photon interactions an intense source of high-energy photons is required. A possible way of achieving this was proposed by Low (1.1) in 1960. He proposed to measure the π^0 lifetime in an e^+e^- collider by utilizing the fact that the electrons and positrons are surrounded by a cloud of virtual photons which are continually being radiated and reabsorbed. It is possible for these photons to interact before being reabsorbed, producing a π^0 or other new final state. It was not until 1971-1972 that the first photon-photon interactions were observed at Novosibirsk, where the reaction

$$e^+e^- \rightarrow e^+e^-e^+e^-$$

was observed. Since then things have progressed rapidly and there has been a great deal of work done at SPEAR, PEP and PETRA.

Photon-photon physics can effectively be split into four main groups of study, each having specific characteristics.

1) QED events where the photons interact through a lepton-antilepton pair ie

$$e^+e^- \rightarrow e^+e^-e^+e^-$$
$$e^+e^- \rightarrow e^+e^-\mu^+\mu^-$$
$$e^+e^- \rightarrow e^+e^-\tau^+\tau^-$$

2) Resonance production where the photons couple to an even charge

conjugation particle (C = +1) ie

$$\gamma\gamma \rightarrow \eta, \eta', f_0, f'$$

3) Hadronic final states which are not resonant ie

$$\gamma\gamma \rightarrow \rho^0\rho^0, \pi^+\pi^-, K^+K^-$$

4) Inclusive hadronic final states, usually studied in two main groups,

1) The photon structure function. A brief description of this is given in Chapter 2.

2) The study of the general kinematic and jet properties of hadronic photon-photon interactions as well as the total cross-section ($\sigma_{\gamma\gamma}^{TOT}$). The two colliding photons can be shown to interact by two characteristically different processes. The photons can both couple to vector mesons which then interact. This is intrinsically similar to hadronic scattering processes such as pp, πp scattering. This process dominates at low Q^2 where both photons are on mass shell (ie nearly real photons), and because the interaction is hadronic in nature it is peaked at low transverse momenta (p_t). This is the region of non-perturbative quantum chromodynamics (QCD) where there are low momentum transfers and it is difficult to apply QCD to the problem. However the photons can also interact when one photon scatters off a quark-antiquark pair produced by the other photon. This process dominates at the higher Q^2 of the 'single tagged' mode where the massive photon probes the nearly real target photon. Because the photons are coupling directly to the quark charge (basically a QED reaction or zeroth order QCD, where quark-gluon, gluon-gluon interactions are ignored) the interaction involves hard scattering and consequently high momentum transfers are produced. It is the study of these processes and the different ways that they contribute to the data that is the subject of this thesis.

1.2 The Basic Notation for $e^+e^- \rightarrow e^+e^- X$

Before going further it is necessary to describe the notation used in photon-photon reactions (1.2). Fig 1.2 shows the basic diagram for

$$e^+e^- \rightarrow e^+e^- X$$

and displays the main kinematical variables on it. The important 4-vectors (in the laboratory system) are defined as follows.

$p_1 = (\vec{p},E_b)$ and $p_2 = (-\vec{p},E_b)$ are the 4-vectors for the incoming positron and electron respectively, where E_b is the beam energy.

$s = (p_1+p_2)^2 = 4E_b^2$ is the square of the initial centre of mass energy.

$p'_1 = (\vec{p}'_1,E_1)$ and $p'_2 = (-\vec{p}'_2,E_2)$ are the 4-vectors for the scattered positron and electron respectively, where $E_{1,2}$ are the energies of the scattered leptons.

$q_1 = (\vec{q}_1,E_{\gamma 1})$ and $q_2 = (\vec{q}_2,E_{\gamma 2})$ are the 4-vectors of the virtual photons radiated by the positron and electron, where $q_i = (p_i - p'_i)$.

$$k = (q_1 + q_2) = \sum_{i=1}^{N} k_i ,$$

where k is the 4-vector describing the final state system X, where X consists of N particles with 4-vectors k_i.

$W^2 = k^2$ and is the square of the hadronic mass of the final state X.

$\theta_{1,2}$ are the scattering angles made by the electron and positron with respect to the beam axis.

φ is the angle between the electron and positron in the plane perpendicular to the beam axis (not shown on diagram).

$Q_i^2 = -q_i^2$ where q_i is the invariant mass of the virtual photon i. Because the photons are spacelike it is always the case that $Q_i^2 > 0$.

It is useful to define some of the variables defined above. Specifically the Q^2 of the virtual photons is a useful quantity to measure.

$$\begin{aligned} Q_i^2 &= -q_i^2 = -(p_i - p'_i)^2 \\ &= -(2m_e^2 - 2p_i p'_i) \\ &= -(2m_e^2 - 2(\vec{p}_i \bullet \vec{p}'_i - E_b E'_i)) \\ &= -2(m_e^2 + E_b E'_i - \sqrt{(E_b^2 - m_e^2)(E_i'^2 - m_e^2)}\cos\theta_i) \end{aligned}$$

For $\theta >> m_e/E$ we can neglect the electron mass and the above simplifies to;

$$Q_i^2 = 2E_b E'_i(1 - \cos\theta_i)$$

Another important quantity is the hadronic mass $W_{\gamma\gamma}$ of the final state system X.

$$W_{\gamma\gamma}^2 = (q_1 + q_2)^2$$
$$= 4E_{\gamma 1}E_{\gamma 2} - 2E_1'E_2'(1 - \cos\theta_1 \cos\theta_2 - \sin\theta_1 \sin\theta_2 \cos\phi)$$
$$\approx 4E_{\gamma 1}E_{\gamma 2}$$

1.3 Characteristics Of Photon-Photon Reactions.

It is necessary to describe the basic characteristics of photon-photon reactions, and compare them with those of the annihilation channels (when the beam leptons couple to a single virtual photon which then produces a fermion-antifermion pair). The photons emitted from the electron and positron are radiated with a $1/E_\gamma$ spectrum (to a good approximation). This means that the photon-photon final states are produced at predominantly low hadronic masses. This is in contrast to the annihilation spectrum where (ignoring the radiative corrections) the events contain the full c.m.s. energy $\sqrt{s}$. This is an important practical feature which allows the two processes to be distinguished. The W dependence of the process

$$e^+e^- \rightarrow e^+e^-X$$

is shown to be (see section 1.6).

$$\frac{d\sigma}{dW} \approx \frac{1}{W} \ln\left(\frac{s}{W^2}\right)\sigma_{\gamma\gamma}(W)$$

where $\sigma_{\gamma\gamma}(W)$ is the cross-section for the process $\gamma\gamma \rightarrow X$. This clearly shows the strong W dependence present. It also shows that the cross-section rises logarithmically with s. The annihilation channel cross-section falls as $1/s$ due to the photon propagator present. Fig 1.3 shows the cross-sections for

$$e^+e^- \rightarrow e^+e^-\mu^+\mu^-$$
$$e^+e^- \rightarrow \mu^+\mu^-$$

and their dependence on E_{beam}. It can be seen that although the photon-photon interaction contains an α^4 term, because it has two e-γ vertices in the Feynman diagram as opposed to the annihilation channel's α^2 term, the photon-photon channel's logarithmic energy dependence overwhelms the $1/s$ dependence of the annihilation channel.

The other important feature of photon-photon events is that the final state particles are predominantly produced at small angles θ with respect to the beam-axis. There are three main reasons for this effect:

1) The photons radiated from the electron or positron are radiated with a distribution of the form;

$$\frac{d\sigma}{d\theta} \approx \frac{1}{\theta}$$

(ie a Bremsstrahlung spectrum)

2) Because the two photons in the reaction are not required to have the same energy then the final state X will usually have a strong boost along the beam-axis, often forcing the final state particles to low θ values in the lab.

3) The process $\gamma\gamma \rightarrow X$ is also usually strongly forward-backwards peaked (1.2). In order to demonstrate this fact it is useful to look at the angular distribution of the process $\gamma\gamma \rightarrow \mu^+\mu^-$ and compare it with that for $e^+e^- \rightarrow \mu^+\mu^-$

$$\frac{d\sigma}{d\Omega}(\gamma\gamma \rightarrow \mu^+\mu^-) \approx \left\{\frac{(1+\cos^2\theta)}{(1-\cos^2\theta)}\right\}$$

$$\frac{d\sigma}{d\Omega}(e^+e^- \rightarrow \mu^+\mu^-) \approx (1+\cos^2\theta)$$

(It should be noted that these are zero mass approximations). Fig 1.4 shows the photon-photon process is more strongly forward-backward peaked than the annihilation process. The process $\gamma\gamma \rightarrow q\bar{q}$ will tend to have similar kinematics.

Unfortunately, although at PETRA energies the total hadronic photon-photon cross-section is several orders of magnitude higher than that for the annihilation channel the actual numbers of events observed for the two processes are similar.

There are several important reasons for this small experimental acceptance. As has already been mentioned photon-photon events occur predominantly at low invariant masses. These events are characterised by low multiplicities and low momentum tracks which are difficult to trigger on. The particles produced are mainly at small angles, and either stay in the beam-pipe or are at such small angles that the detector cannot measure them.

1.4 Tagging

One of the important consequences of photon-photon interactions is that the electron and positron are both scattered. Although most stay in the beam-pipe some are scattered by angles θ which are large enough to be measured in the detector. The detection of these scattered beam leptons is a powerful way of identifying a photon-photon event. If the energy E' of the scattered electron and its scattering angle θ can be measured then using

$$Q_i^2 = 2E_b E'_i(1 - \cos\theta_i)$$

the Q^2 of the radiated virtual photon can be calculated.
This is known as 'tagging' and tagged events can be split into three main categories.
1) Double tagged: this is an event where both the electron and the positron are scattered into areas of the detector which can measure their properties. This provides a complete understanding of the kinematics of the final state X because the 4-vectors of the virtual photons can be calculated. This provides the Q^2 and invariant mass $W_{\gamma\gamma}$ of the final state. Double tagged events are almost entirely free of background contamination because of the almost unique signature provided by the detected electron and positron plus hadrons. However this method has two main drawbacks. Firstly, the scattering angle of the beam leptons falls as

$$\frac{d\sigma}{d\theta} \approx \frac{1}{\theta}$$

This causes the number of double tagged events to be small ($\approx$1% of all photon-photon events, assuming each tag needs to have a $\theta > 38$ mrads). Secondly the large measurement errors associated with the electron, positron mean that $W_{\gamma\gamma}$ cannot be measured very accurately (although the Two-Gamma group have done an analysis using this method, ref. 1.3).
2) Single tagged events: as the name suggests only one of the beam leptons is detected in the detector. The remaining one gives an "antitag". This means that because it is unobserved it is assumed to have remained in the beam-pipe (ie $\theta < 38$ mrads for CELLO). The antitagged leptons photon therefore has a low Q^2, and is nearly on mass-shell. The number of single tagged

events is much greater than that of double tagged events, being ≈ 10% of the total number of photon-photon events. Single tagged events, however, have a larger background contamination than double tagged events, the major contribution being from annihilation events which radiate an initial photon or high momentum pion which fakes an electron.

3) Untagged events: here neither the electron or positron is detected in the event. They are both assumed to have stayed in the beam-pipe. Because the leptons have low θ values the photons have a low Q^2. The majority (90%) of photon-photon events are untagged. The main problem in untagged photon-photon events is that there is a large annihilation background. This can only be removed by applying kinematical cuts to the data sample, ie rejecting high energy events and events without a strong boost along the beam-axis.

1.5 The Exact Photon-Photon Cross-Section Formalism

The exact cross-section for the process $e^+e^- \rightarrow e^+e^- X$ can be found by applying the Feynman rules (1.4) to the diagram shown in Fig 1.2. This results in the following matrix element.

$$M = -e^2\{\bar{u}(p_i', s_i')\gamma_\mu u(p_1, s_1)\}\frac{g^{\mu\alpha}}{q_i^2}T_{\alpha\beta}\frac{g^{\beta\nu}}{q_i^2}\{\bar{v}(p_2', s_2')\gamma_\nu v(p_2, s_2)\}$$

The matrix element for the process contains two Dirac spinors u for the electron and v for the positron with momentum p and spin s. The e^2 term arises from the pointlike coupling of the photons to the leptons. Each photon introduces a γ matrix and a photon propagator (proportional to $1/q_i^2$) The matrix $T_{\alpha\beta}$ is the tensor describing the process $\gamma\gamma \rightarrow X$. We now introduce an unnormalized density matrix to describe the virtual photon generated by lepton i.

$$\rho_i^{\alpha\beta} = \frac{1}{-2q_i^2}\sum_{\text{spins}} \bar{u}(p_i', s_i')\gamma^\mu u(p_i, s_i)\,\bar{u}(p_i', s_i')\gamma^\nu u(p_i, s_i)$$

Because this matrix is non-diagonal the photons produced are polarized. The summation is over the spins of the incoming leptons. Combining the matrix element for the reaction with the phasespace terms yields the cross-section:

$$\sigma = \frac{(4\pi\alpha)^2}{q_1^2 q_2^2} \rho_1^{\mu\mu'} \rho_2^{\nu\nu'} T^{*\mu\mu'} T^{\nu\nu'} \cdot \frac{(2\pi)^4 \delta(q_1 + q_2 - k) d\Gamma}{4\left\{(p_1 p_2)^2 - m_1^2 m_2^2\right\}^{1/2}} \frac{d^3 p_1' d^3 p_2'}{2E_1 E_2 (2\pi)^6}$$

where $d\Gamma$ is the Lorentz invariant phasespace element summed over j final state particles

$$d\Gamma = \prod_j \frac{d^3 k_j}{2E_j (2\pi)^3}$$

After integrating over the final state X the cross-section will include the quantity

$$W^{\mu'\nu'\mu\nu} = \frac{1}{2} \int T^{*\mu'\nu'} T^{\mu\nu} (2\pi)^4 \delta(q_1 + q_2 - k) d\Gamma$$

This is a rank 4 tensor and contains 256 (4^4) terms. Fortunately this number can be considerably reduced by considering invariance principles. After taking T invariance, gauge invariance, conservation of momentum, parity and time reversal into account the number of independent terms reduces to eight (1.4), which depend on W, q_1^2, q_2^2. These can be expressed in the helicity basis denoting four cross-sectional terms and four interference terms for photons with transverse polarization T (which can have helicity ±1) and longitudinal photons (which have helicity 0). These give terms which depend on the definite polarization states of the two photons (1.4):

$$\begin{aligned}
W_{TL} &= W_{+0,+0} && = 2\sqrt{X}\,\sigma_{TL} \\
W_{LT} &= W_{0+,0+} && = 2\sqrt{X}\,\sigma_{LT} \\
W_{LL} &= W_{00,00} && = 2\sqrt{X}\,\sigma_{LL} \\
W_{TT}^{\tau} &= W_{++,--} && = 2\sqrt{X}\,\tau_{TT} \\
W_{TL}^{\tau} &= \frac{1}{2}(W_{++,00} + W_{0+,0+}) && = 2\sqrt{X}\,\tau_{TL} \\
W_{TT}^{a} &= \frac{1}{2}(W_{++,++} - W_{+-,+-}) && = 2\sqrt{X}\,\tau_{TT}^{a} \\
W_{TL}^{a} &= \frac{1}{2}(W_{++,00} - W_{0+,-0}) && = 2\sqrt{X}\,\tau_{TL}^{a}
\end{aligned}$$

where X is the Moller flux factor

$$X = (q_1 q_2) - q_1^2 q_2^2$$

Integrating over the final state X now provides the total cross-section in terms of photon-photon cross-sections σ_{ab} and photon-photon interference terms τ_{ab} (1.4):

$$d\sigma_{e^+e^- \to e^+e^- X} = \frac{\alpha^2}{16\pi^4 Q_1^2 q_2^2} \left\{ \frac{(q_1 q_2)^2 - q_1^2 q_2^2}{(p_1 p_2)^2 - m_1^2 m_2^2} \right\}^{\frac{1}{2}} \cdot$$

$$\left\{ \begin{array}{l} 4\rho_1^{++}\rho_2^{++}\sigma_{TT} + 2\rho_1^{++}\rho_2^{00}\sigma_{LT} + 2\rho_1^{00}\rho_2^{++}\sigma_{TT} \\ + \rho_1^{00}\rho_2^{00}\sigma_{LL} + 2\left|\rho_1^{+-}\rho_2^{+-}\right| \cos 2\bar{\varphi}\tau_{TT} \\ - 8\left|\rho_1^{+0}\rho_2^{+0}\right| \cos \bar{\varphi}\tau_{TL} + A\tau_{TT}^a + B\tau_{TL}^a \end{array} \right\}$$

$$\cdot \frac{d^3 p_1'}{E_1'} \frac{d^3 p_2'}{E_2'}$$

where φ is the azimuthal angle between the scattering planes of the leptons in the $\gamma\gamma$ centre of mass frame. For untagged or single tagged events this cannot be measured and the integration from 0 to 2π causes these terms to vanish. The values A and B are non zero only for polarized lepton beams. Consequently for PETRA data these interference terms vanish. Due to symmetry arguments

$$\sigma_{TL}(W, q_1^2, q_2^2) = \sigma_{LT}(W, q_1^2, q_2^2)$$

leaving three independent terms which need to be considered.

$$\sigma_{TT}(W, q_1^2, q_2^2) \to \sigma_{TT}(W)$$
$$\sigma_{TL} \propto q_1^2$$
$$\sigma_{LT} \propto q_2^2$$
$$\sigma_{LL} \propto q_1^2 q_2^2$$

The longitudinal terms go to zero as q^2 goes to zero, because real photons cannot be longitudinally polarized. For untagged events ${q_1}^2, {q_2}^2 \to 0$, and all the terms vanish except $\sigma_{TT}(W)$ leaving:

$$d\sigma_{e^+e^- \to e^+e^-X} = \frac{\alpha^2}{16\pi^4 Q_1^2 q_2^2}\left\{\frac{(q_1q_2)^2 - q_1^2q_2^2}{(p_1p_2)^2 - m_1^2m_2^2}\right\}^{\frac{1}{2}} \cdot \{4\rho_1^{++}\rho_2^{++}\sigma_{TT}\} \cdot \frac{d^3p'_1}{E'_1}\frac{d^3p'_2}{E'_2}$$

However for single tagged events q_1^2 is not small and the σ_{TL} terms are not negligible, and the cross-section becomes

$$d\sigma_{e^+e^- \to e^+e^-X} = \frac{\alpha^2}{16\pi^4 Q_1^2 q_2^2}\left\{\frac{(q_1q_2)^2 - q_1^2q_2^2}{(p_1p_2)^2 - m_1^2m_2^2}\right\}^{\frac{1}{2}} \cdot$$

$$\{4\rho_1^{++}\rho_2^{++}\sigma_{TT} + 2\rho_1^{++}\rho_2^{00}\sigma_{TL}\} \cdot \frac{d^3p'_1}{E'_1}\frac{d^3p'_2}{E'_2}$$

It is important to note that the above equation can be rewritten as a product of a cross-section for $\gamma\gamma \to X$ and a term L which describes the photon fluxes emitted by the leptons. This is often called a luminosity function.

$$d\sigma_{e^+e^- \to e^+e^-X} = \int dL(p'_1, p'_2)\sigma_{\gamma\gamma}(W, q_1, q_2)dq_1dq_2$$

1.6 Equivalent Photon Approximations

It is very useful to split the above equation into two parts, allowing one to generate photon fluxes to combine with a suitable differential cross-section for $\gamma\gamma \to X$. There are some important approximations which are required before this can be done, the most important being the neglecting of the contribution of longitudinally polarized photons to the cross-section. This is acceptable under normal conditions for untagged and single tagged events, but errors will creep in if the tagging angle is allowed to become large. It is also assumed that σ_{TT} is independent of Q^2. For the case of single tagged events the cross-section can be written as (1.5):

$$d\sigma_{e^+e^- \to e^+e^-X} = L^{TT}[\sigma^{TT} + \varepsilon\sigma^{TL}]\frac{dp'_1}{E'_1}\frac{dp'_2}{E'_2}$$

and L^{TT} can be split into a term Γ_t describing the tagged lepton scattered into a range $\theta^{MIN} < \theta < \theta^{MAX}$ and an untagged term N_γ for the quasi-real photons with scattering angles $\theta_2{}^{MAX} < \theta^{MIN}$.

$$d\sigma_{e^+e^- \to e^+e^-X} = \Gamma_t[\sigma_{TT} + \varepsilon\sigma_{TL}]N_\gamma(z_2, \theta_2^{MAX})dz_2, dE_1', d\Omega_1'$$

where

$$\Gamma_t = \frac{\alpha E_1'(1+(1-y)^2)}{2\pi^2 Q_1^2 y}$$

and

$$N_\gamma(z_2, \theta_2^{MAX}) = \frac{\alpha}{\pi}\frac{1}{z_2}\left[(1+(1-z^2))\ln\left(\frac{E_b\theta_2^{MAX}(1-z_2)}{m_e z_2}\right) - 1 + z_2\right]$$

and

$$y = \frac{(q_1q_2)}{(p_1q_2)} \approx 1 - \left(\frac{E_1'}{E_b}\right)\cos^2\left(\frac{\theta_1}{2}\right) \qquad z_2 = \frac{E_{\gamma 2}}{E_b}$$

In terms of y, ε can be expressed as;

$$\varepsilon(y) = \frac{\rho_1^{00}}{2\rho_1^{++}} = \frac{2(1-y)}{1+(1-y)^2}$$

It should be noted that Γ_t and ε depend only on the momentum of the scattered lepton and N_γ only on the untagged lepton. The fluxes are shown to be separated into a flux Γ_t of virtual photons emitted from a lepton which scatter off N_γ nearly real photons of energy z_2E_b into a solid angle dΩ with energy E_1'. This method is accurate to within 1% for CELLO energies and angles (1.5).

For untagged events more assumptions can be made: since both photons are quasi-real, only the σ_{TT} needs to be included and it can also be assumed that the cross-section $\gamma\gamma \to X$ depends only on W, ie $\sigma_{TT}(W)$. We use the Weisacker-Williams or equivalent photon approximation (1.6), that is that dL/dz can be expressed as the product of two fluxes of real photons from each lepton-γ vertex. Then the number of photons dN_γ in the scaled photon energy range dx where

$$x = \frac{E_\gamma}{E_b}$$

can be written as

$$\frac{dN_\gamma}{dx} = \left(\frac{\alpha}{\pi}\right)\left(\frac{1+(1-x)^2}{x}\right)\ln\frac{2E_b}{m_e},$$

and to a leading-log approximation this provides a differential luminosity function

$$\frac{dL}{dz} = 4\left(\frac{\alpha}{\pi}\right)^2 \frac{1}{z}\left(\ln\frac{2E_b}{m_e}\right)^2 \left\{2\left(1+\frac{1}{2}\sigma\right)^2 \ln\frac{1}{\sigma} - (1-\sigma)(3+\sigma)\right\}$$

where $z^2 = \sigma \approx x_1 x_2$. If both photons are integrated over all energies subject to the constraint that

$$W^2 = 4E_{\gamma 1}E_{\gamma 2}$$

then (1.2):

$$\frac{d\sigma}{dW} \approx \frac{1}{W}\ln\left(\frac{s}{W^2}\right)\sigma_{\gamma\gamma}(W)$$

The errors associated with these approximations have been examined by various authors and the conclusion is that the leading-log estimation can overestimate the luminosity by up to ~10% depending on W and s (1.7).

1.7 The Production of Hadrons from Photon-Photon Collisions

This analysis is concerned with the processes by which photons collide with each other and interact to produce final state hadrons which can be detected. Having seen in the previous section how the photons are radiated by the beam leptons, we now concentrate on the interaction $\gamma\gamma \rightarrow X$. Photons can form low mass C = +1 resonances which decay into hadrons. Photons can also interact through a quark-antiquark pair being formed from the vacuum. In its simplest form this is a zeroth order QCD interaction where gluon-gluon and quark-gluon interactions are ignored, and corresponds to the Quark Parton Model (QPM). The photons couple to the quarks' fractional charge, the reaction being similar in nature to;

$$e^+e^- \rightarrow e^+e^-\mu^+\mu^-$$

where the quark takes the place of the muon as shown in fig 1.5. This is a fundamental pointlike QED process with the quarks coupling directly via their charge to the photons. This can result in large momentum transfers and the high transverse momentum (p_t) collisions characteristic of point-like interactions.

However it is well known from photoproduction experiments, ie e-p (1.8), that photons can couple to neutral vector mesons (ρ, ω, ϕ) by fluctuating to bound quark-antiquark states with the same quantum numbers as the photon. These mesons then collide, interacting strongly but in a 'softer non-pointlike' manner than in QPM, the momentum transfers being smaller. These collisions are characterised by their low Q^2, low p_t nature. This process is known as vector-meson-dominance or the vector dominance model (VDM) and is illustrated in fig 1.6. This is a phenomenological model used to describe the hadronic region where non-perturbative QCD is dominant.

The QPM and VDM processes are at opposite kinematic extremes and there is a middle ground where both processes will merge into the other, possibly combining perturbative QCD in some way. This may for instance, may be exhibited in "multijet events" where hard gluons are emitted. If so, then due to the small final state hadronic masses being produced, these events will be difficult to isolate from the overall QPM and VDM processes which dominate.

1.8 The Vector Meson Dominance Model

VDM is a parameterised model which attempts to describe the coupling of photons to neutral vector mesons which interact to form final state hadrons (1.9). These interact through a soft hadronic process and display a distinct W, Q^2, p_t dependence. This section explains these interactions.

The VDM cross-section can be factorised into a term that depends on the hadronic mass W, and a Q^2 term (1.9), normally written as

$$\sigma_{\gamma\gamma}^{VDM}(W, q_1^2, q_2^2) = \sigma_{\gamma\gamma}^{VDM}(W)F(q_1^2)F(q_2^2)$$

This splits the cross-section into two form factors for the photon propagators, which depend on their invariant mass (Q^2), and a term for their scattering

which depends only on the hadronic mass of the final $\gamma\gamma$ system. The W dependence of the process is usually split into two terms (1.9).

$$\sigma_{\gamma\gamma}^{VDM}(W) = A + \frac{B}{W}$$

The first term A is independent of W and is due to Pomeron exchange between the two vector mesons. An estimate of the magnitude of this component can be derived through an indirect method (Fig 1.7) as follows. Pomeron exchange has been studied in pp and γp collisions. Splitting the cross-sections for these processes into a product of two terms, one for each interaction leads to the relationship;

$$\sigma_{\gamma\gamma}^{VDM}(W \to \infty) = \frac{\sigma_{\gamma p}(W \to \infty)^2}{\sigma_{pp}(W \to \infty)} = \frac{(120\mu b)^2}{60mb} = 240nb$$

The second term B is due to higher order Regge trajectories and has been estimated to be 270nb.

There is a form factor for each virtual photon which depends on its Q^2. This form factor can be split into terms for the contribution from transverse and longitudinal components.

$$F_{VDM}(Q^2) = F_T(Q^2) + F_L(Q^2)$$

The simplest model is the ρ-meson propagator which only includes the exchange of transversely polarised ρ-mesons.

$$F_\rho(Q^2) = \frac{1}{\left(1 + \frac{Q^2}{m_\rho^2}\right)^2}$$

However, this model ignores the ω and φ vector mesons and the mesons' possible longitudinal polarisations. There is evidence (1.9) that these are important and this leads to the Vector Meson Dominance Model with a form factor given by

$$F_{VDM}(Q^2) = \sum_{\upsilon=\rho,\omega,\varphi} r_\upsilon \frac{1+\frac{Q^2}{4m_\upsilon^2}}{\left(1+\frac{Q^2}{m_\upsilon^2}\right)^2}$$

The terms r_υ are taken from the TPC analysis (1.10).

$$r_\rho = 0.833$$
$$r_\omega = 0.103$$
$$r_\varphi = 0.064$$
$$m_\rho = 0.769\text{GeV}$$
$$m_\omega = 0.783\text{GeV}$$
$$m_\phi = 1.020\text{GeV}$$

where υ sums over the vector mesons with masses m and mixing ratios r.

A further refinement of this model suggested by ref. 1.9 includes an extra term to take into account the continuum of higher mass states. This is the Generalised Vector Meson Dominance Model (GVDM).

$$F_{GVDM}(Q^2) = \sum_{\upsilon=\rho,\omega,\varphi} r_\upsilon \frac{1+\frac{Q^2}{4m_\upsilon^2}}{\left(1+\frac{Q^2}{m_\upsilon^2}\right)^2} + \frac{0.22}{\left(1+\frac{Q^2}{m_0^2}\right)}$$

The values of the constants used are

$$r_\rho = 0.65$$
$$r_\omega = 0.08$$
$$r_\varphi = 0.05$$
$$m_\rho = 0.769\text{GeV}$$
$$m_\omega = 0.783\text{GeV}$$
$$m_\phi = 1.020\text{GeV}$$
$$m_0 = 1.4\text{GeV}$$

The different Q^2 dependences for the three models are shown in fig 1.8. As can be seen the GVDM and VDM terms extend to higher Q^2 than the simple ρ-VDM term.

The last of the important kinematical characteristics is the transverse momentum (p_t) spectrum of the final state particles. As before, hadronic data provides us with information on this. There are two important experimental facts which must be incorporated into the model.
1) The particle p_t should fall off as an exponential function of the form (1.11):

$$\frac{d\sigma}{dp_T^2} \approx e^{-kp_T^2}$$

typical values for k being ≈ 5-7 GeV^{-2}. Thus VDM processes will be characterised by low p_t events.
2) The mean p_t of the particles with respect to the collision axis $\langle p_t \rangle$ is independent of the hadronic mass of the event and is limited to ~ 300MeV. This is one of the characteristics of jets, that is that $\langle p_t \rangle$ does not grow with energy as does the momentum of particles longitudinally to the collision axis $\langle p_l \rangle$. The VDM predicts two narrow back to back jets of hadrons from the fragmenting vector mesons (in the $\gamma\gamma$ cms). These will be produced at predominantly low angles with respect to the beam axis due to the limited p_t of the process.

1.9 The GLM Model

This model (1.17) firstly assumes that the pointlike component of the data is well described by the QPM process described below and attempts to describe the hadronic component of the data with a parameterised model. The parameterisation is done using data from the PETRA and Novosibirsk experiments. They present a hadronic cross-section which is a function of W and Q^2 (note this is not factorised into separate components as in the VDM ansatz).

$$\sigma_{\gamma\gamma}^{HAD}(Q^2, W) = (1-x)^a\left[\frac{A}{(Q^2+b)} + \frac{B}{W\sqrt{Q^2+b}}\right]$$

The parameters A, B, a, b given in ref 1.24 are A = 36.8 ± 10.9 nb GeV, B = 252.5 ± 36.8 nb GeV, a = 1.23 ± 0.22, b = 0.26 ± 0.05 GeV. At $Q^2 = 0$ this gives

$$\sigma_{\gamma\gamma}^{HAD}(Q^2, W) = A_1 + \frac{B_1}{W} \qquad \left(A_1 = \frac{A}{b},\quad B_1 = \frac{A}{\sqrt{b}}\right)$$

similar to the VDM formalism for the W dependent component for the cross-section. However at high Q^2 the function exhibits Bjorken scaling (ie it is only a function of x).

1.10 The Quark Parton Model

Unlike the VDM model, the quark parton model is exactly calculable from QED (1.12). The assumptions made are that the photons couple to the charge of a quark-antiquark pair. The quarks are assumed to have no strong interactions and therefore all QCD corrections (gluon emission, exchange) are specifically ignored. The kinematics of this process are similar to the QED process

$$e^+e^- \rightarrow e^+e^-\mu^+\mu^-$$

where the muons replace quarks. The standard fractional charges for the quarks are used. Because the free quark masses are not known the standard constituent masses are used. Fortunately the cross-section for this process is relatively insensitive to the mass, especially in the important region of high p_t. For this analysis the up, down, strange and charm quarks are treated separately and their different fragmentation characteristics are taken into account. The only difference between $q\bar{q}$ production and $\mu\mu$ is a summation over the 3 quark colours introducing an increase in the cross-section by a factor of 3. The masses used for the u, d, s, c quarks were 0.3 GeV, 0.3 GeV, 0.5 GeV, 1.5 GeV respectively. The W dependence of the process, as calculated in ref. 1.4, is

$$\sigma_{\gamma\gamma}^{QPM}(W) = \frac{4\pi\alpha^2}{W^2}\sum_q e_q^4\left[\left(1+\frac{4m_q^2}{W^2}-\frac{8m_q^4}{W^4}\right)L-\left(1+\frac{4m_q^2}{W^2}\right)\Delta t\right]$$

where

$$L = 2\log\left[\frac{W}{2m_q}+\sqrt{\frac{W^2}{4m_q^2}-1}\right]$$

and

$$\Delta t = \sqrt{1 - \frac{4m_q^2}{W^2}}$$

The summation includes all quark flavours with mass $2m_q < W$. This can be simplified, if terms of order (m_q^2/W^2) are ignored, to

$$\sigma_{\gamma\gamma}^{QPM}(W) = \frac{4\pi\alpha^2}{W^2} \sum_q e_q^4 \left[\log\left(\frac{W^2}{m_q^2}\right) - 1 \right]$$

This demonstrates a $\approx 1/W^2$ fall for QPM, contrasted to an approximately flat W cross-section for VDM. Fig 1.9 contrasts the cross-sections for the QPM and VDM at $Q^2=0$. This shows that the QPM process is enhanced in the low W region and the VDM will be dominant at high W. It should be noted that the cross-section is dominated by the charge 2/3 quarks, namely the u and (above its threshold) the c. Also, the above approximation $m_q^2 << W^2$ does not hold for the c quark at the W values of most of our present data.

QPM exhibits a much flatter Q^2 dependence than VDM and, as already stated can be exactly calculated in QED. The cross-section can be split up into two components, namely, one component for the interaction between two transversely polarised photons and one component for the interaction between a longitudinal photon and a transverse photon. The cross-section can be written as

$$\sigma_{\gamma\gamma}^{QPM} = \sigma_{TT}^{QPM} + \sigma_{LT}^{QPM}$$

At low Q^2 only the first term contributes whereas as Q^2 increases the second term becomes important. Neglecting terms of order m_q^2/W^2 gives (1.4)

$$\sigma_{TT}^{QPM} = \frac{4\pi\alpha^2}{W^2\left(1 + \frac{Q^2}{W^2}\right)} \left\{ \ln\left(\frac{W^2}{m_q^2}\right)\left[1 + \frac{Q^4}{W^4}\right] + \frac{Q^2}{W^2} - 1 \right\}$$

and

$$\sigma_{LT}^{QPM} = \frac{4\pi\alpha^2}{W^2\left(1+\frac{Q^2}{W^2}\right)}\left(\frac{4Q^2}{W^2}\right)$$

Fig 1.10 shows the Q^2 dependence for VDM and QPM . It should be noted that whereas VDM exhibits a strong fall with Q^2. The QPM process is flat for $W^2 >> Q^2$ and for $Q^2 >> W^2$ it shows a $1/Q^2$ fall.

The p_t distribution for the primary quarks produced is the same as for the process:

$$e^+e^- \rightarrow e^+e^-\mu^+\mu^-$$

and can be shown to be

$$\frac{dN}{dp_t^2} \propto \frac{1}{p_t^4}$$

as expected from dimensional considerations. These quarks fragment into jets of particles which will have limited transverse momentum with respect to the original parton direction (or jet axis) of mean value ~ 300 MeV. Thus the particle p_t distribution should follow that of the original quarks. It should be remembered throughout that this hard scattering processes p_t dependence has a high p_t tail which dominates over the VDM process which exhibits a much stronger fall-off with p_t.

1.11 Higher Order Processes

QPM can be regarded as the lowest order QCD contribution expected to produce high transverse momentum (p_t) jets in photon-photon reactions. There are, however, higher order QCD diagrams which can form high p_t jets when for instance a quark emits a high p_t gluon. It is important to understand these processes, as they may contribute appreciably to the cross-section at medium and high p_t. A comprehensive study of these processes has been presented by Brodsky et al (1.13). The momentum transfers are assumed to be large allowing an approximate method to be used to calculate the hard scattering process in the Feynman diagram (see Fig 1.11). Here a and b are the components of particles A and B which undergo a hard scattering into C and X, where C is detected at high transverse momentum and could

be a hadronic jet. We define the Mandelstam variables as

$$\hat{s} = (p_a + p_b)^2$$
$$\hat{t} = (p_a - p_c)^2$$
$$\hat{u} = (p_b - p_c)^2$$

The cross-section for the hard scattering process (boxed in fig 1.11) can now be written as (1.15):

$$\frac{E_c d\sigma}{d^3 p_c}(AB \rightarrow CX) = \int_0^1 \int_0^1 dx_a dx_b G_{a/A}(x_a) G_{b/B}(x_b)$$
$$\times \frac{d\sigma}{d\hat{t}}(ab \rightarrow CX) \frac{\hat{s}}{\pi}(\hat{s} + \hat{t} + \hat{u})$$

where $G_{i/I}(x_i)$ is the fragmentation function giving the probability of finding a parton i with fractional momentum x_i within particle I. Thus the diagram can be seen as a combination of two processes: firstly the particles emitting partons, a soft fragmentation, and secondly these partons undergoing a hard scattering interaction. Hard scattering processes are naturally specified by their p_t dependence. This led Brodsky and Farrar (1.14) to parameterise the subprocess (ab $\rightarrow$ CX) in the formalism

$$\frac{d\sigma}{d^3 p / E} = \frac{1}{(p_t^2)^{N-2}} F(\theta_{cm}, x_T)$$

where N is the number of constituent partons involved in the hard scattering process, F is a function of C's angle in the centre of mass with respect to the a, b collision axis, and x_T is its fractional momentum.

$$x_T = \frac{2p_T}{\sqrt{s}}$$

Because the process (ab $\rightarrow$ CX) is a strong reaction (ie between quarks and gluons) an additional factor $\alpha_s(p_t^2)$ must be included, which includes the QCD scale parameter Λ. However to first order this term can be neglected, the dependence on p_t^N being dominant. For the values of x_T which can be probed in this analysis, then for 2-jet events $F(x_T)$ can be shown (1.15) to be

$$F(x_T) \approx \ln \frac{2}{x_T}$$

This causes the cross-section to fall slightly faster than p_t^{-4}, but the effect does not invalidate this method. Fig 1.12 shows the theoretical dependence on x_r for some p_t^{-4} processes. The hard scattering component is boxed, each extra γ-q vertex introduces an extra term $(1-x_r)$, and each γ-meson vertex introduces an extra term $(1-x_r)^2$ where

$$x_r = \frac{E_{jet}}{E_b}$$

Notice that as $x_r \rightarrow 1$ the higher order terms are suppressed relative to the lowest order QPM term. It is interesting to note that the VDM process can contribute to these diagrams.There are other diagrams which can produce multijet events known as higher twist diagrams. These fall as p_t^{-6} but are thought to contribute less than 10% falling with p_t (1.13, 1.16, 1.17). Very little is known about these higher order processes and the exact amount that they should contribute to the total photon-photon cross-section. One reason for this is that it is very difficult to distinguish between 4, 3, 2 jet events at the typical $W_{\gamma\gamma}$ being studied (~ 5 GeV). The third jet will have little energy and the event will rarely appear 3-jet like, the third jet being smeared into another, or lost due to detector acceptance, making the event appear more spherical than the two-jet QPM events. However fig 1.13 shows the expected ratio of 3/2 , 4/2 and (2+3+4)/2 jet ratios (1.16), and as can be seen at low x_t these are quite large. This calculation was done for untagged (quasi-real photons) events.

Recent studies on the p_t and Q^2 dependence of higher order multijet processes (1.18) have produced theoretical predictions for the total yield of the higher order processes as compared to the lowest order QPM term. These predict excesses over QPM of ~ 50% which fall only weakly with increasing p_t, Q^2.

These diagrams are firmly predicted by QCD and therefore it is interesting to see if they are present in the data.

1.12 Background Processes

Apart from the processes described above, there are other processes which contaminate the hadronic photon-photon data. We consider here the main background processes.

1) Multihadronic annihilation events. These events occur when the positron and electron annihilate through a single virtual photon to a quark-antiquark pair (Fig 1.14).

$$e^+e^- \rightarrow q^+q^-$$

This process usually carries the complete centre of mass energy from the two leptons producing an event with $\sqrt{s}$ = 35 GeV. These can of course usually be separated from photon-photon data because of the energy in the event. If however the jets travel down the beam-pipe then a large amount of the event's energy goes undetected. This considerably distorts the event and can make it appear similar to a photon-photon event. As well as this, the first order QED correction to the above process is where one lepton radiates a photon before annihilating. This has a bremsstrahlung spectrum $1/E_\gamma$ which means the energy removed from the quark-antiquark pair is usually small. When the energy radiated by the initial photon becomes large then the quark-antiquark pair will have a low hadronic mass W as well as a boost down the beam axis, very similar to a photon-photon event. Moreover the centre of mass energy $\sqrt{s}$ of such an annihilation event will be substantially lowered, increasing the cross-section which is proportional to $1/s$. Sometimes the hard photon can simulate a 'tag' and look like a tagged photon-photon event. Because of the nature of this process the events will be produced at high p_t. It is therefore very important that this process is completely understood and that QED radiative corrections are taken into account.

2) A second important class of backgrounds is due to the two processes

$$e^+e^- \rightarrow \tau^+\tau^-$$

and

$$e^+e^- \rightarrow e^+e^-\tau^+\tau^-$$

These channels simulate photon-photon events when the τ decays into an invisible neutrino and hadrons. For

$$e^+e^- \rightarrow \tau^+\tau^-$$

the τ will carry approximately the full beam energy. The neutrino will carry a fraction of this, and if the decay is into hadrons it could fake a photon-photon event. The case is similar for the

$$e^+e^- \rightarrow e^+e^-\tau^+\tau^-$$

except that the events will have less energy on average.

3) Beam gas/pipe backgrounds can occur when a beam lepton interacts with a nuclei present in the vacuum or when an off momentum beam lepton interacts with the beam pipe. These are discussed later.

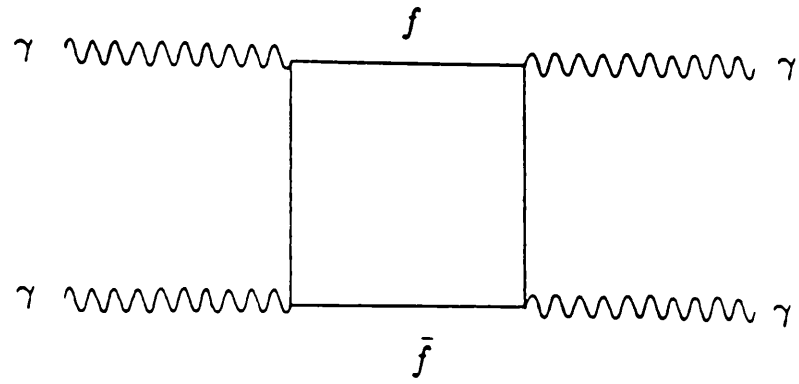

Fig 1.1 The lowest order box diagram for photon-photon scattering via a fermion-antifermion loop.

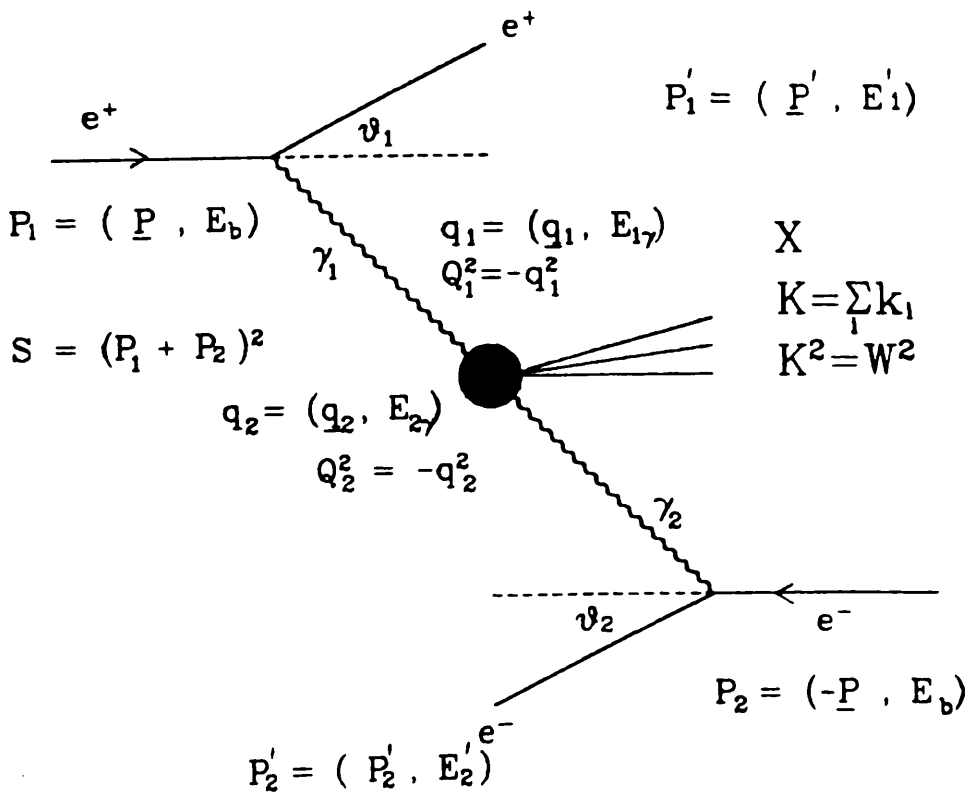

Fig 1.2 The basic notation for a photon-photon reaction.

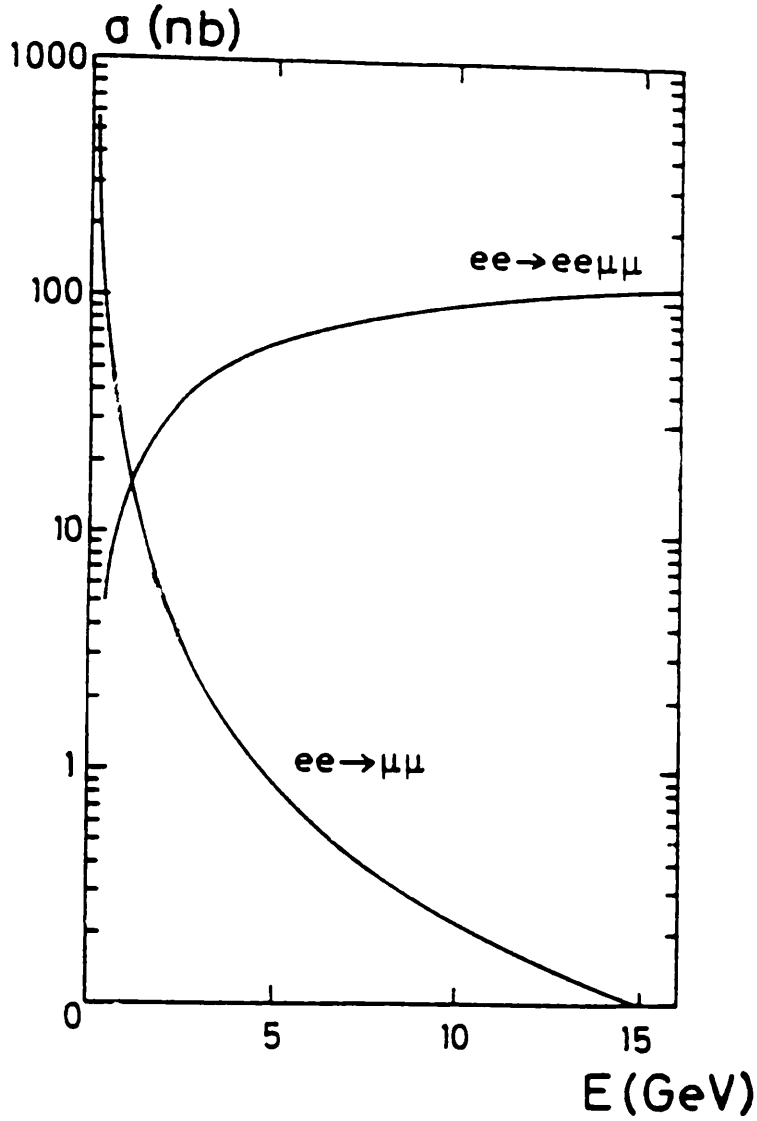

Fig 1.3 The cross sections for μμ production through the single photon channel and the two-photon channel.

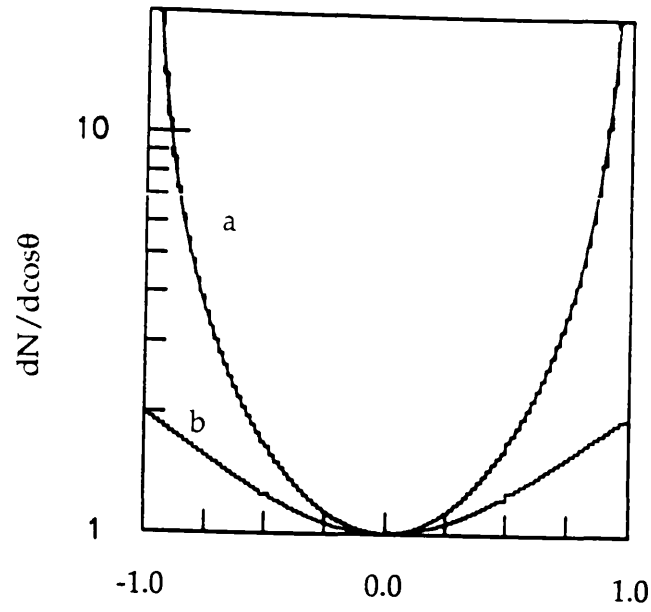

Fig 1.4 The angular distributions (in cosθ) for $\gamma\gamma \rightarrow \mu\mu$ (a) and $e^+e^- \rightarrow \mu\mu$ (b).

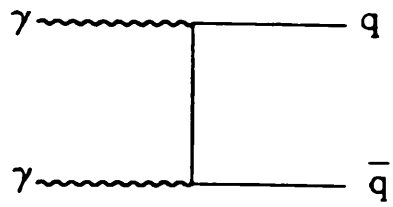

Fig 1.5 The Feynman diagram for the basic quark parton model. A quark-antiquark pair coupling to two photons. The quarks then fragment to hadrons

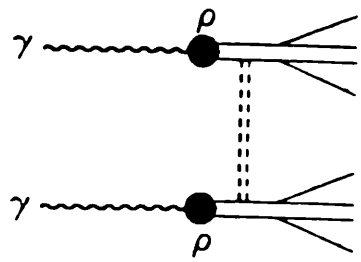

Fig 1.6 Two photons coupling to rho mesons which interact through Pomeron exchange causing fragmentation into hadrons.

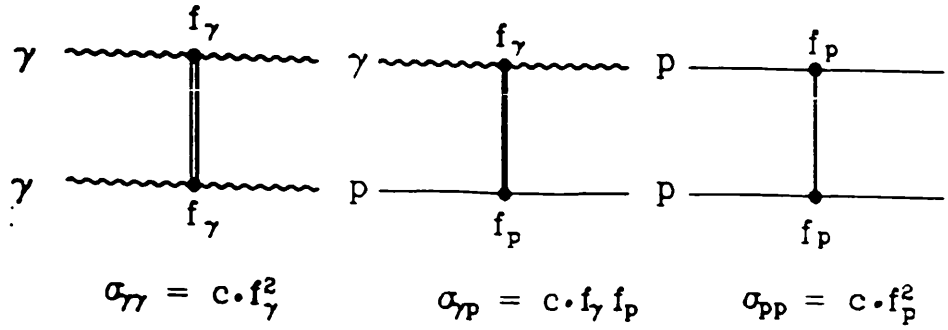

Fig 1.7 The cross-sections for pomeron exchange in $\gamma\gamma$, γp and pp interactions.

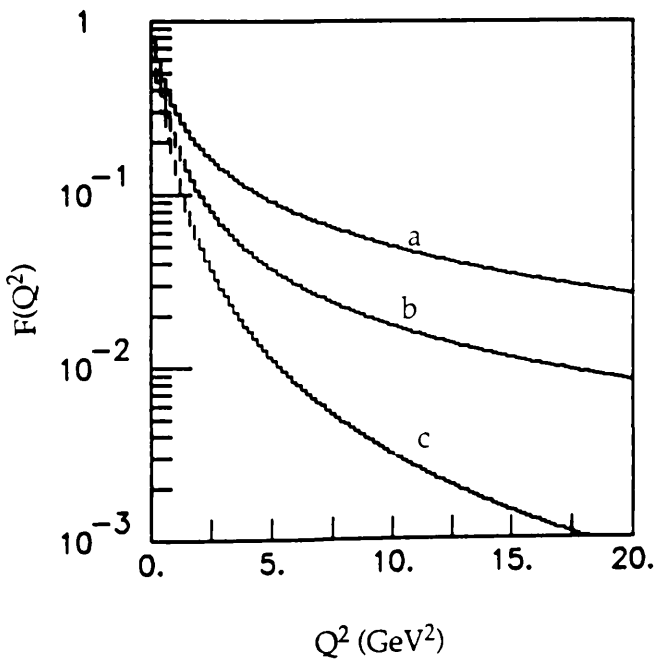

Fig 1.8 The Q^2 dependence of the GVDM (a), VDM (b) and ρ-VDM (c) form-factors.

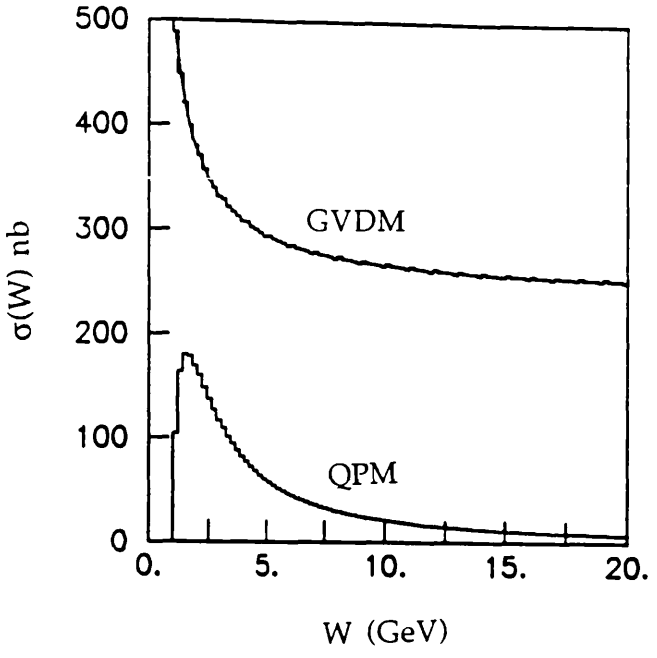

Fig 1.9 The W dependence of the QPM and GVDM processes at $Q^2 = 0$

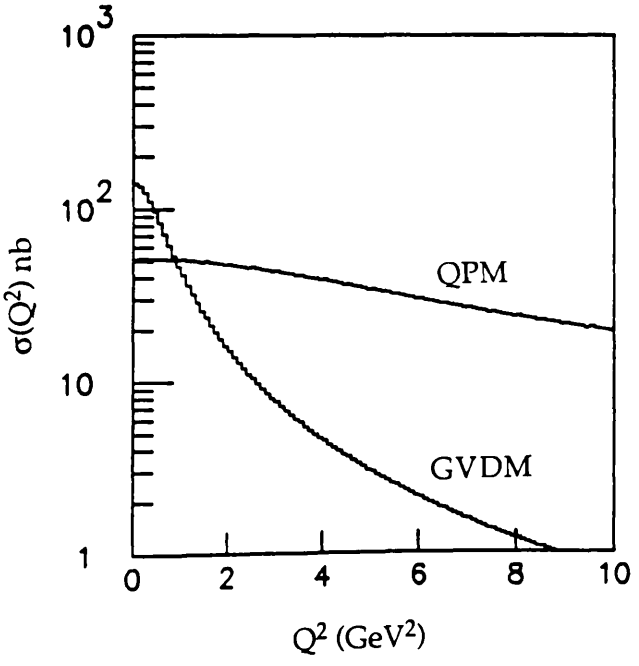

Fig 1.10 The Q^2 dependence of the QPM and GVDM processes at W = 10 GeV

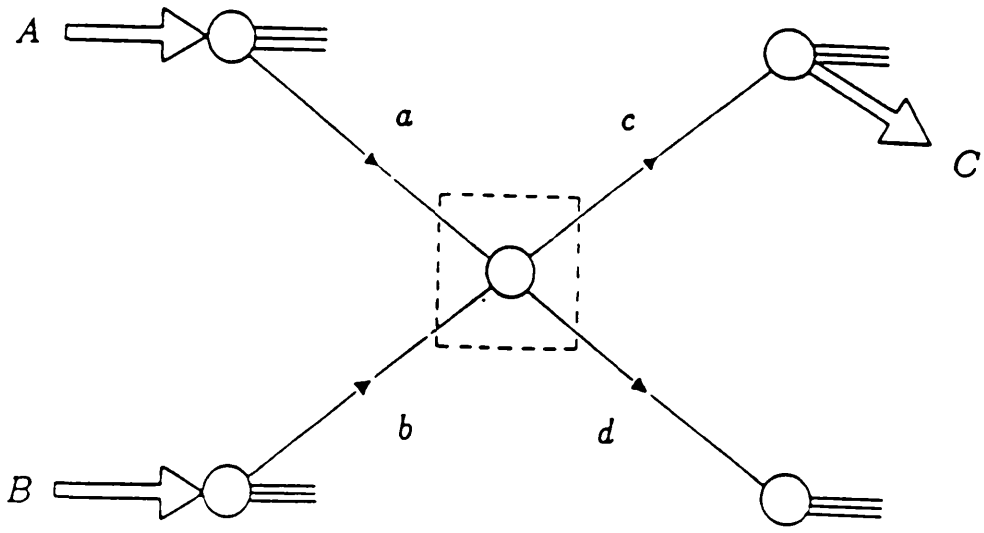

Fig 1.11 The diagram for the process A+B→C+X which includes a hard scattering component a+b→c+x

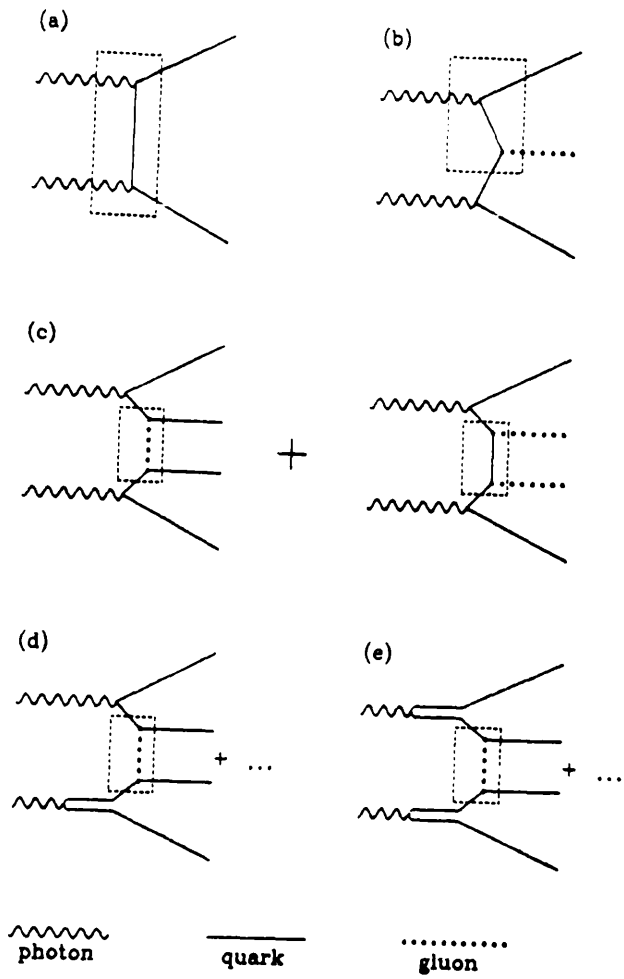

a) $\gamma\gamma \rightarrow q\bar{q}$ $\quad \frac{d\sigma}{dp_t^2} \propto (1 - x_r) p_t^{-4}$

b) $\gamma\gamma \rightarrow q\bar{q}g$ $\quad \frac{d\sigma}{dp_t^2} \propto (1 - x_r)^2 p_t^{-4}$

c) $\gamma\gamma \rightarrow q\bar{q}q\bar{q}$ $\quad \frac{d\sigma}{dp_t^2} \propto (1 - x_r)^3 p_t^{-4}$

$\gamma\gamma \rightarrow q\bar{q}gg$ $\quad \frac{d\sigma}{dp_t^2} \propto (1 - x_r)^3 p_t^{-4}$

d) $\gamma\rho \rightarrow q\bar{q}q\bar{q}$ $\quad \frac{d\sigma}{dp_t^2} \propto (1 - x_r)^4 p_t^{-4}$

e) $\rho\rho \rightarrow q\bar{q}q\bar{q}$ $\quad \frac{d\sigma}{dp_t^2} \propto (1 - x_r)^5 p_t^{-4}$

Fig 1.12 The Feynman diagrams for some p_t^{-4} processes and their theoretical dependence on x_r.

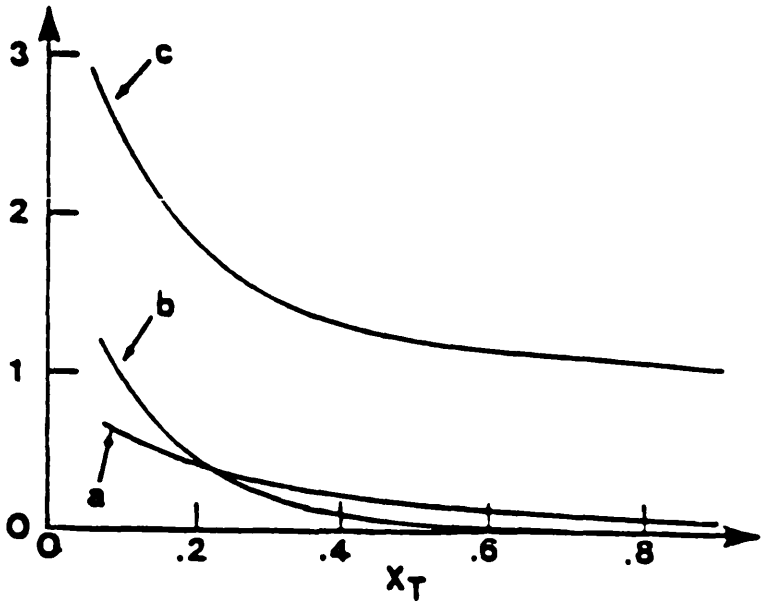

Fig 1.13 The jet ratios for photon-photon jet production
a) 3 Jet / 2 Jet
b) 4 Jet / 2 jet
c) 4+3+2 Jet / 2 Jet

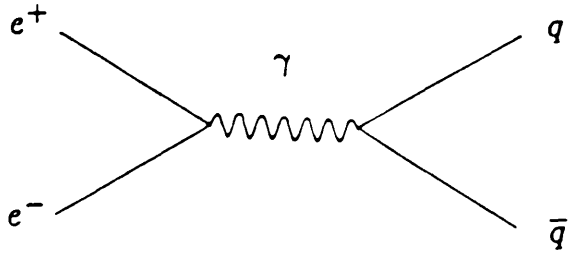

Fig 1.14 The Feynman diagram for single photon annihilation producing a quark-antiquark pair. The quarks then fragment to hadrons.

Chapter 2

Review of Previous Experimental Results.

2.1 Introduction

In this chapter we review previous results obtained in photon-photon physics relevant to the present analysis and some of the experimental methods used. Firstly brief descriptions of the leptonic and resonance channels are given, then a discussion of the photon structure function formalism. The topics pursued further in this thesis are then examined in detail. Specifically the total photon-photon cross-section and jet production are reviewed.

The leptonic channels are theoretically fully calculable, being examples of α^4 QED processes. The virtual photons couple purely to the charge of the leptons. The processes

$$e^+e^- \rightarrow e^+e^-e^+e^-$$
$$e^+e^- \rightarrow e^+e^-\mu^+\mu^-$$

have been studied at all the PETRA experiments, results being published by CELLO, PLUTO, JADE, TASSO, MARK-J (2.1). The process has been studied where production occurs from both nearly real photons (untagged data) and virtual photons (single tagged data) The PLUTO Collaboration have studied muon pair production from $0 \leq Q^2 \leq 100$ GeV^2. The absolute QED cross-section predicted and all kinematical distributions were found to agree well with the data. AMY has also recently published work on these channels (2.2).

A third leptonic channel is that of tau pair production. The fundamental difficulty in the analysis of tau production is due to the presence of an undetected neutrino in the final state, ($\tau \rightarrow \upsilon + X$). This plus the strongly falling energy dependence of the cross-section for the process and its low multiplicity make an analysis of this channel extremely difficult and consequently no analysis of it has yet been made.

Resonance production occurs in photon-photon events when the photons couple to a C=+1 meson. Because the photon itself is not involved in the strong reactions, it is well suited to studying hadrons and their component structures. A great deal of information about QCD has been gained from

knowledge on the internal structure of hadrons, and therefore the study of hadron production in photon-photon reactions is of great interest. For further reading on this and vector meson pair production the reviews of Field and Olsson can be consulted (2.3).

2.2 The Photon Structure Functions

One method of studying hadronic photon-photon events has its roots in e-p physics. Here the quarks and gluons present in the proton are probed by a highly virtual photon. The highly virtual photon interacts with the constituent quarks and gluons present in the target proton, forming hadrons. The momentum distributions of these partons can be described by structure functions. The study of these provides a useful method of analysing the different components present in the proton, in particular the predictions made by QCD. This method was taken over to photon-photon interactions where the proton target is replaced by a nearly real target photon which is probed by a highly virtual photon. This corresponds to an experimental requirement of an untagged photon and a tagged photon in the event.

The cross-section for the deep-inelastic electron scattering off a photon target (Fig 2.1) can be parameterised using two structure functions (2.4).

$$\frac{d\sigma}{dxdy} = \frac{16\pi\alpha^2 EE_\gamma}{Q^4}\left[(1-y)F_2(x, Q^2) + y^2 xF_1(x, Q^2)\right]$$

where F_1 and F_2 depend on the longitudinal and transversely polarized components of the photon cross-section.

$$F_1 = F_T$$
$$F_2 = 2xF_T + F_L$$

and the terms x and y are the Bjorken variables which are defined as

$$x = \frac{Q^2}{Q^2 + W^2}$$

$$y = 1 - \frac{E}{E'}\cos^2\left(\frac{\theta}{2}\right)$$

θ being the scattering angle of the tagged lepton and E' its measured energy. It is important to note that the term y^2x is experimentally small (when the angle θ of the tagged lepton is small), and consequently the cross-section is only sensitive to $F_2(x,Q^2)$. There is a third structure function F_3 which relates to the cross-section interference term τ_{LL}. However this relates to polarization affects and is only relevant when both photons are highly virtual, corresponding to double tagged events. There has been an analysis of the structure function for double tagged events by PLUTO (2.5).

As has been shown, the structure function F_2 can be measured by examining the photon-photon cross-section as a function of x. This has to be compared to theoretical predictions. There are two components which need to be taken into account, the VDM process where the photon couples to a vector meson which interacts with the quarks in the target photon, and the QCD process. (The zeroth order QCD is equivalent to the QPM model where gluons are ignored.)

The VDM contribution can be estimated from the Drell-Yan measurements of the pion structure function and is a term falling linearly with x (2.6).

$$F_2^{VDM}(x, Q^2) = (.2 \pm .05) \bullet \alpha \bullet (1 - x)$$

More recently the GLM model has been proposed to provide a better description of the hadronic component (2.7). This model is a parameterised fit to data taken over a wide range of W, Q^2 (see section 1.9).

The simple QPM component (ignoring terms of order m^2_q/W^2) can be written as a function of x as (2.8)

$$F_2^{QPM}(x, Q^2) = 3\frac{\alpha}{\pi}\sum_q e_4^q x \bullet \left[\left[x^2 + (1-x)^2\right]\log\left(\frac{Q^2(1-x)}{m_q^2 x}\right) + 8x(1-x) - 1\right]$$

where the sum is over all possible quark flavours present. If the gluon interaction terms are included then the lowest order QCD term becomes

$$F_2^{QCD}(x, Q^2) = 3\frac{\alpha}{\pi}\sum_q e_q^4 f(x)\log\left(\frac{Q^2}{\Lambda^2}\right)$$

where f(x) is calculated in QCD (2.9).

Various experiments have measured the photon structure function. The data is usually unfolded in x using various models to determine the detectors acceptance in W, Q^2 and thus in x. Using this information the data is corrected for acceptance enabling absolute comparisons of the data with theoretical predictions. One problem with this method is the dependence of the unfolding matrix on the model used to create it, the data being a superposition of various models. Fig 2.2 shows the results from the PLUTO analysis. As can be seen, the hadronic VDM component alone does not fit the data and an extra QCD term is used. Various values of Λ_{MS} are fitted and it can be seen that the data is fairly insensitive to this variable. Also, the QCD model and the QPM model give similar predictions and it can be said that a sum of QPM and VDM would also describe the PLUTO data.

2.3 The Total Hadronic Cross-Section and Jet Production in Photon-Photon Interactions

The total cross-section of the hadronic photon-photon data is usually studied as a function of W and Q^2. The QPM component of the data is usually examined by excluding the low jet p_t data which removes the VDM component. The cross-section of the VDM component can be most simply described by factorising it into separate W and Q^2 terms. This method of factorising the cross-sectional dependence is argued from the phenomenological standpoint and is likely to be an oversimplification of the truth. The cross-sectional dependence on the hadronic mass W is predicted from a phenomenological model providing (2.10)

$$\sigma_{\gamma\gamma}^{VDM}(W) = A + \frac{B}{W}$$

where A is 240 nb and B is 270 nb (W in GeV). The constant term corresponds to pomeron exchange and the 1/W term to f_2 and a_2 exchange. The 1/W term can be seen to only be important in the low W region.

TPC/2γ and PLUTO have published cross-sections for the total hadronic cross-section from single tagged data as a function of W and Q^2. Both collaborations use the method of unfolding the data to determine the true W from W_{VIS} using MC simulations to determine the unfolding matrix. This method is dependent on the fragmentation scheme used for the hadronisation of the W system and also the Q^2 of the event (higher Q^2 events

have a final state with a transverse momentum imbalance caused by the scattered lepton, which pushes the final state hadrons into the detector improving the acceptance).

The PLUTO analysis (2.11) measured single tagged events over the Q^2 range 0.1 to 100 GeV^2 and over the W range of 1.5 to 10 GeV. They concluded that the data could be well described over this kinematical range by an incoherent sum of a QPM model (using the constituent quark masses) and a vector meson dominance model utilising the GVDM form factors and a W independent cross-section of 232 ± 15 nb. Fig 2.3 and 2.6 show the unfolded cross-section of the data compared with QPM and GVDM models as a function of W and Q^2. They comment on the possibility that the method of adding QPM and GVDM may lead to double counting of events in certain kinematical regions, but point out that the sum of both models does fit the data well.

TPC/2γ (2.12) have published cross-sections for tagged hadronic data at similar energies and compare the data with a variety of vector meson dominance inspired models plus QPM. They show the W dependence of the total cross-section $\sigma_{\gamma\gamma}$ in two Q^2 ranges. Fig 2.4 shows this data compared to the PLUTO results. In the low Q^2 data the two experiments have significantly different values for $\sigma_{\gamma\gamma}$, the TPC values being (within errors) flat in W, whereas the PLUTO data falls strongly with W. The high Q^2 results, however, agree within errors. The Two-Gamma collaboration (2.13) have used a novel approach of calculating the W of the photon-photon final state by using double tagged events, and determining W from the detected energy and scattered angles of the tags. This is possible because of the excellent energy and position resolutions of the taggers. Fig 2.5 shows $\sigma_{\gamma\gamma}$ extrapolated to $Q^2 = 0$ for TPC/2-γ, Two-Gamma and PLUTO. In order to extrapolate back from the Q^2 range used to $Q^2 = 0$ each experiment used the GVDM form factor. The PLUTO data has a strongly falling W dependence whereas the TPC/Two-Gamma data and the Two-Gamma data have a much flatter distribution. Above W = 4 GeV all the data flattens out, but the PLUTO cross-section is substantially less than the TPC/Two-Gamma and the Two-Gamma results.

The Q^2 dependence of the reaction is represented by a form factor, one for each virtual photon. The PLUTO collaboration favoured a GVDM representation (Fig 2.6) whereas the TPC collaboration favour a VDM term (Fig 2.7). TPC/2-γ also proposed using a p_t^{min} cut on the QPM model as suggested in ref. 2.14 to reduce double counting effects where the vector

meson dominance channel is dominant. This was essentially a cut on the minimum transverse momentum of the primary quarks in their centre of mass frame. They found the data was best fitted by a sum of VDM plus QPM with a p_t^{min} cut of 1.0 GeV. Both experiments reject the simple ρ-VDM model as falling too steeply with Q^2. Two-Gamma compare the data with either a ρ-VDM or GVDM model and favour GVDM. They find little evidence for a W dependent term to the cross-section.

In ref. 2.7 Field compares the GVDM and GLM models with the PLUTO, Novosibirsk and TPC data. He comments that these collaborations have extrapolated their $Q^2=0$ results back using a GVDM form-factor which he claims is neither consistent with the GLM model (a parameterised fit) or the data itself. In other words he claims the hadronic part is not factorisable into separate W, Q^2 components (the GLM model certainly does not factorise). The GLM model is compared with the data in fig 2.8 and as can be seen it agrees well with the PLUTO and Novosibirsk data. The TPC points are consistently higher at high W as has been seen previously. It should be noted that the GLM model was fitted to the PLUTO 1984 data and the Novosibirsk data, but not the PLUTO 1986 untagged data. The authors of the GLM model (2.7) also comment that they find inconsistencies between their model and the TPC/2-γ data. It should be noted that the GLM and GVDM parameterisations are both consistent with the PLUTO data. However the GLM has a theoretical advantage in that because it exhibits Bjorken scaling at high Q^2 it causes $F_2^{\gamma VDM}$ to fall linearly with x at high x.

In contrast to these analyses which have all used unfolded data, the PLUTO collaboration have also presented results on the Q^2 and transverse momentum dependence of jet production in photon-photon reactions (2.15), where the data was compared to a MC simulation after detector affects. They found good agreement of their data with an incoherent sum of GVDM and QPM over a wide Q^2 range ($0.1 \leq Q^2 \leq 100$ GeV^2). Fig 2.9 shows the W_{VIS} and Q^2 distributions of the data compared with the sum of GVDM and QPM in the three different tagging ranges used. The GVDM model used a flat cross-section in W of 240 nb. No evidence for a 1/W term was found; however the data would be expected to be insensitive to this in the W_{VIS} analysed ($4 \leq W_{VIS} \leq 12$ GeV) where the term becomes small. The lower W_{VIS} limit was chosen to reduce resonance production in the data sample and also to ensure the event had enough energy present to form jets.

2.4 Jet Production In Photon-Photon Interactions.

Jets are characterised by having limited transverse momentum with respect to some axis in the event, known as the jet axis. PLUTO applied a jet analysis to the data. This consisted of boosting the final state particles into the $\gamma\gamma$ centre of mass system. The event was then subjected to a thrust analysis. The thrust of an event is defined as

$$T = \max\left[\frac{\sum|P_{L_i}|}{\sum|\vec{P}_i|}\right]$$

This function maximises the longitudinal momentum along a specific jet direction by altering this until the momentum vector along the axis of the jet is maximised. Only one unique jet direction is found making it well suited to the CMS of the photon-photon final state where any jets formed should be back to back. Thrust varies from 0.5 for a perfectly isotropically distributed event to 1.0 for a perfect two jet event. From the jet axis the mean longitudinal and transverse momenta of the particles within the jet can be calculated. There are various other jet measures which will be mentioned later. If events whose final state particles are produced with a phasespace distribution are subjected to a jet analysis the mean transverse momentum of the particles within the jet should grow with the total hadronic mass (W) of the final state. It should be mentioned that any jet axis found in a purely phasespace event is arbitary and depends on factors such as the effects of the detector acceptance. However, events where jet production occurs should display a limited mean transverse momentum of the particles within the jet as the energy in the events increases. This is demonstrated in fig 2.10 where PLUTO compare the single tagged data (in the three tagging regions) with their GVDM + QPM ansatz and also a simple phasespace MC. As can be clearly seen, whereas the mean longitudinal momentum of the particles within the jets increases with energy similarly in both models, the transverse momentum distribution is radically different in the two different approaches. The two-jet MC (GVDM + QPM) displays the same limited transverse momentum as the data. This is a clear indication that the photon-photon interactions taking place are jetlike. It is also important to note that the jet MC and the phasespace MC are clearly distinguishable and that the smearing of the event by the detector did not prevent the difference between

the two different reactions being detected. Once the overall two-jet nature of the data was established, the jet p_t of the data was examined. The jet p_t of an event can be defined as the transverse momentum of a defined jet with respect to its $\gamma\gamma$ axis. Firstly the momenta of the jet is calculated by summing over the particles in the jet

$$\vec{p}^{JET} = \sum_i \vec{p}_i$$

and this is related to the jet's transverse momentum by

$$\vec{p}_t^{JET} = \vec{p}^{JET} \bullet \sin\theta$$

where θ is the angle between the jet axis and the $\gamma\gamma$ axis in the final state centre of mass frame. The $\gamma\gamma$ axis is taken to be the beam axis in the untagged data and for single tagged data can be calculated from the scattered beam lepton and the hadronic final state centre of mass frame.

Fig 2.11 shows the overall jet p_t in the three Q^2 ranges measured comparing the data with GVDM and also QPM. As can be clearly seen from these plots the QPM model dominates at high p_t, the GVDM model falling off rapidly with p_t. In the low Q^2 data the GVDM dominates at low p_t. The fall off of the GVDM with increasing Q^2 is shown by the domination of the GVDM in the lowest Q^2 region changing to only a small contribution in the high Q^2 data. A variable which is often used to compare the data with the pointlike contribution is $R_{\gamma\gamma}$ which is defined as

$$R_{\gamma\gamma} = \frac{\text{observed no of events}}{\text{no of events predicted by QPM}}$$

This is useful in showing the specific amounts of QPM and GVDM present at a given p_t, Q^2 etc. Fig 2.12 shows $R_{\gamma\gamma}$ for the PLUTO tagged data in five Q^2 regions. They show that

1) the data converges to the QPM prediction at high p_t or Q^2.

2) the amount of GVDM present is greatest at low p_t and decreases with increasing Q^2.

3) Although the overall description of GVDM + QPM gives a good description of the jet p_t distribution, there is a discrepancy in the data with

$<Q^2>$ = 0.3 GeV^2 at medium jet p_t, a clear excess over the predicted amount being seen.

In order to check the topology of these events, the thrust distribution of all data with jet $p_t \geq 2$ GeV is plotted for each Q^2 region (Fig 2.13). Although the high and medium Q^2 data is well described by the two jet models, the low Q^2 data has a lower overall thrust distribution than predicted. This suggests a non two-jet like component present in the low Q^2 data.

Because of these results, PLUTO continued the investigation of the low Q^2 data ($<Q^2> \sim 0.001$ GeV^2) by analysing the untagged photon-photon events (2.17). This analysis confirmed the previous result that there was an excess of data over the amount predicted by an incoherent sum of GVDM + QPM. Fig 2.14 shows the $R_{\gamma\gamma}$ of the untagged data demonstrating the excess of data at intermediate jet p_t. A thrust analysis of this data suggested that the data was more isotropic than the two jet like models predicted (Fig 2.15a,b). They concluded between 10% and 26% of the data did not have a two jet topology. They then attempted to describe the data with the GVDM and QPM models plus an extra isotropic component. Two multijet models which produced 3 and 4 jet photon-photon events as well as a simple phasespace model were tried, and it was found that taking statistical errors into account the excess could be described by any of the isotropic components.

TPC/PEP and TPC/2γ have also analysed low Q^2 data and have published plots for $R_{\gamma\gamma}$ which substantially agree with the PLUTO results (Fig 2.16, ref. 2.16). TPC/2γ (2.18) also presented thrust distributions for tagged and untagged hadronic photon-photon data. A clear excess of low thrust events is observed in the untagged data (Fig 2.17). $R_{\gamma\gamma}$ plots are presented with the QPM and VDM components subtracted. These show a large excess of events at medium jet p_t and low Q^2 (Fig 2.18). Both these results shows excesses over the lowest order QPM prediction at medium, high p_t and low Q^2 which are significantly larger than the 70-40% predicted in (2.19).

In this thesis the analysis concentrated on two major topics concerning hadronic photon-photon interactions.

1) The W, Q^2 dependence of the soft hadronic component of the data is examined. This has been done in a wide range $0 < Q^2 < 30$ GeV^2 using untagged events (where both scattered photons were nearly quasi-real) and single tagged events (using two different angular tagging regions, where one photon was virtual and one remained quasi-real).

2) A jet analysis of the data is undertaken in order to ascertain whether any

discrepancies in the GVDM + QPM ansatz existed. In particular any excesses over the pointlike QPM term at high jet p_t's and low Q^2 are searched for and their jet topology examined in order to determine whether any evidence for higher order multijet processes can be identified.

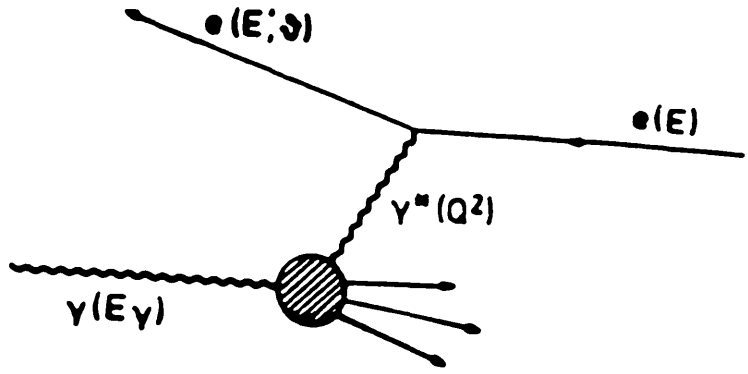

Fig 2.1 A deeply inelastic photon probing a nearly real photon target.

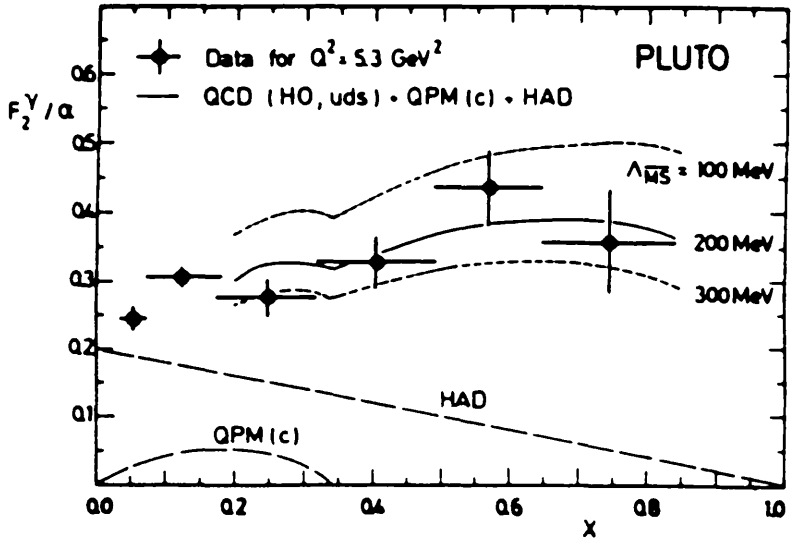

Fig 2.2 The PLUTO results for F_2^γ showing the VDM and QCD predictions.

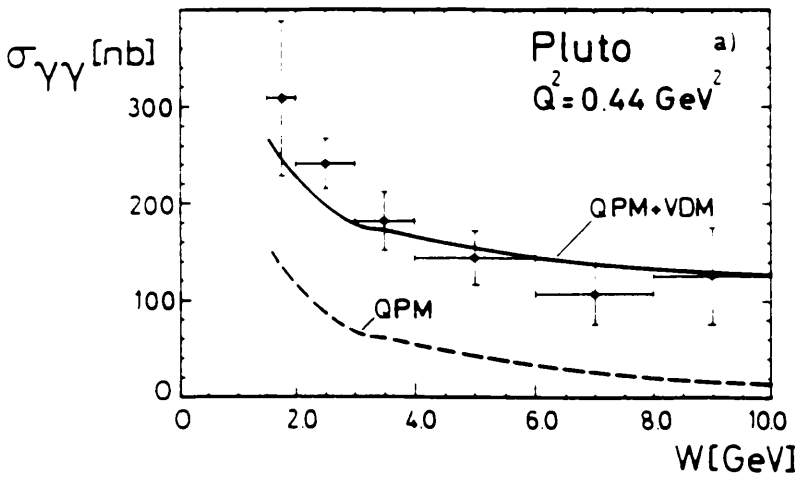

Fig 2.3 The PLUTO cross section for hadron production as a function of W (unfolded). It is compared with the QPM model (dashed) and also a sum of QPM and GVDM (solid).

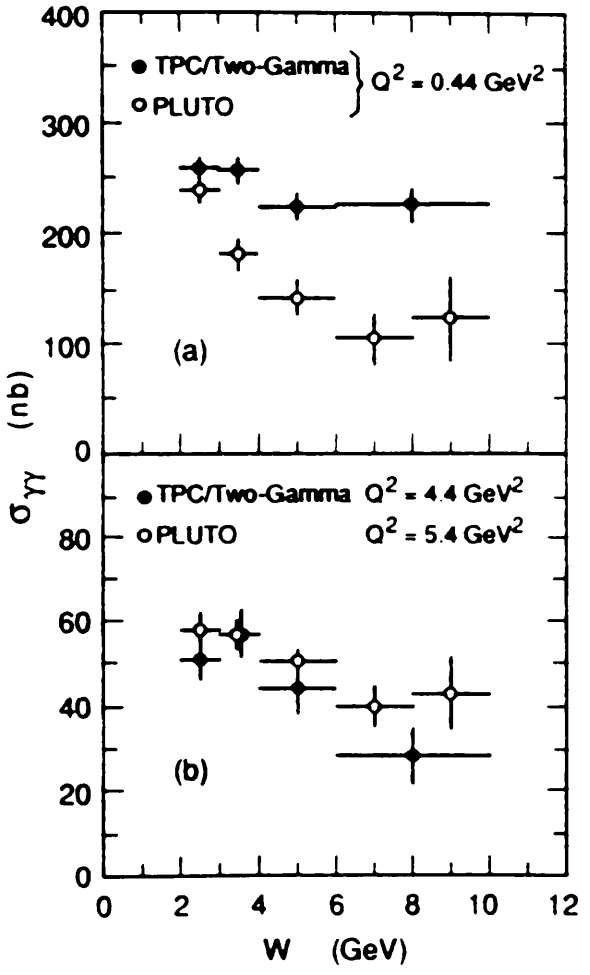

Fig 2.4 The TPC cross section for hadron production as a function of W (unfolded) in two separate Q^2 ranges. It is compared with the PLUTO data. The PLUTO error bars shown do not include systematics which are included in fig 2.3 above

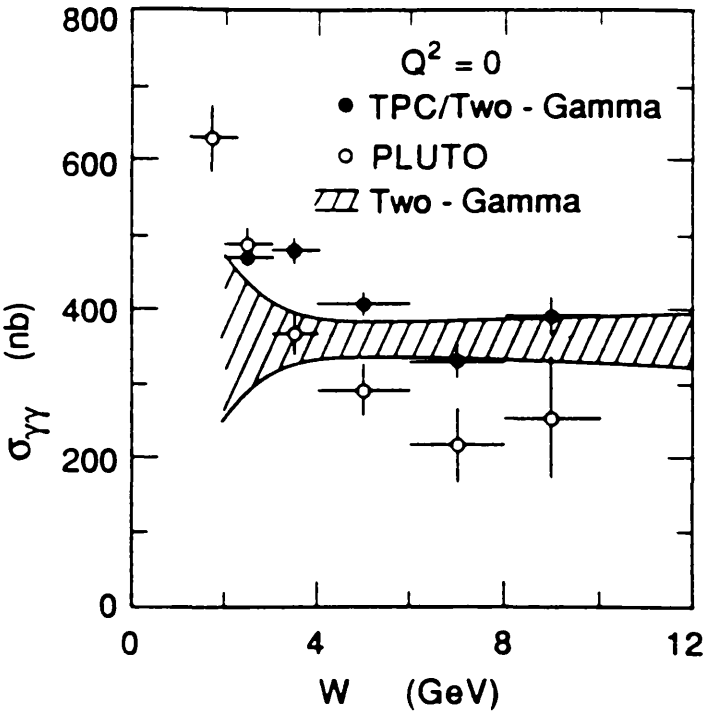

Fig 2.5 The cross sections of hadron production as a function of W extrapolated to $Q^2=0$ for TPC/2-γ, PLUTO and 2-γ.

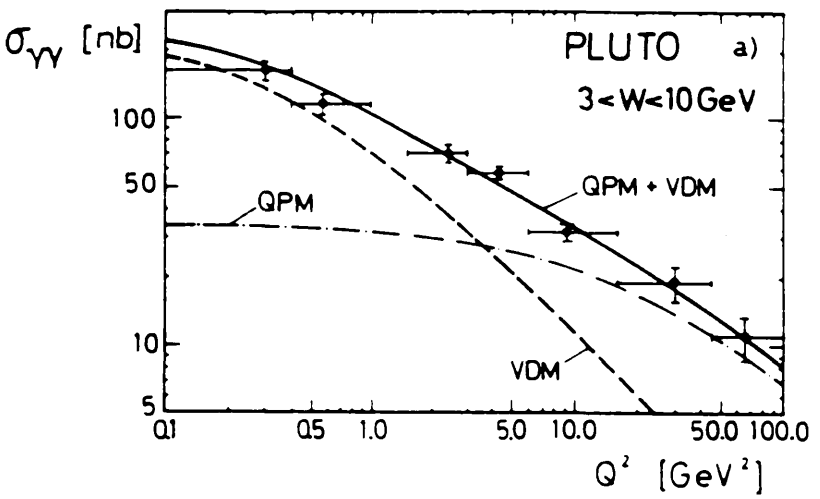

Fig 2.6 The PLUTO unfolded cross section for hadron production as a function of Q^2 in the range $3 < W < 10$ GeV. It is compared with QPM (dot-dash), VDM (dashed) and a sum of QPM and GVDM (solid).

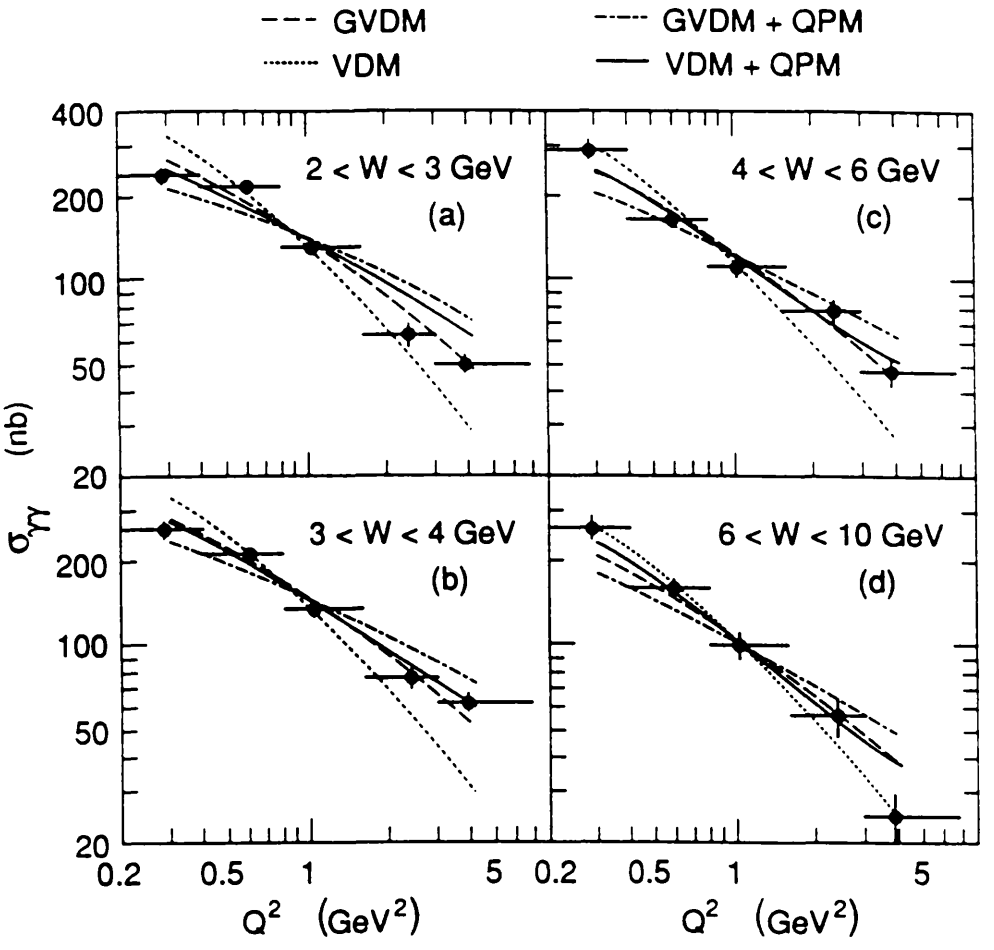

Fig 2.7 The TPC/2-γ unfolded cross section as a function of Q^2 in four different W regions. The data is compared with both GVDM and VDM, with and without the QPM contribution.

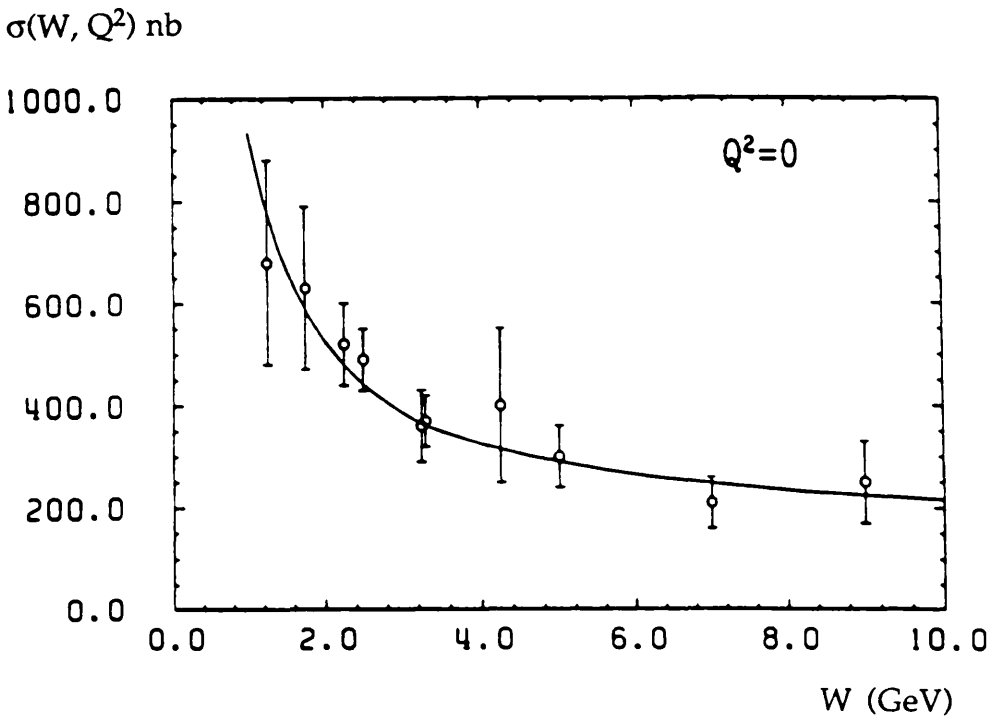

Fig 2.8 The data points show PLUTO and Novosibirsk data compared with the GLM model.

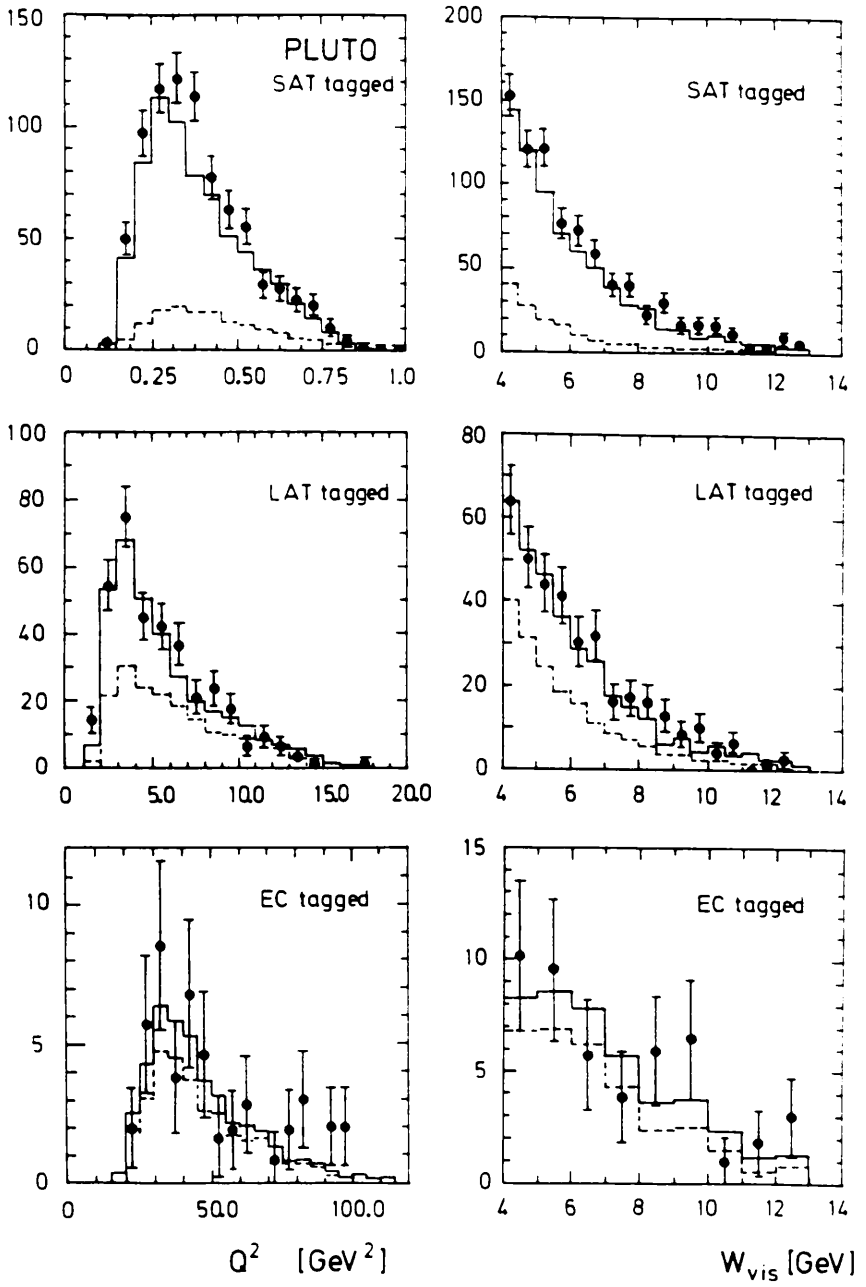

Fig 2.9 The PLUTO results for numbers of events produced as a function of Q^2, W_{VIS} for three different Q^2 ranges, corresponding to three different tagging regions.

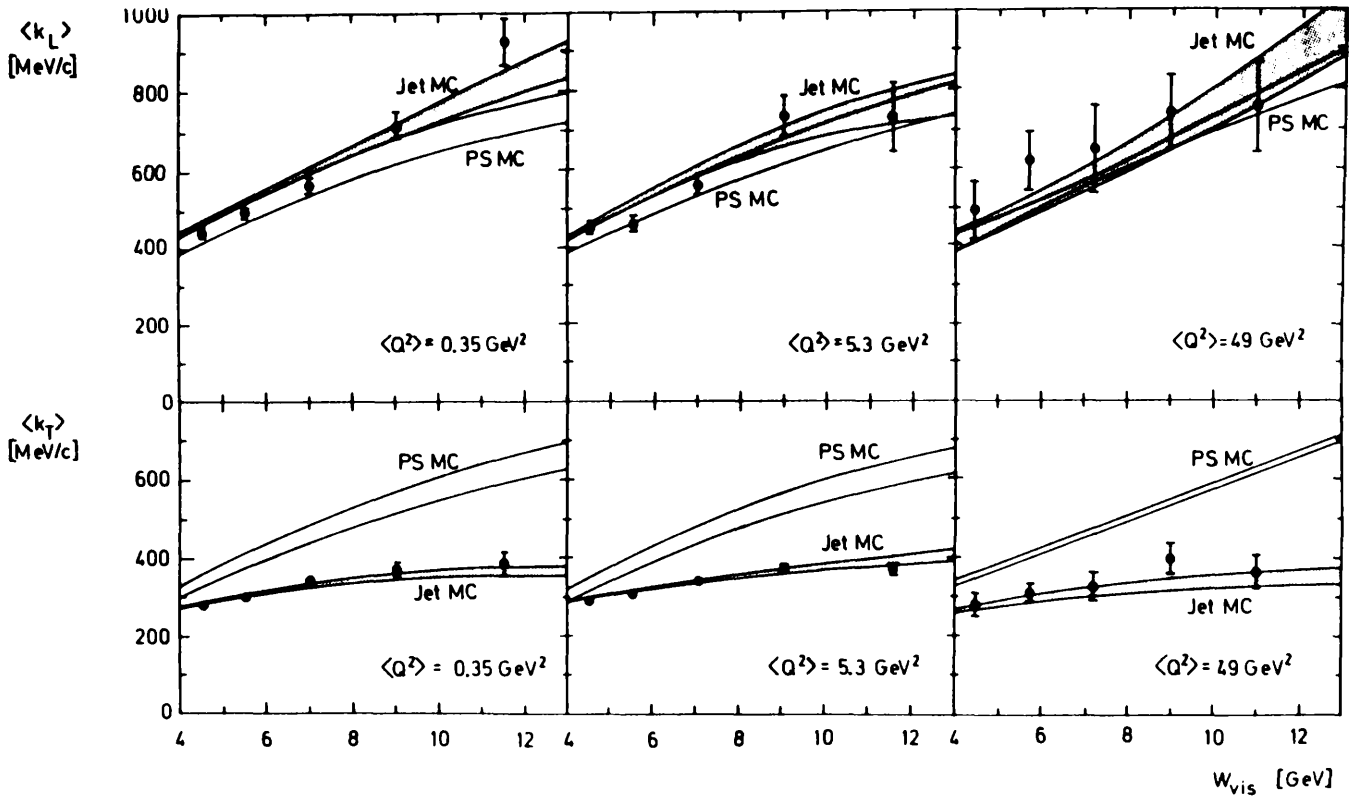

Fig 2.10 The PLUTO results for the mean longitudinal, $<k_l>$ and transverse, $<k_t>$ momentum components of the jet axes of data (defined using the thrust algorithm). These are compared with both a two-jet model and a phasespace model

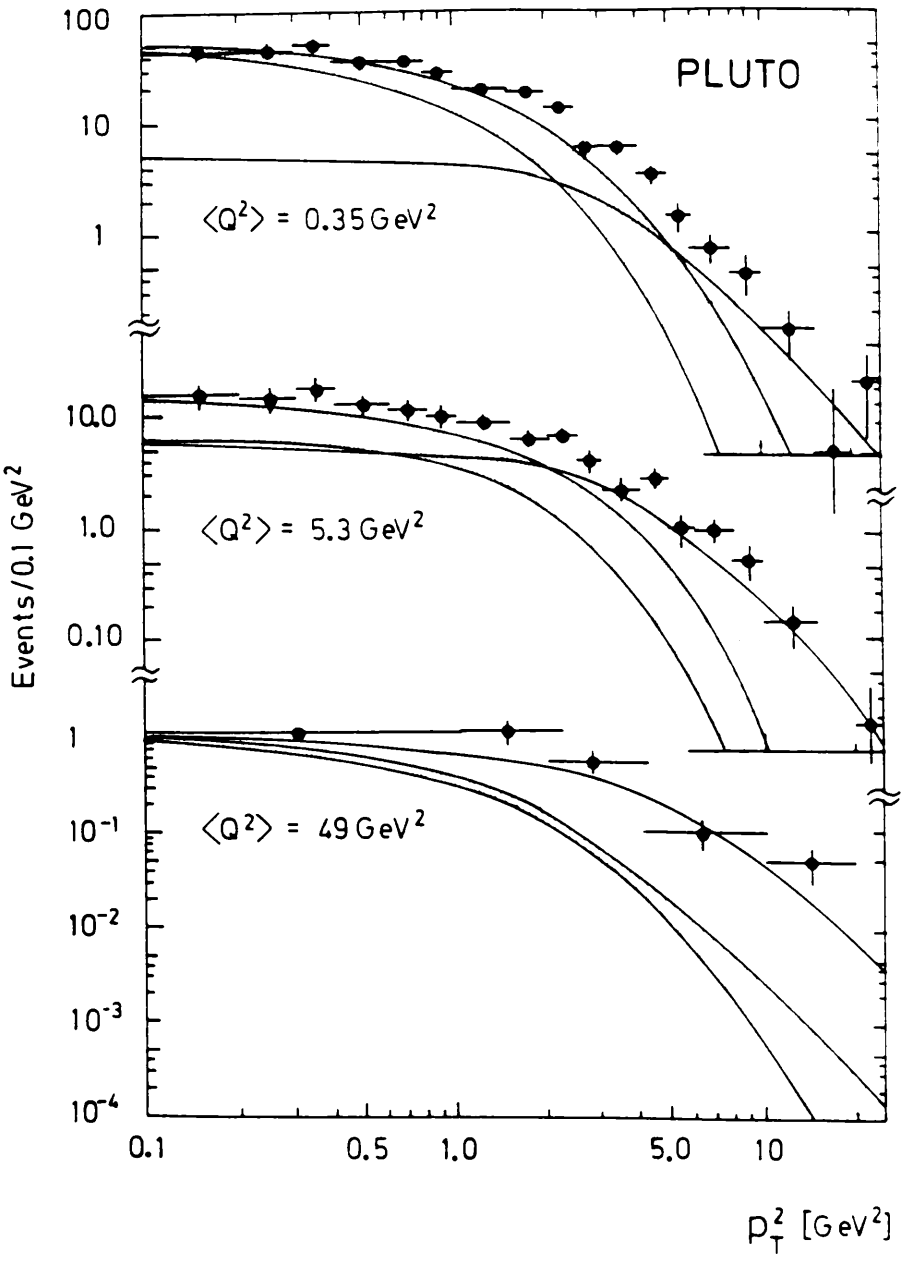

Fig 2.11 The PLUTO results for the jet p_t^2 in three different Q^2 ranges. The data is compared with QPM (solid) and GVDM (band).

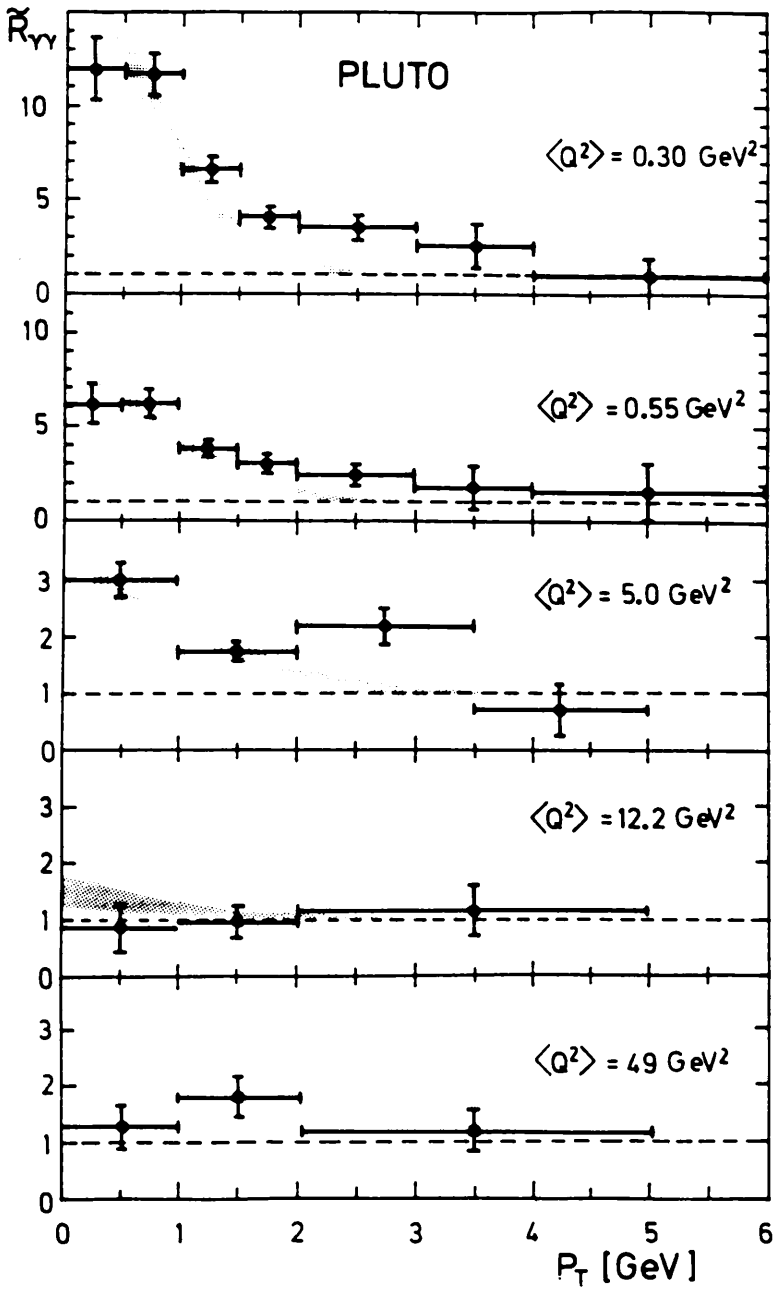

Fig 2.12 $R_{\gamma\gamma}$ for the PLUTO data is presented in five Q^2 bins. The QPM prediction is unity and the band shows the predicton for the sum of QPM and GVDM.

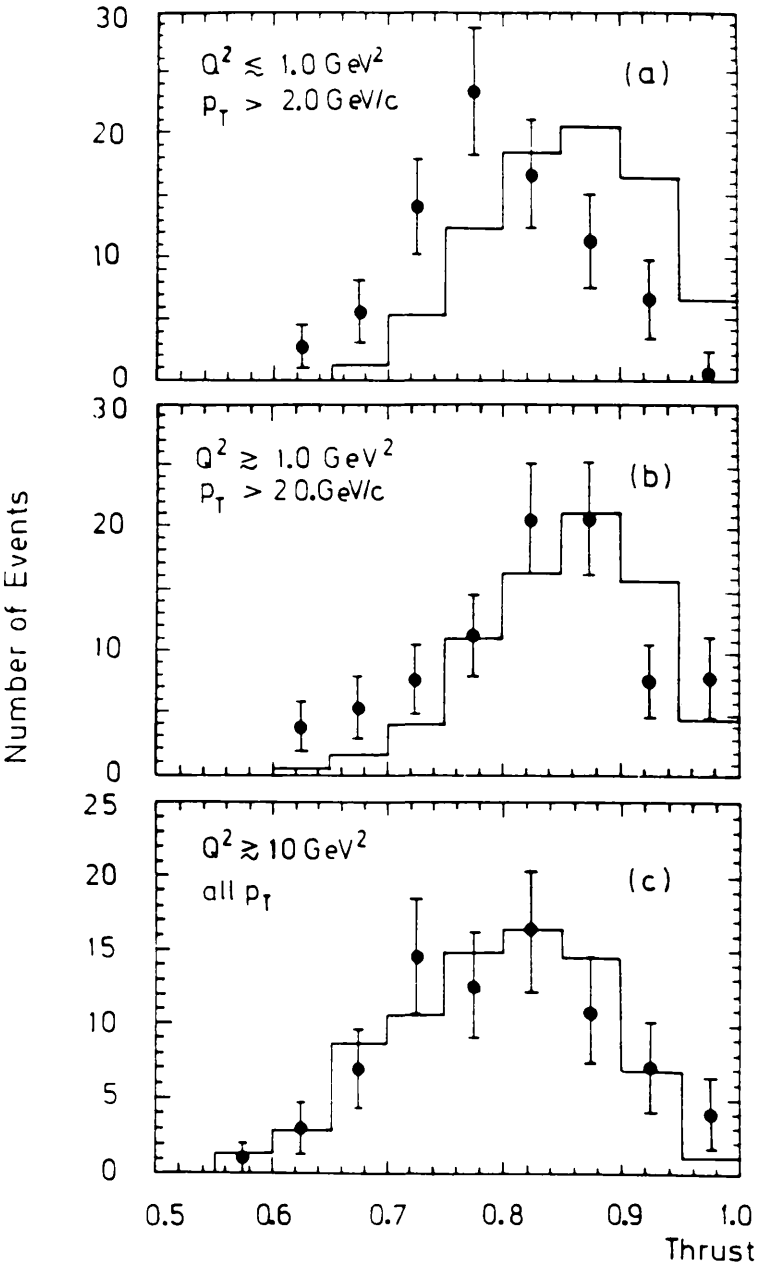

Fig 2.13 The thrust distributions for the single tagged PLUTO data with certain jet p_t and Q^2 requirements, compared with QPM plus GVDM.

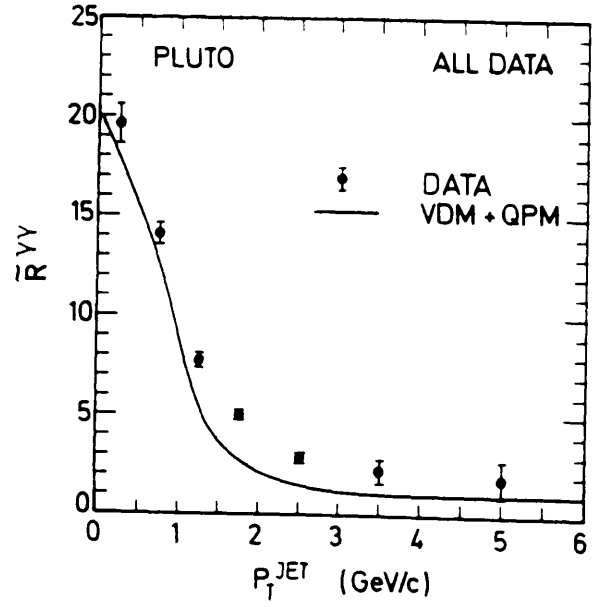

Fig 2.14 The $R_{\gamma\gamma}$ for the low Q^2 data from the PLUTO untagged analysis is compared to QPM + GVDM.

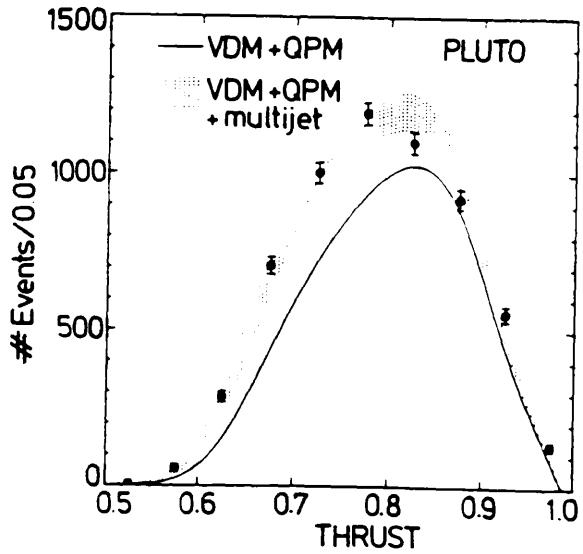

Fig 2.15a The thrust distribution of the low Q^2 untagged PLUTO data, compared with both the sum of QPM and GVDM (solid) and GVDM, QPM and a multijet component (band).

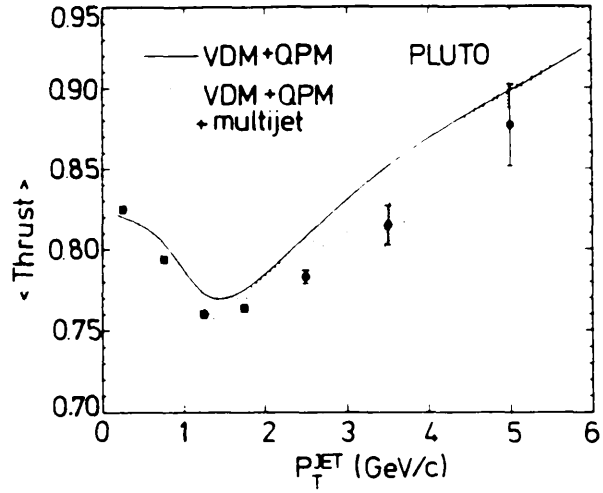

Fig 2.15b The mean thrust of the low Q^2 untagged PLUTO data as a function of jet $p_{t,}$ compared with both the sum of QPM and GVDM (solid) and GVDM, QPM and a multijet component (band).

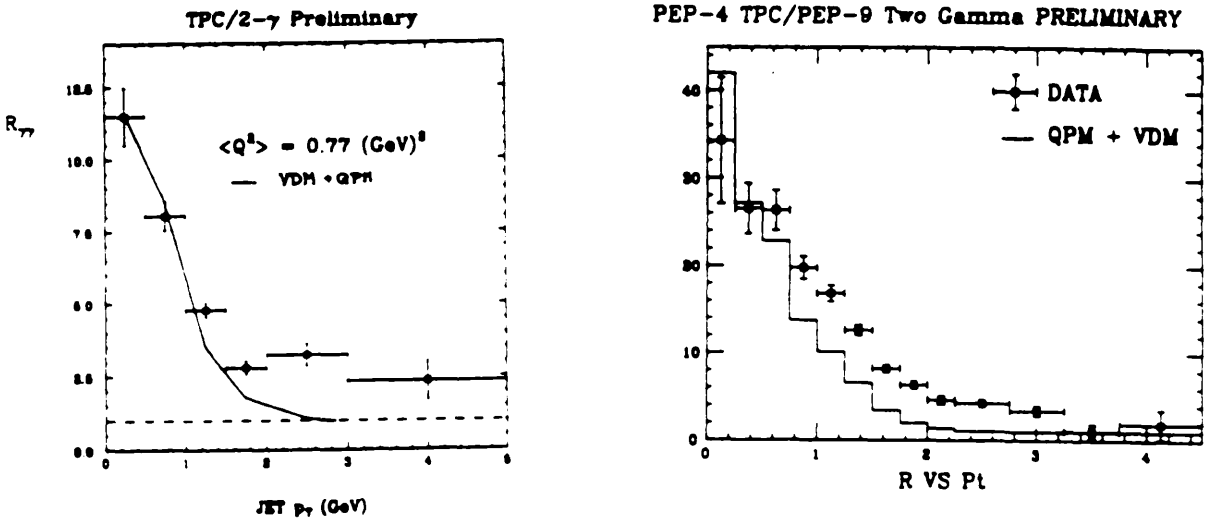

Fig 2.16 The $R_{\gamma\gamma}$ for the TPC experiments at low Q^2 is compared to QPM and VDM.

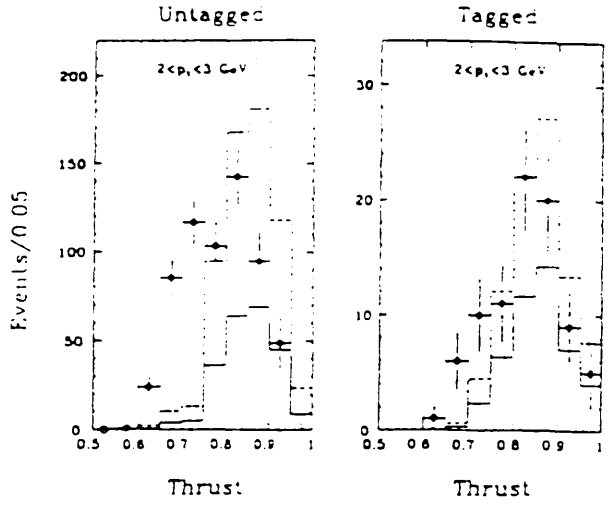

Fig 2.17 TPC/2-γ result showing thrust distributions for medium jet p_t data for low and medium Q^2 data. Data is compared with the VDM + QPM term

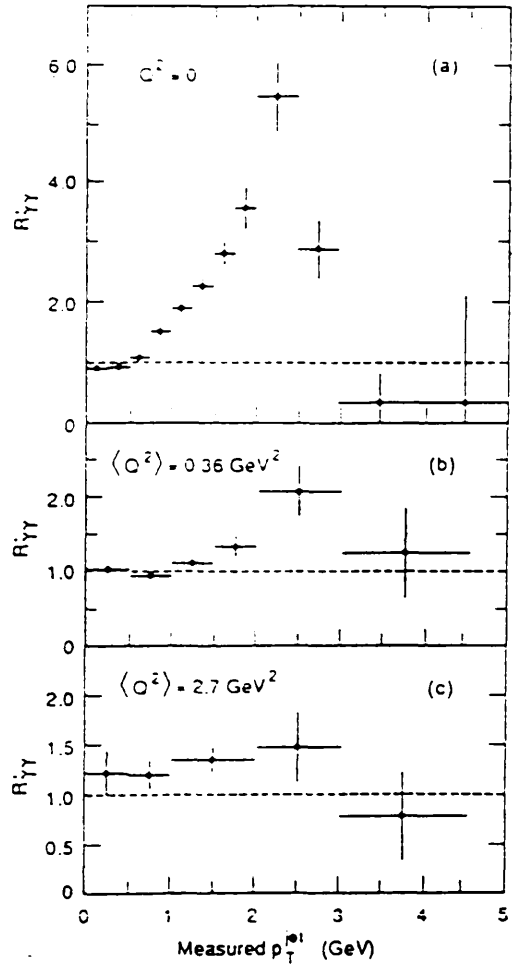

Fig 2.18 TPC/2-γ result showing $R_{\gamma\gamma}$ plot (where data is divided by VDM + QPM) to show excess of events at low Q^2 and medium jet p_t.

Chapter 3

Experimental Apparatus

3.1 PETRA

PETRA (Positron-Electron Tandem Ring Accelerator) is an electron-positron collider built at DESY (Deutches Elektronen-Sychrotron) in Hamburg (3.1). The proposal for PETRA was submitted in 1974 and the first collisions were seen in September 1978. PETRA was designed to accelerate electron/positron beams up to energies of 22 GeV per beam and to provide luminosities of $10^{31}cm^{-2}s^{-1}$. PETRA (Fig 3.1) has a circumference of 2.3 km and comprises of eight straight sections and eight curved sections with a radius of 256m. Four of the straight sections contain the radio-frequency accelerating cavities . During the time that the data for this analysis was collected there were 60 cavities which operated at 500MHz and 4MW. A list of parameters concerning PETRA is shown in Table 3.1. The four straight sections contained the experiments CELLO/PLUTO, JADE, TASSO, MARK-J.

Electrons were produced in LINACI and injected into the old DESY sychrotron where they were accelerated up to an energy of 7 GeV whereupon they were injected into PETRA. The positrons were produced in LINACII and stored in the PIA (Positron Intensity Accumulator). They were then sent to PETRA in a similar manner to the electrons. When both the sets of bunches were in PETRA, they were then accelerated up to the desired operating energy. The highest centre of mass energy obtained at PETRA was 46.8 GeV. Unfortunately machine difficulties meant the luminosity at these energies was poor and the background due to sychrotron radiation was high. It was therefore decided to run for the final year at a reduced centre of mass energy of 35 GeV in order to maximise the integrated luminosity. It was this data which was used in this analysis and amounted to an integrated luminosity of 86 pb^{-1}. The luminosity was determined using large angle bhabha events, these being well understood theoretically and experimentally.

3.2 CELLO An Introduction

The nature of e^+e^- colliding beam accelerators means that the event rate is low. At PETRA, hadronic events occurred on average one every ten minutes. Because of this low event rate, e^+e^- detectors are designed to be able to study as many interesting processes as possible. The detectors on PETRA differ from one another in the importance that they put on the different information that can be measured from an event. All detectors involve compromises between different requirements, and CELLO (Fig 3.2) was no exception. It was basically a multipurpose standard solenoidal magnetic detector (3.2) which paid particular attention to identifying electrons and photons. It utilized liquid-argon calorimetry which had a good energy resolution but paid little attention to specific particle identification. It was one of many multipurpose detectors, following in the footsteps of MARK1 at SLAC and PLUTO at DORIS.

Its main design features were (see Table 3.2):

1) Cylindrical wire chambers to provide position and momentum measurements of charged tracks. The chambers were enclosed in a superconducting solenoid which produced an axial field of 1.3 Tesla parallel to the beam-axis.
2) Multilayer lead-liquid argon calorimetry to provide good energy and spatial measurements of showers and also good photon-electron separation.
3) Large iron return yoke for the superconducting solenoid which also acts as a hadron absorber, surrounded by large planar drift chambers for muon identification.
4) Forward detectors consisting of lead-glass calorimetry and scintillator strips for bhabha detection and for tagging electrons in photon-photon events.
5) A single level fast trigger which utilizes information from the central tracking chamber and also from the lead-liquid argon calorimetry.

Importance was placed on a large solid angle coverage (Fig 3.3) as well as good electron-photon identification at the expense of specific particle identification.

The CELLO coordinate system is defined with the z direction along the beam axis, following the path of the electrons, and the x direction in the plane of the ring pointing outwards. When viewed end on from the beam axis the y direction faces upwards with $y = x \times z$. In the x, y plane (facing along

the beam axis) the polar coordinates r, φ are used and θ is measured with respect to the z axis.

3.3 The Central Tracking Chamber

The aim of the tracking chamber was to provide good positional and momentum measurement of charged tracks passing through it. It was also required to operate in a large magnetic field and to provide information for a fast charged trigger.

The tracking chamber consisted of a mixture of interleaved cylindrical drift chambers and proportional chambers (see table 3.3). These were surrounded by a thin superconducting solenoid which provided a uniform axial field of 1.3 Tesla. The inner wall of the chamber was the beampipe and had a radiation thickness of only 4%, to keep photon conversions to a minimum. It could measure charged particles over 97% of 4π. The resolution for the measurement of a charged track was determined to be (3.3):

$$\frac{\sigma_{p_t}}{p_t} \approx 1.2\% \; p_t \qquad (p_t \text{ in GeV})$$

and the vertex position of a track could be measured to σ=330μm in rφ (3.4).

3.3.1 The Proportional Wire Chambers

There were five proportional wire chambers. These were interleaved in between the seven drift chambers. Each consisted of axial anode wires and two sets of cylindrical cathode strips which were orientated at 30^o and 90^0 to the wire axis. The charge distribution from the finely segmented strips was used to provide an accurate z measurement for the hits produced by a track. They could provide a measurement to $\sigma \approx 440$ μm in z.

3.3.2 The Cylindrical Drift Chambers

There were seven drift chambers (3.5) whose purpose was to provide good rφ measurement for tracks. They had an open cell drift structure (see Fig 3.4). The cell measured 15mm across with a signal wire in the middle and three potential wires at one end to separate the cells electrostatically. Their small size meant the likelihood of two tracks passing through the same cell was

small. The gas mixture used was an equal mix of argon and ethane. Each sense wire was attached to its own onboard preamplifier which was connected via long cables to CAMAC TDC's. A computer simulation was used to correct for the effect of the large magnetic field on the drift process. Using this parameterisation tracks could be reconstructed to $\sigma \approx 170\mu m$ in $r\varphi$.

3.3.3 The Beam Pipe Chambers

Situated directly outside the beam pipe were the beam pipe chambers (Fig 3.5) which consisted of two closely spaced sets of drift tubes (3.3). Their purpose was to provide good spatial information on tracks as near to the interaction point as possible. Each cell is housed in an individual tube to protect it from background damage due to the large amounts of synchrotron radiation present near the beam. Like the cylindrical drift chambers they used a computer parameterisation for the drift times which were again affected by the magnetic field. They also utilized the same gas mixture as the central drift chambers. The reconstructed point resolution in $r\varphi$ was $\sigma \approx 170\mu m$.

3.3.4 The Endcap Proportional Chambers

Charged tracks which were emitted at low angles with respect to the beam pipe (ie $|\cos\theta| \leq 0.87$) could not pass through all the chambers of the central tracking chamber. This meant that due to the reduced number of chambers a particle passed through, it was difficult to reconstruct the track. To assist this situation, sets of multiwire proportional chambers were added to the front of each lead-liquid argon endcap. These consisted of four semicircular units each having two separate chambers, one to provide an x-coordinate for a track and one for the y-coordinate. These could provide an $r\varphi$ measurement with an accuracy of approximately 5mm. Using the endcap chambers, track measurement could be made down to $|\cos\theta| \leq 0.97$, but with decreased accuracy on the momentum determination.

3.3.5 The Superconducting Solenoid

In order to measure the momenta of charged tracks as they passed through the central tracking chamber, it was necessary to provide an axial magnetic field to bend them. This was done by a superconducting solenoid which provided a uniform field of 1.3 Tesla. Including its cryostat the solenoid had

a thickness of only 0.5 radiation lengths. This reduced the likelihood of electrons or photons beginning to shower before reaching the lead-liquid argon calorimetry and degrading their energy resolution.

3.4 The Lead-Liquid Argon Calorimetry

The calorimeter used in CELLO was required to give good energy resolution and electron-photon-hadron separation (by examining where in the stack the energy of a shower was deposited) over a large solid angle. It had to resolve low energy photons and also to provide information for a neutral trigger. To this end a fine-grained lead-liquid argon calorimeter consisting of a barrel section and adjoining endcaps covering 96% of 4π was used. The barrel section consisted of 16 identical modules or stacks, arranged in two sets of eight forming an octagonal pattern (Fig 3.6). They were contained in a single large cryostat, this having the advantage that the modules could be positioned in close proximity to one another (ie 2cm separation) to reduce dead areas. The barrel covered a solid angle of 86% of 4π. Each stack was 2m long and 43cms deep. This corresponded to 20 radiation lengths, which was sufficient to contain electrons and photons at the highest PETRA energies. Each stack was composed of alternating layers of 1.2mm thick lead anode strips and 1.2mm solid lead cathode plates with a high voltage (2-5 kV) applied between them. They were separated by a gap of 3.6mm filled with liquid argon. The strips were orientated in three different directions (Fig 3.7a). These were 0^0 (known as the u strips) , 45^0 (w strips), 90^0 (v strips) with respect to the beam axis. The u strips provided the z measurement for a shower, the v strips provided the φ measurement and the w strips removed ambiguities produced when there was more than one shower in a module. The strips became broader deeper into the module where good spatial resolution was less important, reducing the number of readout channels required. To enable the development of a shower to be studied and to give good π-e separation, the u strips and the w strips were read out in seven separate depth intervals and the v strips in five intervals (Fig 3.7b). Information from a selection of the u and v strips was used for the neutral trigger.

The endcap calorimeters had a similar design philosophy to the barrel calorimetry. Each endcap consisted of two semicircular modules housed in one cryostat. Each stack was composed of 42 layers of lead strips alternated

with lead plates (Fig 3.7c). This was equivalent to 21 radiation lengths, and again this was sufficient to contain the highest PETRA electron and photon energies. The layers of lead strips were orientated in three different directions, horizontally, vertically and circularly with respect to the beam axis, providing good spatial resolution without ambiguities. The endcaps covered the solid angle $.92 \leq |\cos\theta| \leq .99$.

The lead-liquid argon calorimetry had 10688 readout channels in total. The signals were taken from the strips to pre-amplifiers situated around the cryostat and thence to amplifiers and ADC's. Channels which had a signal below a specified pedestal level were suppressed. This was safe since minimum ionizing particles deposit a signal at least four times larger than the average pedestal value.

The energy resolution of the calorimetry was determined from an analysis of bhabhas over a long running period:

$$\frac{\Delta E}{E} = 5\% \oplus \frac{10\%}{\sqrt{E}} \quad (E \text{ in GeV})$$

The proportional term is due to the counting fluctuations and the constant due to systematic errors, calibration etc (the terms being added in quadrature). The angular resolution for an ordinary shower was approximately 4 mrad.

3.5 The Muon Chambers

If a particle was not absorbed by the lead-liquid argon calorimetry it had to pass through the iron return yoke of the solenoid. This acted as an effective hadron absorber being the equivalent of 5-8 interaction lengths. This should absorb the majority of hadrons leaving essentially only muons to pass through into the muon chambers (Fig 3.8). These consisted of 32 large proportional chambers positioned outside the iron return yoke and covering 92% of 4π (3.6). Because of multiple scattering in the iron a high precision spatial measurement was not required, but a definite position without ambiguities was important. To this end, wire chambers were used with anode wires 1.3cms apart, with copper foil strip cathodes mounted on mylar and orientated at $+35^0$ and -35^0 with respect to the beam axis. This geometry gave a position measurent accurate to 6mm parallel and perpendicularly to the anode wire.

3.6 The Forward Detector

The forward detector (3.7) was designed to detect electrons emitted between 40mrad and 100mrad with respect to the beam axis. This was useful for studying low-angle bhabhas (for a luminosity measurement for instance) or for tagging a scattered electron from a photon-photon event. Because the forward detectors are by their nature close to the beam line, they were subjected to a great deal of radiation from both real events (ie bhabhas) and from machine background (ie sychrotron radiation). Therefore they had to be resistant to radiation damage. The final design consisted of blocks of lead glass scintillator positioned behind semicircular strips of scintillator (Fig 3.9). The main purpose of the scintillator strips was to provide a positional measurement of the lepton. The specific strip fired gave a θ measurement. The φ measurement was obtained by comparing the signal collected from each end of the strip. Although the scintillator strips gave some indication of the deposited energy, the lead-glass blocks provided the best energy resolution. The centre of gravity of the shower in the blocks also gave a position measurement. Unfortunately after the installation of mini-beta magnets around the beam pipe the forward calorimeters had to be repositioned and there was an unknown quantity of lead sheet placed around the beampipe in front of the calorimeters. Because of problems simulating the effect of this material the useful acceptance for a good tag was reduced to the range θ = 55–80 mrads. The energy resolution was

$$\frac{\Delta E}{E} = \frac{10\%}{\sqrt{E}} \quad \text{(E in GeV)}$$

and θ could be measured to an error of $\pm$ 3 mrad.

3.7 The Hole Tagger

Between the lead-liquid argon calorimeter barrel and endcap there was a gap in the calorimetry corresponding to $.86 \leq |\cos\theta| \leq .92$. The hole tagger was designed to fill this gap and provide crude calorimetry in this region. It purpose was to give some identification of photons which escaped between the barrel and endcap calorimeter. The hole tagger consisted of four segments at each end of the detector. Each one was a sandwich of two layers of 1cm

thick scintillator material with a layer of lead 2cm thick in the middle. The scintillators were connected via wavelength shifters and light guides to photomultipliers outside the solenoids magnetic field. The hole taggers were useful for detecting photons when looking for exclusive processes. In practice, it could only detect photons above 200 MeV and then without any useful energy measurement. It was also not implemented in the Monte-Carlo and was consequently not used in this analysis.

3.8 The CELLO Trigger

The vast majority of events in CELLO were not caused by interesting physics at all but by electronic noise, beam gas/pipe interactions and synchrotron radiation. These would, if allowed to, completely swamp the readout system and had to be effectively suppressed. This was done by using electronic triggers which looked at basic information from an event and did a crude physics analysis on it, to decide whether the event was worthwhile recording or not. The CELLO triggers can be split into two main parts. These were the charged triggers which used information from the central tracking chamber and the neutral triggers which used information from the lead-liquid argon calorimetry. Information from the forward detectors and muon chambers was also used. The data from the various detectors was received by the master trigger unit which evaluated the available information to build up specific triggers. If the master trigger unit managed to construct a trigger then the entire event was read out. This had to be done quickly and efficiently due to the beam crossing rate of 4μs, and because of the low readout rate allowed of ≈ 2Hz. This reduction was done on one level and required a decision within 3μs of a beam crossing.

3.8.1 The Charged Trigger

The charged trigger (3.8) could make a decision in less than 1.5 μs after a beam crossing. It utilized crude pattern recognition to decide whether a set of hits pointed back to the interaction region. It used the readout from five of the proportional chambers and two of the drift chambers. The trigger split the chamber into 64 rφ sectors and 37 rz sectors (Fig 3.10). A dedicated track finding processor searched for tracks in each of the rφ and rz sectors. These were then compared with all possible track combinations (known as masks or overlays) which were stored in RAM . The advantage of this method was

that because the masks were stored in RAM which is easily available (and fast), then the chamber efficiencies, dead channels could be effectively taken into account in the trigger. In the rφ plane a track will be accepted by the $r\varphi_l$ mask if it had $p_t \geq 250$ MeV and by the $r\varphi_h$ mask if it had $p_t \geq 650$ MeV. In the rz plane a track was accepted by the rz mask if at least 3 from 5 proportional chambers fired, and the track pointed to within 15 cms from the interaction point. In this analysis an event was accepted if at least one of the five charged triggers was fired (only the charged triggers were used because these could be accurately simulated for Monte-Carlo events).

The specific triggers using these masks were

Trigger 5; At least two $r\varphi_h$ masks fired, and at least one rz mask fired. The opening angle between the tracks was required to be $\geq 135^0$.

Trigger 15; At least two $r\varphi_h$ masks fired, and at least one rz mask fired. There were no angular cuts, but the number of hits in the beam pipe chambers was required to be less than 50 and the number of hits in the two inner proportional chambers had to be less than 16 (these cuts reduced triggers being fired due to beam-gas/pipe events where showering produced many hits in the inner chambers).

Trigger 16; At least two $r\varphi_l$ masks fired, and at least one rz mask fired. The tracks had to have an opening angle $\geq 135^0$ (later changed to 45^0) and the number of hits in the two inner proportional chambers was required to be less than 16 (again to suppress beam-gas/pipe events).

Trigger 7; This trigger is specifically designed to accept tagged photon-photon events. Both an $r\varphi_l$ and an rz mask fired as well as an energy deposit of ≥ 2 GeV in the forward lead-glass are required.

Trigger 10; Again designed to accept photon-photon events, this time with a tag in the lead-liquid argon endcaps. Both an $r\varphi_l$ and an rz mask fired as well as a total energy deposit of ≥ 1.5 GeV in one of the endcap modules are required.

3.8.2 The Neutral Trigger

The information for the neutral trigger came from the lead-liquid argon barrel, endcaps and from the forward lead-glass blocks.

The barrel readout for the trigger information was done by FADC's and was split into two separate combinations of the available layers. These were called SUMA and SUMB. SUMA consisted of the sum of the u strips in layers 2, 4-7, producing a sampling over 2-21 radiation lengths. SUMB consisted of the sum of the u strips in layer 3 and the v strips in layer 4, giving a sampling in the range 4-7 radiation lengths. This was the region where an electromagnetic shower would be expected to deposit the most energy. SUMA and SUMB were both read out 1.5μs after a beam crossing and were both required to produce a significant signal to cause a trigger, reducing the possibility of electronic noise etc causing a false signal. SUMB was also read out 0.5μs after the beam crossing to provide a signal before any real showers have developed. This was useful for rejecting signals due to processes not synchronised with the beam crossing such as cosmics. The threshold energy for each barrel module could be chosen between 1-3 GeV depending on the trigger conditions required. The endcaps were treated slightly differently by summing the energies from the semicircular strips of each module. These energies were compared with preset thresholds.

The neutral triggers were;

1) A deposit of ≥ 2GeV in one barrel module read out from both SUMA and SUMB

2) Two barrel modules with ≥ 1.8 GeV from SUMA only and separated by ≥ 45^0 in $r\varphi$.

3) One endcap module with ≥ 2 GeV combined with a charged trigger (one track with $p_t \geq 250$Mev) or a barrel module with a deposit ≥ 2GeV.

4) Two energy deposits in opposite endcaps (no charged triggers required). This was designed to be a Bhabha trigger.

5) A deposit of ≥ 2GeV in one of the forward Lead-Glass detectors combined with a charged trigger (one track with $p_t \geq 250$MeV) or a barrel module with a deposit ≥ 2GeV.

3.9 The Data Aquisition System

The detector components were read out onto a CAMAC ROMULUS system. Each separate detector component had its own branch in the system. The trigger also had its own branch. Each branch could be accessed by its own onboard microcomputer which could be used to monitor the state of the specific detector component or by the local online computer which oversaw the whole detector readout operation. This online computer (a PDP) read the information from the separate branches (when it had received a favourable trigger) and formed it all into an event record which was then buffered onto disk. These events were then passed onto the DESY IBM where they were again stored on disk and eventually written onto tape. As well as controlling the data stream, the PDP also operated the detector control program. This program enabled physicists to monitor the detector's performance. The PDP also made a quick analysis of each event, and flagged candidates for multihadronic and bhabha events. These could then be viewed with the CELLO display program on the DESY IBM. This was an important feature enabling the physicists on shift to determine the luminosity and hadronic cross section, as well as check the detector components were working correctly.

Circumference	2304m
Injection energy	6-7 GeV
Beam energy	5-23 GeV
Energy spread	$2.3 \times 10^{-5} * E_{beam}$
Luminosity	max. $17 \times 10^{30} cm^{-2} s^{-1}$
Beam lifetime	3-5 hrs
Number of bunches	2 per beam
Bunch length	10 mm rms
Bunch width	0.7 mm
Bunch height	0.1 mm
Bunch crossing time	$3.8 \mu s$
Beam current	20 mA max.
RF	500 MHz
RF power	4 MW
Klystrons	8
RF cavities	60

Table 3.1 Some general machine parameters of PETRA.

Detector Component	Number of Modules	Solid angle $\frac{\Delta\Omega}{4\pi}$	Typical Dimensions (cm)	Important Properties
Central Tracker	2 BPCs 5 CPCs 7 CDCs	0.87	Length 220 Radius 10.9 to 70	$\sigma_{r\phi} = 440\mu m$ $\sigma_{r\phi} = 170\mu m$ $\frac{\sigma_P}{P} = \frac{0.02}{P(GeV)}$
Endcap Tracker	8 PWCs	0.10	$z = \pm 140.5$ $z = \pm 142.5$	Thickness=0.02 X_0
Central Solenoid	1		Length 400 Radius 80	Superconducting Thickness=0.59X_0
Calorimeter	16 around the central tracker + 4 endcaps	0.86 0.07	Length 400 radius 80	$\frac{\sigma_E}{E} = .05 \oplus \frac{0.10}{\sqrt{E(GeV)}}$ $\sigma_\phi = \sigma_\theta$ =4mrad typically
Muon Chambers	32	0.92	200 × 300 to 300 × 400	$\sigma_{x,y} = 6mm$
Forward Detector	96 scint 112 Pb glass Shower Counters			$\frac{\sigma_E}{E} = \frac{0.10}{\sqrt{E(GeV)}}$

Table 3.2 Some general parameters of the main detector components of CELLO.

Layer	Type	Radius (cm)	Number of anode wires or drift cells	Wire spacing or drift cell width (mm)	Number of Cathodes 90°	30°
1	BPC	10.9	128	5.35	–	
1	BPC	11.4	128	5.35	–	
3	CPC	17.0	512	2.09	258	256
4	CPC	21.0	512	2.58	228	256
5	CDC	25.5	104	15.41	–	
6	CDC	30.4	128	14.92	–	
7	CPC	35.7	1024	2.19	366	512
8	CDC	40.2	168	15.03	–	
9	CDC	45.1	192	14.76	–	
10	CDC	50.0	208	15.10	–	
11	CPC	55.3	1536	2.26	420	768
12	CDC	59.8	256	14.68	–	
13	CDC	64.7	256	15.88	–	
14	CPC	70.0	1536	2.86	494	768

Table 3.3 The layered structure of the central tracking chamber.

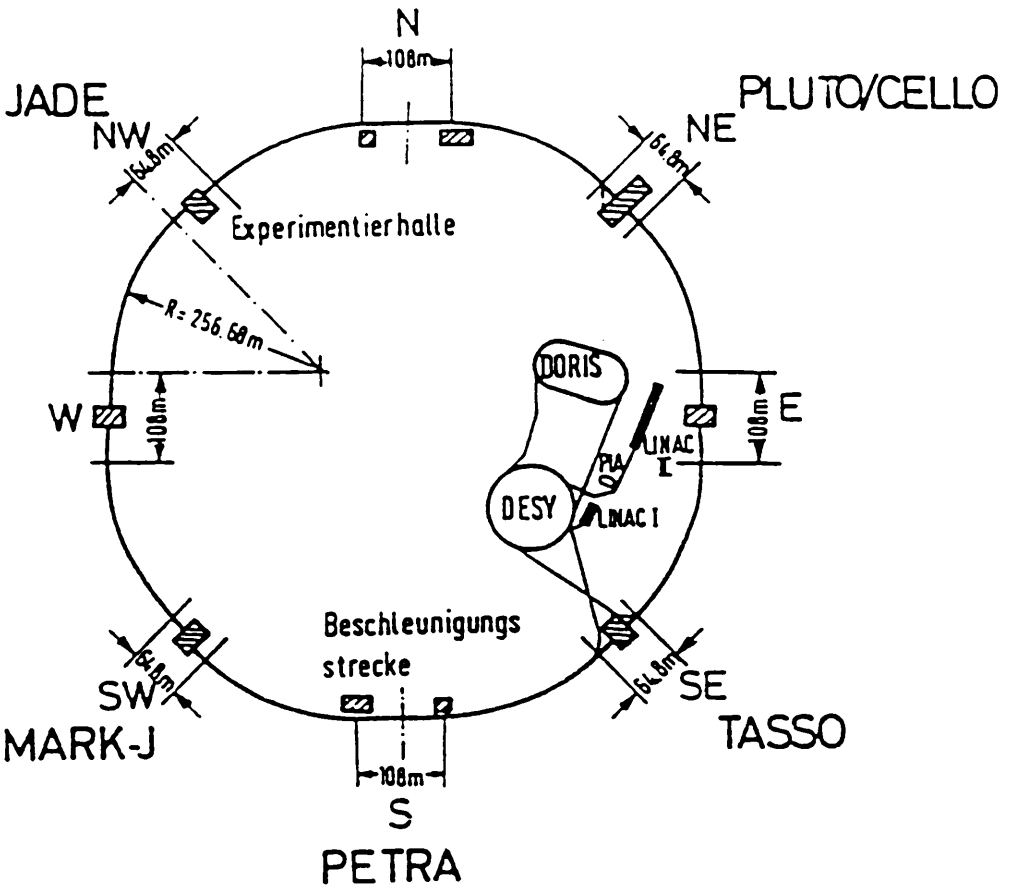

Fig 3.1 Schematic diagram of PETRA.

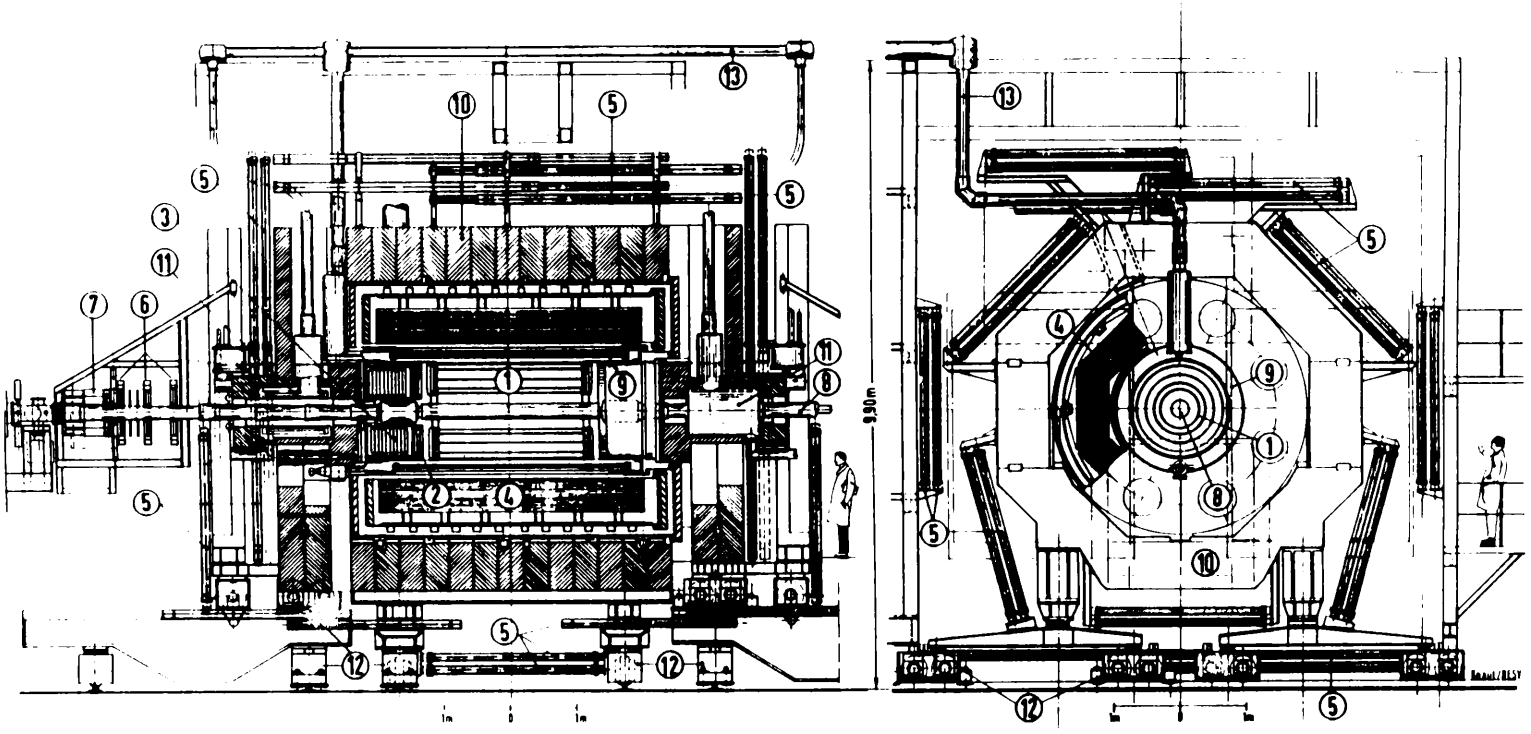

1 Central Drift-and Proportional Chambers
2 Endcap Proportional Chambers
3 Endcap Shower Counters (liquid Argon)
4 Cylindric Shower Counters (liquid Argon)
5 Proportional Chambers for Muon Detection
6 Drift Chambers for Forward Detector
7 Shower Counter for Forward Detector
8 Vacuum Beam Pipe
9 Superconducting Coil of Detector
10 Iron Yoke
11 Compensation Coils
12 Moving Devices
13 Feed Lines for Liquid Helium

Participants:
Orsay
Saclay
University (VI) of Paris
MPI, München
GfK, Karlsruhe
DESY, Hamburg

DETECTOR CELLO
Total Weight: ~1400 t
Magnet Field: 15 kΓ

Fig 3.2 CELLO

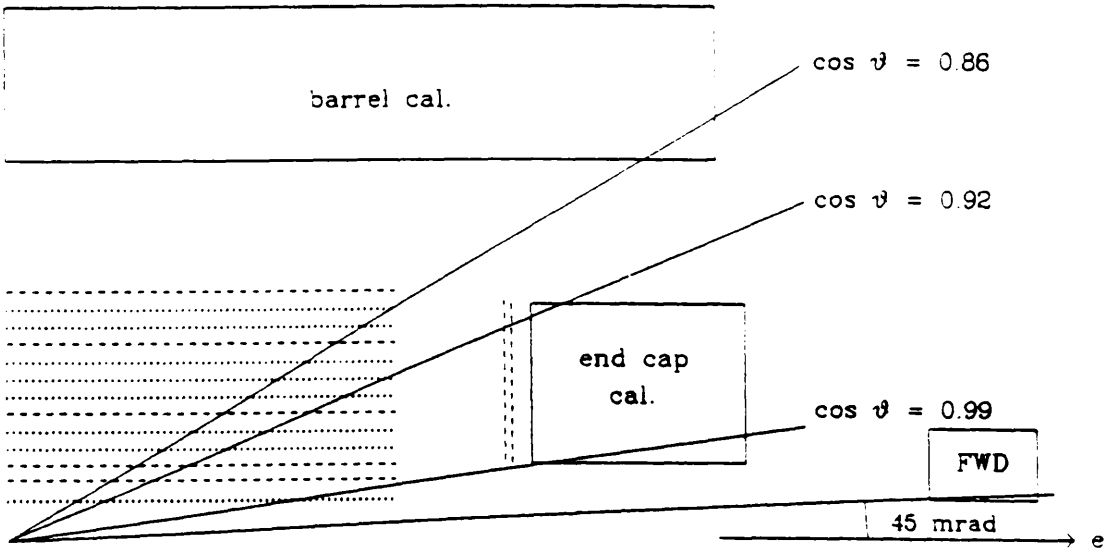

Fig 3.3 Details of the CELLO acceptance.

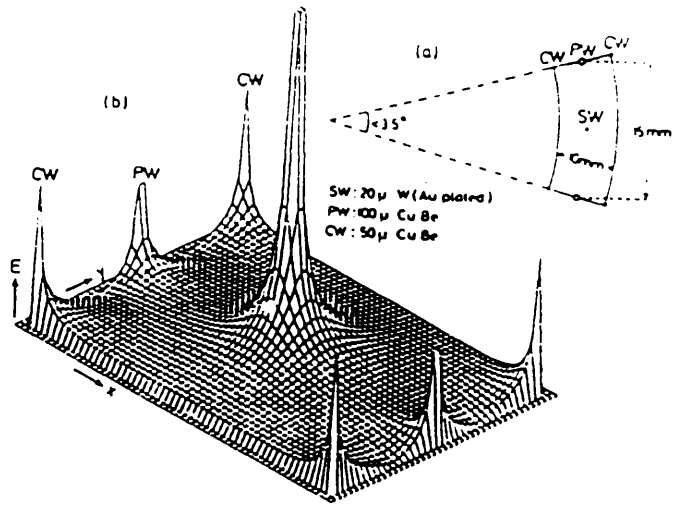

Fig 3.4
a) The dimensions of one of the cylindrical drift chambers.
b) The electric field distribution inside the chamber.

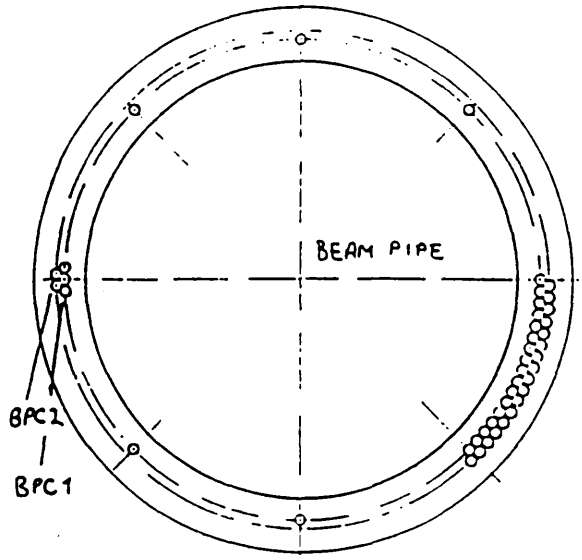

Fig 3.5 The end view of the beam pipe drift chambers.

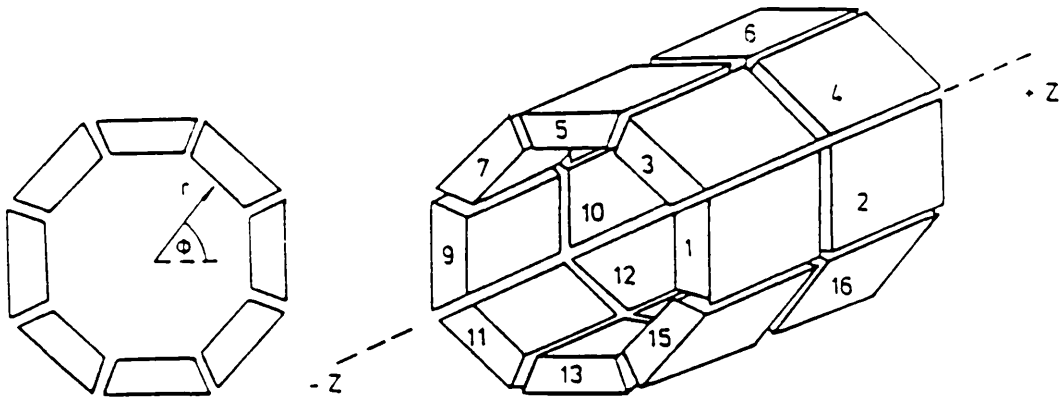

Fig 3.6 The layout of the lead liquid argon barrel modules.

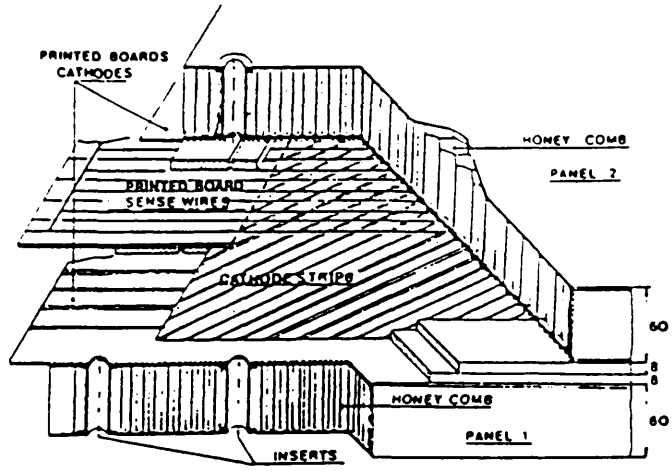

Fig 3.8 Constructional details of a CELLO muon chamber.

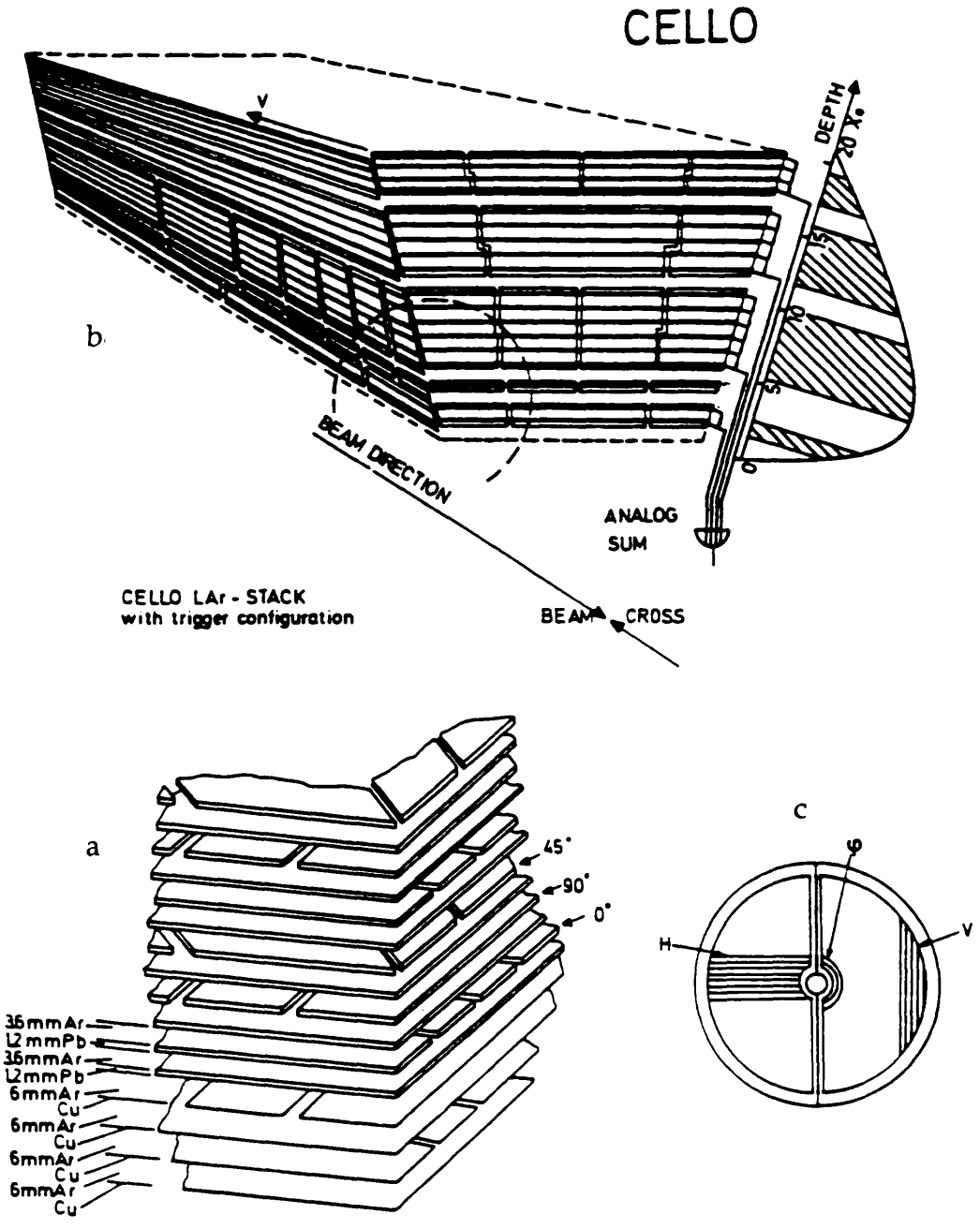

Fig 3.7

a) The orientation of the u, v, w strips in a barrel module.

b) The layered structure of a barrel module.

c) The layered structure of an endcap module.

a

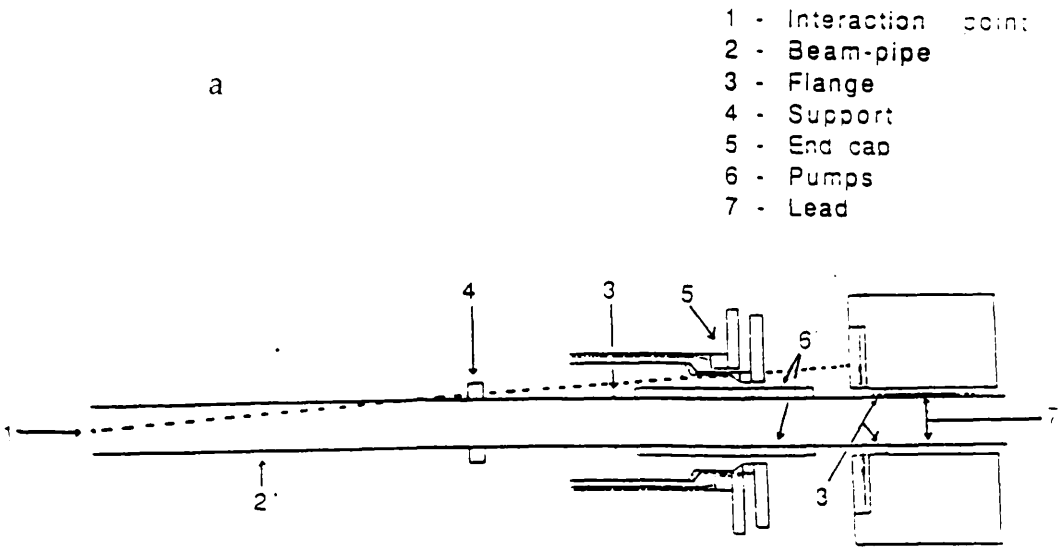

b

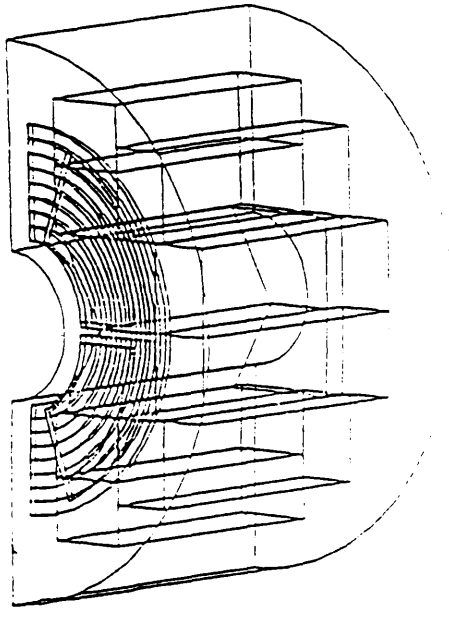

Fig 3.9

a) Side view of the forward detector.

b) The arrangement of the lead glass blocks in the forward detector showing the scintillator strip positions on the inward face of the structure.

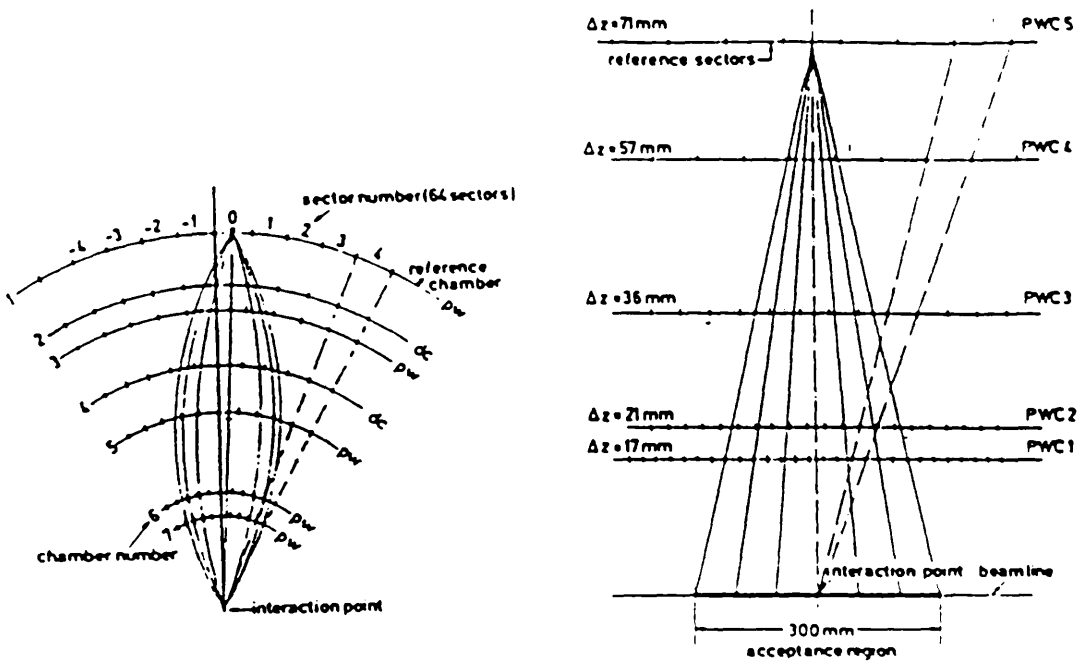

Fig 3.10 The rφ and rz sectors used in the charged trigger logic.

Chapter 4

Data Selection and Software

4.1 The Filter

The online trigger had two main negative features: the acceptance requirements that it placed on events had to be be relatively loose in order that it did not reject good physics (such as photon-photon events). It was also limited in the reconstruction it could perform because of the short time available between beam crossings. Because of this, a large number of background events originating from beam-gas/pipe interactions, synchrotron radiation and electronic noise fired the trigger and were consequently read out from the detector. These accounted for the large majority of events read out, and therefore had to be suppressed in some way before being passed through the time-consuming full reconstruction program. This was done by the filter program (4.1). The filter did a simple reconstruction of events using the information from the tracking chamber and the calorimetry. It then made a decision as to whether an event be marked good or bad.

While the data was being stored on an online disk on the DESY IBM (waiting to be written to tape), a 370/E emulator read these events and processed them through the filter marking them either GOOD or BAD. The emulator was used to reduce the workload on the IBM. Unfortunately, due to time limitations the emulator was only able to process approximately half of the events on the disk before they were written to tape. Consequently the tapes were reprocessed on the DESY IBM. The unfiltered events were passed through the same filter program, and as a check a small fraction (5%) of the events which had been marked BAD by the emulator were run through the filter again, and checked that they were still marked BAD. The events were all written to the DUMP tapes. Those marked GOOD were also written to the FILTER tapes. The filter program reduced the data sample relevant to this analysis from 61.5 million events to 7.5 million. This was a substantial reduction of 88%.

The filter tried to confirm that recorded information was present which agreed with at least one of the fired triggers, by means of a simple event reconstruction using data from the central tracking chamber and the liquid-argon. If it was able to do this, it then marked the event GOOD, and if not it

was marked BAD. In principle the filter should not have rejected good events, but in practice it did reject a small fraction. This inefficiency could be estimated by running Monte-Carlo events through a trigger simulation and the filter (see section 5.10).

The filter firstly tried to reconstruct tracks in the central tracking detector. A search was done in rφ, requiring a track to have 9 hits and point to within 3cms (in the rφ plane) of the interaction point. Tracks were then reconstructed in the rz plane and a fit to the interaction point was again made. A decision on whether to accept an event on the basis of the charged track information depended on the number of reconstructed tracks, the sum of their absolute charge and the largest opening angle between two tracks.

The energy deposits in each of the lead-liquid argon modules were split into different classes depending on the energy. For each module the FADC's were read out at two specific times after the beam crossing to confirm the showers developed at the expected time as already mentioned. This was a powerful method of rejecting showers which did not coincide with a beam crossing, such as those due to cosmics or electronic noise. Showers developing from real events would peak at a specific time after the beam crossing, whereas background showers would not be correlated with the beam crossing time. A further reconstruction was done using the information from the single strips.

4.2 OFFRAM

The FILTER tapes were then distributed to the various institutes involved in the CELLO collaboration where they were passed through OFFRAM. The purpose of OFFRAM was to fully reconstruct the events and produce useful physical quantities such as the track momenta of charged tracks and the shower energies of neutral deposits.

OFFRAM contains various sub-programs which handle the reconstruction for CELLO's various sub-detectors, steering the data through these sub-programs, providing them with information on the state of the detector, run dependent calibration constants, inefficient/dead channels etc. It also provides instructions on how to proceed with the reconstruction. The physical quantities are stored using the BOS memory management system (4.2), each sub-detector having its own banks. Each charged track has its own SPUR bank (German for track), and each identified shower has its own LATR bank (liquid argon track). For each event, the original raw data plus the banks

created by OFFRAM were written on to the data summary tapes (DST tapes). The sub-programs in OFFRAM are described below.

4.2.1 CELPAT

CELPAT reconstructs charged tracks from the hits detected in the central tracking chamber. It has three main parts; ANOCAT, RFIPAT, RZPAT.

ANOCAT combines the signals from the proportional chamber anodes and the $30^0, 90^0$ cathodes to produce 3-dimensional space points.

RFIPAT splits the $r\varphi$ region into a set of overlapping sectors. In each sector it tries to form a track using the points available. The points are required to lie on a circle which points to within 15cms of the interaction point. A track is required to have at least 7 points on it (6 for low momentum tracks) in order to be accepted. If a track is found, the points on it are removed from the set available for the subsequent search. This process is iterated until no more tracks are found. In successive iterations the $r\varphi$ sectors begin narrow to identify the high momentum tracks with a low radius of curvature, widening to allow the low momentum tracks which have larger curvatures to be identified.

RZPAT searches for sequences of points which lie on a straight line pointing towards the interaction point in rz. The information from ANOCAT is combined with the tracks found in $r\varphi$ and rz to form a set of 3-dimensional tracks. This information is written to a SPUR bank.

4.2.2 CLGEOM

The tracks found in CELPAT are then subjected to a fit which uses the interaction point as a point on the track and also uses an accurate map of the 1.32 Tesla field (this not being completely uniform over the tracking chamber). The interaction point for each run was determined using bhabha events (see GLOFIT). Using the interaction point as a point on a track improves its momentum resolution, but is not of course useful for tracks which are formed from a secondary vertex. The information is added to the end of the tracks SPUR bank.

4.2.3 ECCPAT

Tracks produced at low angles with respect to the beam cannot pass through all the inner tracking chambers. ECCPAT uses hits in the chambers close to the beampipe, and combines them with the hits in the endcap proportional chambers to form tracks. This allows tracks to be reconstructed down to angles of $\cos\theta \leq .97$ ($\sim 14^0$). Tracks with endcap chamber hits are only required to have 5 hits lying on them (because of the limited number of chambers available to be traversed).

4.2.4 GLOFIT

The program GLOFIT subjected the track points in collinear 2 track events (bhabhas , $\mu^+\mu^-$) to a common fit (they should all lie on one curve). Because the interaction point is not included in this fit, an accurate measurement for it can be obtained from this procedure. The precise position of the beam interaction point was important for the trigger and also the analysis programs (ie the filter and CELPAT). This program was therefore run online and the interaction point stored in a runfile.

4.2.5 LATRAK

LATRAK is the sub-program responsible for the reconstruction of the electromagnetic showers produced in the lead-liquid argon calorimeter. The strip readouts are used to provide the energy, spatial position and direction of showers. This is first done by forming 2 dimensional clusters using the three strip types (u, v, w) in each of the layers. These clusters are examined to see if they display any signs of two overlapping showers. The program then tries to link these clusters to tracks in the tracking chamber. Charged tracks are extrapolated to the liquid argon. If they point to any 2-dimensional clusters these are linked together to form a 3-dimensional shower. A fit is performed to ascertain whether the shower does point towards the track. If it does, then that shower is connected to the track. The program then attempts to form 3-dimensional showers with the remaining 2-dimensional clusters. These are assumed to be photons.

4.2.6 MUCH

This sub-program attempts to link tracks found in the inner tracking chamber with hits in the muon chambers. Tracks are extrapolated (taking their momentum into account) through the calorimeter and iron return yoke into the muon chambers. If the track points towards the muon chamber hits, then the track is deemed to be a muon.

4.3 Data Selection

Because the beam conditions in 1986 were very good, the triggers were made as loose as possible in order to allow photon-photon events to be detected. To reduce the data sample, the fully reconstructed events on the DST tapes were passed through a program (4.3) which selected both annihilation and photon-photon events. This program also removed forward and endcap bhabhas from the events sample.

For this analysis the most important selection requirements were those designed to pass multihadronic photon-photon events. Many of these events would be passed by the standard annihilation selection criteria. However, since photon-photon events have a lower average energy and track multiplicity, additional pass requirements were designed to pass photon-photon events. These had much looser cuts than the annihilation selection requirements. These consisted of the following pass requirements.

1) There were ≥ 2 SPUR banks present. No vertex constraint is made so as to preserve tracks originating from secondary vertices (ie K^0_s to $\pi^+\pi^-$).

2) The tracks did not all have the same charge (this will remove some beam-gas events).

3) There were less than 50 hits recorded in the beam-pipe chambers (this removes a fraction of beam gas/pipe events which shower and caused the beam-pipe chambers to saturate or 'light up').

4) There are not exactly 2 tracks in opposite endcaps with shower energies of ≥ 5 GeV (This removed endcap bhabhas).

The events that passed the SELECT job were then written to the DST.SELECT tapes. This is the origin of the data used in this analysis.

4.4 VIOLA

Because of the typical nature of photon-photon events (low momentum tracks, low multiplicity and low overall energy compared with the e^+e^- cms energy), it was found that improvements were needed to OFFRAM in order to analyse these events effectively. To this end a package was developed that went much further than the reconstruction implemented in OFFRAM. VIOLA (4.4) is again a main program which controls a set of processors which do extra reconstruction of the data from the various sub-detectors, as well as some particle identification.

VCHARG looks at the SPUR banks created by CELPAT and

1) Rejects spurious tracks which have been reconstructed from points very close to another track but missed in its reconstruction. These two tracks will have almost identical parameters. VCHARG will reject the track with the worse track χ^2 (where the χ^2 relates to the fit of the points to the track).

2) Tracks which did not have the interaction point included in the fit performed on them are rejected if their minimum distance to the interaction point is $\geq$ 2cm. Tracks which did have the interaction point included in the fit are not affected. Note this does not affect the search for secondary vertices in V0CAND (see below).

VSHOWR looks at the LATR bank information and recalibrates the shower energies, taking dead, bad and noisy channels into account. It also tries to distinguish between electrons, muons, hadrons and photons by looking at the characteristics of the shower deposition (4.5).

V0CAND tries to reconstruct neutral particles (K^0_s, Λ) which have decayed into a pair of oppositely charged tracks in the tracking chamber (4.6). The program starts by choosing a charged track, then choosing another charged track (with the opposite charge) and performs a fit to determine whether they originate from the same secondary vertex (this fit is done in the rφ plane only). If the fit is good and the effective $\pi^+\pi^-$ is close to the K^0_s mass then the pair of tracks is deemed to be a K^0_s. The program loops around all possible $\pi^+\pi^-$ candidates. (Λ's are treated similarly.)

FWDMPP reads the raw data concerning the forward detectors. It looks at the readout from the lead-glass blocks and the scintillator strips directly in front of them. The energy of a particle is determined from the showers produced in the lead-glass blocks. The θ, φ information is determined by looking at the centre of gravity of the showers in the lead-glass, (and combining this with the readout from the scintillator strips). The scintillator strip which is hit provides a good θ measurement; the φ measurement is determined from the ratio of the signal collected from each end of this strip. If a scintillator strip is fired then the information from the lead-glass blocks and the scintillators is combined taking account of the errors on each measurement. If no scintillator is fired then only the lead-glass information is used. A calibration of the forward detectors was done using tagged lepton pairs (see section 6.2).

TRACKI: Because the track reconstruction program is not 100% efficient it does not always identify all the tracks present in an event, especially low momentum tracks, which have a small radius of curvature. Unidentified tracks will sometimes cause showers in the lead-liquid argon which will be mistakenly identified as photons because they are not linked to a charged track. Backscattered electrons and hadrons also produce mistakenly identified photons. These occur when particles interact with the solenoid and knock a charged particle back into the tracking chamber. These curve through the chamber and exit into the lead-liquid argon, producing a shower. Because the track producing this shower did not originate from the interaction point (but from the solenoid) it is unlikely to be successfully reconstructed by CELPAT, and therefore the shower will be presumed to be a photon. It is obviously important to try and minimize this effect, and consequently TRACKI was designed to identify these unreconstructed tracks and link them to their associated shower, removing these from the set of final photon candidates. TRACKI used the unassigned hits available in the inner tracking chamber and tried to fit them to a circle in the $r\varphi$ plane only. If it was able to link a this circle to a shower in the lead-liquid argon, then the shower was removed from the set of photon candidates.

Chapter 5

Monte-Carlo Methods and Models.

5.1 Introduction

When the detector records an event during a run, the tracks and showers measured by the detector represent only an approximation to the true picture. The picture is blurred somewhat by the fact that the event is distorted by the measurement errors present, the limited acceptance of the detector etc. This makes it very difficult to interpret the physical processes which produce the detected 'event'. It is therefore very important to understand this smearing, the effect it has on the data and how to correct for it.

A widely used method is not to try and correct the data for the smearing it received, but to produce a theoretical model of what the data might be expected to look like, and then distort this model in the same way as the detector is expected to do to the real data. In other words, we simulate the detector's effect on the events. After this model has been passed through a detector simulation it can be compared with the real data. This approach is known as the Monte-Carlo (MC) method (the name originating from the random nature of the event generation).

The MC procedure can be split into two separate sections.

1) The theoretical model is used to produce a set of events, each comprising primary 4-vectors which describe the angles and energies of the particles. These quantities are distributed according to the prescription of the model. If these primary particles are unstable (ie quarks, taus etc), then they must be further fragmented using one of the well known fragmentation procedures available such as Feynman-Field (5.3), LUND (in its various versions, 5.5). Thus for each event a set of particle 4-vectors is produced, along with their masses, charges and particle codes. This data set is then passed onto the second stage.

2) In order to determine the effect of the detector on an event, the particle 4-vectors are then passed through a detailed simulation of the detector. This program simulates the passage of each particle through the various sub-detectors. It simulates the particles' interactions with the detector, ie scattering with the materials present, the effect of the magnetic field on

charged particles, gas ionisation for charged tracks, shower development in calorimeters and subsequent decays of unstable particles. This program outputs a set of numerical data identical in format to that collected from the real detector, ie simulated ADC, TDC readings from each sub-detector. These can then be reprocessed using the same reconstruction program as the data, ie OFFRAM. A simulation of the triggers applied to the data is also required to be applied to the MC events. The MC events can then be further analysed in exactly the same way as the data.

MC simulations also supply information as to where the cuts on the data sample should be placed, so as to maximise the content of the required process, and to minimise the content of unwanted backgrounds. It should be noted that MC simulations of all possible backgrounds will be required in order to understand their effect on the data sample.

In this analysis MC simulations were produced for the QPM and VDM models as well as all expected backgrounds (see later). Phasespace and multijet generators were also studied.

5.2 A short note on Cross-Sections and Luminosities.

In the data sample for this analysis the total integrated luminosity was calculated by using large angle Bhabhas and using the known cross-section for this process (5.1). L is the total integrated luminosity and l is the luminosity per unit time. The variable l will vary from run to run and also during the run. It will depend on the numbers of electrons and positrons in the bunches, and the bunch dimensions among other things.

$$L_{DATA} = \int l dt = 86 \pm 3 \text{ pb}^{-1}$$

The error is mainly due to the systematic errors and these are smallest for large angle Bhabhas. The luminosity, the cross-section for a process, and the number of events produced can be related using the following equation.

$$N_{TOT} = \sigma L_{DATA}$$
$$N_{DATA} = \varepsilon N_{TOT}$$

where N_{TOT} is the total number of events produced for a process with a cross-section σ and total integrated luminosity L_{DATA}. The number of

detected events N_{DATA} is less than the total number because of the limited efficiency of the detector for any given process (due to trigger inefficiencies, acceptance, cuts etc), this efficiency being ε.

The same equations apply to simulated events where for a given cross-section and luminosity the final number of events can be calculated, the MC program providing the value of ε. To make possible any comparisons between data and MC, their luminosities must of course be equal. However this means that the statistical error on the MC data would be the same as for the data. This is undesirable since the statistical errors on the MC data should ideally be much smaller than those of the data, and therefore it is usual to generate a larger luminosity of MC data and 'weight' it with a correction factor Wt such that

$$L_{DATA} = L_{MC} \times Wt$$

In this analysis the luminosity of MC generated was 180 pb^{-1}. This was limited by the amount of CPU time available to generate the MC events. The CELLO MC program used a large amount of computer time due to its complexity, taking approximately a minute to simulate the passage of a multihadronic event through the detector.

The MC 4-vector generators for the QPM, VDM and background processes are now described.

5.3 The QPM Generator.

The QPM 4-vector generator is based on the diagram for the production of a fermion-antifermion pair by two photons scattered from the beam leptons. This is exactly calculable in QED. The fermions chosen in this case being quarks, they are assigned the quarks' mass and charge (depending on quark type). They are then subjected to fragmentation into hadrons .

Two programs were used to produce quark-antiquark pairs. The first used the Vermaseren program to generate the quark-antiquark pair (5.2).

$$e^+e^- \rightarrow e^+e^-q\bar{q}$$

The only diagrams calculated are the top two in Fig 5.1. The program calculates the total cross-section over the total phasespace allowed by the cuts used, and then produces each event with a weight which is proportional to

its likelihood of being formed. Random numbers are generated over the spectrum of possible weights and if an event weight is greater than this random number it is accepted as an event with unit weight. The cross-section for these unit weighted events is related to the number generated by the equation.

$$N_{MC} = 3e_q^4 L_{MC} \sigma$$

where σ is the total cross-section for unit charged leptons, the factor of 3 comes from the number of quark colours which can be produced and the 4th power of the quark charge is due to the two quark-photon vertices in the Feynman diagram. Events were produced for the 4 lightest quark flavours u, d, s, c with the constituent masses 0.3 GeV, 0.3 GeV, 0.5 GeV and 1.5 GeV respectively.

Once the quark 4-vectors are produced they must then be fragmented into hadrons in order to pass through the detector simulation. The Vermaseren generated quarks were fragmented using the Feynman-Field program (5.3). Feynman-Field fragments each quark independently. The initial quark (let us suppose it is a u quark) creates a colour field into which a quark-antiquark pair is formed, say a $d\bar{d}$, forming a $u\bar{d}$ meson with fractional momentum z of the original quark's momentum. The d quark then continues to form another quark pair and forms a new meson. This continues recursively until there is no momentum left in the chain (Fig 5.2). This process can be described by an arbitary function f(z) (if transverse momentum, spins, flavour are ignored), which must be normalized to 1 since the probability for each step to occur for any value of z is 1, thus

$$\int f(z)dz = 1$$

In fact the original Feynman-Field approach identified z with the energy fraction $E+p_L$ and used the distribution

$$f(z) = 1 - a + 3a(1 - z)^2$$

where a is an arbitary constant determined from data. The standard value of a=0.77 was used. The ratio of vector mesons to scalar mesons produced was

1:1. The fragmented hadrons were given a gaussian p_t distribution with σ = 350 MeV (with respect to the parton axis).

A second set of QPM events was generated using the Daverveldt generator (5.4). This supercedes the Vermaseren generator, generating all possible diagrams for the process

$$e^+e^- \rightarrow e^+e^- q\bar{q}$$

including all first order QED corrections where an extra lepton-photon vertex is included. Fig 5.1 shows all the possible zeroth order diagrams. The quark-antiquark pairs were then fragmented using the LUND 7.2 fragmentation package (5.5) which used the parton shower fragmentation system, this being the most up-to-date package available. Fig 5.3 shows some comparisons of the two different models. The different generators produce slightly different charged multiplicities, affecting the total numbers accepted after final selection cuts. However, as can be seen the jet p_t, thrust distributions agree closely. The general properties of the two models show good overall general agreement. It should also be pointed out that the Daverveldt generator also takes account of the inelastic-compton process. This is a background process which is negligible except at high W, Q^2 (5.6). The LUND program also used a more up-to-date treatment of D meson decay, this being important for the correct modelling of charm decays. *

As already implied, there are specific cuts applied to the generated phasespace integrated over in this program. In order to reduce the number of events to be processed through the detector simulation, all events were required to have a hadronic mass W $\geq$ 3 GeV. In the final data sample the measured W_{VIS} was required to be $\geq$ 4 GeV. By plotting the generated W of all the QPM events that passed this and all other final cuts (Fig 5.4) it was verified that the number of events generated with W $\approx$ 3 GeV which were smeared such that $W_{VIS} \geq 4$ GeV and subsequently passed all the final cuts was negligible. In fact the W_{VIS} of the measured events is usually considerably less than the true W because of the acceptance of the detector. This is demonstrated by a plot of W_{VIS}/W_{GEN} in fig 5.5. The mean value of this quantity will depend on the nature of the process (its angular dependence) and is ~ 0.75 for QPM events. The number of events generated and their appropriate cross-sections which were passed through the MC simulation are shown in table 5.1. The cross-sections cover all kinematical Q^2 possibilties and are shown separately for each quark flavour.

* The Daverveldt generator (with LUND) was subsequently used in the analysis

5.4 The VDM Generator

Unlike the QPM process which can be calculated exactly, the VDM is a parameterised model. The generator was split into two distinct pieces. Firstly, photons were produced as if radiated from the beam leptons using the equivalent photon approximations. (Studies showed that in the kinematical region used the errors introduced by using the EPA were < 2%.) The cross-section for each event was obtained by taking the product of the photon luminosity functions, a GVDM term depending on the Q^2 of the photons and a flat W term of 240 nb. As well as using a GVDM term it was possible to examine the Q^2 dependence of the VDM and ρ-VDM models by replacing the GVDM Q^2 dependence by the required form factors used in the two models (see sections 1.8, 1.9). This was done by reweighting the GVDM events after final selections by the term;

$$\text{WEIGHT} = \frac{F_{\gamma 1}\left(Q^2_{\gamma 1}\right)_{VDM} \bullet F_{\gamma 2}\left(Q^2_{\gamma 2}\right)_{VDM}}{F_{\gamma 1}\left(Q^2_{\gamma 1}\right)_{GVDM} \bullet F_{\gamma 2}\left(Q^2_{\gamma 2}\right)_{GVDM}}$$

where the form factors are defined in chapter 1. Consequently the data could be compared with both GVDM and VDM models. As with the QPM model, events were generated only above a W_{GEN} of 3 GeV. These 4-vectors were then added to produce a photon-photon hadronic mass $W_{\gamma\gamma}$ which was fragmented into two back to back sets of hadrons, using the Feynman-Field fragmentation scheme, but with non-standard parameters. The parameters were obtained from analyses of two photon data at PLUTO and JADE (5.6). The ratio of quarks in the sea available to be formed into mesons was u ; d ; s ; c = 2 ; 2 ; 1 ; 0, a = 0.45 and the transverse momentum distribution of the fragmenting hadrons (along the parton axis) changed to σ = 450 MeV. This tuning is necessary because the ρ–meson hadronisation is softer than that for quarks. These parameters were fitted to agree with low p_t data where the VDM process is dominant (5.6). The partons produced were tilted with respect to the $\gamma\gamma$ axis with an exponential p_t distribution.

$$\frac{dN(\text{jet})}{dp_T^2} \sim \exp(-kp_T^2)$$

In this equation the value k = 5 was used, as suggested from e-p data (5.7). In order to study the effect of altering these parameters, the Feynman-Field fragmentation scheme using the tuned parameters was compared with the LUND fragmentation scheme where σ = 350 MeV was used for the jet fragmentation. This causes the jets of hadrons to be more collimated. Because the jets produced are predominantly at low p_t, the width of the jets strongly affects the acceptance of the process. It was observed that the acceptance using the LUND scheme was 14% less than for the Feynman-Field scheme. The different fragmentation schemes also produced different W_{VIS}, thrust and jet p_t distributions after the detector as shown in fig 5.6. The different σ values alter the jet p_t, W_{VIS}, and thrust distributions because this affects the jet shape and acceptance of the models. Fig 5.7 shows the W_{GEN} plot. This extends to higher values than for the QPM model because the VDM process has a much flatter cross-section in W. Fig 5.8 also shows the plot for W_{VIS}/W_{GEN} has a lower mean value than that for QPM. This is because the VDM process has a lower acceptance, because its p_t dependence forces more particles down the beam-pipe. Table 5.1 shows the numbers of generated events and the associated cross-section for each Q^2 region. The events were combined for the final analysis. It was found that single tagged events (where the scattered lepton remained undetected) were a sizeable background to the untagged data sample, although the number of untagged events which faked a tagged event was small (mainly due to the large energy deposit > 10 GeV required for a good tag). No double tagged GVDM events were generated since the large Q^2 of both scattered leptons made the cross-section small enough to be neglected.

5.5 The Phasespace Generator

The phasespace generator (5.8) was used to compare with the two-jet models mentioned in the above sections. Whereas these produce hadrons in two back to back jets in the photon-photon final state centre of mass, the phasespace model produces an isotropic distribution of hadrons in the photon-photon final state centre of mass system. The final state is composed of an all-pion decay mode, the multiplicities of the charged and neutral channels being taken from annihilation data at similar centre of mass energies. The final state was generated with the same Q^2 distribution as the GVDM model and a flat W dependence. A $1/W^2$ dependence could also be folded into the cross-section.

5.6 The Multijet Generators

The multijet models described here were designed to simulate 3 and 4 jet structures (5.8) and are used to investigate the nature of the discrepancy in the untagged data. As discussed in section 1.11 these higher order components are expected have a cross-section at least as large as the QPM component. It is therefore relevant to try and model these higher order processes. Here only reactions with the p_t^{-4} hard scattering processes $\gamma\gamma \rightarrow q\bar{q}g$ and $\gamma\gamma \rightarrow q\bar{q}q\bar{q}$ shown in fig 1.12 b, c are considered. The $\gamma\gamma$ cross-section is generated with a $1/W^2$ dependence (assuming a pointlike coupling as in the QPM) using a Vermaseren generator.

In the case of the $\gamma\gamma \rightarrow q\bar{q}g$ generator the first virtual photon is converted into a $q\bar{q}$ pair where the distribution of the photon's momentum carried by each quark is flat. One of these quarks then interacts with the second photon in the hard scattering process (shown in the hatched box in fig 1.12b) $\gamma q \rightarrow qg$. This has a p_t^{-4} dependence in its cms frame. The system is then fragmented using the LUND fragmentation scheme. The process $\gamma\gamma \rightarrow q\bar{q}q\bar{q}$ is similar. Here both photons are converted into $q\bar{q}$ pairs (with a flat momentum distribution between both quarks). Two of these then interact in a p_t^{-4} hard scattering process (shown in the hatched box in fig 1.12c) $qq \rightarrow qq$. Again the quarks are fragmented using the LUND fragmentation scheme.

Although these models only simulate the p_t^{-4} processes and ignore the possible p_t^{-6}, p_t^{-8} components it is reasonable to argue that at such low final state centre of mass energies these would be indistinguishable anyway. These are simply basic models in order to ascertain whether the discrepancy observed in the untagged data can be described by a simple multijet model.

5.7 Backgrounds

5.7.1 Multihadronic Annihilation

The MC simulation of backgrounds is particularly important in this analysis because they are a significant fraction of the data in certain kinematical regions of interest. It is important that the simulation is accurate in the kinematical regions being studied so they can be subtracted from the data samples with confidence. By far the largest background present which needs to be studied is due to multihadronic annihilation events. Although mainly

produced with high centre of mass energies, these events fake hadronic photon-photon events when

1) Most of the event is undetected when the jets of particles pass down the beampipe causing the detected multiplicity and energy to be a small fraction of the true values.

2) There is an initial-state photon radiated causing the final state energy to be reduced.

These events can also fake tags in a number of different ways. The radiated initial photon can sometimes pass into the forward lead-glass calorimeters and fake a scattered electron/positron. Because there are no drift chambers in this region these are indistinguishable from electrons. Also, a jet of hadrons with sufficient energy can sometimes cause an energy deposit in the forward calorimeters large enough to fake a tag. It is therefore important that the simulation of energy deposition by all types of particles is correctly simulated in the forward calorimeters. Endcap tags can be faked by high energy pions or photons from the final state. Again initial-state photons can pass into the endcap calorimeters faking tags. Unfortunately, charged tracks cannot be reconstructed with good efficiency at the low angles the endcaps cover, because the tracks pass through few tracking chambers. This means again that photons and electrons cannot be distinguished. Unfortunately, the endcaps had many dead layers, making any identification by looking at shower developments problematic.

The generator used was based on the LUND 6.3 fragmentation model (5.5). It simulated initial-state radiation allowing photons with up to 99% of the energy available to be radiated. There is a rise in the cross-section at low energies in the W spectrum, because although the photons are radiated with a $1/E_\gamma$ bremsstrahlung distribution, the annihilation cross-section scales as $1/s$ and therefore is higher at lower cms energies (Fig 5.9). The model simulated u, d, s, c, b quark production as well as gluon emission up to 2nd order in QCD. The fragmentation parameters used in the generator to hadronise the radiated quarks and gluons depend on their energy and this is important when looking at events with energies $\leq$ 9 GeV compared with the usual 35 GeV. Although these parameters are not expected to change significantly they are taken into account in the generator.

5.7.2 Tau Production

The production of the τ lepton is another background that must be taken account of, because of its hadronic decay channels. There are two different channels which cause τ production, specifically:

$$e^+e^- \rightarrow \tau^+\tau^-$$
$$e^+e^- \rightarrow e^+e^-\tau^+\tau^-$$

These are produced in a similar manner to μ production, the cross-section and angular distributions being affected only by the higher mass of the τ, namely 1.784 GeV. The difference is that unlike μ's, which have a relatively long lifetime and rarely decay in the detector, the τ has a much shorter lifetime and sometimes decays into hadrons, faking hadronic photon-photon events. The τ generators are based on similar generators to the $q\bar{q}$ pair generators. In the annihilation channel initial-state radiation is accounted for up to first order, and the τ's are decayed with an isotropic phasespace distribution using the CELLO branching ratios (Fig 5.10). For the photon-photon channel the Daverveldt program with initial-state radiation was used with the same decay method as for the annihilation channel. As is expected the events that pass the final data selection cuts have a low mean multiplicity. This background could be eradicated by increasing the minimum number of charged tracks required from ≥ 4 to 5, but since the background is already very small this was not deemed necessary. It would also have reduced the numbers of hadronic photon-photon data unnecessarily.

5.8 The Detector Simulation

Once the required luminosity of generated 4-vectors has been produced, they are ready to be passed into the full detector simulation programs. These can be split into three specific programs which deal with different aspects of the simulation. A flow diagram showing the stages in the chain is shown in fig 5.11.

Firstly PTRAK tracks the particles through a detailed model of the detector materials and geometry. Each particle is subjected to the effect of the magnetic field present. In each volume of material the program takes into

account the effects of multiple scattering, ionisation, hadronic interaction, bremsstrahlung, absorption, pair production (for photons) and decays of unstable particles into secondary particles with secondary vertices, each with their corresponding probabilities. All secondary particles produced are further tracked through the detector. The electromagnetic and hadronic showers were modelled using the EGS and HETC packages (5.9). All energy deposits, ionisation charges, and where relevant the distance of showers to anodes, cathodes were recorded and passed onto the second step in the Monte-Carlo chain.

CELINT takes this information and uses it to simulate the response of the detector. Distances of ionisation charges from wires are turned into drift times and thence to a TDC reading. Energy deposits are turned into ADC readings. However, in order for this simulation to be a good description of the real detector, a detailed knowledge of the status of each channel is required. This means that the calibration constants, pedestals, efficiencies for wire chambers and calorimeter channels must all be taken into account. The calibration of all the readout electronics must also be taken into account. Because the state of the detector changed during the period of the data taking (six months) these constants are run-dependent (Fig 5.12). To this end all the calibration constants and efficiencies used were divided into 9 separate sets for different run-ranges (the run numbers where these changed were chosen to coincide with major trigger changes, see later). For each range the efficiencies of the chambers were taken into account (these were determined from Bhabha events). For each range the noise characteristics of the electronic channels were written on status files.

The MC events were assigned run numbers distributed suitably over the entire range. The detector response used the above files along with the measured calibration constants for a given run. Background due to synchrotron radiation was also taken into account. Because the treatment of the noise characteristics of the liquid-argon was critical to correctly simulate low energy photon acceptance efficiencies, the noise levels of each channel in the calorimeter for each run range was simulated using the measured noise characteristics of each of the ~10000 channels in the detector in each particular run range.

The digitised output was then formed into standard CELLO output format ready to be passed through the full reconstruction program OFFRAM in exactly the same manner as the data.

Separate from the main detector simulation is the forward lead-glass

shower development simulation program. This program was written at a later date than the full detector simulation. In order to simulate particles which pass through the forward calorimeters the program firstly reads the MC generated 4-vector bank and looks to see if a particle passes near to the forward calorimeters, this region defined by some loose cuts as 38mrad $\leq \theta \leq$ 100 mrad. If an event does contain such a track it is then passed on to undergo a full simulation. The simulation of the shower development in the blocks of lead-glass is undertaken by the GEANT program (5.10). The different showering of photons, leptons and hadrons is taken into account, as is ageing of the lead-glass blocks due to radiation damage (5.11). The simulation is therefore capable of simulating the faking of an electron by high energy photons or a jet of hadrons. These are important in this analysis since they are a background to genuine tags.

5.9 The Charged Trigger Simulation

In this analysis data events were only accepted if they had fired one of the charged triggers (see section 3.8). For untagged events these were triggers 5, 15, 16. For tagged events they were 5, 7, 10, 15, 16. This requirement rejected only 2.5% of untagged events after final data selections (these events triggered on neutral triggers only) and a negligible number of tagged events. This is because events with $\geq$ four charged tracks and a $W_{VIS} > 4$ GeV have a high probability of firing a charged trigger (the triggers were designed to have a high efficiency for detecting events with several charged tracks). In order to quantify the inefficiency it was necessary to simulate the charged triggers on the Monte-Carlo data. This could be done with a high degree of accuracy by using the same logic as was used on the real data. The hits produced on the tracking chamber were compared with exactly the same rz and rφ masks as used on data. For the tagged triggers this was combined with the energies deposited in the lead-glass forward calorimeter blocks or the lead liquid-argon endcaps. Because the charged trigger conditions changed during the run (ie different rz, rφ masks were used), the trigger simulation changed these masks depending on the run-range of each Monte-Carlo.

In order to check the accuracy of the trigger simulation the program was applied to a selection of real data events which had passed final data selection cuts (except for the trigger requirement). For untagged data the charged trigger selection was incorrect for ~1.3% of events and for tagged data the charged trigger selection was incorrect for ~1% of events. Thus it can be seen

that the simulation worked well.

5.10 The Filter Program

Because the data had been passed through the filter program (see section 4.1) it was necessary to check whether this program rejected good Monte-Carlo events. Although it should not in principle remove good physical events from the data sample, the filter program was known to contain errors which might possibly affect its performance. To this end a set of Monte-Carlo events which had passed the full final section requirements were passed through the same filter program as had been used on the data. It was found that the filter program threw away 0.7% of untagged events and an even smaller number of tagged events. These numbers being negligible, the filter program was therefore not run on the Monte-Carlo events.

Process	Cross-Section	No of Events
QPM $u\bar{u}$	0.644 nb • 16/27 = 0.382 nb	68760
$d\bar{d}$	0.644 nb • 1/27 = 0.024 nb	4293
$s\bar{s}$	0.534 nb. • 1/27 = 0.020 nb	3560
$c\bar{c}$	0.148 nb • 16/27 = 0.088 nb	15573
GVDM (untagged, $0 < \theta < 38$ mr)	2.121 nb	381780
(single tag, 38 mr $< \theta < \pi/2$)	0.214 nb	38592
1-$\gamma \rightarrow q\bar{q}$	0.375 nb	67500
1-$\gamma \rightarrow \tau\tau$	0.1 nb	18000
2-$\gamma \rightarrow \tau\tau$	0.113 nb	20376

Table 5.1 shows the cross-sections and corresponding numbers of generated MC events passed through the full detector simulation chain.

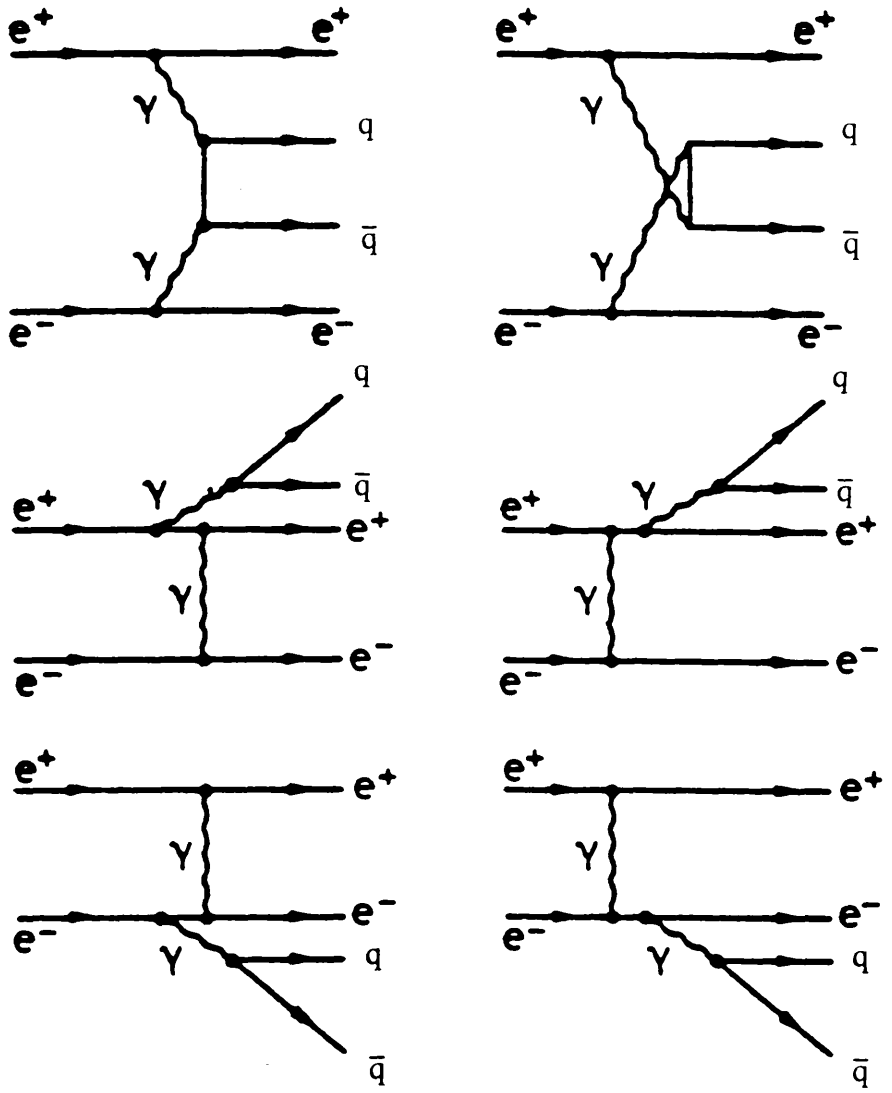

Fig 5.1 The six zeroth order QED diagrams generated by the Daverveldt QPM generator.The first two diagrams only are used in the Vermaseren generator.

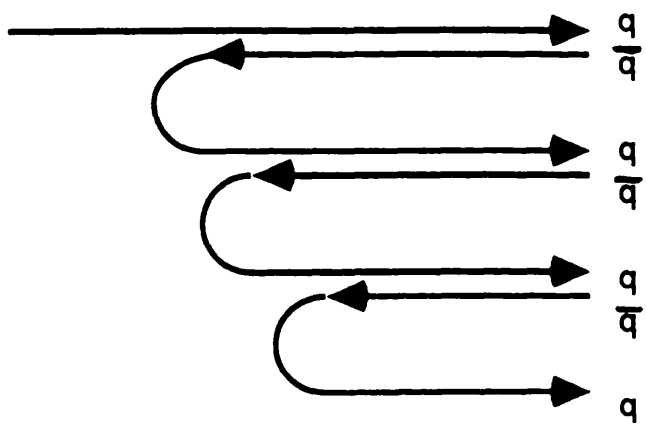

Fig 5.2 The recursive production of quark pairs being pulled from the vacuum demonstrating the Feynman-Field fragmentation model.

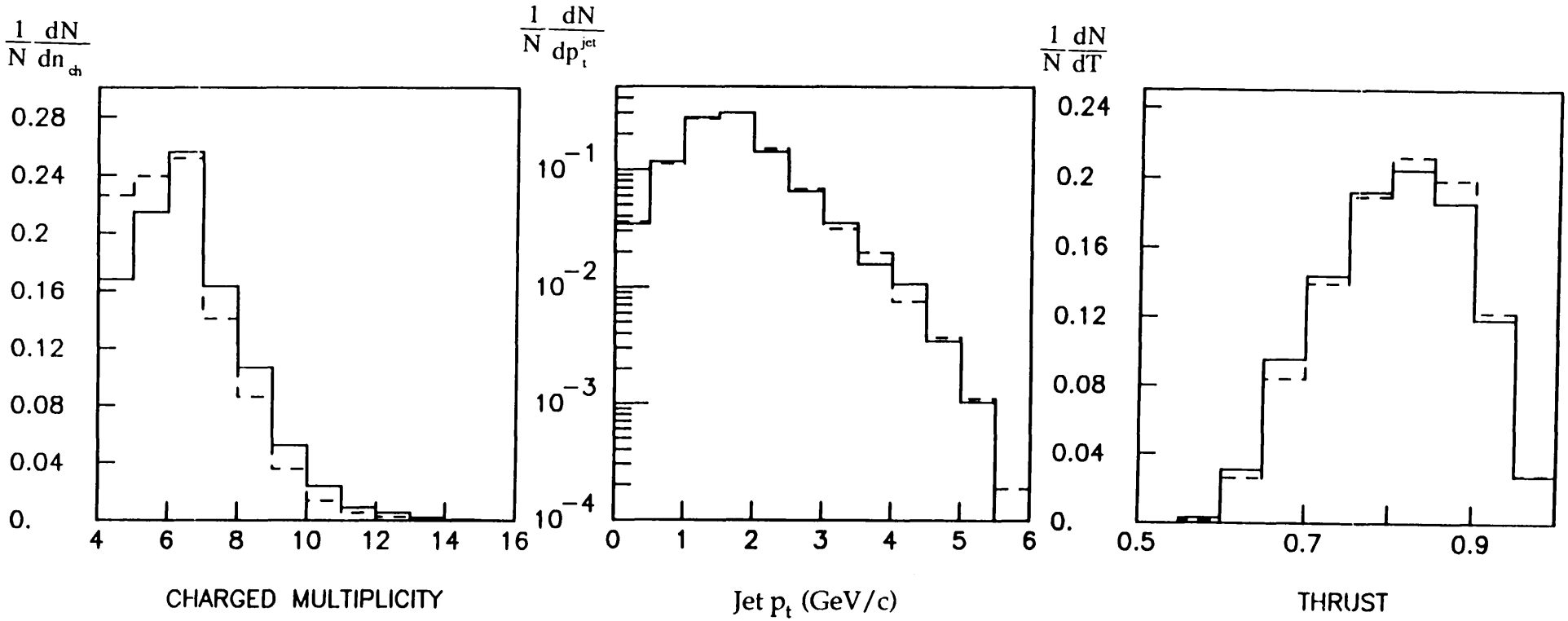

Fig 5.3 Comparison of the QPM generator after final data selection cuts using either the Feynman-Field fragmentation scheme (solid) or LUND (dashed).

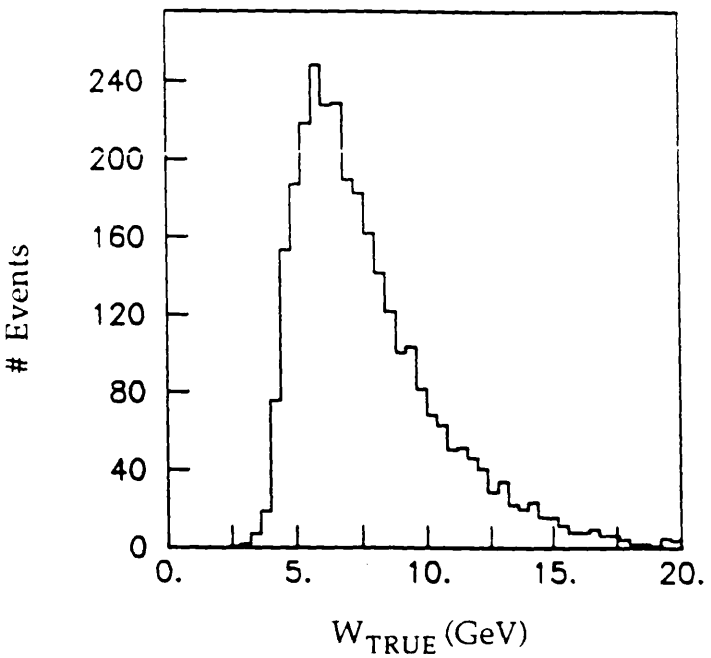

Fig 5.4 The generated hadronic mass W for the antitagged QPM model after final selection cuts.

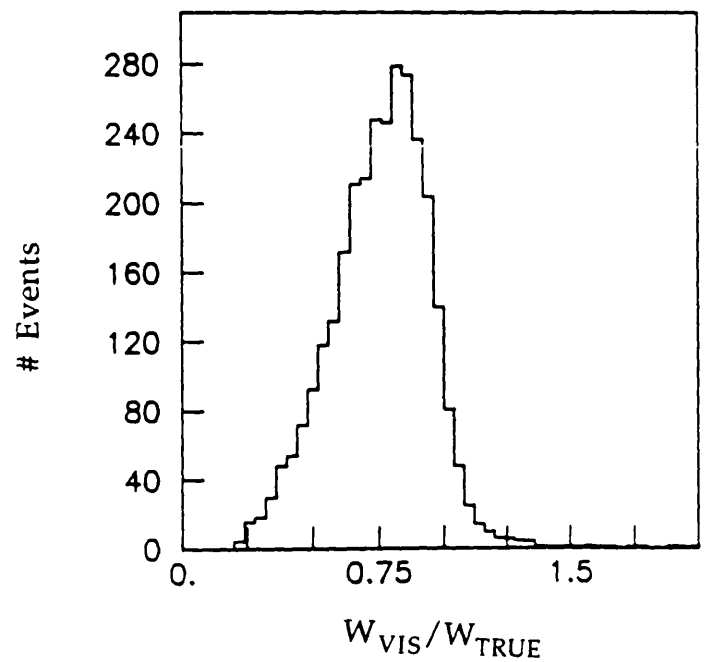

Fig 5.5 The fraction of the true hadronic mass W reconstructed after the detector simulation and final selection cuts for the antitagged QPM model.

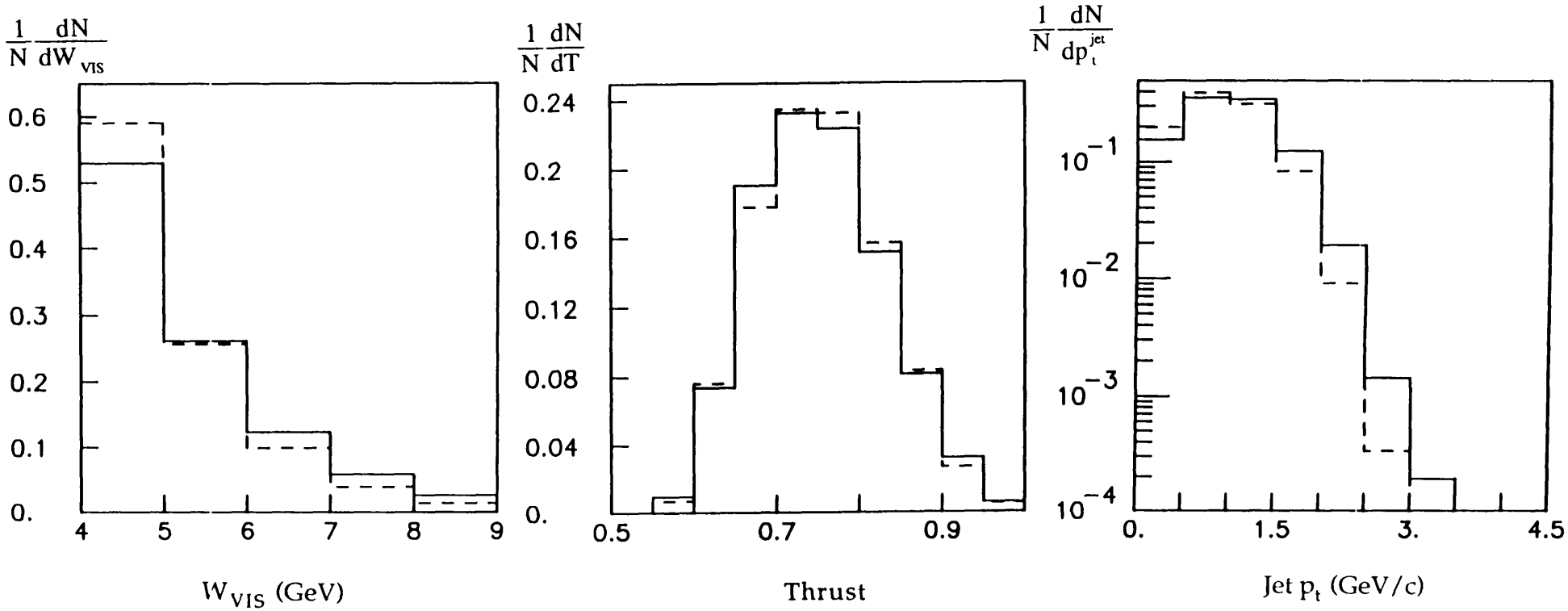

Fig 5.6 Comparison of the VDM generator after final data selection cuts using either the tuned Feynman-Field fragmentation scheme (solid) or standard LUND (dashed).

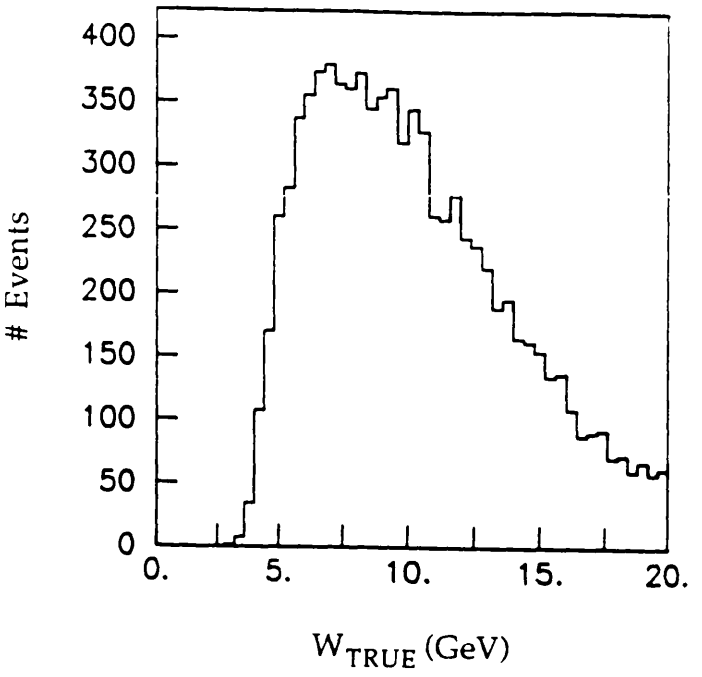

Fig 5.7 The generated hadronic mass W for the antitagged VDM model after final selection cuts.

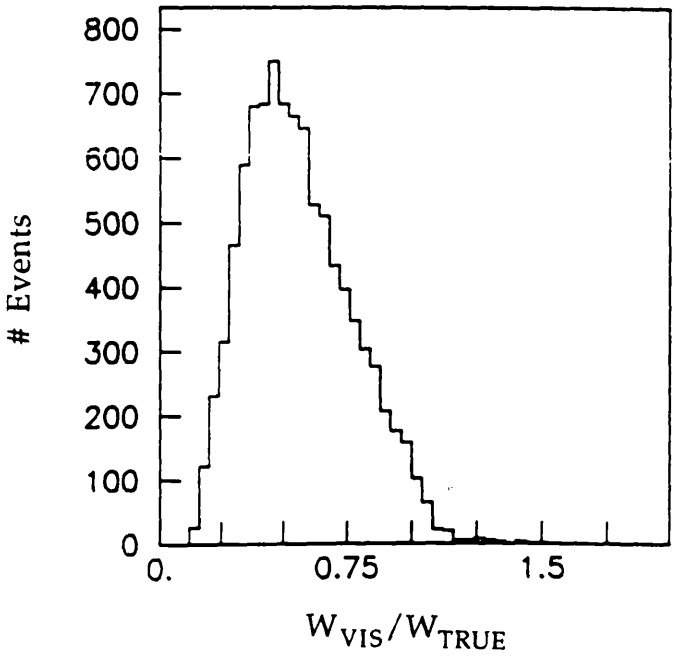

Fig 5.8 The fraction of the true hadronic mass W reconstructed after the detector simulation and final selection cuts for the antitagged VDM model.

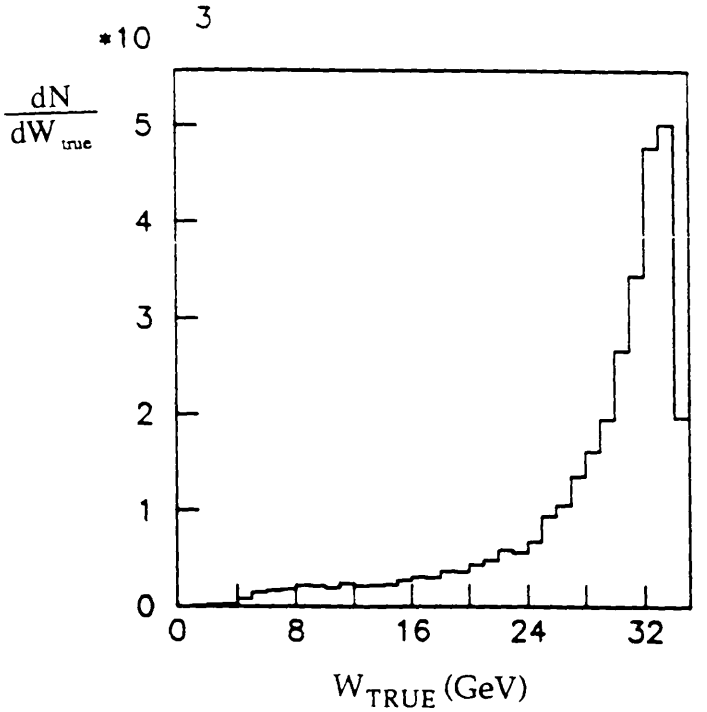

Fig 5.9 The generated hadronic mass W for the multihadronic annihilation model.

The Tau Decay Branching Ratios	
Decay Modes	Branching Ratios %
$\tau^- \rightarrow e^- \upsilon_e \upsilon_\tau$	17.9%
$\tau^- \rightarrow \mu^- \upsilon_\mu \upsilon_\tau$	17.9%
$\tau^- \rightarrow \pi^- \upsilon_\tau$	10.9%
$\tau^- \rightarrow K^- \upsilon_\tau$	0.7%
$\tau^- \rightarrow \rho^- \upsilon_\tau$	22%
$\tau^- \rightarrow K^{*-} \upsilon_\tau$	1.4%
$\tau^- \rightarrow a_1 \upsilon_\tau$	15.6%
$\tau^- \rightarrow 4\pi \upsilon_\tau$	9%

Fig 5.10 The CELLO branching ratios used for tau fragmentation.

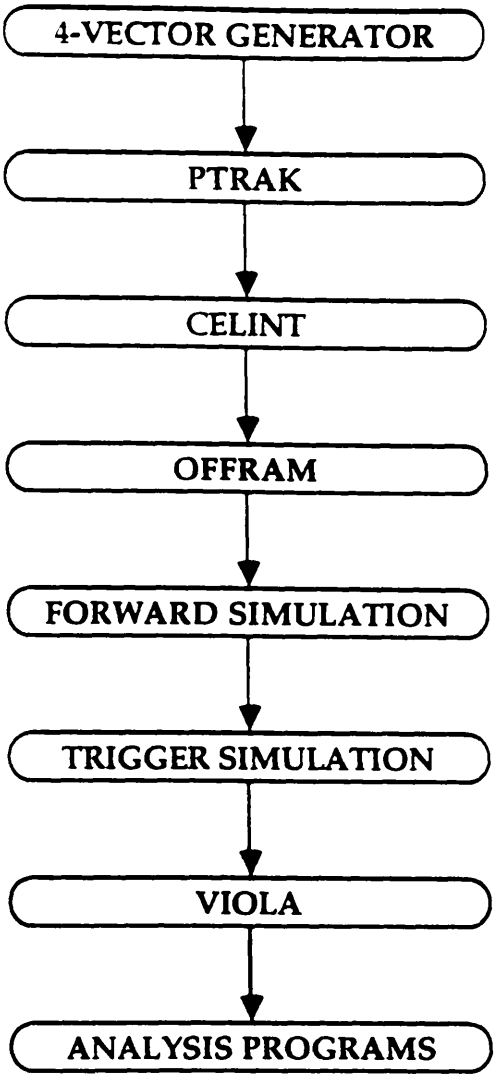

Fig 5.11 A flow diagram showing the various stages in the Monte-Carlo chain.

Run-Interval	Chosen Run	Luminosity %
9690-9788	9730	1.85
9789-10005	10000	5.28
10006-10148	10050	2.89
10149-10327	10200	5.28
10328-10479	10400	4.18
10480-11073	11000	18.89
11074-11274	11100	6.32
11275-11869	11500	19.73
11870-13004	12000	35.58

Fig 5.12 The run ranges and their equivalent luminosities used for the MC and trigger simulation.

Chapter 6

Calibrations and Backgrounds.

6.1 Introduction

This chapter comprises two sections. The first section describes the calibration of the forward lead-glass calorimeters and endcap lead liquid-argon calorimeters, using tagged lepton pairs. The second section concerns backgrounds to the hadronic photon-photon data.

6.2 The Calibration of the Forward and Endcap Taggers.

It is important for the medium Q^2 hadronic photon-photon data that the tags detected in the forward and endcap calorimeters are well understood. As well as providing the Q^2 for the event, the tag information is used in cuts to suppress background processes. 'Fake' tags usually originate from initial state radiated photons, high momentum hadrons or whole jets of hadrons causing large shower deposits in the tagging calorimeters. A useful way to reduce this background is to apply a minimum energy cut to the tag. Furthermore background and badly measured events can be reduced by applying a maximum cut on the summed transverse momentum (Σp_t) of the event (including the tag). This can be useful in removing poorly measured 1-γ multihadronic and τ events where a large fraction of the event escaped detection due to the detector acceptance or due to neutrino decays. Another useful cut to remove background from the hadronic photon-photon data is a cut on the reconstructed p_z of the undetected lepton which remains in the beam-pipe. For photon-photon events this quantity should be large, in contrast to 1-γ background where it should be peaked at lower values. It can therefore be seen that the reconstructed energy of the detected tags requires to be well understood.

To this end it was decided to analyse the forward and endcap tags using tagged lepton pairs with the tag detected in the forward or endcap tagger. In this case lepton refers to either electrons or muons. The τ can be ignored since its mass causes the cross-section to be small. A typical tagged electron pair is shown in fig 6.1. This provides a good method to compare the absolute Monte-Carlo prediction with the data, in order to study the

acceptance, energy and angular distributions of detected tags. The cross-section of the process is also large enough to provide useful statistics. The events were generated with the Daverveldt generator which generated all the diagrams for

$$e^+e^- \rightarrow e^+e^-e^+e^-$$
$$e^+e^- \rightarrow e^+e^-\mu^+\mu^-$$

along with all diagrams for the first order QED corrections. At least one of the scattered beam leptons was required to be scattered with an angle $\theta > 30$ mrads, in order to provide a tag. The numbers of events generated are given in the following table:

Number of generated events, $W_{GEN} \geq 1$ GeV

	σ(nb)	N	L(pb^{-1})
ee→eeee	0.174	31320	180
ee→ee$\mu\mu$	0.168	30240	180

The data selection started from a sample which contained two oppositely charged tracks and an energy deposit in the forward or endcap taggers of ≥ 5 GeV. There are two important backgrounds which must be taken into account.

The first is the resonance production of the f_2 (1270) resonance.

$$\gamma\gamma \rightarrow f_2 \rightarrow \pi^+\pi^-$$

One possible way to remove these events would have been to identify the charged hadrons by examining their shower topologies in the lead liquid-argon. However it was decided to apply a minimum W_{VIS} cut to the data, since the cross-section for $\pi^+\pi^-$ production with $W \geq 1.5$ GeV is negligible (6.1). The second relevant background is due to the presence of radiative Bhabhas in the data sample. These occur when a Bhabha is created with a radiated photon which has a large enough energy to fake a tag in one of the taggers. The radiated photon kicks the electron, positron so they are no

longer back to back. They can be removed by requiring the two charged tracks to have a total energy ≤ 10 GeV.

The final selection requirements for the tagged lepton pairs were:-

1) One positive track and one negative track both accepted by VIOLA. No identified photons in the barrel or endcap, calorimeters. No holetagger energy and no energy in the taggers except for the tag.

2) $|\cos\theta|_{TRK} \leq 0.85$ This constrains the tracks to the region of the detector where they pass through at least 7 chambers and are consequently well measured.

3) $W_{VIS} \geq 1.5$ GeV, to remove $\pi^+\pi^-$ events.

4) $E_{VIS} \leq 10$ GeV, to remove radiative Bhabhas.

5) $|Z_{EVT}| \leq 2$ cms, to remove badly measured events.

6) At least one charged trigger was also required to be fired.

This selection produced a clean data sample which could be compared with the generated Monte-Carlo events to provide information on the cuts to use for the tags. The Monte-Carlo data was treated in exactly the same manner as the data. It was passed through the filter (which removed 1% of the events) and the charged triggers were simulated in exactly the same manner as in the data.

Cuts were applied to the measured θ range of the tags to remove badly measured tags where the shower had been produced near the edge of the calorimeters, where they were not fully contained and the Monte-Carlo did not describe the acceptance adequately. This was especially important for the forward tags. Below θ angles of 55 and above 80 mrad the Monte-Carlo described the data less accurately. This was probably due to the precise amount of material beneath and in front of the detector being unknown. It was decided that to try and correct the θ dependence of the acceptance would be problematic, because the systematic errors would be large. Consequently all forward tags were restricted to measured θ angles of $55 \leq \theta \leq 80$ mrad in this analysis. Some forward tags could be linked to showers formed in the

lower edge of the endcap, and these were also rejected as badly measured.

Endcap tags were accepted in the region $150 \leq \theta \leq 360$ mrad, which is away from the edges of the acceptance. The endcaps were known to be poorly calibrated and thus some work had been done on their calibration using Bhabhas (6.2). The reconstructed energies of Bhabha showers was seen to depend on run-range and position in the module. This was due to faulty layers, and voltage changes during the runs which had not been correctly incorporated into the Monte-Carlo. The comparison of Data and Monte-Carlo was done after these calibrations were made. Fig 6.2 shows the E, Q^2 distributions for the data with the absolute Monte-Carlo predictions. Fig 6.3 shows the E, Q^2 resolutions for tags with $E \geq 10$ GeV (the cut at 10 GeV is made because this cut was used for the hadronic data). Also shown (Fig 6.4) are W_{VIS}, p_t, $|p|$, $\cos\theta_{TRKS}$ which all show good agreement between data and Monte-Carlo.

Event statistics for tagged lepton pairs

	Forward Tags	Endcap tags
Data	1877±43	996±32
M.C.	1926±31	1065±23

The above table shows that good agreement is found between the data and the numbers of events predicted by the Monte-Carlo. There are discrepancies, however, in the values of the endcap tag energies. This quantity should therefore be used with caution.

6.3 Barrel Tags

Barrel tags are those where an identified charged track is linked to a shower in the barrel lead liquid-argon calorimeter. If the energy deposited in the calorimeter agrees with the momentum of the track measured (from its curvature) and has ≥ 5 GeV then it is assigned to be a tag (and also an electron/positron depending on its charge). One advantage the barrel tags have is that their charge is known, and this can be used to distinguish background. The number of real barrel tagged photon-photon events with

the tag scattered with $\theta_{TAG} \geq \pi/2$ is negligible because this corresponds to a very high Q^2. However the distribution of fake tags from the 1-γ multihadronic background should have the tags distributed symmetrically. Unfortunately the number of detected barrel tagged events was too small to be statistically useful.

6.4 Backgrounds

The second part of this chapter concerns the background processes which occur in the final hadronic photon-photon data sample. The largest backgrounds present are those produced through the annihilation channels. These are

$$e^+e^- \rightarrow q\bar{q}$$
$$e^+e^- \rightarrow \tau^+\tau^-$$

Unfortunately these cannot be totally excluded from the final data sample by the use of kinematical cuts. Therefore they must be simulated and subtracted statistically. It is impossible to check if the simulation used is correct in the low W region (4 GeV $\leq W_{VIS} \leq$ 9 GeV) chosen for the final data sample simply because of the photon-photon data present. Because of the need to check that the cross-sections being used do agree with the data, it is necessary to compare the numbers of events predicted with the data in the high W region, where these backgrounds dominate. Here, the photon-photon processes have become small because of their $\sim 1/W^2$ dependence. The absolute Monte-Carlo prediction for the processes

$$e^+e^- \rightarrow q\bar{q}$$
$$e^+e^- \rightarrow \tau^+\tau^-$$

was firstly compared with the data for the whole W_{VIS} region. Certain requirements were made on the charged and neutral particles for them to be accepted, and requirements were also made on the final event. These were:

For charged tracks.

1) $|\cos \theta_{TRK}| \leq 0.95$, to remove tracks with large measurement errors on the edge of the acceptance.

2) closest approach to interaction point of track in rø ≤ 10 mm to remove badly measured tracks or tracks scattered by the beam pipe.

3) $|p| \geq 5$ GeV/c reset to 5 GeV/c to remove problem of straight tracks having very high momenta due to measurement errors.

Requirements for neutrals

1) $|\cos \theta_{NEU}| \leq 0.85$, only barrel photons accepted.

2) All neutrals ≤ 4 milliradians from edge of a module rejected, to remove badly measured showers.

3) $E_\gamma \geq 200$ MeV, to remove low energy noise photons from data.

Event requirements for entire W region.

1) $4 \text{ GeV} \leq W_{VIS} \leq 35 \text{ GeV}$

2) $|z_{EVT} - z_{BEAM}| \leq 4$ cms To remove beam gas/pipe events.

3) At least one charged trigger to be fired.

4) The summed transverse momentum imbalance of the events to be ≤ 3 GeV/c to remove badly measured events.

5) The charged multiplicity to be ≥ 4 and the summed charge imbalance to be ≤ 2

Fig 6.5 shows the W_{VIS} distribution of events over the whole W_{VIS} range

after these cuts. As can be clearly seen, the annihilation MC's describe the data well at high W, whereas the excess due to hadronic photon-photon production is evident at lower W_{VIS} values. This gives a good indication as to where the upper W_{VIS} cut should be made for the hadronic photon-photon data sample. The final W_{MAX} cut was made at 9 GeV and fig 6.5 shows the background contributes to approximately half the data at this W_{VIS}. Fig 6.6 shows the summed transverse momentum imbalance for data with $4 \leq W_{VIS} \leq 9$ GeV and it is clearly seen that above ~ 3 GeV/c the data is clearly dominated by the annihilation channels. This cut was used in the final data samples.

6.5 Beam Gas/Pipe Background

Background occurs when the beam leptons collide with gas molecules present in the beam pipe (the vacuum in the beam-pipe is never perfect) and when off-momentum beam-leptons collide with the beam-pipe wall. The majority of events which cause the detector to trigger and record an event are due to these reactions. In principle the FILTER program should effectively remove these events from the data sample. However, in practice many of these events look sufficiently like good physics to pass onto the final data selection tapes. A beam gas/pipe event can usually be characterised by certain features. These are:

1) an excess of positive charge in the detected final state, due to the fragmentation of a positively charged nucleus by the beam-lepton.

2) usually many poorly reconstructed tracks and unlinked hits in the tracking chambers, caused by low momentum particles spiralling round. There is also usually less neutral energy present in the event as well as large imbalances in the transverse momentum.

A typical beam-gas/pipe event is shown in fig 6.7. These events can be suppressed in the data sample by a number of methods, such as p_t imbalance cuts, cuts on events with excess positive charge and cuts on events with noisy beam pipe wire chambers etc. However, these cuts will never remove all the beam gas/pipe events. Unfortunately no simulation of this type of event was existing to give an estimation on the amount and characteristics of this background. Fortunately, beam gas/pipe events have one feature uncommon to real events, which is that they should be distributed uniformly along the z axis, unlike real events which should be gaussianly distributed around z = 0. Fig 6.8 shows a plot of the $|z_{EVT} - z_{BEAM}|$ for the

untagged data and MC before any $|z_{EVT} - z_{BEAM}|$ cuts have been applied. A gaussian fit was made to this distribution, and it clearly disagrees with the data in the high z regions. The excess observed in the data at high z values is assumed to originate from beam-gas events. MC studies also showed that these tails were not expected to be produced from the data. It is therefore asssumed that these tails at high $|z_{EVT} - z_{BEAM}|$ are beam gas/pipe events.

An estimation of the beam gas/pipe background can therefore be made from the data collected in the $|z_{EVT} - z_{BEAM}|$ sidebands, where all the events are assumed to be solely due to beam gas/pipe collisions. The data in these sidebands (4 cms $\leq |z_{EVT} - z_{BEAM}| \leq$ 8 cms) can then be subtracted statistically from the data. Previous analyses (6.3) have assumed that this background is distributed uniformly in z. However, it has been suggested (6.4) that constraints in the reconstruction chain might bias the acceptance of events in favour of those with a lower $|z_{EVT} - z_{BEAM}|$. This was checked by analysing the data taken in EXP 46. This run differed from EXP 44 in that the beams were separated from each other at the crossing point by a few millimetres in order that only beam gas/pipe interactions were able to occur. Although the statistics were limited (EXP 46 ran for only one week compared to six months for EXP 44), the data provided a $|z_{EVT} - z_{BEAM}|$ distribution for beam gas/pipe events. The recorded events were processed in exactly the same manner as the data from EXP 44. The $|z_{EVT} - z_{BEAM}|$ distribution for all the events after final selection cuts is shown in fig 6.9. Although studies indicated a flat background before the cuts, a $|z_{EVT} - z_{BEAM}|$ dependence for the beam gas/pipe events is now clearly evident. Consequently for the final data sample the following strategy was adopted. A $|z_{EVT} - z_{BEAM}|$ cut of $\leq$ 4 cms was required to define the intersection region. Sidebands were chosen between 4 cms $\leq |z_{EVT} - z_{BEAM}| \leq$ 8 cms and these events were subtracted statistically from the data with a weight of 2.0. This weight was obtained by comparing the numbers of events from EXP 46 in the sidebands, 4 cms $\leq |z_{EVT} - z_{BEAM}| \leq$ 8 cms and in the centre region, $|z_{EVT} - z_{BEAM}| \leq$ 4 cms, as illustrated in fig 6.9. This method introduces a systematic error due to the uncertainty in the weighting of the sideband events; additionally a small fraction of the events in the sidebands will not be beam gas/pipe events but real data with very badly measured tracks distorting the measured $|z_{EVT} - z_{BEAM}|$.

The tagged data sample had a greatly reduced fraction of beam gas/pipe events present, largely due to the requirement of a 'good tag'. Here it has

been suggested that some form of photoproduction is occurring where a beam-lepton radiates a photon which interacts with the nuclei of a gas molecule or the beam wall. The events recorded in the sidebands were again subtracted statistically with a weight of 2.0 applied. Although this value obviously has a large statistical and systematic error it was decided that this was a better method of determining the beam-gas/pipe contribution than the other possible method of fitting to the charge imbalance distribution. This was because of possible systematic errors involving the identified charge of a track. It was known from Bhabha studies that CELPAT was slightly biased towards reconstructing positively charged tracks because it searched for these first. Any small discrepancy between data and MC would strongly affect any fitting of a beam gas/pipe component to the charge imbalance distribution.

6.6 $e^+e^- \rightarrow e^+e^-\tau^+\tau^-$

This background produces low multiplicity hadronic decays with a $\sim 1/W^2$ distribution, the final measured W_{VIS} being further reduced due to the τ decaying via an escaping neutrino. The final W_{VIS} before cuts is shown in fig 6.10. After a $W_{VIS} \leq 4$ GeV cut, a charged track ≥ 4 cut and a p_t imbalance cut, the number of events which entered into the final event samples were negligible.

6.7 The Inelastic Compton Effect and C= –1 Final States

These are events where a 1st order radiated photon produces a quark-antiquark pair in the reaction (Fig 6.11).

$$e^+e^- \rightarrow e^+e^-q\bar{q}$$

The final quark-antiquark pair is created from only one photon producing a C= –1 state, unlike genuine photon-photon events which have a C= +1 final state. These events are only a small fraction ($\leq 1\%$) of the final data sample (at high W, Q^2) and are simulated as 1st order corrections in the Daverveldt generator used for the QPM events.

6.8 The Background and Final Event Samples

The final selections made to the data were designed to reduce the backgrounds to a minimum whilst retaining the hadronic photon-photon events. The charged and neutral track requirements used were the same as for the entire W_{VIS} region as described above. Further requirements were made to remove resonance production (a W_{MIN} cut) and to remove the 1-γ backgrounds (a W_{MAX} cut and a p_t imbalance cut). A cut on the missing p_z of the untagged lepton was also made for the single tagged events. The final event requirements for the hadronic photon-photon data sample were;

1) $4 \leq W_{VIS} \leq 9$ GeV. To reduce background from the resonance and 1-γ channels

2) The total charged multiplicity ≥ 4 and the absolute charge ≤ 2 to reduce backgrounds.

3) The summed transverse momentum imbalance Σp_t of the events to be ≤ 3 GeV/c (including any detected tags) to reduce the background from the 1-γ channels. Fig 6.6 shows the transverse momentum imbalance for the untagged data sample compared with the sum of the backgrounds before this cut was applied. As can be seen, above 3 GeV/c the data is dominated by the backgrounds.

4) The reconstructed missing momentum along the beam axis of the untagged lepton (in single tagged events) to be ≥ 8 GeV/c for the forward, endcap and barrel tagged events. No p_z cuts were made on the untagged data since the distribution was peaked at zero for both the data and the background.

5) Untagged events were required to have no possible tag candidates with ≥ 5 GeV. No angular requirements were made for these tag candidates. Forward and endcap tagged events were required to have a tag in the good tagging regions ($55 \leq \theta \leq 80$ mrad for forward tagged and $150 \leq \theta \leq 360$ mrad for endcap tagged events) with $E \geq 10$ GeV, and no other tag candidates with ≥ 5 GeV (no angular requirements being required). Barrel tagged events were required to have an identified electron/positron in the barrel with $E \geq 5$ GeV and no other tag candidate with ≥ 5 GeV.

6) It was found that the MC did not simulate the firing of the beam pipe chambers effectively, the data events having more hits on average in these chambers due to noise. Although this is not a problem at higher W_{VIS} values, where the multiplicity (and therefore the number of hits expected) is high, at low W_{VIS} (≤ 9 GeV) the number of hits in these chambers should not be large, ie < 50. Studies of this problem showed that the number of hits observed in the beam pipe chambers increased with the charged multiplicity of the event. Therefore a parameterised cut depending on the charged multiplicity of an event was implemented on the data.

After these cuts the numbers of events for the final data sample and the simulated backgrounds are given in the following table:

Channel	Untagged	Forward-tag	Endcap-tag	Barrel-tag
Data	15610±125	371±19	302±17	7±3
1-$\gamma\rightarrow$qq	1354±26	20±3	36±4	0
1-$\gamma\rightarrow\tau\tau$	56±5	0	0	0
$\gamma\gamma\rightarrow\tau\tau$	7±2	0	2±1	0
Beam-gas	442±30	10±4	16±6	0

The backgrounds are a significant fraction of the data. Fig 6.12 shows the W_{VIS} distribution for the final untagged data sample compared with the sum of the backgrounds. It can be seen that the backgrounds are largest at high W_{VIS} values, as would be expected since the main backgrounds are the 1-γ channels. Because the main background channel, 1-$\gamma \rightarrow q\bar{q}$ should be characterised by two jet like events it is interesting to compare the thrust and jet p_t characteristics of the data with the sum of the backgrounds. Not surprisingly the background becomes dominant at high jet p_t and high thrust values.

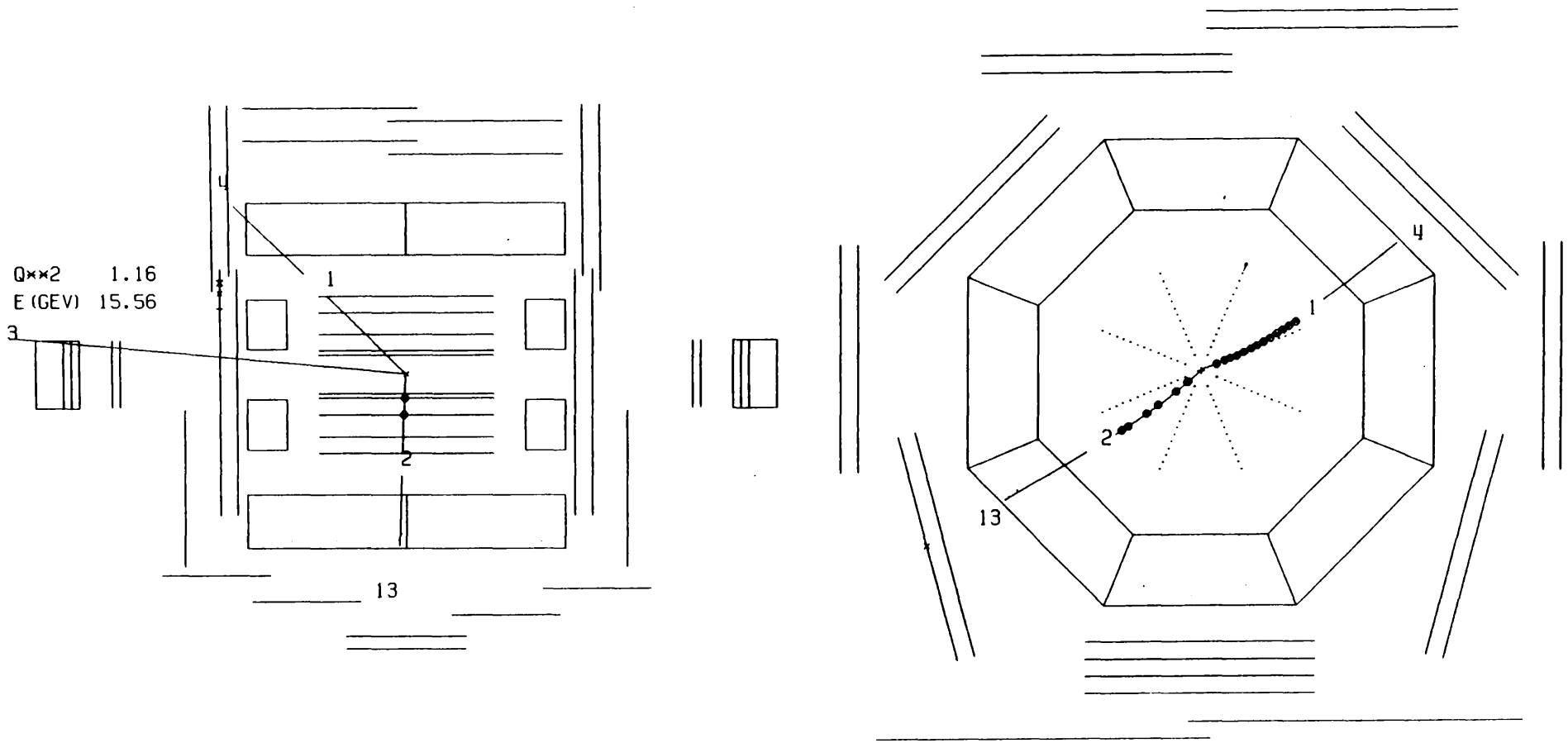

Fig 6.1 The CELLO display showing a Forward tagged lepton pair.

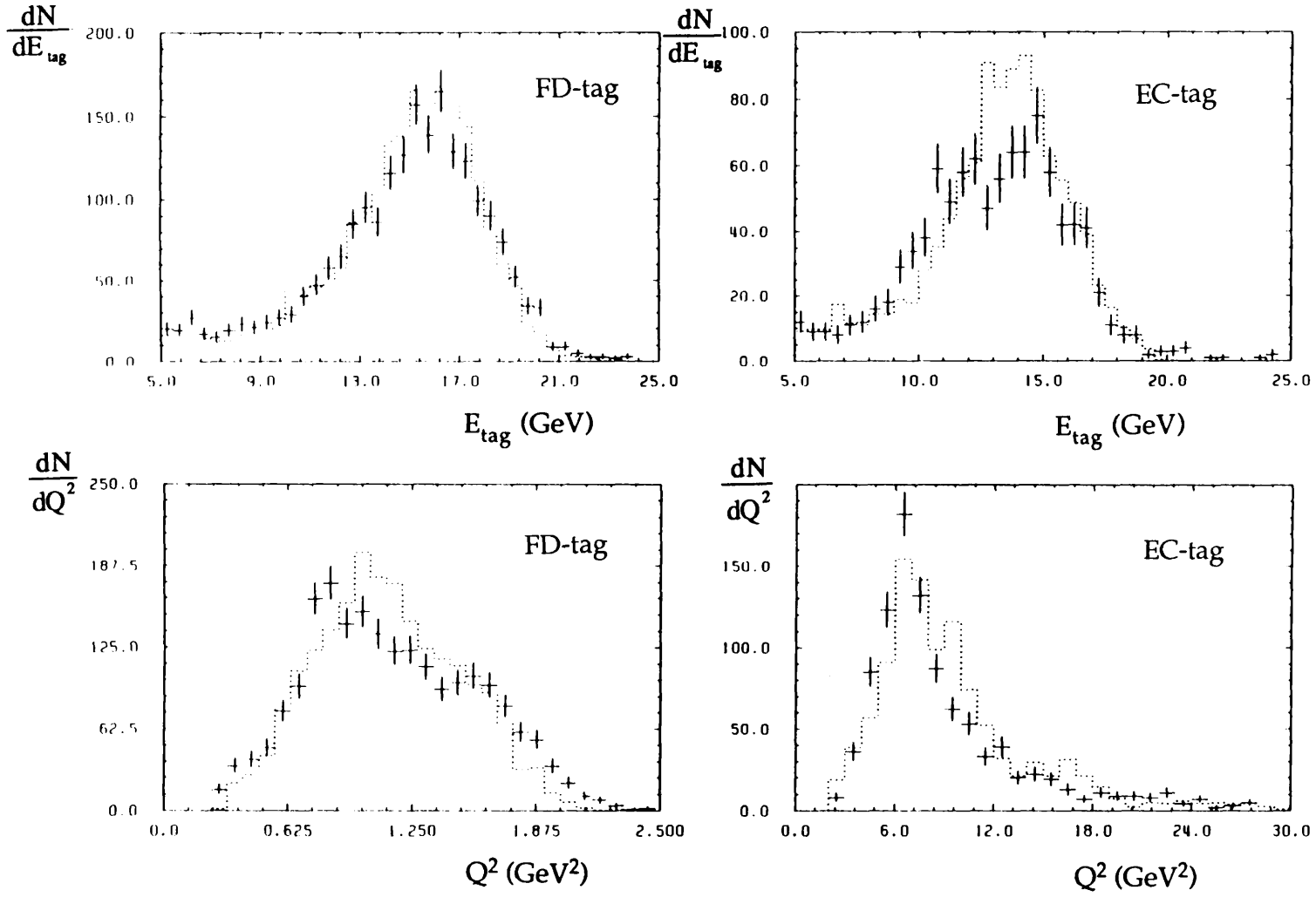

Fig 6.2 The measured Tag Energy and Q^2 for the forward and endcap tagged lepton pairs. The crosses represent data with associated statistical errors and the dotted line represents the absolute MC prediction.

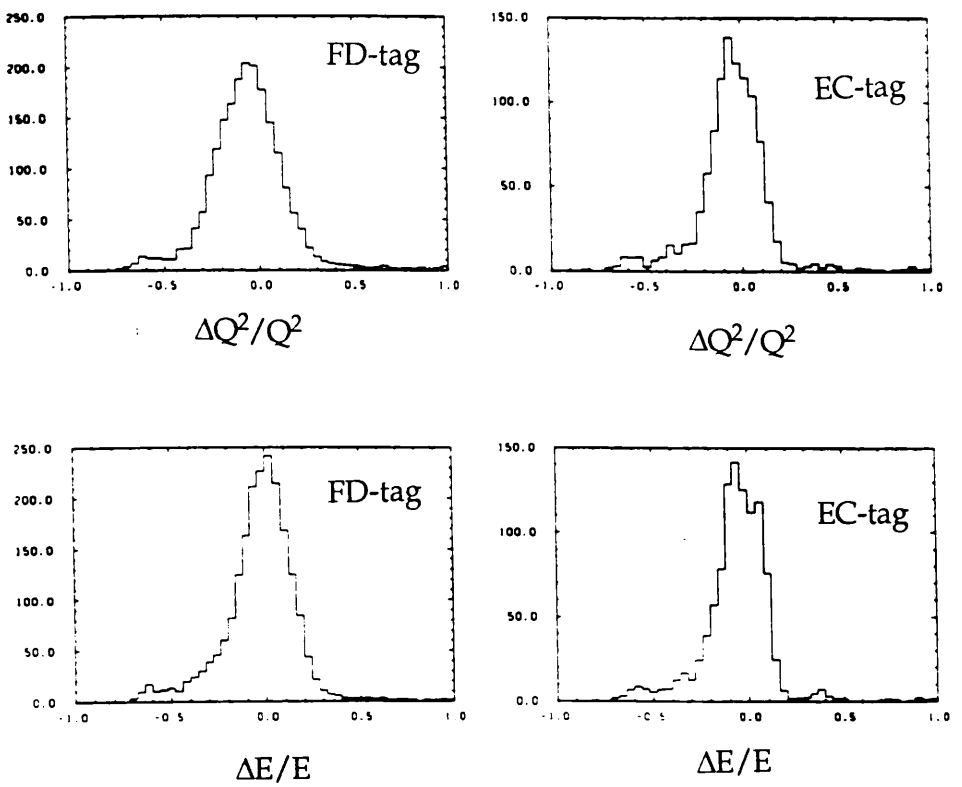

Fig 6.3 The resolutions of measured Tag Energy and Q^2 are plotted for forward and endcap tags

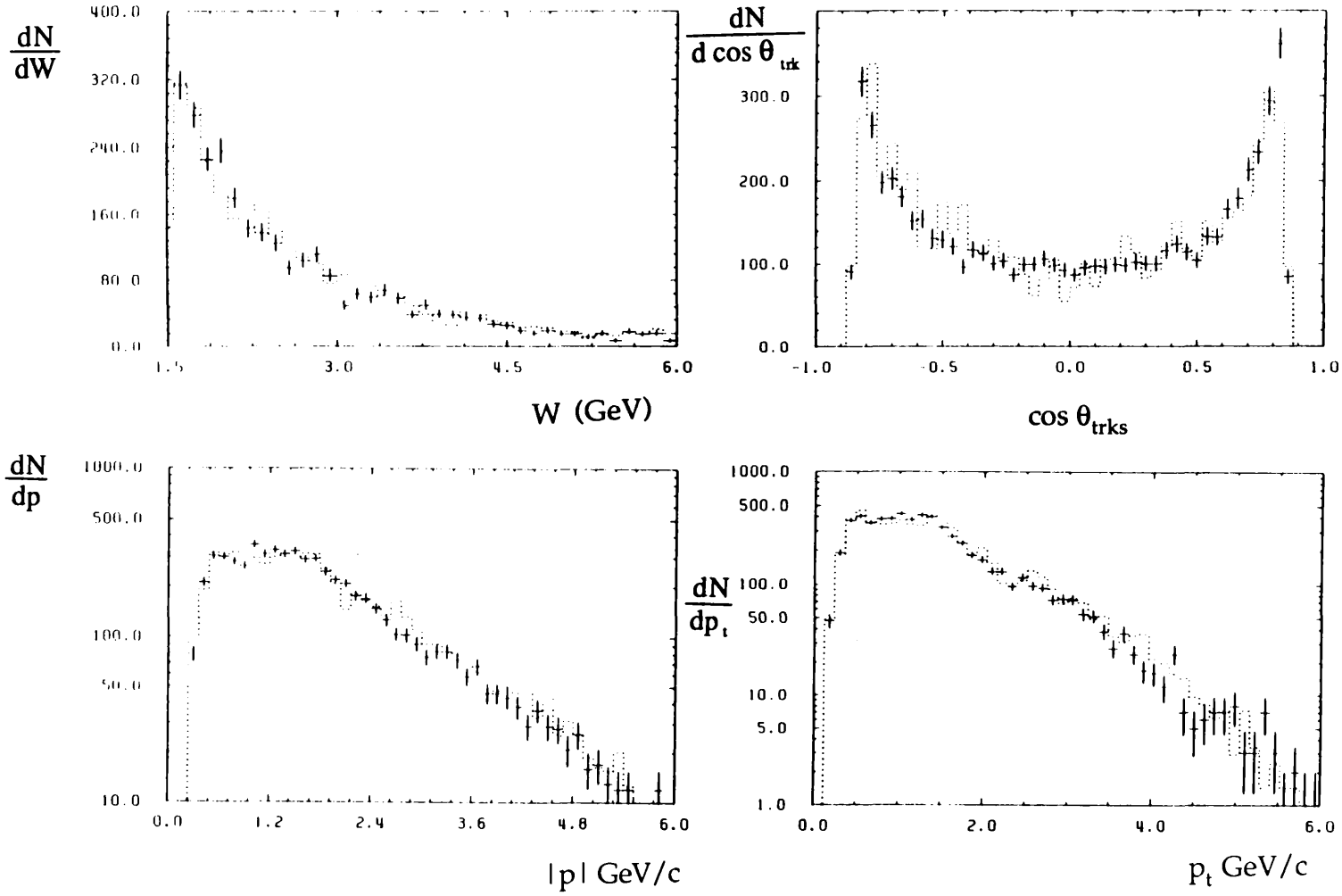

Fig 6.4 Some general event properties of the tagged lepton pairs are plotted. The data is represented with statistical errors by the crosses and the absolute MC prediction is represented by the dashed line.

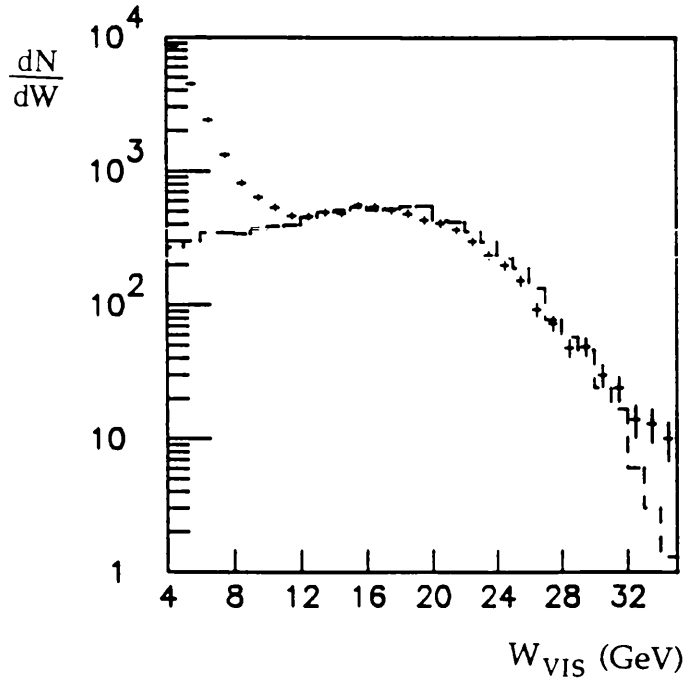

Fig 6.5 The measured W_{VIS} for all the hadronic data above 4 GeV is compared with the absolute prediction of the 1-γ MC's represented by the dashed line.

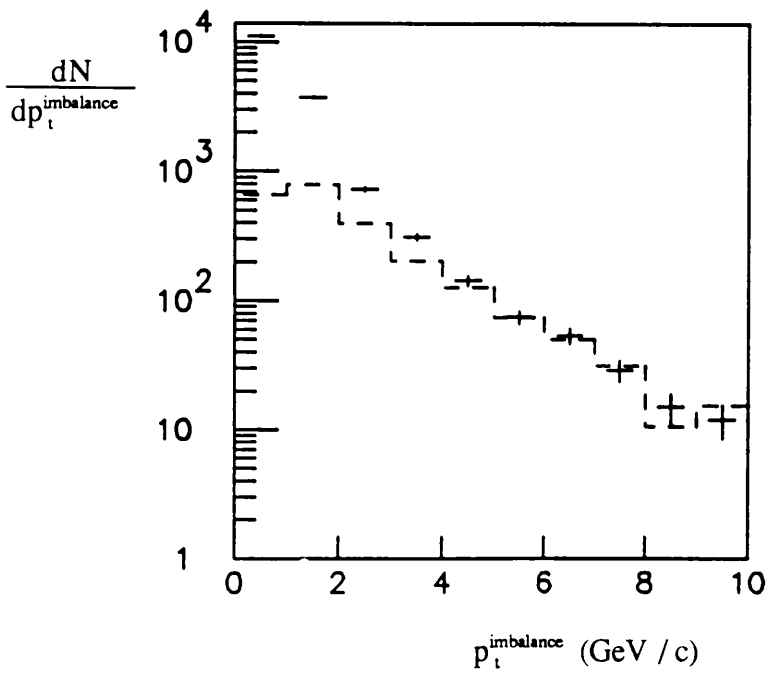

Fig 6.6 The measured p_t imbalance of the untagged data sample ($4 \leq W_{VIS} \leq 9$ GeV) is compared with the background simulation represented by the dashed line.

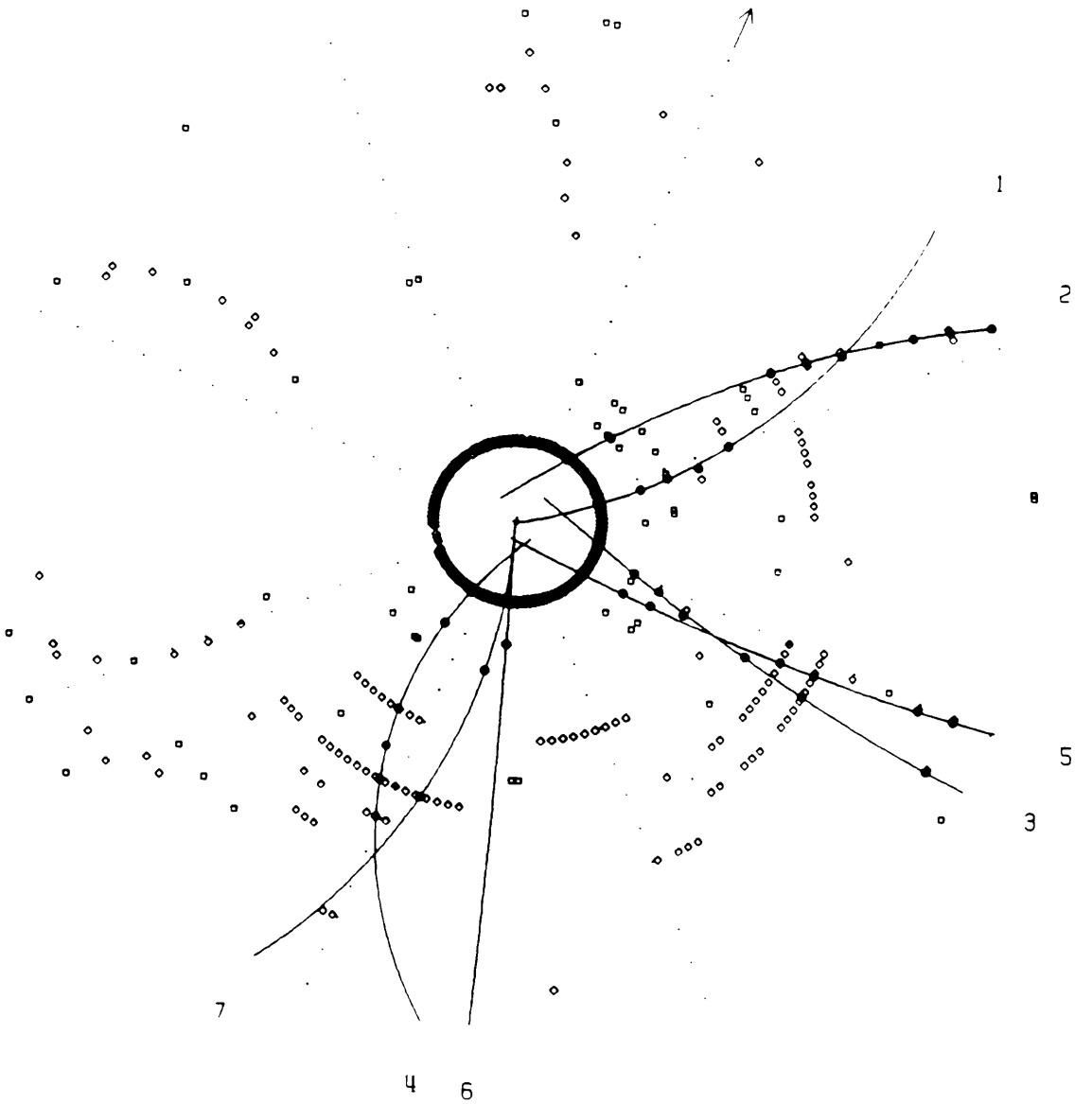

Fig 6.7 The CELLO display showing a typical beam gas/pipe event. As can be seen it is characterised by having noisy beam-pipe chambers, many unreconstructed hits, and poorly or wrongly reconstructed tracks which do not point directly back to the interaction point.

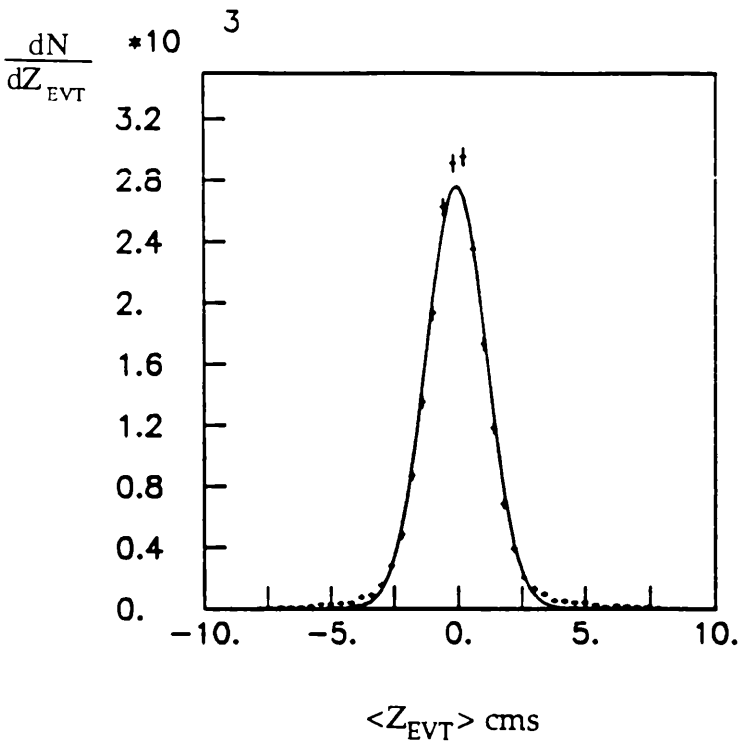

Fig 6.8 The average z position of the reconstructed charged tracks in the untagged data sample before cuts. The dashed line has been fitted to a gaussian with σ = 1.2 cms This agrees well with the known beam lengths of σ = 1.0 cms.

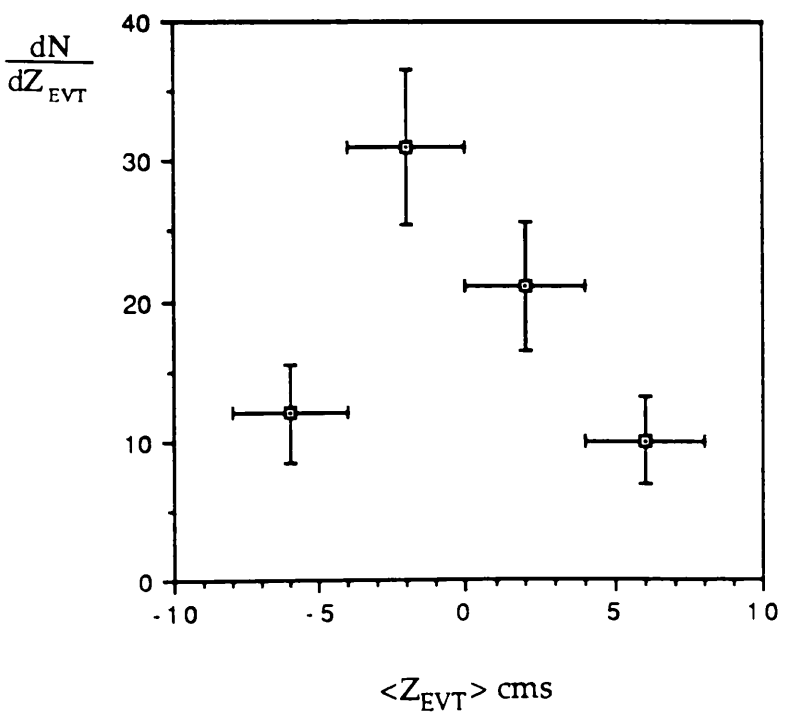

Fig 6.9 The average z distribution of the reconstructed charged tracks in the data collected from EXP 46 after final selection cuts.

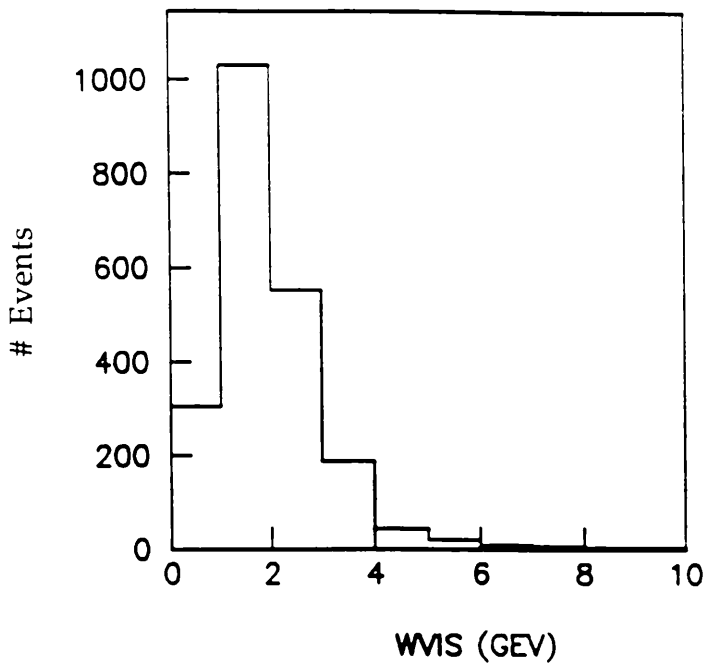

Fig 6.10 The W_{VIS} distribution of $\gamma\gamma \rightarrow \tau\tau$ events before a final $W_{VIS} \geq 4$ GeV is made.

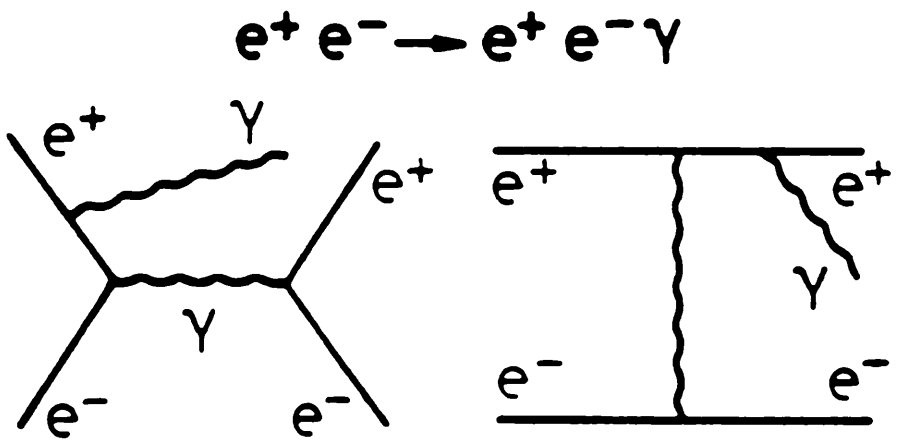

Fig 6.11 Two of the Feynman diagrams for the C = −1 channels where ee→eeγ and the γ forms a quark-antiquark pair.

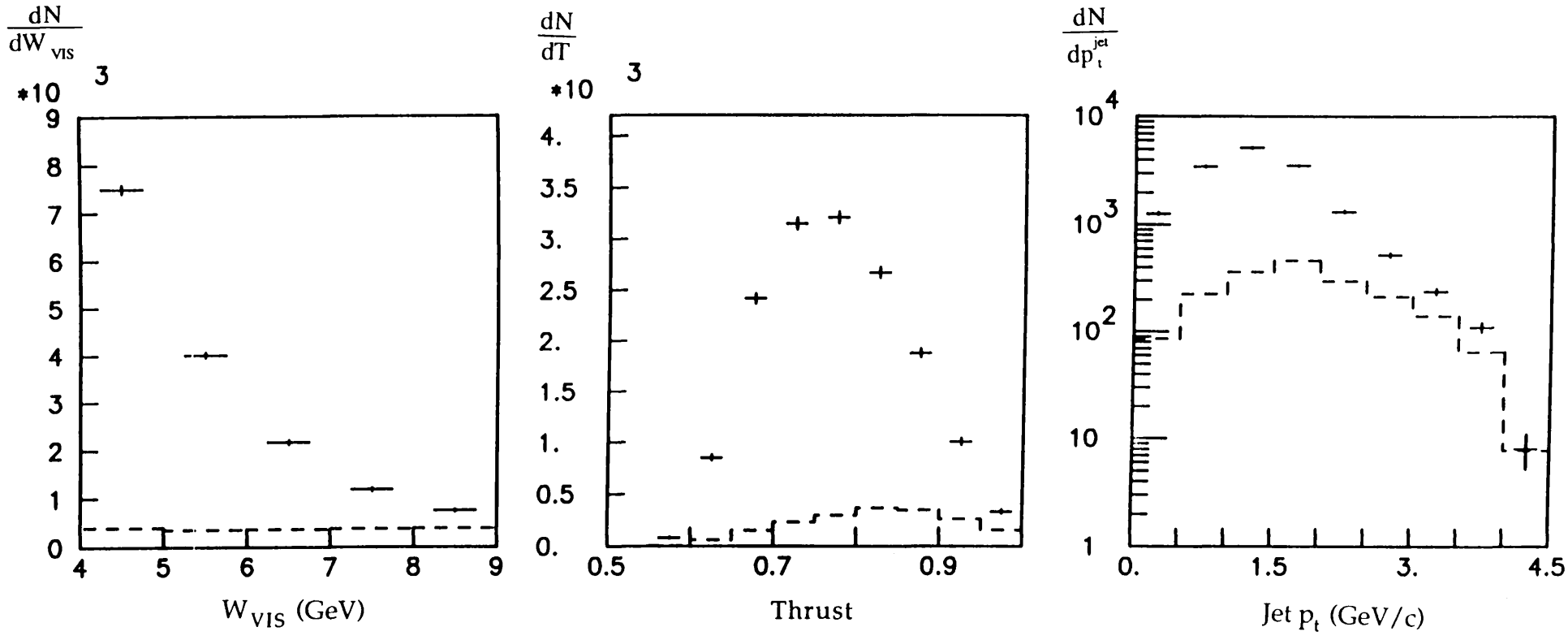

Fig 6.12 The untagged data after final selection cuts compared with the sum of the backgrounds. The W_{VIS}, Thrust and Jet p_t distributions are shown.

Chapter 7

The General Characteristics Of The Data

7.1 Introduction

This chapter examines the general kinematical properties of the multihadronic photon-photon data over the full Q^2 range measured. Firstly the W_{VIS} and Q^2 distributions of the data are compared to an incoherent sum of a hadronic term plus a QPM term. A variety of models for the hadronic part of the process are considered, namely GVDM, VDM, ρ–VDM and GLM (see sections 1.7, 1.8, 1.9), (The GVDM has been already been shown (see section 2.3) to give a reasonable description of the data over a wide Q^2 range when used in conjunction with QPM). Neither the QPM nor the hadronic terms is able to describe the data alone, the hadronic VDM processes having a too steeply falling Q^2 dependence, together with a particle p_t distribution which is limited due to the low momentum transfers expected from reactions of this type. The pointlike QPM process has a much flatter Q^2 dependence and produces large particle p_t's, but also has a predicted cross-section (assuming the use of the constituent quark masses is correct) which cannot explain the numbers of events seen in the data, particularly at low Q^2.

Consequently the data is compared to an incoherent sum of a hadronic component plus QPM. After demonstrating that the data can be described reasonably well over a wide Q^2 range by an incoherent sum of GVDM and QPM, the normalisation and Q^2 dependence of the hadronic component are studied further in order to find which hadronic Q^2 dependent form-factor best describes the data. The data is also compared with the GLM model for hadron production plus QPM.

In the following sections all figures presented show the data with background processes subtracted. The error bars shown on the data points are statistical only. It should also be noted that since the equivalent luminosity of MC generated was 180 pb^{-1}, the MC has statistical errors ~ 0.7 of those of the data. When the background was subtracted from the data the statistical error of the background was taken into account in the data error points (including the weights used). The inclusive particle p_t distributions are calculated with respect to the $\gamma\gamma$ axis in the visible hadronic final state centre of mass frame.

7.2 A Comparison of the Data with an Incoherent Sum of QPM and a Soft Hadronic Component.

In chapters 1 and 2 the various processes expected to occur in hadronic photon-photon interactions were discussed. The data is expected to be composed of a hard pointlike component and a soft hadronic component, with the possibility of some additional higher order QCD component. In section 2.3 it was pointed out that the PLUTO analysis of single tagged events demonstrated that an incoherent sum of GVDM and QPM could reasonably describe the data over a wide Q^2 range, although an excess was seen at low Q^2. It was therefore a natural starting point for this analysis to begin by attempting to reproduce the PLUTO results. This is made possible by the wide Q^2 range available to be studied from the three different tagging ranges possible, $0 \leq Q^2 \leq 30$ GeV, (the limited statistics of the barrel tags ruled out their use). The QPM component was produced using the generators, fragmentation schemes and analysis chain discussed previously. All possible quark flavours were taken into account and the constituent quark masses mentioned in section 5.3 used. It should be mentioned that the b quark contribution is negligible due to the threshold of $W > 10$ GeV and because both its mass (~ 5 GeV) and its charge of $\pm 1/3$ suppress the cross-section. The GVDM component was produced using the same parameters that were used in the previous PLUTO analyses. The cross-section used in the generator was chosen to be a flat term independent of W, and used the GVDM form-factor for the Q^2 dependence described in chapter 1. The data used in this section is naturally split into three separate Q^2 regions dictated by the angular acceptance of the tagging regions used. These have mean Q^2 values of 0.1, 1.0 and 12.7 GeV^2 for the untagged, forward and endcap regions respectively. Tables 7.1, 7.2 & 7.3 show the numbers of events detected in each region which passed the final selection requirements described in the previous chapter. They are compared to the QPM, GVDM and background contributions. Also shown in this table are the numbers of events produced for each region by the ρ-VDM, VDM and GLM predictions.

Table 7.1 The numbers of events and percentages for the untagged data.

PROCESS	Number of Events	(%)
DATA	15610±125	100
$1\text{-}\gamma \rightarrow qq$	1354±26	8.7
$1\text{-}\gamma \rightarrow \tau\tau$	56±5	0.4
$2\text{-}\gamma \rightarrow \tau\tau$	7±2	0.04
Beam Gas/Pipe	442±30	2.8
Σ Backgrounds	1859±40	11.9
DATA-Σ Backgrounds	13751±131	88.1
QPM	2364±34	15.1
GVDM	10710±73	68.6
QPM + GVDM	13074±81	83.6
QPM + VDM	12714±80	81.4
QPM + ρ-VDM	12444±79	79.7
QPM + GLM	13314±82	85.3

Table 7.2 Numbers of events and percentages for the forward tagged data.

PROCESS	Number of Events	(%)
DATA	371±19	100
$1\text{-}\gamma \rightarrow qq$	20±3	5.4
$1\text{-}\gamma \rightarrow \tau\tau$	0	0.0
$2\text{-}\gamma \rightarrow \tau\tau$	0	0.0
Beam Gas/Pipe	10±4	2.7
Σ Backgrounds	30±5	8.1
DATA-Σ Backgrounds	341±20	91.9
QPM	115±8	31.0
GVDM	237±11	63.9
QPM + GVDM	352±13	94.9
QPM + VDM	274±12	73.8
QPM + ρ-VDM	224±11	60.4
QPM + GLM	365±14	98.4

Table 7.3 The numbers of events and percentages for the endcap tagged data.

PROCESS	Number of Events	(%)
DATA	302±17	100
$1\text{-}\gamma \rightarrow qq$	36±4	11.9
$1\text{-}\gamma \rightarrow \tau\tau$	0	0.0
$2\text{-}\gamma \rightarrow \tau\tau$	2±1	0.7
Beam Gas/Pipe	16±6	5.3
Σ Backgrounds	54±7	17.9
DATA-Σ Backgrounds	248±18	82.1
QPM	161±9	53.3
GVDM	93±7	30.8
QPM + GVDM	254±11	84.1
QPM + VDM	194±10	64.2
QPM + ρ-VDM	168±9	55.6
QPM + GLM	259±11	85.8

The numbers of events observed in the data agree well with both the QPM + GVDM and the QPM + GLM terms within 7%. The error on the integrated luminosity measurement of the data (7.1) is 3%. The effects of the fragmentation parameters used in the hadronic term were estimated by observing the change in acceptance using different parameters and this introduces a systematic error in the observed number of events produced by the hadronic component of ~ 14%. This is the dominant systematic error and when this is taken into account the number of events observed in the data are predicted well within errors.

7.3 The General Characteristics of the Data.

Although the QPM has a fixed cross-section predicted from QED (assuming the constituent quark masses used are correct) the cross-section used in the GVDM is essentially a free parameter and it is perfectly reasonable to scale this within reason to fit the data. Therefore the GVDM contribution was scaled to make the sum of GVDM and QPM equal the number of events seen in the data for comparisons of the distributions. This was done for the three Q^2 ranges independently. Fig 7.1 shows the W_{VIS} distributions of the

untagged, forward tagged and endcap tagged events. As can be seen the model describes the W_{VIS} distributions well and no evidence for the requirement of a W dependent term is suggested at this point. This is not surprising as above a W_{VIS} of 4 GeV (which corresponds to true W's > 5 GeV typically), any W^{-1} dependent term will be small. This can be seen in fig 1.9 where the 270nb/W term is most prominent at low W's only. Fig 7.2 Shows the Q^2 distributions of the forward and endcap regions. Both the QPM and the GVDM + QPM predictions are shown. As can be seen the QPM component is a larger fraction of the overall prediction in the higher Q^2 range. The agreement between data and MC is good. The discrepancy between the endcap data and MC is attributed to the poor understanding of the endcap energy measurements which affect the Q^2 value assigned to the event. This does not affect the total number of endcap tagged events seriously, but introduces a systematic smearing in the Q^2 distribution of typically ± 2 GeV^2 in Q^2. Fig 7.3 shows the reconstructed charge imbalance of events for each region, and as can be seen, the MC effectively describes the data.

In studying the hadronisation processes which are important if a jet analysis is intended, it is useful to plot the charged and neutral multiplicities (Figs 7.4, 7.5) as well as their reconstructed momentum and energy (Figs 7.6, 7.7), and again, within statistics the MC describes the data (except the excess of high momentum charged tracks in the untagged data, which was greatly improved with the addition of an additional component, see chapter 8). However the energy distribution of the neutrals from the data show an excess over the MC at low energies. This was believed to originate from two main sources. Firstly, hadrons creating secondary particles which backscattered into the calorimeter simulating photon showers, and secondly, noise in the liquid argon being incorrectly interpreted as showers caused by photons (although this should be simulated by the MC). It was found that increasing the minimum energy cut for neutrals to 300 MeV removed this discrepancy. However it was decided that since this had no other noticeable effects on the data other than to reduce the statistics the cut was left at 200 MeV. Overall the hadronisation processes occurring in the data appear to be well described by the two jet MC models.

In order to see if any event characteristics are W dependent, the untagged data is split into two W_{VIS} regions, $4.0 \leq W_{VIS} \leq 5.3$ GeV and $5.3 \leq W_{VIS} \leq 9.0$. The charged and neutral multiplicity distributions are plotted in figs 7.8 and

7.9 and again the MC effectively describes the data. A small discrepancy is seen in the untagged charged multiplicity in the $5.3 \leq W_{VIS} \leq 9.0$ region which is also seen in the overall charged multiplicity distribution. The fact that it is not seen in the low W region suggests this is not a phenomenon due to resonance production contaminating the data. The magnitude of the effect is also within the systematic errors (~14%) which we assume.

7.4 The Q^2 Dependence of the Hadronic Component of the Data.

We now examine the Q^2 dependence of the VDM component and which particular form-factor best describes the data. In order to obtain a value for the W dependent cross-section we normalise the hadronic component such that the hadronic plus QPM components equal the number of events in the untagged data sample (except for the GLM model which makes a specific prediction for the hadronic component). We can then examine which model best describes the Q^2 dependence of the data in the Q^2 ranges available. Because of the low mean Q^2 of the untagged data (~ 0.1 GeV^2) the cross-section obtained for this data should be relatively insensitive to the form-factor used for the hadronic model. This can be seen in the table 7.1, where the GVDM, VDM and ρ-VDM models produce similar numbers of events (for a cross-section flat in W of 240 nb). However, the numbers start to differ more noticeably in the higher Q^2 ranges. Table 7.4 shows the cross-sections of the hadronic component calculated for each Q^2 range separately, again such that the sum of QPM plus hadronic component provides the number of events seen in the data. Also shown in table 7.5 are the hadronic cross-sections required to give a best least squares fit to the W_{VIS} distributions for the various models.

Table 7.4

PROCESS	Untagged	Forward	Endcap
GVDM	252.2±2nb	228.9±16nb	224.5±26nb
VDM	264.0±2nb	341.1±24nb	632.7±73nb
ρ-VDM	271.1±2nb	497.6±35nb	2982±343nb

Table 7.5

PROCESS	Untagged	Forward	Endcap
GVDM	252.4±4nb	218.4±22nb	199.2±41nb
VDM	264.0±4nb	321.6±43nb	552.0±100nb
ρ-VDM	278.8±4nb	475.2±83nb	2661.6±735nb

These tables clearly show that the GVDM description provides a cross-section which within errors is not dependent on the Q^2 of the reaction, whereas the cross-sections of the other models increase with Q^2 indicating that these models have form-factors which fall too strongly with Q^2. In the formalism put forward in section 1.7 a correct model has a cross-section which is independent of Q^2. In table 7.5 the cross-sections for the GVDM + QPM ansatz were calculated to minimise the χ^2 to the W_{VIS} distributions. The cross-sections obtained agree within errors with the cross-sections obtained in table 7.4 by normalising the numbers of events. This demonstrates that the assumption of a flat W independent cross-section is valid. However it is interesting to compare the χ^2 values of the W_{VIS} distributions for the GVDM + QPM term and the GLM + QPM term. Whereas the GVDM term has an assumed flat W dependent cross-section the GLM uses a parameterised model which is both a function of W and Q^2 and does includes a W^{-1} term (see section 1.9). An overall least squares fit to the W_{VIS} distributions of the low Q^2 region yielded a χ^2/d.f. of 3.1 for the QPM + GVDM ansatz and 7.5 for the QPM + GLM ansatz. Whilst it can be said that the GVDM term provides a better fit, the results are compatible when the systematic errors are taken into account.

In Fig 7.10 we plot $R_{\gamma\gamma}$ (see section 2.4) as a function of Q^2 for the data compared with GVDM + QPM. $R_{\gamma\gamma}$ is a variable which is often used to compare the data with the pointlike contribution and is defined as

$$R_{\gamma\gamma} = \frac{\text{observed no of events}}{\text{no of events predicted by QPM}}$$

This shows the fall-off of the hadronic component with Q^2. At very high Q^2 values, $R_{\gamma\gamma}$ is expected to fall to 1.

It has been shown above that the GVDM form-factor describes the Q^2 dependence of the data well. The GLM model makes a specific prediction concerning the W, Q^2 dependence of the hadronic component. The $R_{\gamma\gamma}$ plot (Fig 7.10) shows that this describes the Q^2 dependence of the data well. Tables 7.1, 7.2, 7.3 show that the predicted number of events in the various Q^2 regions agree well with the data. This is important since as previously mentioned, the GLM model is parameterised from previously published data, and hence shows that the data presented here are in agreement with, in particular, the PLUTO data.

Fig 7.11 shows the energy distributions for both tagging regions. As can be seen, the forward tags energy distribution is good, whereas the endcap energy distribution is poor. Fortunately, this does not affect the acceptance of tags significantly, this being most dependent on their angular distribution. The poor energy calibrations did not affect the excellent angular resolution of the endcap tags (where the fine grained lead strips provided excellent resolution). This can be seen in fig 7.12 which shows the angular distribution of tags in both regions. The forward taggers had a poor angular resolution (primarily due to the poor understanding of the scintillators used to determine θ) and this is reflected in the plot.

7.5 The Inclusive Particle p_t and Angular Distributions.

The inclusive particle p_t is now examined. This is measured with respect to the $\gamma\gamma$ centre of mass in the hadronic final state rest frame. Fig 7.13 shows the plots for the inclusive particle p_t distributions in each tag region compared with the QPM as well as the GVDM + QPM prediction. As can be seen the GVDM component dominates at low p_t in the low Q^2 data. As the Q^2 increases the GVDM component decreases in size, as expected from its strong Q^2 dependence. The QPM component has quite different characteristics. It does not fall as strongly with Q^2, and it is not limited to low particle p_t values. The sum of the two models can be seen to reasonably describe the distributions both in the forward and endcap Q^2 data. However, there is a clear discrepancy in the particle p_t distribution for the low Q^2 data. An excess is observed at medium and high particle p_t. An excess of events at high particle p_t's in low Q^2 (untagged) hadronic photon-photon data has previously been observed (7.2). This excess of events is discussed later in chapter 8. However for the general purpose of describing the data by a sum of GVDM and QPM, this excess is small and does not affect the overall good

description offered by this model.

Finally we examine the angular distribution of the charged and neutral particles (in the lab frame) and plot their distribution for the three tagging regions in figs 7.14 and 7.15 respectively. The angular distribution of charged tracks in the forward and endcap regions is good within statistics. The neutral particle distributions show a small excess at low energies as mentioned above. One notices that the distributions become less forward-backward peaked as the Q^2 increases. This is due to the tag kicking the tracks into the centre of the detector. In the untagged data a clear discrepancy is observed in the charged track angular distribution at small angles. The neutral particles again show an excess attributable to noise. Thus two systematic errors are observed. These effects are small when compared to the large statistical errors for the tagged data. Their effect on the untagged data is discussed further in section 8.6.

7.6 Conclusions

In conclusion this chapter has shown that the general characteristics of the data can be well represented by an incoherent sum of QPM and a soft hadronic component. It is found that the GVDM ansatz best describes both the W and Q^2 dependence of the data. Although the GLM model correctly predicts the overall numbers of events and their Q^2 dependence, the GVDM term provides a better desciption of the W dependence (although the difference is within the systematics). A discrepancy in the particle p_t distribution of the low Q^2 data is observed. It is noted that this excess at high particle p_t has been observed by previous experiments (7.2).

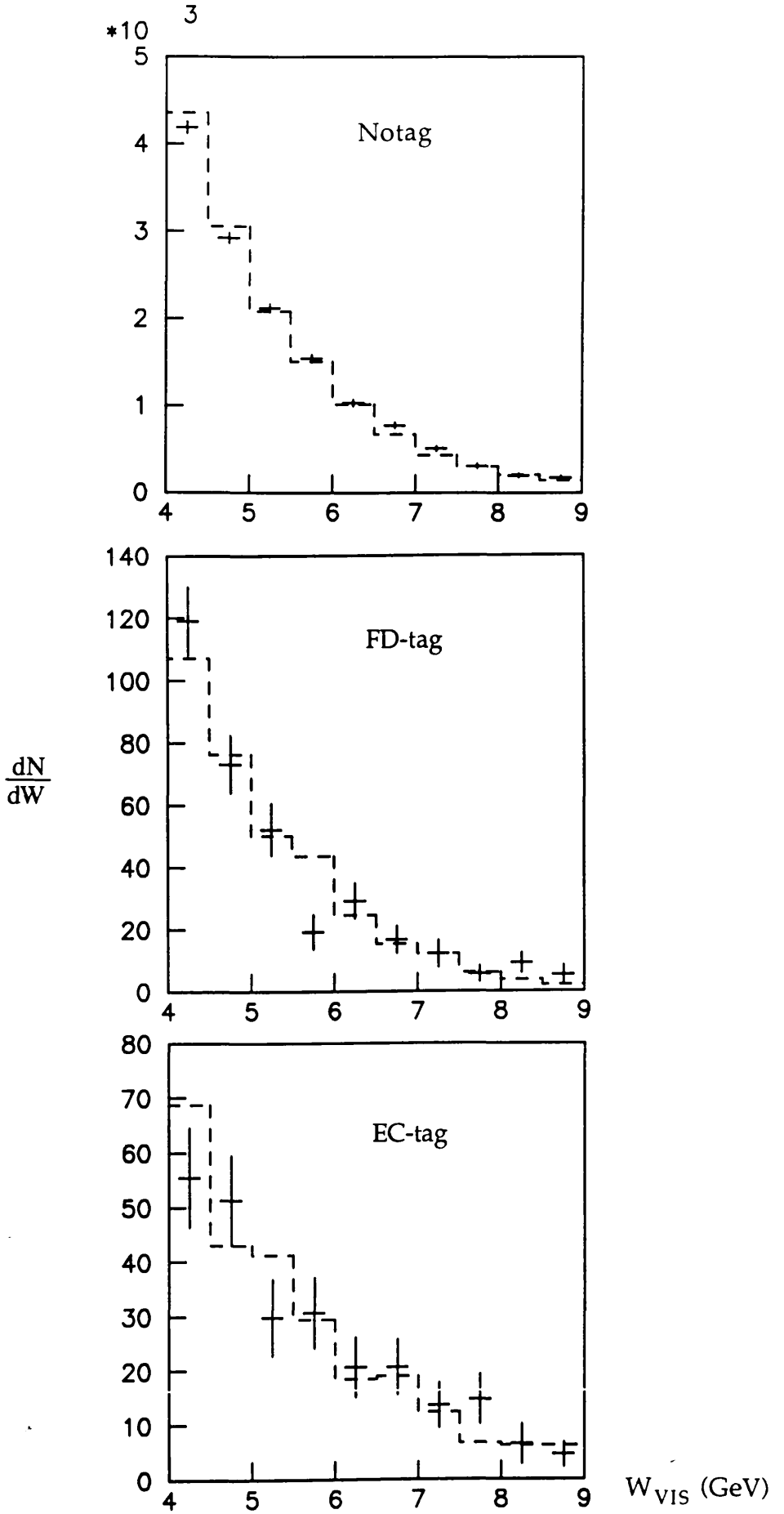

Fig 7.1 The W_{VIS} distributions for the untagged, forward tagged and endcap tagged data, compared with QPM + GVDM.

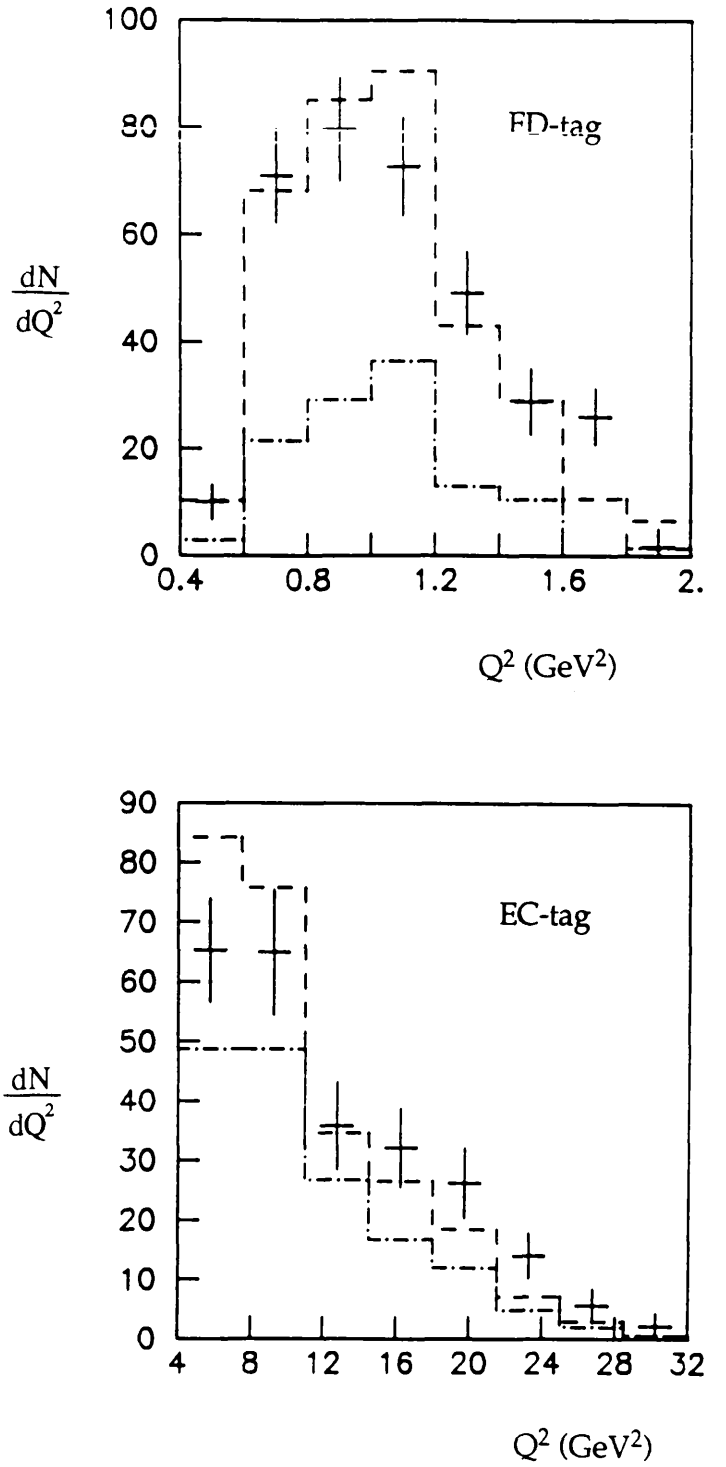

Fig 7.2 The Q^2 distributions for the forward tagged and endcap tagged regions. The dashed line shows the GVDM + QPM prediction and the dashed-dotted line shows the QPM prediction.

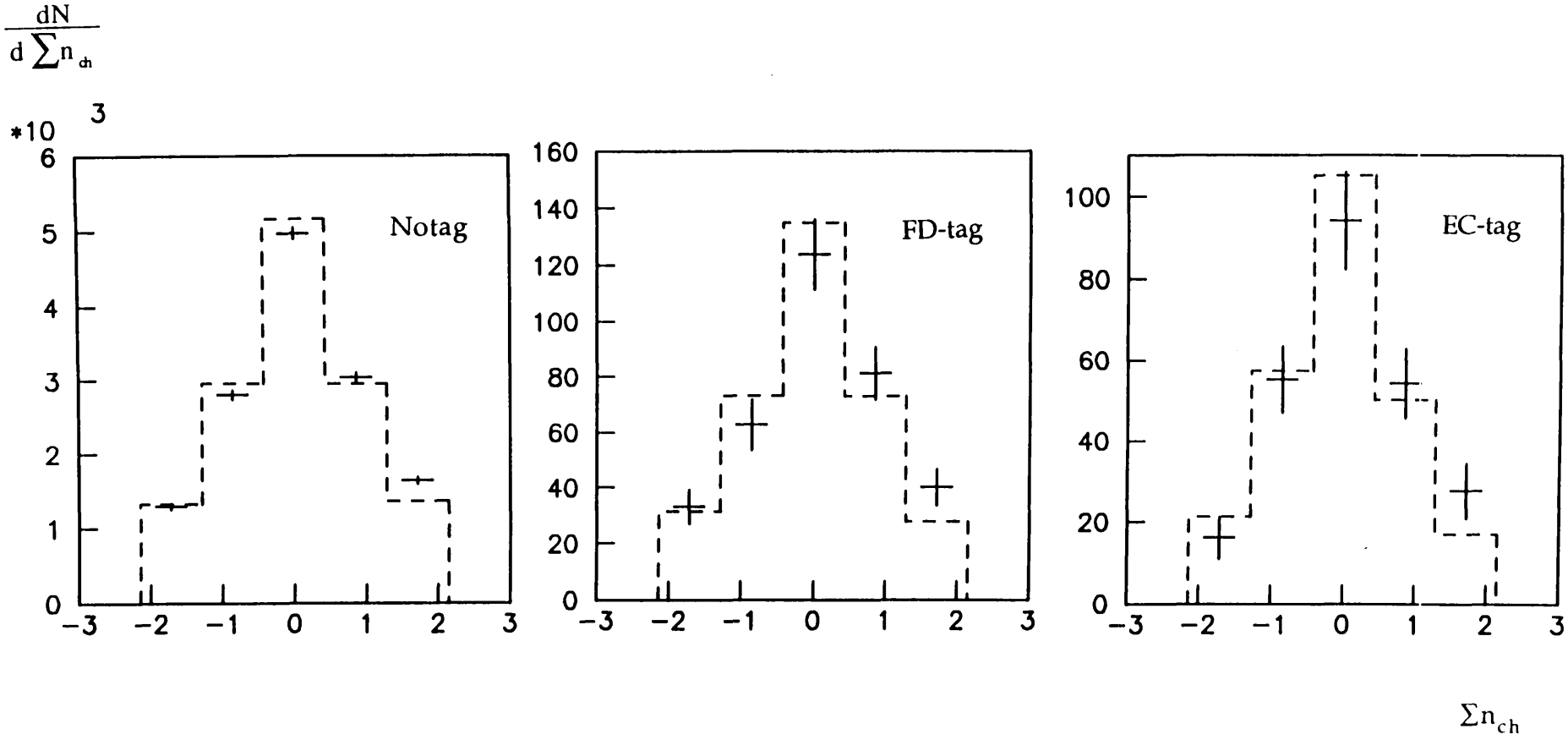

Fig 7.3 The total charge imbalance of untagged, forward and endcap tagged events.

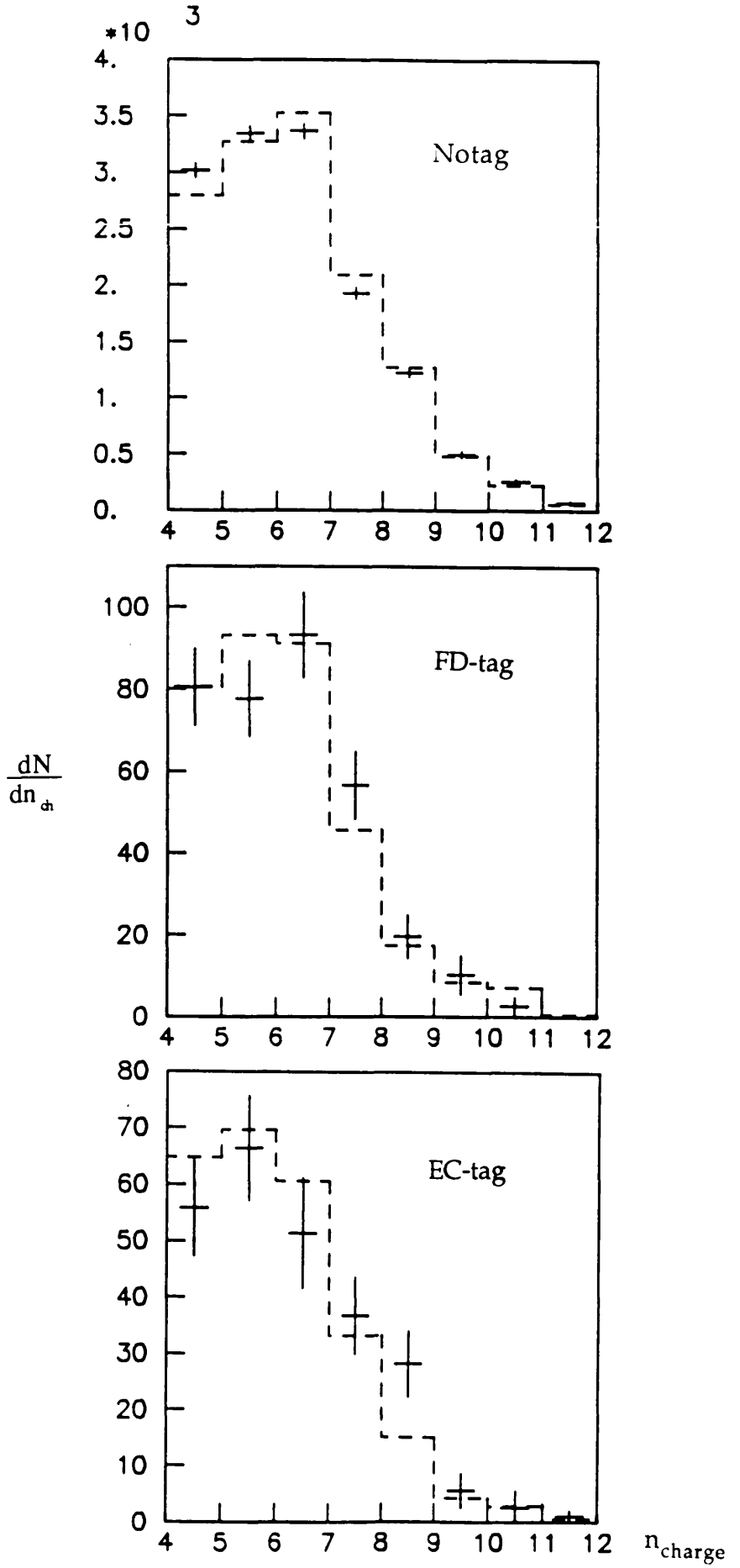

Fig 7.4 The multiplicity distributions for charged tracks for the untagged, forward tagged and endcap tagged regions, compared with QPM + GVDM.

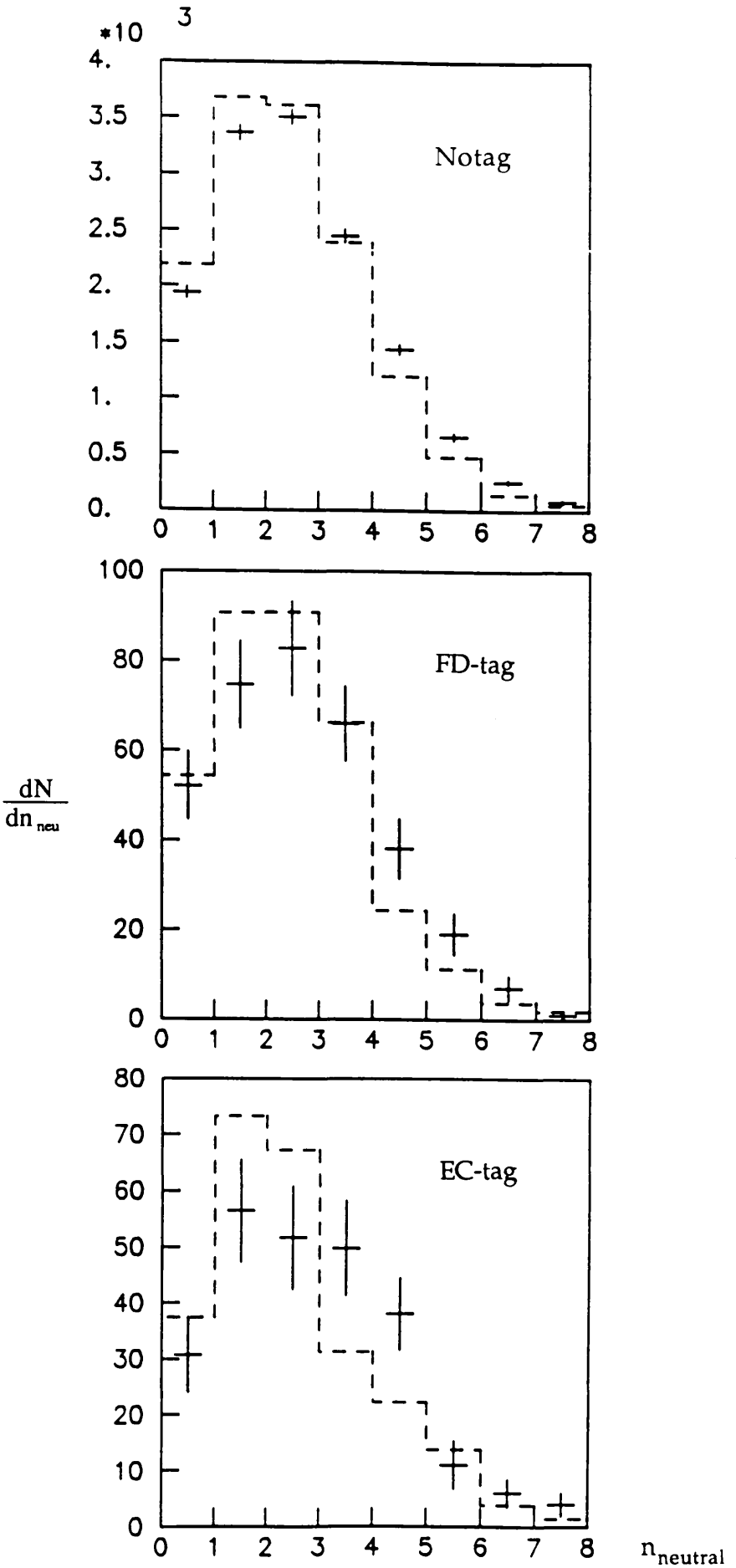

Fig 7.5 The multiplicity distributions for neutral particles for the untagged, forward tagged and endcap tagged regions, compared with QPM + GVDM.

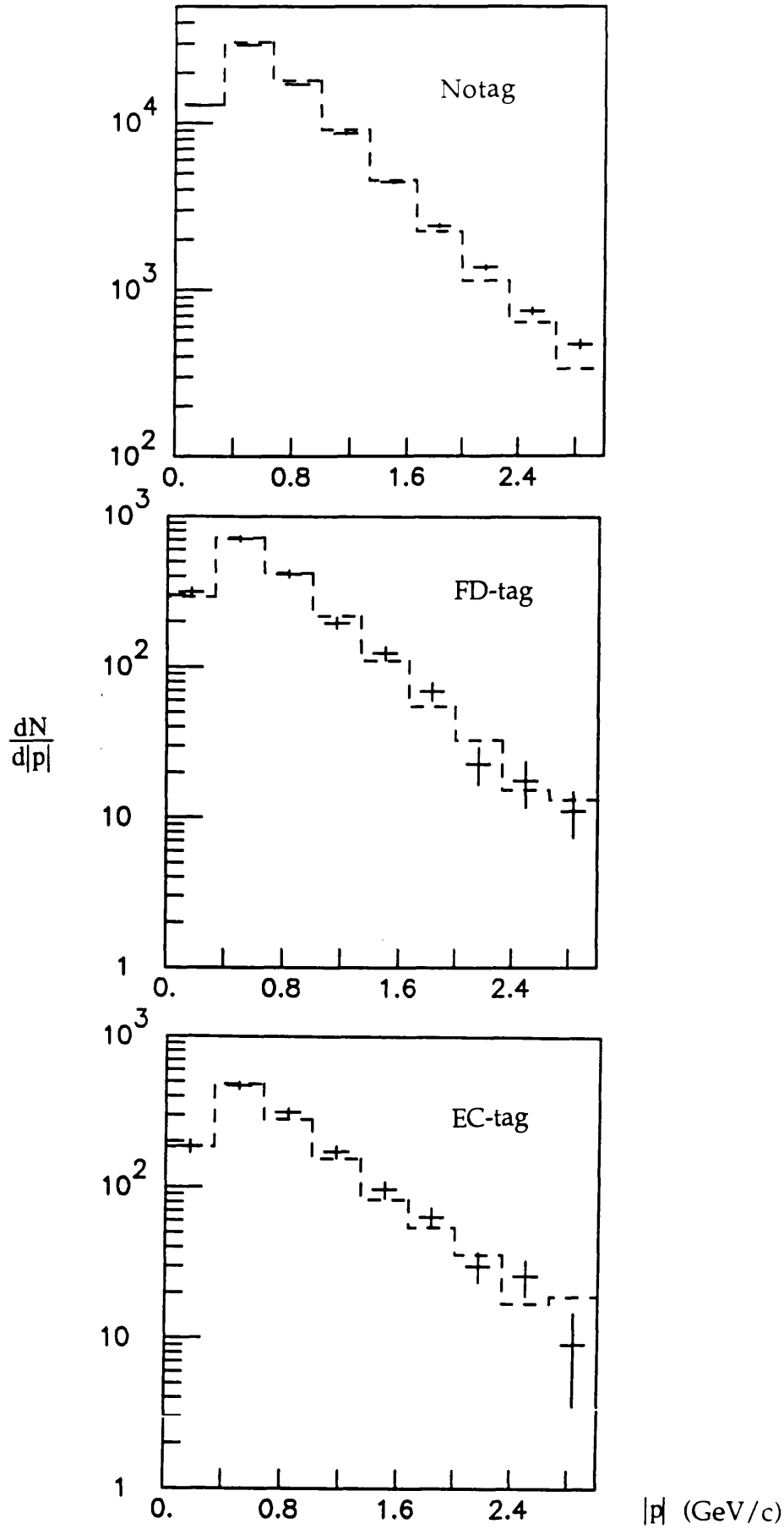

Fig 7.6 The momentum distributions for charged tracks in the untagged, forward tagged and endcap tagged regions.

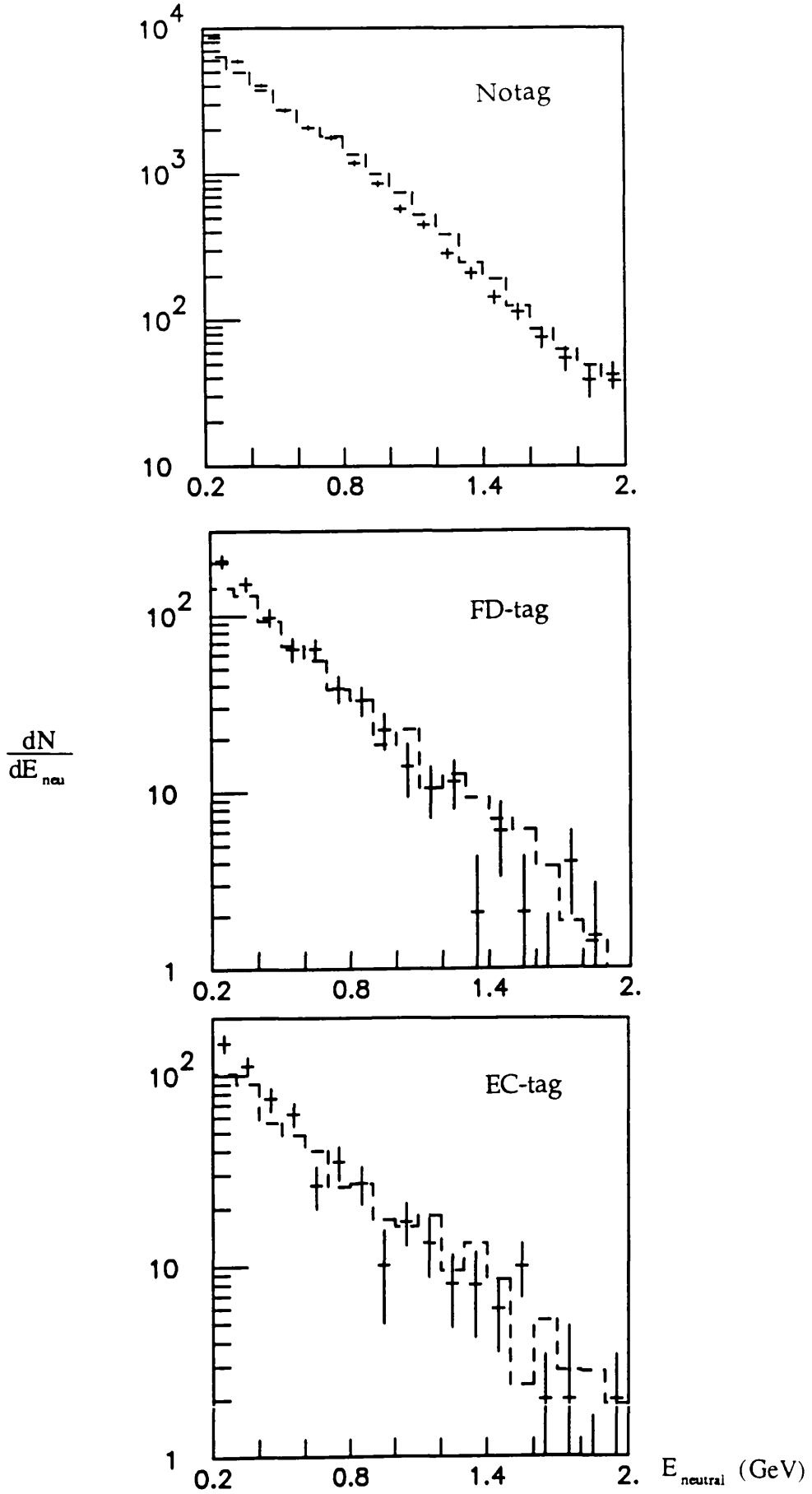

Fig 7.7 The energy distributions of neutral particles for the untagged, forward tagged and endcap tagged regions, compared with QPM + GVDM.

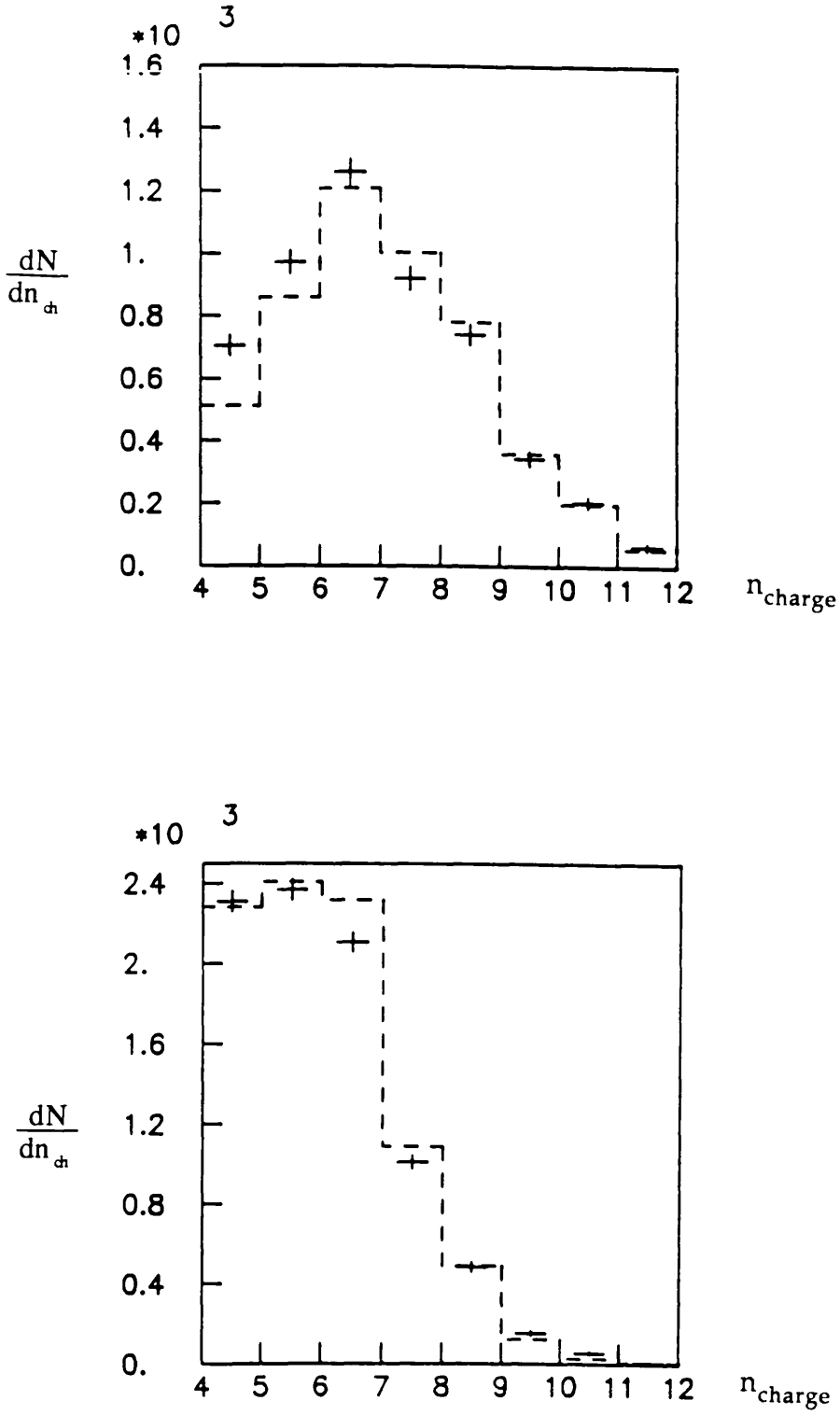

Fig 7.8 The multiplicity distributions of charged tracks for the untagged data in the region $4 \leq W_{VIS} \leq 5.3$ GeV (bottom) and $5.3 \leq W_{VIS} \leq 9$ GeV (top)

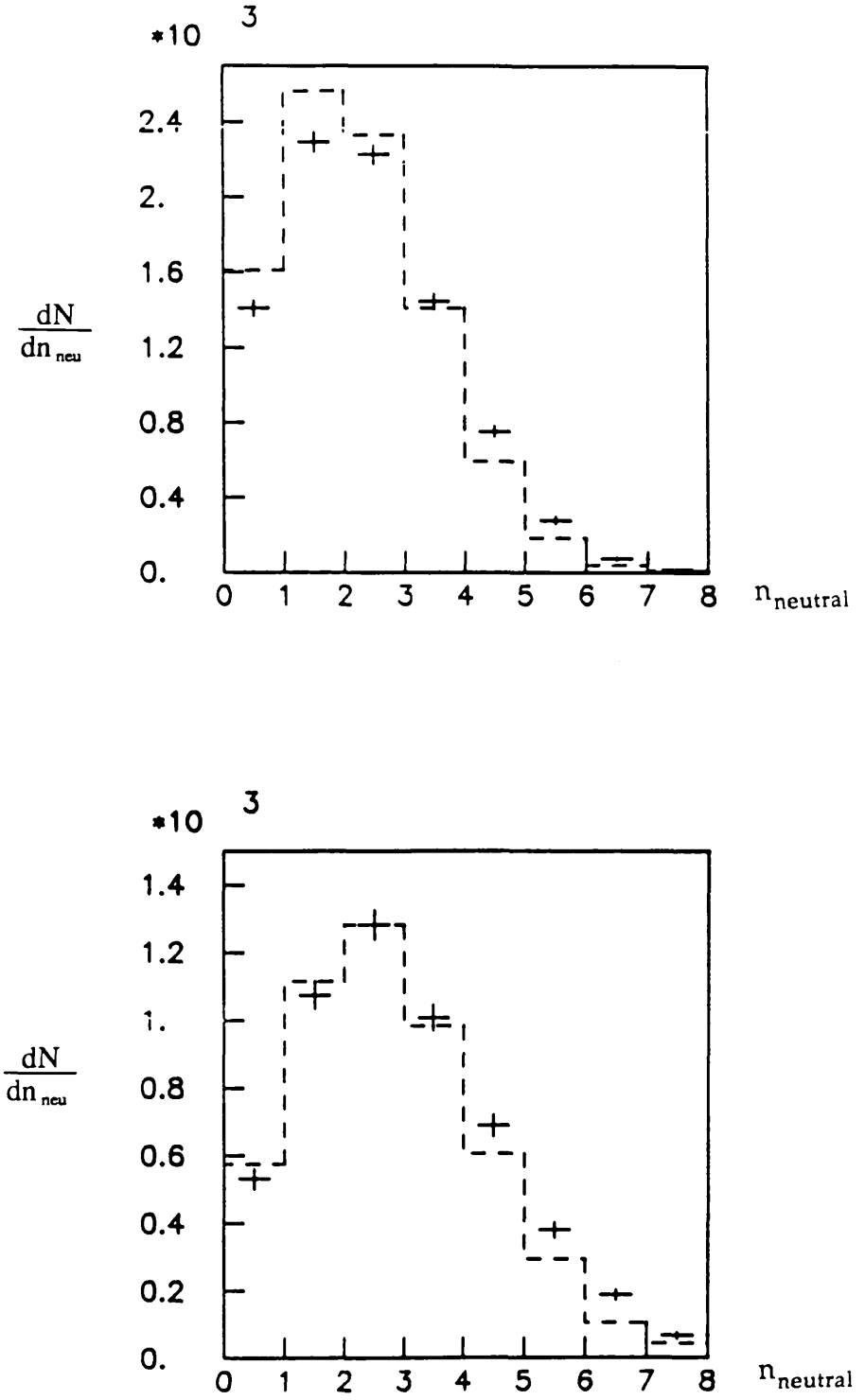

Fig 7.9 The multiplicity distributions of neutral particles for the untagged data in the region $4 \leq W_{VIS} \leq 5.3$ GeV (bottom) and $5.3 \leq W_{VIS} \leq 9$ GeV (top)

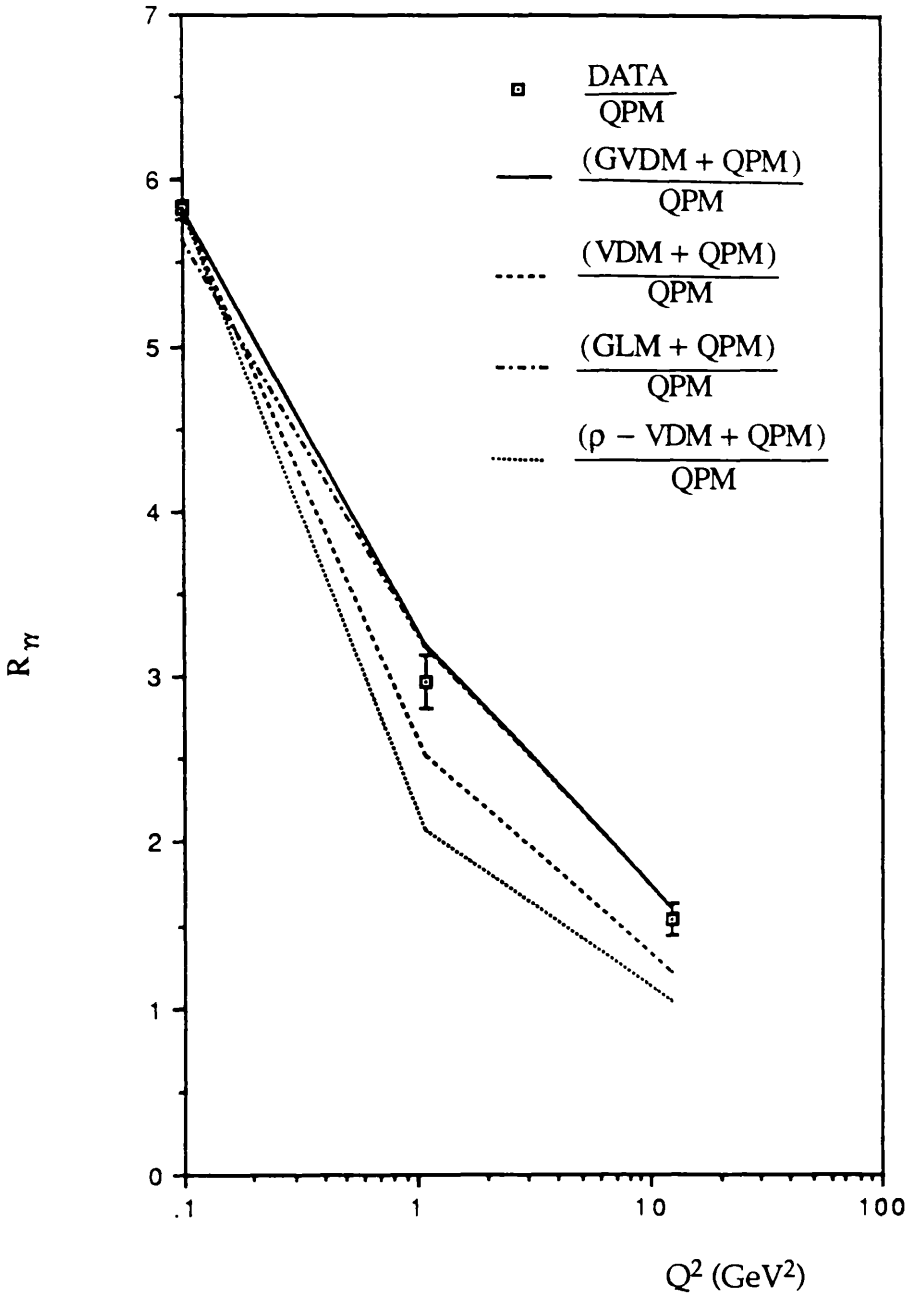

Fig 7.10 $R_{\gamma\gamma}$ is plotted as a function of Q^2. The data is compared with the GVDM, VDM and ρ-VDM predictions.

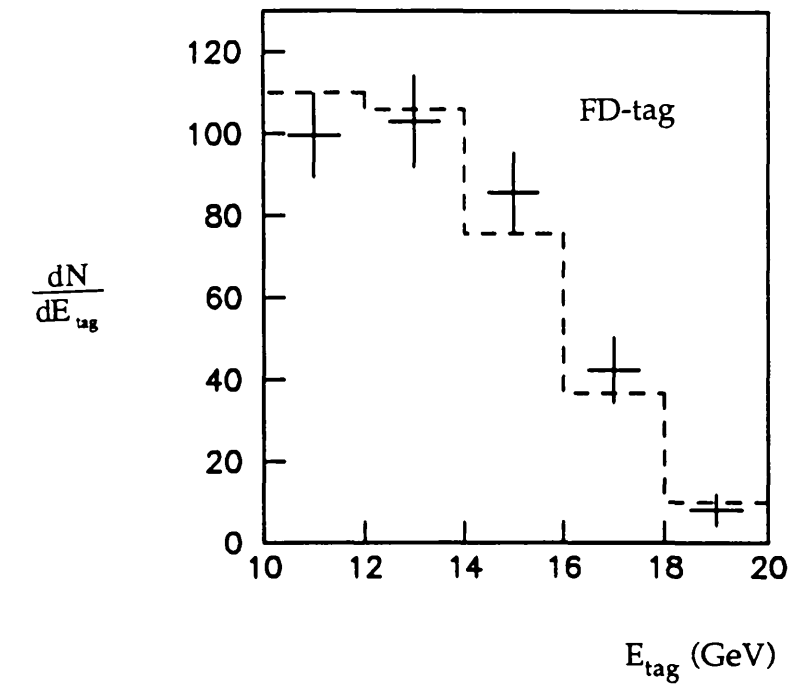

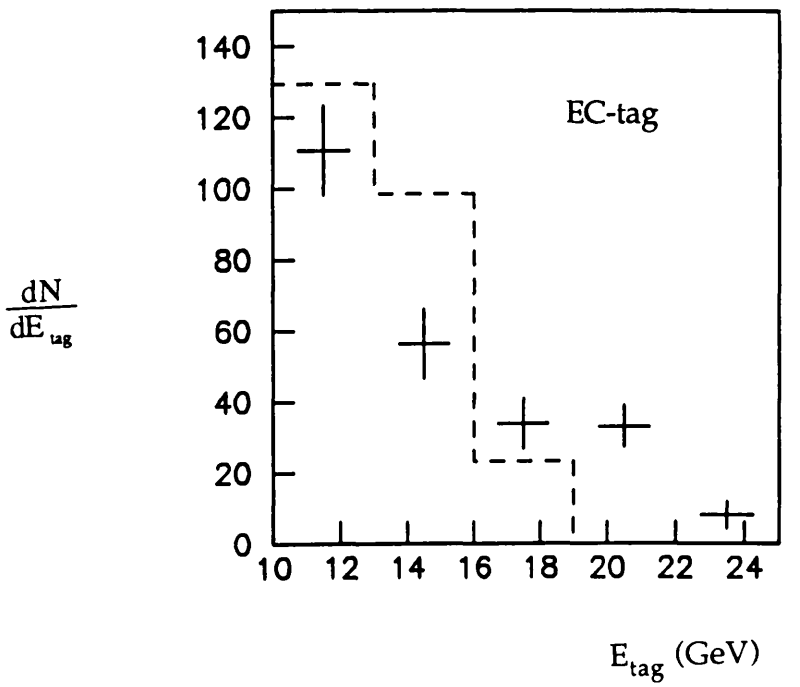

Fig 7.11 The energy distributions of forward (top) and endcap (bottom) tags.

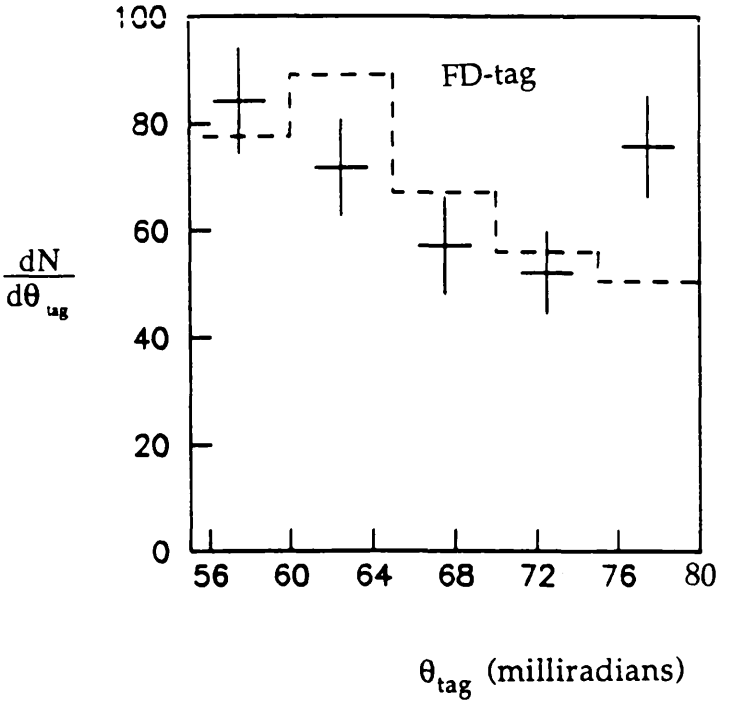

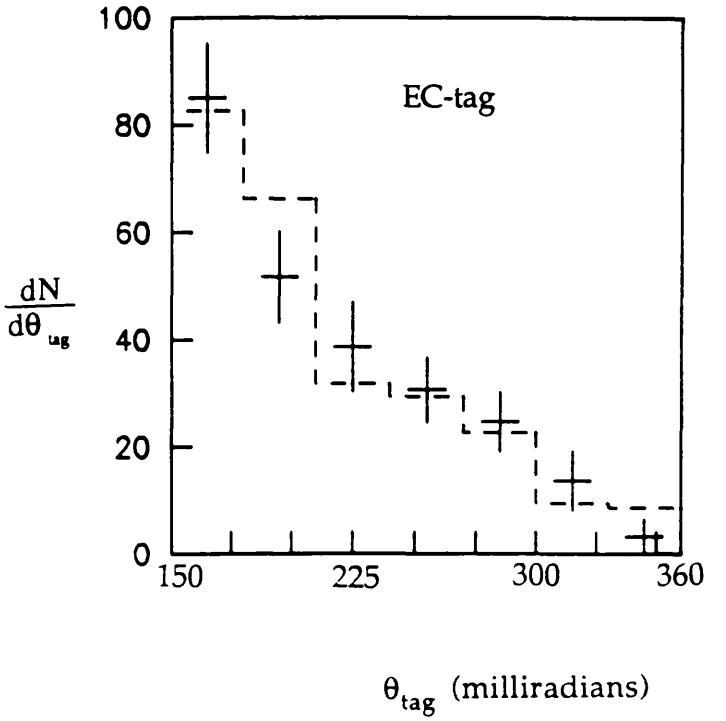

Fig 7.12 The θ distributions of forward (top) and endcap (bottom) tags.

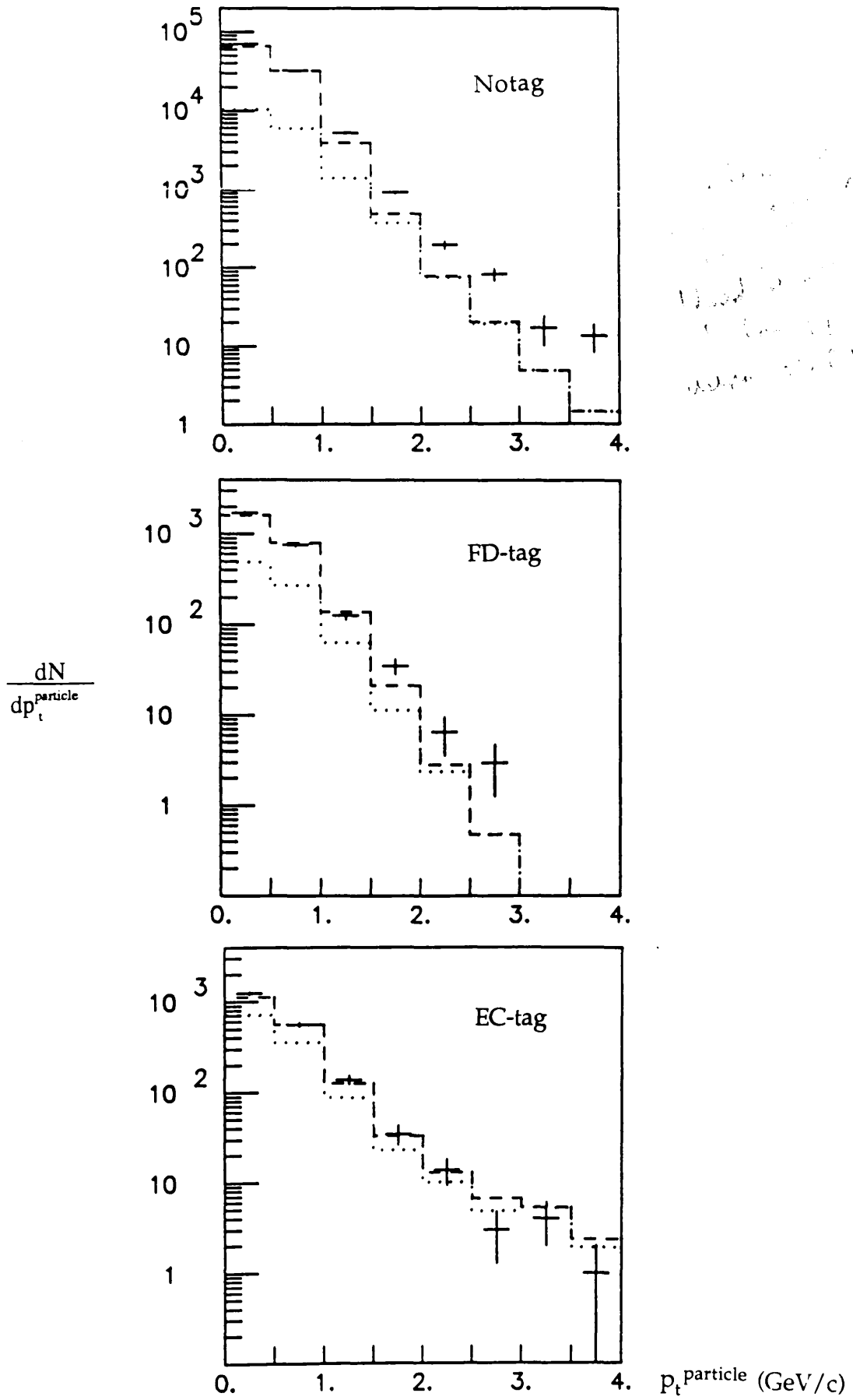

Fig 7.13 The inclusive particle p_t distributions for the untagged, forward tagged and endcap tagged regions respectively. The data is compared to a sum of GVDM and QPM (dashed) and the QPM term (dotted).

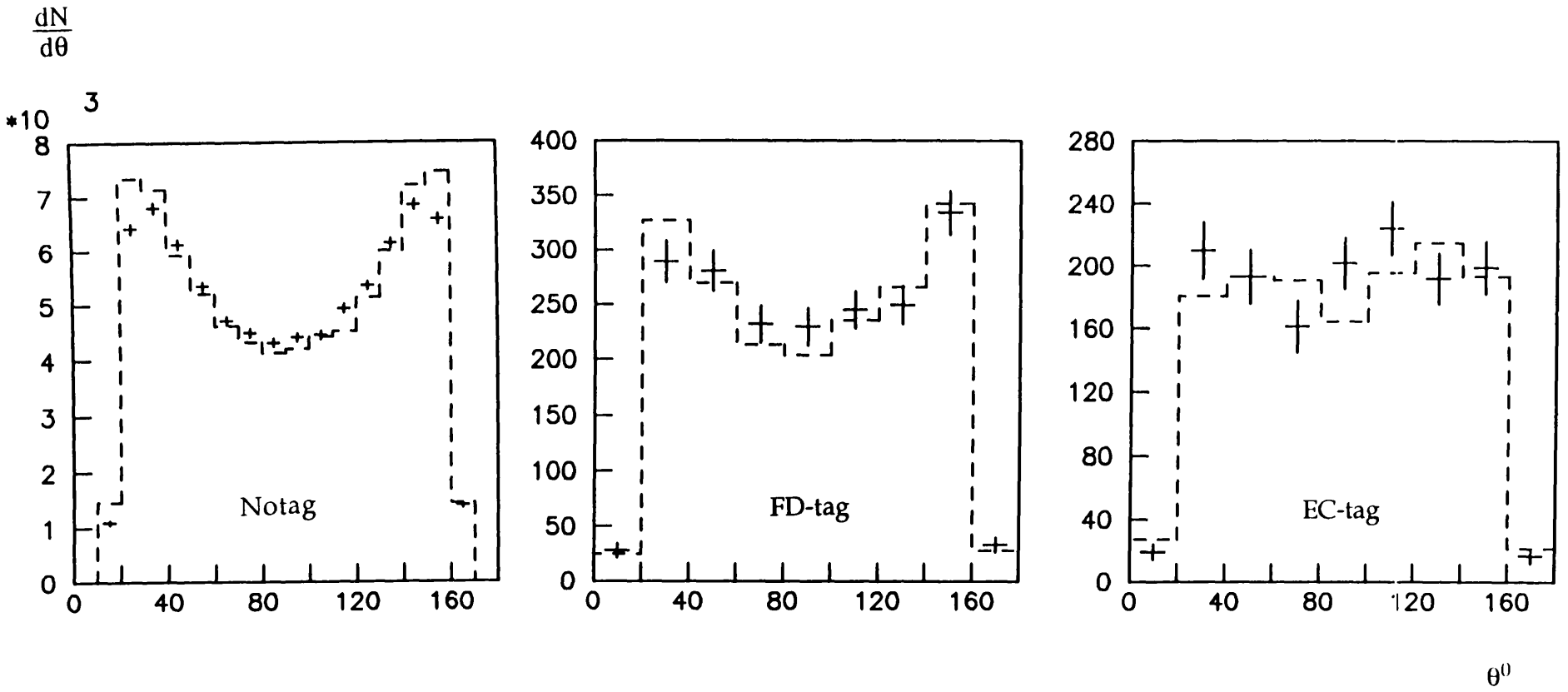

Fig 7.14 The angular distribution of charged tracks measured with respect to the beam-axis for the untagged, forward and endcap tagged data.

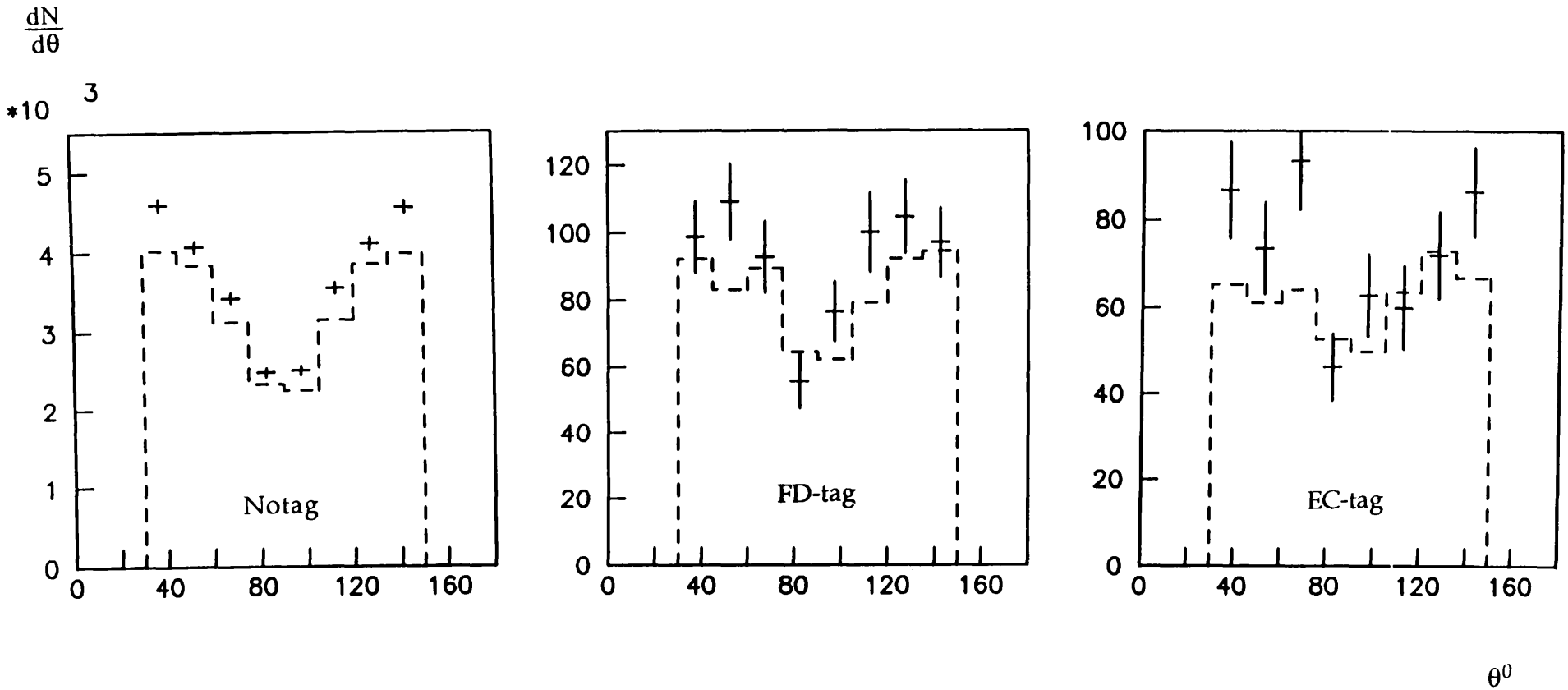

Fig 7.15 The angular distribution of neutral particles measured with respect to the beam-axis for the untagged, forward and endcap tagged data.

Chapter 8

A Jet Analysis Of Hadronic Photon-Photon Events.

8.1 Introduction

In the previous chapter the general characteristics of the events were examined. It was concluded that a good description of the data, in terms of W, Q^2 was provided by an incoherent sum of a pointlike component (QPM) and a soft hadronic component with a GVDM form-factor. A discrepancy was noted in the inclusive particle p_t distribution in the low Q^2 data.

In this chapter the analysis of the data is extended to examine the jet structure of the data. Hadronic photon-photon events are expected to form jets of particles in a similar manner to multihadronic annihilation events at similar energies. As previously mentioned, a jet is a set of hadrons which have a limited transverse momentum with respect to their momentum axis. Since an important component of the hadronic photon-photon events consists of the process $\gamma\gamma \rightarrow q\bar{q}$, and since the hadronic component is also expected to produce hadrons with limited p_t an analysis of the events in terms of their jet properties is appropriate. The jet structure of hadronic photon-photon events at these $W_{\gamma\gamma}$ values is, however, by no means as clearly seen as in higher energy e^+e^- annihilation events. A typical hadronic photon-photon event is shown in fig 8.1.

The aim of this chapter is to examine the jet structure of the data and determine if it can be described by the QPM + GVDM ansatz, and whether any further components can be identified. Section 8.2 discusses the various methods used to measure the event topology of events. Section 8.3 examines the event topologies of the MC models used in this analysis and the effects that the detector acceptance has on these topologies. In sections 8.4 and 8.5 a jet analysis of the data is undertaken and the data is compared to the QPM + GVDM ansatz. Finally in sections 8.6 and 8.7 discrepancies in the jet p_t and thrust distributions are examined and the inclusion of a third component is examined in sections 8.8 and 8.9.

8.2 Methods of Jet Analysis.

In the $\gamma\gamma$ centre of mass frame a two-jet event is characterised by two back to back sets of hadrons, with a specific jet axis which should have approximately the same direction as the original partons which fragmented to form the jets. The most important characteristic of a jet is that whereas the mean longitudinal momentum of the particles with respect to the jet axis should grow with the total energy contained in the event, the mean transverse momentum of the particles with respect to the jet axis should be limited. This is in contrast to an isotropic distribution where the mean transverse momentum is not constrained. Isotropic events do not even have a true jet axis, although they may be given one by any event topology algorithm that is used. In order for a jet to be identified it is first necessary that it contains tracks with a longitudinal momentum component significantly larger than their transverse component, otherwise the jets will be poorly defined. We therefore need to make use of variables which measure the shape of an event, such as thrust and sphericity. These assign a measure of how jet-like an event is. This is in contrast to the other popular method of jet analysis which involves using cluster algorithms to determine how many jets are present in an event. These were first used on multihadronic annihilation data at PETRA. However, since the events being studied in this analysis have an average W of ~ 5 GeV the jets formed are usually poorly defined, and it was realised that this method was not particularly useful. It should be noted that photon-photon events often have a strong boost along the beam axis which can distort their appearance in the laboratory frame of reference. It is therefore necessary to boost the event into the $\gamma\gamma$ centre of mass frame before examining its jet structure. In principle, this should be the final state centre of mass frame, however this cannot be fully reconstructed due to detector acceptance. We therefore use the centre of mass frame of the observed final event.

The thrust algorithm (8.1)

$$T = \max\left[\frac{\sum|p_{L_i}|}{\sum|\vec{p}_i|}\right]$$

sums over all the particles of an event choosing the best jet axis by maximising the longitudinal momentum along it. The quantity p_l are the

longitudinal components of the particle momenta along the assumed jet axis. This function assumes the event is formed from two back to back jets and is therefore useful for analysing data which are predominantly two-jet in nature. The value of this function varies between 1/2 for an isotropic event to 1 for a perfect two jet event. This function provides a jet axis which can be used to calculate the jet p_t. Firstly the momentum of the jet is calculated by summing up the momenta of the particles along the jet axis.

$$\vec{p}^{JET} = \sum_i \vec{p}_i$$

This is related to the jet's transverse momentum relative to the $\gamma\gamma$ axis by

$$\vec{p}_t^{JET} = \vec{p}^{JET} \bullet \sin\theta$$

where θ is the angle between the jet axis and the $\gamma\gamma$ axis in the final state centre of mass frame. In untagged events where the beam leptons are only scattered through small angles the beam axis is a good approximation to the $\gamma\gamma$ axis. In tagged events the $\gamma\gamma$ axis is obtained using the tag's 4-vector and its associated beam lepton (in the $\gamma\gamma$ cms).

Sphericity (8.2) is a similar variable to thrust; here the momentum tensor M

$$M_{\alpha\beta} = \sum_{j=1}^{N} p_{j\alpha} p_{j\beta}$$

is used where $p_{j\alpha}$ is the momentum component along the axis α (which runs over x, y ,z) for the j^{th} particle (which runs over the n particles in the event). When this tensor is diagonalised it provides three normalised eigenvalues where

$$Q_1 + Q_2 + Q_3 = 1$$

and three normalised eigenvectors

$$\hat{n}_i \ , \ i = 1, 2, 3$$

These are ordered such that $Q_1 < Q_2 < Q_3$ and the sphericity is defined as

$$S = \frac{3}{2}(Q_1 + Q_2)$$

The normalised eigenvector n_3 provides the sphericity axis. Sphericity can also be written more clearly as

$$S = \frac{3}{2} \min\left[\frac{\sum_i (p_i)_t^2}{\sum_i (p_i)^2}\right]$$

where the jet axis is defined as the unit vector which minimises the square of the total relative transverse momenta with respect to the jet axis. This is similar to the axis defined by the thrust algorithm and therefore thrust and sphericity are highly correlated. Fig 8.2 shows the angular difference between these definitions of the jet axis for two-jet MC events. As can be seen this is peaked at a small angle. In this analysis the thrust axis is used to calculate jet p_t. Thrust is preferred to sphericity because it is a linear function and reconstructs the jet axis more effectively. This is because being linear in momentum it is less sensitive to the presence of decaying resonances among the fragmenting particles. Sphericity varies between 0 for a perfect two-jet event and 1 for a perfectly spherical or isotropic event. Aplanarity is obtained from the same normalised eigenvalues as sphericity and is defined as

$$A = \frac{3}{2}Q_1$$

and measures how planar or flat an event is.

Thrust and sphericity are variables which define a specific jet axis for an event. An alternative approach is given by the Fox-Wolfram moments (8.3) which do not provide a jet axis. These rely on angular correlations between the final state particles, and it is claimed (8.4) that these are more sensitive to multijet final states. The n^{th} Fox-Wolfram moment is defined as

$$H_n = \frac{1}{E_{vis}} \sum_{ij} |p_i||p_j| P_n(\cos\theta_{ij})$$

where E_{vis} is the total energy in the final state event (= W_{vis} in the centre of

mass frame), p_i is the momentum of particle i, P_n is the n^{th} Legendre polynomial and θ_{ij} is the angle between the particles i and j. The summation runs over all particles in the event and includes the case i = j. Energy and momentum conservation requires $H_0 \approx 1$ and $H_1 = 0$. For a perfect two jet event $H_{even} = H_0$ and $H_{odd} = 0$ for any order polynomial.

8.3 Jet Production in MC models and the Effects of Detector Acceptance on Jet Reconstruction.

In this section the jet nature of the various MC models and the effect of the detector's acceptance are examined. The previous chapter upheld the hypothesis that the data can be described by an incoherent sum of GVDM and QPM. These models both produce events with two back to back jets of hadrons when viewed in the final state centre of mass frame.

In order to ascertain whether jet production is occuring in events, it is useful to plot the mean transverse and longitudinal momenta of particles with respect to the reconstructed jet axis. The mean longitudinal momentum component should increase with the energy contained in the event, whereas the transverse component should be limited. Fig 8.7 shows the transverse $<p_t>$ and longitudinal $<p_l>$ components as a function of W_{VIS} for the simulated QPM and GVDM events, and compares them with the phasespace model (see section 5.5). It should be noted that this is after the detector acceptance has been taken into account. As can be seen the two-jet terms display a marked difference between the longitudinal and transverse components, the transverse component being limited compared to the longitudinal component. It is important to note that the phasespace term is very different in character, the $<p_t>$ term displaying no limitation with W_{VIS}. This demonstrates that the detector permits the distinguishing between jet-like and isotropic models. The difference between the QPM and GVDM terms is due to the different fragmentation parameters used. It is important to note that the W dependence of the phasespace model does not affect these variables.

These models are expected to produce quite different jet p_t distributions because of the different nature of the interactions. The GVDM component will produce jets with predominantly low jet p_t, whereas the QPM component can scatter the quark-antiquark pair with high transverse momenta, consequently producing a high jet p_t tail. This is demonstrated in fig 8.3 which shows the jet p_t (after detector acceptance effects) for the GVDM

and QPM predictions. As can be seen the GVDM term falls off strongly with jet p_t and no longer contributes to the data above ~ 3 GeV/c, whereas the QPM term contains a tail of events with high transverse momenta jets. The fall off at low jet p_t is due to the lack of detector acceptance for jets close to the beam line.

Fig 8.4 shows a scatter plot between the parton p_t and reconstructed jet p_t before detector effects have been taken into account. There is a significant correlation between the two variables which demonstrates that the jet p_t is a good variable to reflect the underlying transverse momentum distribution of the partons at the heart of the fragmentation process. Fig 8.5 shows a scatter plot for the true jet p_t and the measured jet p_t after detector effects have been taken into account. Although the measured jet p_t is systematically lower due to the acceptance effects reasonably good correlation is observed. However it was observed that there appears to be a cluster of events where the reconstructed jet p_t is larger than the true jet p_t. More light is shed on this by looking at a similar scatter plot (Fig 8.6) for the angle of the reconstructed jet axis (with respect to the $\gamma\gamma$ axis, or the beam axis for untagged events) before and after detector effects. Here a correlation is seen betweeen true and measured jet angles. (Half of the events have the jet axis reversed by 180^0 which is of no important significance.) However, as can be seen there are clusterings where the true jet angles are small and yet the jet angle reconstructed after the detector acceptances are approximately perpendicular to the $\gamma\gamma$ axis. These clusterings are due to events with low jet angles (and consequently low jet p_t) which are very badly reconstructed due to the majority of the particles going along the beam axis. The detector only picks up the edges of the event and consequently gets the jet axis completely wrong. This is even more of a problem for VDM type events where the events are peaked at these low jet p_t's (Fig 8.3). In fact the reconstructed jet angle for VDM type events is heavily biased to larger angles. This is sensitive to any flaws in the detector simulation and the fragmentation models used. It is interesting to compare this situation with annihilation MC events (at high energies). Here the events are much less forward backward peaked and the correlation for the jet angle is much improved as shown in fig 8.11.

Fig 8.8 show the thrust distributions for the GVDM and QPM models before and after detector acceptance effects. Systematic shifts occur in the distributions due to the detector acceptance. The GVDM model produces events with a higher average thrust value than the QPM model (before detector) because the events have a higher average hadronic mass, and can

therefore produce more collimated jets. This is because the GVDM model has a flat W cross-section compared with the $1/W^2$ term in the QPM. Because the two models have quite different p_t distributions they undergo significantly different topology distortions due to the detector acceptance, which causes different shifts in the average thrust values. Fig 8.9 shows the difference between measured thrust for the QPM and GVDM components before and after detector effects. Poor resolutions are observed due to the acceptance of the detector. Fig 8.10 shows a scatter plot between the true and measured thrust for QPM events. The true thrust measurement is obviously heavily smeared by the detector acceptance, although some correlation is seen. This is again linked to the poor jet angle reconstruction.

We now move on to examine the event structure and topology of the multijet and phasespace models. Fig 8.12 shows the thrust distributions for the two-jet, multijet and phasespace models before detector acceptance has been taken into account. As can be seen, before the detector the thrust distributions for the phasespace and multijet models are concentrated at lower thrust values than that of the two-jet model. This is as expected, these models producing a more isotropic distribution. However the effect of the detector acceptance on the models is also shown in fig 8.12 where the thrust distributions are plotted for each model after detector acceptance has been taken into account. A systematic distortion is noticed. This means that the usefulness of the thrust variable for distinguishing between various jet models is compromised. This smearing is again due to the limited acceptance of the detector missing a fraction of the event and causing the detected event to appear less isotropic than it actually is. It is interesting to note that the W dependence of the phasespace model does not significantly affect its thrust distribution. This is because, unlike jet events, the thrust of phasespace events is not W dependent (ignoring acceptance effects).

Fig 8.13 shows the jet p_t distributions for the multijet and phasespace models. It is important to note that the phasespace term produces a significantly different jet p_t distribution from either of the multijet models, falling off more strongly at low jet p_t's producing the majority of events at high jet p_t. Although the phasespace model does not produce jets, it produces events at high jet p_t because it does not have a strong forward-backward peaked angular distribution. It is interesting to note that the phasespace model with a flat W dependence produces a higher average jet p_t than with the $1/W^2$ dependence (as is expected). Although the multijet models do go to high jet p_t's they also have a large low jet p_t component (in

particular the 4-jet model).

We now study how the thrust changes as a function of jet p_t. Fig 8.14 shows how the mean thrust varies with jet p_t for the GVDM + QPM, phasespace and multijet models after the detector acceptance is taken into account. If the two-jet and multijet components are compared then the mean thrust distributions show only small differences. This is because CELLO lacks the acceptance at low angles which is so important to help resolve the different event topologies of photon-photon events. It also means that any multijet component of the data is going to be difficult to distinguish from the dominant two-jet component. The phasespace component can be resolved from the jet models, the topology being evidently quite different from the jet models. It was again noted that the mean thrust of the phasespace model did not significantly depend on which W dependence was used.

8.4 Evidence of Jet Production in the Data.

Having established the effects of the detector acceptance on various jet models we go on to search for jet production in the data. Fig 8.15 shows the mean transverse $<p_t>$ and longitudinal $<p_l>$ components of the particle momentum with respect to the jet axis (determined from the thrust algorithm) for the untagged data. This is compared to the incoherent sum of GVDM and QPM discussed in section 7.2, and also the phasespace model. As can be seen, the data shows that $<p_t>$ is constrained, evidence of jet production. This is well described by the GVDM + QPM picture, whereas the phasespace model shows no limitation in $<p_t>$ and is in clear disagreement with the data. The $<p_l>$ distribution of the data is also well described by the GVDM + QPM term, and again the phasespace term is incompatible with the data. Fig 8.16 shows the thrust distribution of the data (for each Q^2 region) and again compares it with the GVDM + QPM picture, as well as the phasespace model (for the untagged data). Again the data is well described by the GVDM + QPM, whereas the phasespace model produces a systematically lower thrust distribution which does not account for the data. These figures clearly demonstrate that jet production is occurring in the data and that as a first approximation the GVDM + QPM two-jet model describes it well. They also show that a phasespace model is incompatible with the data and shows clear differences compared with the two-jet model, demonstrating that jet production can be identified after detector acceptance effects. Fig 8.17 show the sphericity, aplanarity and fox-wolfram moments for the data, again

comparing them with the GVDM + QPM and phasespace terms. The data is seen to be well described by the GVDM + QPM term, and again the phasespace model is systematically different. These plots again reinforce the statement that the data is well described by a two-jet model. However it is important to note that this does not exclude discrepancies arising from the two-jet picture in certain sections of the data. Because the thrust and sphericity distributions appear to show the largest distinctions between the two-jet and phasespace terms, and since the thrust variable has the property of being linear in momentum, our analysis concentrates on this jet variable.

8.5 The Jet p_t and Angular Distributions of the Data.

Having established the overall two-jet nature of the data we continue by examining the jet p_t distributions of the data in the three Q^2 ranges studied, and compare them with the incoherent sum of GVDM + QPM, which has been shown to provide a good description of the overall jet nature of the data. Fig 8.18 shows the data compared with the GVDM and QPM terms separately. The GVDM term is seen to dominate at low jet p_t and low Q^2. The fraction of GVDM decreases with Q^2, again demonstrating its strong Q^2 dependence. Whereas the GVDM term is limited to the low jet p_t region, being limited to regions < 3 GeV, the QPM term does not display this constriction and produces a high jet p_t tail. Fig 8.19 shows the data compared with the sum of the GVDM and QPM terms. Good agreement is observed between the MC and data in the endcap tagged data when errors are taken into account. However the forward tagged and untagged data both exhibit an excess of events over the prediction at high and medium jet p_t, although this is not a statistically large effect in the forward tagged data. The excess is much more obvious in the untagged data. As well as an excess at high jet p_t in the untagged data the MC overestimates the low jet p_t region. This region is dominated by the GVDM component and this discrepancy can be linked to the normalisation of the GVDM model. The discrepancy at high jet p_t is much more significant since it occurs in a region where the GVDM term is expected to be small. It can be said that when statistics are taken into account both the tagged regions have jet p_t distributions which are reasonably described by the GVDM + QPM term. However the untagged data displays large systematic differences which are inconsistent with the model used. It is also important to note that this excess cannot be accounted for by the GVDM

component, since it is in a region where the GVDM component is small. It would require very large changes to the GVDM model to produce jets at these high jet p_t's.

After examining the nature of the jet p_t distribution the next logical step is to study the angular distribution of the jet axis with respect to the $\gamma\gamma$ axis (in the events centre of mass frame). This variable is correlated with jet p_t to some extent because of the $\sin\theta^{jet}$ term present. Jets with low p_t will in general be produced at low angles with respect to the $\gamma\gamma$ axis. High p_t jets will be produced at large angles with respect to the $\gamma\gamma$ axis. Fig 8.20 shows the angle of the reconstructed jet axis for the three Q^2 regions. The data is compared with the GVDM + QPM term as well as the QPM alone. The first thing which is immediately obvious is the nature of the QPM component. Its relative contribution to the data increases strongly with increasing Q^2. This is due to the strong Q^2 dependence of the GVDM term, causing it to fall rapidly with increasing Q^2. Secondly it is also very noticeable that the GVDM component is dominant in the low jet p_t and hence low jet angle regions. It is interesting to observe the flat angular distribution of the QPM component as contrasted to the strong angular dependence of the GVDM term. The agreement between the data and GVDM + QPM is good in the forward and endcap tagged regions. However in the untagged region we again see a clear discrepancy between the model and the data. There is an excess of data with a large jet angle and a subsequent over-estimation by the MC at low angles. It is important to note that the GVDM term has been normalised such that the sum of GVDM + QPM agrees with the numbers of events observed in each Q^2 region (as discussed in chapter 7). This causes the data to be overestimated at low angles. It is also important to note that the smearing of the jet angle (due to the detector acceptance) pushes the GVDM component to large jet angles.

8.6 Discrepancies in the Untagged Data.

Because the jet axis (and therefore jet p_t) is strongly dependent on the angular distribution of charged and neutral particles, we examine the effect of the discrepancy in the angular distribution of charged tracks. As was seen in fig 7.14 there was an anomaly in the angular distribution of charged tracks. This was almost certainly due to the poor understanding of tracks which were produced at a low angle with respect to the beam axis. These tracks passed through the endcap proportional chambers and used the hits in these

chambers plus beam-pipe chamber hits to form a track consisting of only five hits. These tracks were known to be suspect, and a systematic error in their reconstruction of ~ 10% is by no means surprising. In the tagged data these tracks were used because the systematic error they introduced was much smaller than the statistical errors present. Removing these low angle tracks reduced the already small data sample by an unacceptably large amount. However, since the statistics in the untagged region were much better, it was decided to try a tighter cut on the angular acceptance of the charged tracks. Therefore the angular cut was reduced from $\cos\theta_{trk} < 0.95$ to $\cos\theta_{trk} < 0.90$. Exactly the same argument applied to the minimum energy requirement for neutral particles, and therefore the minimum energy requirement was increased from > 200 MeV to > 300 MeV. These cuts had the effect of dramatically reducing the number of events in the final untagged data sample to 60% and increasing the background fraction in this sample from 12% to 18.4%. After these cuts had been applied to the data the angular distributions of charged and neutral particles are shown in figs 8.21 and 8.22. As can be seen there is substantially improved agreement. However as can be seen in fig 8.23, the particle p_t, jet p_t and jet angle distributions still exhibit the same discrepancies as before. Neither did the normalisation of GVDM required change significantly. It was therefore concluded that the observed discrepancies were due to physical effects, and not due to systematic errors in the simulation of the detector acceptance. (The tighter cuts were therefore not used, unless specifically mentioned.)

8.7 An Additional Component to the QPM + GVDM Ansatz.

Having shown that the QPM + GVDM formalism does not completely describe the jet p_t and jet angular distribution for the untagged data we continue by investigating the addition of a third component to the GVDM + QPM ansatz in order to describe the data effectively. Before this is undertaken it is important to justify the arguments that the excess of high jet p_t, high jet angle events are real physics and not simply due to an incorrect background subtraction or an incorrect cross-section for the QPM term. Firstly the background subtraction can be regarded as satisfactory by examining figs 6.5 and 6.6. Fig 6.5 shows that the annihilation spectrum correctly matches the data above 15 GeV and is a small fraction of the data below ~ 10 GeV. Fig 6.6 shows that the background simulations describe the data with large transverse momentum imbalances. MC studies showed that the hadronic

photon-photon data was produced only with low transverse momentum imbalances and should not contribute in this region. These facts strongly support the statement that the background subtraction is valid. A systematic error in the background of ~ 10% is estimated. Although this cannot have a significant effect on the overall cross-section it can affect the high jet p_t region. As shown in fig 6.12 the background is dominant in this region and any systematic error can have a large effect in this region. Studies showed that increasing the background contribution by 10% had little effect on the data and that the discrepancies remained. It was found that to remove the excess of data at high jet p_t the background contribution would have had to have been doubled. However, this was inconsistent with the W_{VIS} distribution since the background was all at high W_{VIS} values. It was therefore concluded that the discrepancies in the untagged data were not due to systematic errors in the background subtraction.

The cross-section of the QPM component can be regarded as correct because it describes the high Q^2 endcap tagged data well, both in amount and jet p_t distribution. It is also important to note that changing the constituent quark masses in the QPM simulation only has a small effect on the cross-section of high jet p_t events. This leaves us with no alternative but to consider the addition of a third component to describe the discrepancies in the MC.

8.8 A Fit to the Jet p_t Distribution

As discussed in chapter 1 and 2 we might expect an isotropic or multijet component in the data. Although there is no indication of this in the overall thrust distribution of the data we have already been able to show that the limited acceptance of CELLO affects the resolution of jet topology measures (such as thrust) quite drastically, so that after the detector acceptance has been taken into account there is very little difference between the overall thrust distributions of the 2-jet and multijet models. Therefore a third component was fitted using jet p_t, which is better resolved (we go on to examine the thrust distributions later). To this end a third component was added to the GVDM + QPM term, the cross-section of the GVDM term being varied such that the sum of GVDM + QPM + 3rd component equalled the data. The fraction of the 3rd component was adjusted until the χ^2 of a least squares fit to the jet p_t was minimised. The phasespace and multijet models discussed in sections 5.5, 5.6 were used as the third component.

It was found that the jet p_t distribution was improved by adding a

phasespace component (with a flat W dependence) to the 2-jet MC. This required the cross-section of the GVDM term to be reduced by 13±1% to 219nb. This gave a χ^2/df fit to the jet p_t distribution of 7.3 (as opposed to 37.7 without the phasespace contribution). Using a phasespace component with a $1/W^2$ term also further improved the fit to the jet p_t distribution (χ^2/df = 3.9), requiring the GVDM term to be reduced by 17±1% to 209nb. The fraction of phasespace required did not change significantly when the tighter acceptance cuts were used, again suggesting that the discrepancies were not due to systematic errors in the angular acceptance of particles. Fig 8.24 shows the particle p_t, jet p_t and jet angle with the addition of a phasespace component, (with a flat W dependence; using a $1/W^2$ term in the phasespace model produced similar distributions). We note that the inclusive particle p_t distribution is much improved with the additional phasespace term. (Fig 8.25 show the same distributions for the data with the tighter cuts previously mentioned.) The W_{VIS} fit favoured using a $1/W^2$ term for the phasespace component (see table 8.1).

It was found that when attempting to improve the jet p_t distribution using a multijet component, the fraction of the multijet component required was large and the fit was poor. In fact for the fit to converge 92±8% of the GVDM term was required to be replaced by the 4-jet term (χ^2/df = 16.3) or 41±5% for the 3-jet term, (χ^2/df = 12.1). This was clearly due to the fact that the multijet models dominated at low jet p_t's (particularly the 4-jet model) unlike the phasespace models which dominated at medium and high jet p_t. This is clearly shown in fig 8.13. One possible reason for this is that the multijet generator used a $1/W^2$ cross-sectional dependence for the $\gamma\gamma$ system, instead of for the pointlike sub-component of the system (8.5). Because W and jet p_t are correlated variables this would affect the model's jet p_t distribution.

Since the excess was observed to be at high jet p_t, it is also logical to examine the thrust distribution of the data as a function of jet p_t. Fig 8.26 shows this for each tagging region compared with the original GVDM + QPM ansatz and as can be seen, good agreement on average is observed throughout. It is interesting to note that in the untagged data the low jet p_t region is well described by the MC. This demonstrates that the thrust distribution of the GVDM term, which dominates in this region, describes the data well. Fig 8.27 shows the thrust distribution of all events with jet $p_t \geq 2$ GeV/c compared to the QPM + GVDM ansatz (for each tagging region). A cut of jet $p_t \geq 2$ GeV was chosen since this is where the GVDM term starts to fall strongly, and the

excess in the untagged data becomes noticeable. The thrust distributions of the tagged data show reasonable agreement. However the untagged data demonstrates an excess of events over the QPM + GVDM ansatz as expected.

The addition of a phasespace component to QPM + GVDM predicts the amount but not the thrust of the high jet p_t events, which showed a higher mean thrust than the MC prediction (Fig 8.28). (The W dependence of the phasespace model did not change this distribution significantly.) Given the insensitivity of the observed thrust to the true thrust this discrepancy could be even greater than appears.

As has been previously mentioned, the multijet models were unable to describe the characteristics of the excess in the jet p_t distribution. However, it was found that the addition of a 3 or 4 jet component to the GVDM + QPM term (without renormalising the GVDM term) provided a good description of the thrust of the high jet p_t events (Fig 8.29). χ^2/df values of 2.1 and 4.0 were obtained using the 4 and 3 jet models respectively. This demonstrates that although the multijet models are unable to describe the jet p_t of the excess in the data they can correctly describe its thrust distribution (at high jet p_t). It should also be noted that choosing only high jet p_t events reduces any W dependence in the multijet models, since high jet p_t's are highly correlated with high W's.

We continue by examining whether the characteristics of the excess can be described by renormalising the QPM term. Although we have stated that the cross-section for the QPM term has been shown to fit the single tagged data, it can be argued that a higher order multijet term may very well share certain features of the QPM component. Both QPM and higher order multijet predictions contain a pointlike scattering component producing high p_t jets ($dN/dp_t^{jet} \sim p_t^{-4}$) and should both exhibit a $1/W^2$ cross-sectional dependence. Furthermore the thrust distributions are not expected to be very different after detector acceptances are taken into account. This was exhibited in fig 8.14. Increasing the fraction of QPM produced an improved fit to the jet p_t distribution (χ^2/df = 3.4). This required reducing the GVDM component to 77±1% to 194nb, (see table 8.1). However increasing the fraction of QPM in the data caused the thrust of high jet p_t data to be overestimated somewhat (Fig 8.30). The fit to the thrust (p_t^{jet} >2) distribution was similar to using additional phasespace term, although it was worse than using an additional multijet term (see above).

Table 8.1 shows the χ^2/df values for the different distributions and the numbers of events of each MC model required to obtain them. It is

important to note that in this table the MC has been fitted to the jet p_t distribution of the data, and the χ^2/df values for the thrust (p_t^{jet} >2) and W_{VIS} are for these amounts of MC.

Table 8.1

1) An incoherent sum of QPM plus a normalised GVDM term.
2) GVDM + QPM plus an additional phasespace term (flat W dependence).
3) GVDM + QPM plus an additional phasespace term ($1/W^2$ dependence).
4) GVDM plus a rescaled QPM term.

	χ^2/df Thrust (p_t^{jet} >2)	χ^2/df p_t^{jet}	χ^2/df W_{VIS}	GVDM	QPM	Phase space
1)	16.9	37.7	3.1	11386	2364	0
2)	9.8	7.3	3.9	9906	2364	1480
3)	9.3	3.5	1.8	9450	2364	1936
4)	6.6	3.4	2.1	8767	4983	0

8.9 The $R_{\gamma\gamma}$ Distributions.

Finally we examine the $R_{\gamma\gamma}$ distributions as a function of jet p_t. This is useful in displaying the excess of events observed at high jet p_t as a fraction of the QPM term. Figs 8.31 and 8.32 show the $R_{\gamma\gamma}$ distributions as a function of jet p_t for the three Q^2 ranges. The data in each region is compared with the GVDM + QPM term, and the low Q^2 data is also compared with the models using an extra fitted QPM or phasespace term ($1/W^2$), (see table 8.1). The tagged data can be seen to be reasonably described by the GVDM + QPM term as expected from fig 8.19. However there remains a clear discrepancy in the low Q^2 data. The MC overestimates the data in the low jet p_t region because the GVDM term has been normalised to the event sample. In the high jet p_t region the excess over the QPM term is of order ~ 2 (or 100%). An addition to the GVDM + QPM ansatz of either QPM or phasespace (see table 8.1) is seen to describe the distribution adequately. It is interesting to compare this factor 2 excess of events over QPM with the factor predicted due to higher order processes in ref. 8.6. Excesses of 70% to 50% for $2 < p_t < 4$ GeV/c are predicted

for Q^2's of ~ 0.1 GeV^2. Assuming that the acceptances for these processes are not radically different (at high jet p_t's) then it could be argued that the discrepancy observed is consistent in magnitude with that calculated due to multijet processes in 8.6. Although ref. 8.6 predicts excesses in the order of ~ 50% for the tagged data in the high jet p_t region, these are not excluded when the large statistical errors present in these regions are taken into account.

8.10 Conclusions

We conclude that

1) The angular acceptance of CELLO reduces the resolution available for studying the jet nature of hadronic photon-photon events.

2) The data can be generally characterised as two-jet in nature.

3) Although jet variables such as thrust and jet p_t are well described by GVDM + QPM in the tagged data, discrepancies are observed in the low Q^2 data. A clear excess of events is observed at high jet p_t's.

4) The excess at high jet p_t's can be represented by the inclusion of a phasespace component or rescaling the QPM term. (The justification for rescaling QPM being that it may have similar event characteristics to multijet events.)

5) The inclusion of a multijet models (section 5.6) cannot describe the jet p_t distribution.

6) The thrust distribution of the high jet p_t events is best described using a multijet model. The inclusion of a phasespace model causes the mean thrust to be underestimated, whilst rescaling the QPM term causes it to be overestimated.

7) The fit to the W_{VIS} distribution favours using a $1/W^2$ dependent term for the phasespace model.

8) The excesses of events observed at high jet p_t are consistent with calculations for higher order processes (8.6).

Summing up, the data exhibits a two-jet nature well described by GVDM + QPM, except at low Q^2 and high jet p_t where an excess of events is observed. Renormalising the QPM term or the inclusion of a phasespace term with a $1/W^2$ dependence both improve the jet p_t distribution considerably. However the thrust of the high jet p_t events are best described by a multijet model.

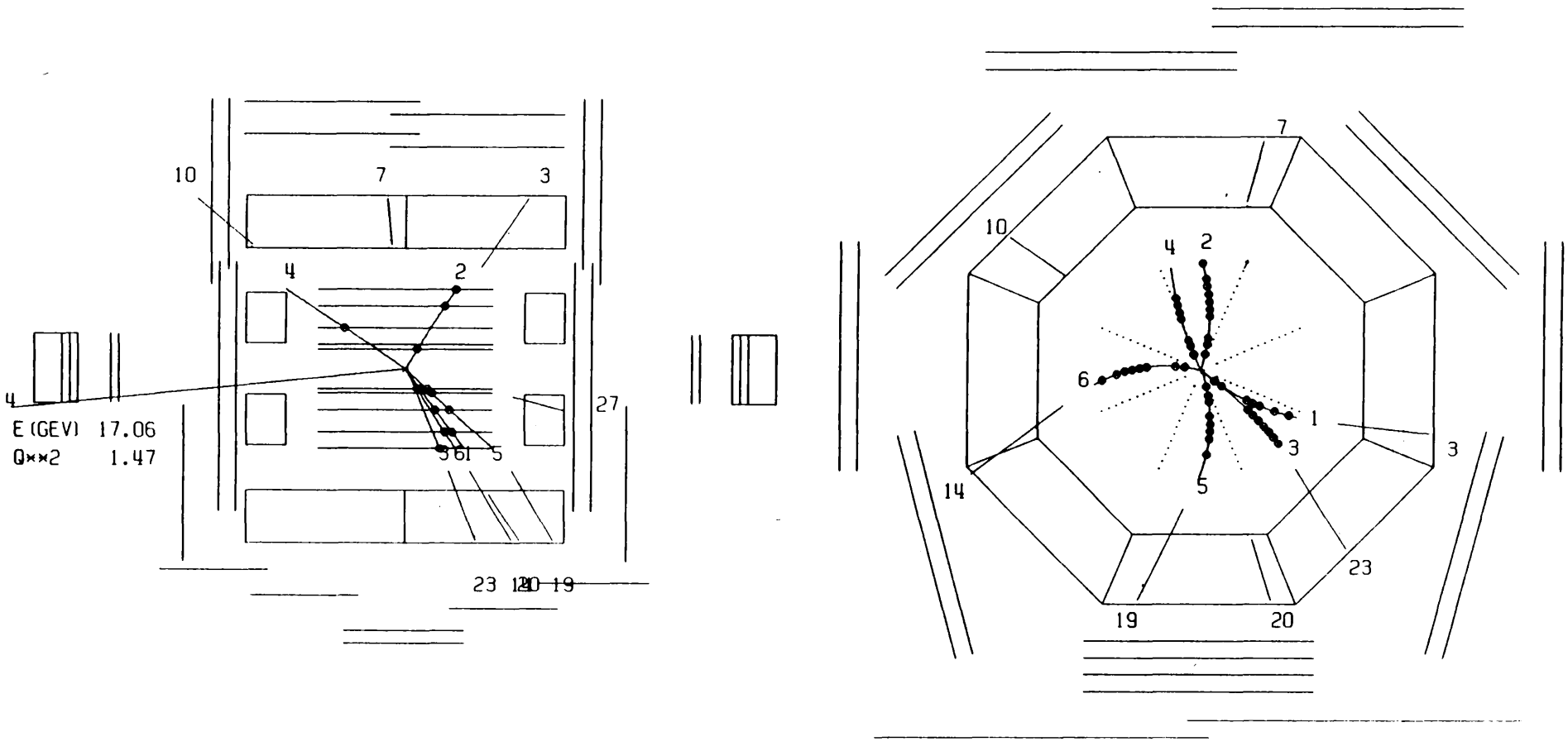

Fig 8.1 A typical two-jet hadronic photon-photon event viewed on the CELLO display program.

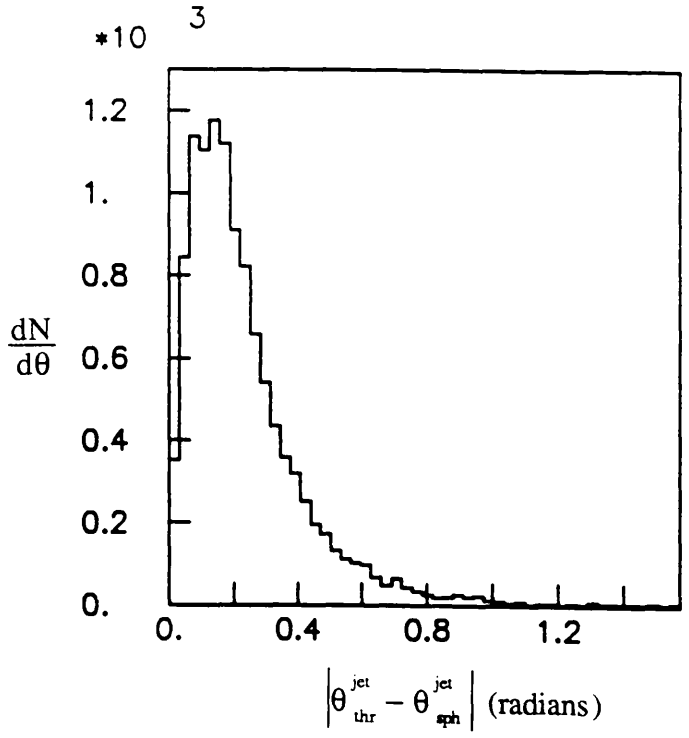

Fig 8.2 The angular difference in the reconstructed jet axis of an event as defined by the thrust or sphericity algorithms, for QPM events.

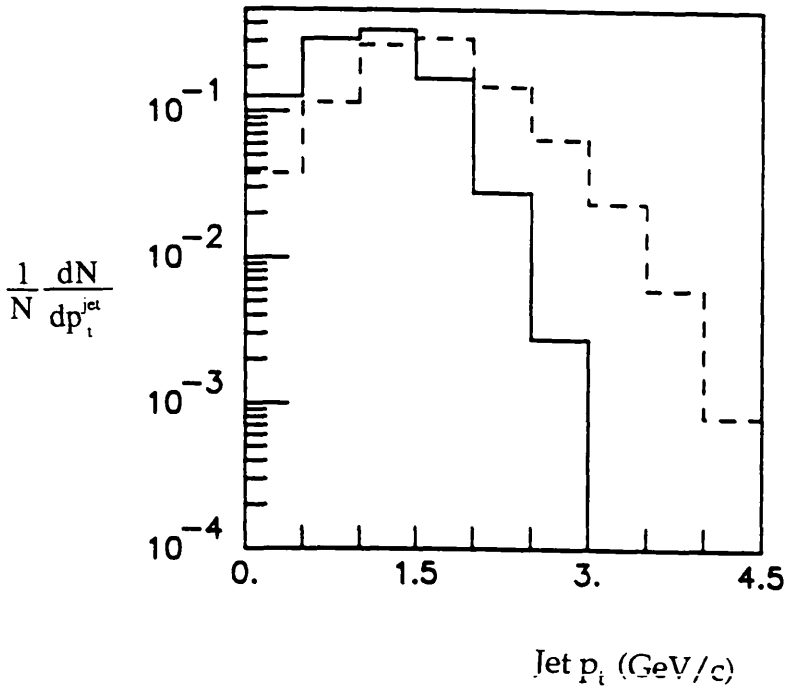

Fig 8.3 The reconstructed jet p_t for the GVDM (solid) and QPM (dashed) components.

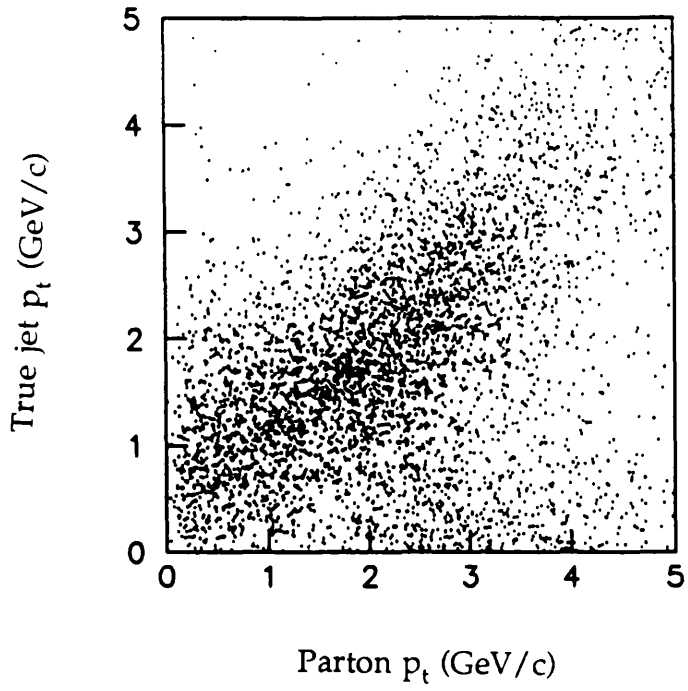

Fig 8.4 A correlation plot of parton p_t vs true jet p_t (ie before detector) for QPM events.

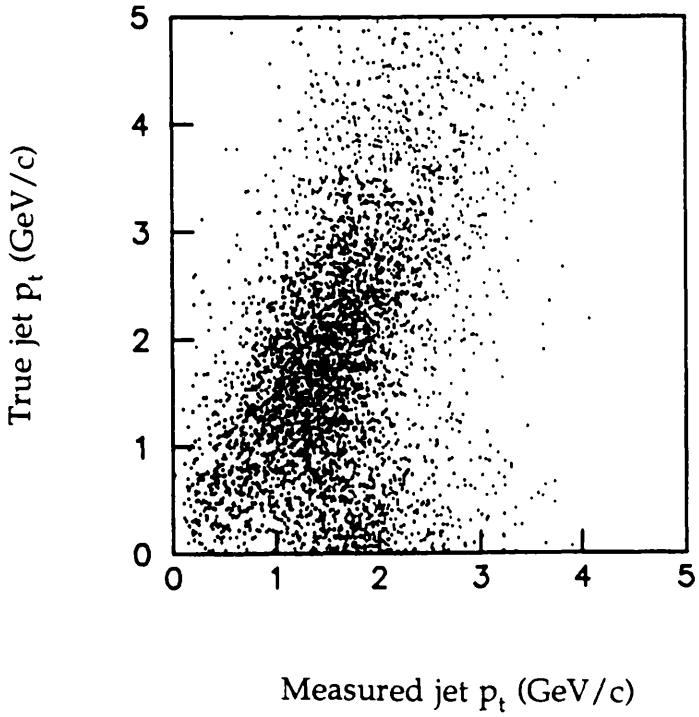

Fig 8.5 A correlation plot for true jet p_t vs jet p_t after detector acceptances have been taken into account for QPM events.

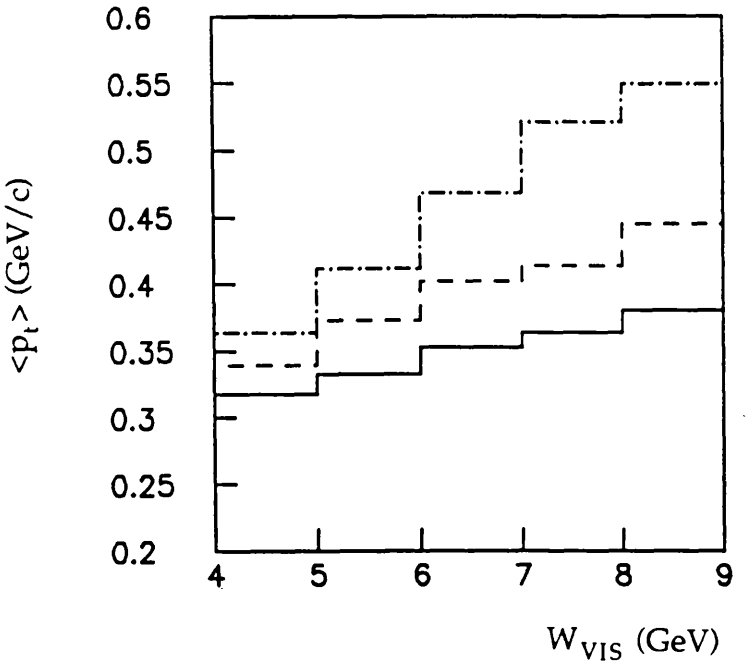

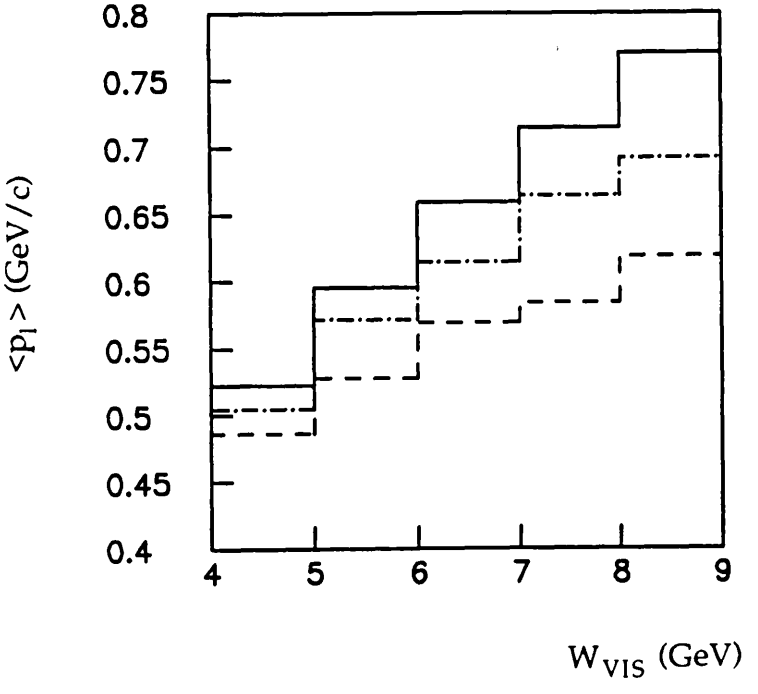

Fig 8.7 The mean transverse momentum of particles in a jet with respect to the jet axis, $<p_t>$ and the mean longitudinal component, $<p_l>$ as a function of the visible hadronic mass, W_{VIS} for the QPM (solid), GVDM (dashed) and phasespace terms (dash-dot).

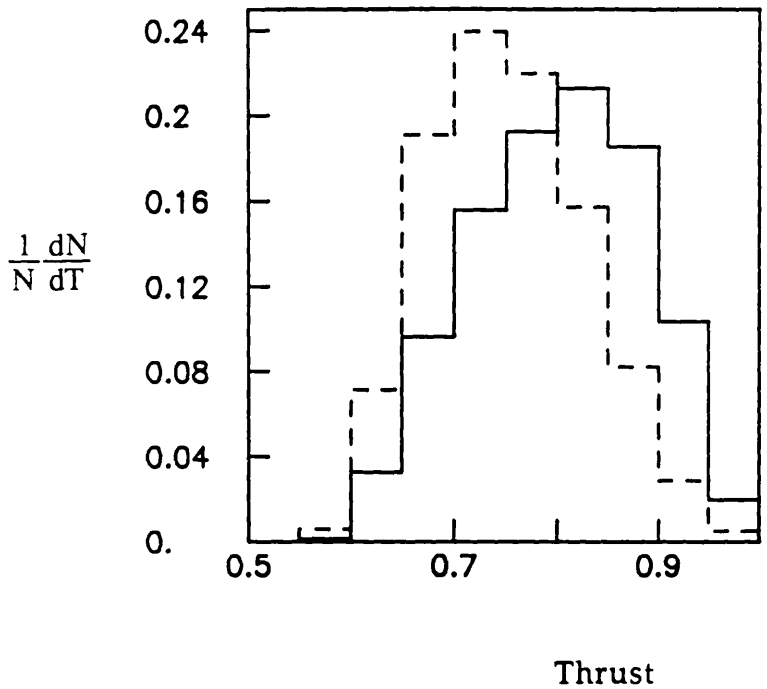

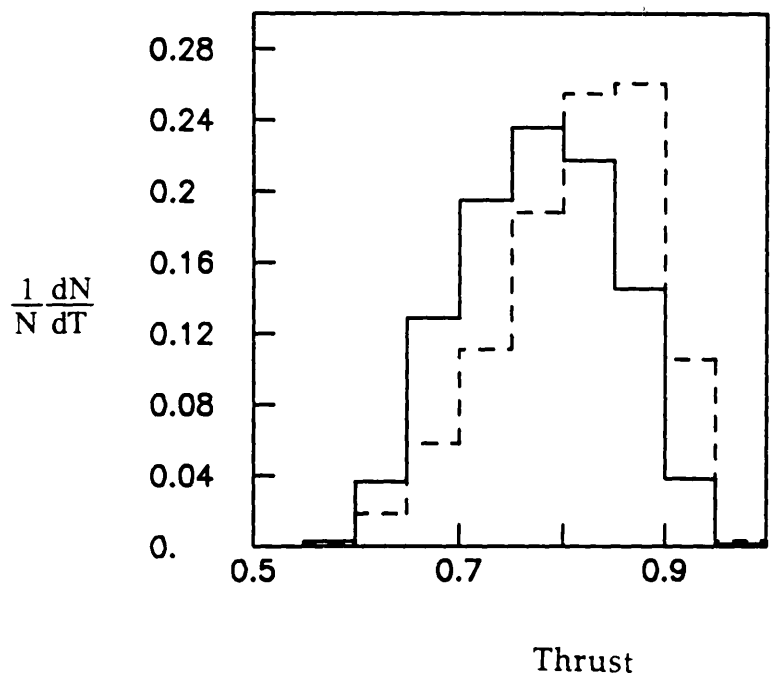

Fig 8.8 The thrust distributions for the QPM (solid) and GVDM (dashed) terms, both before (bottom) and after (top) detector acceptances have been taken into account.

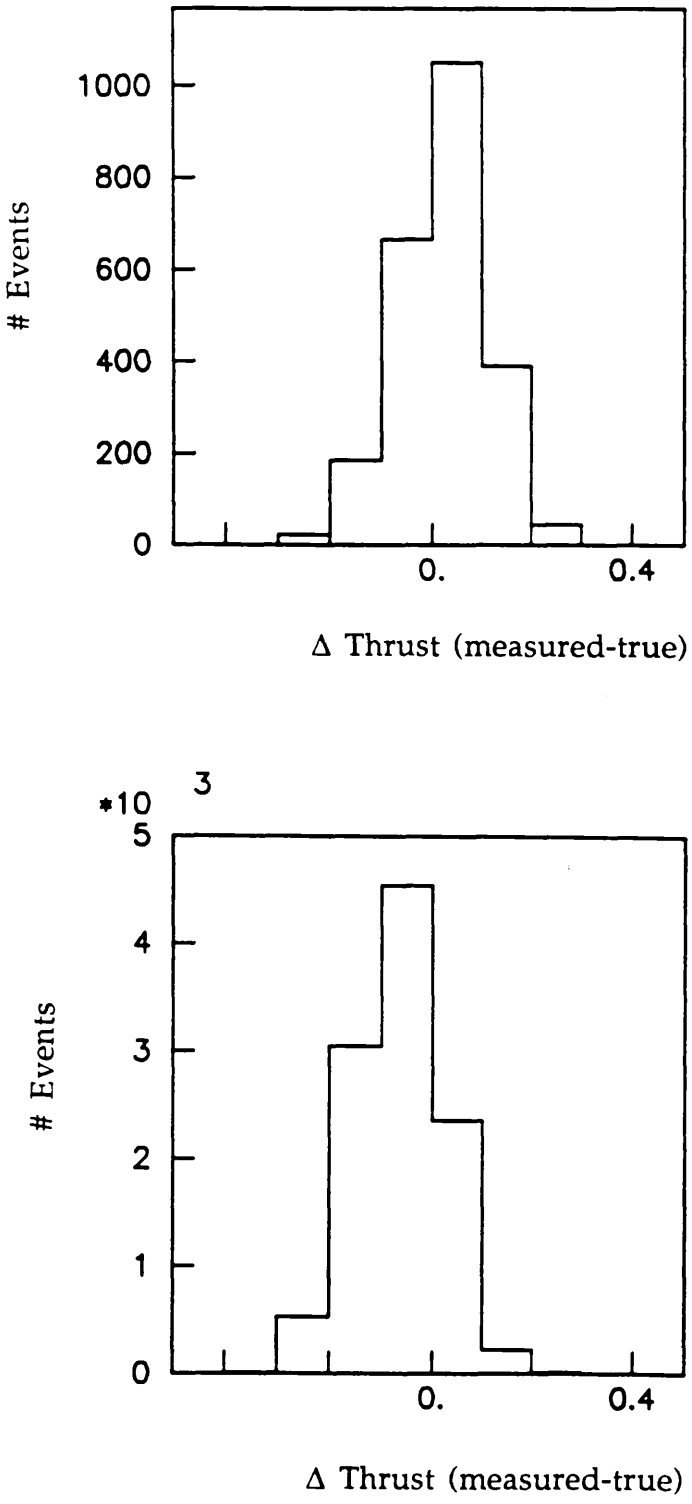

Fig 8.9 The difference in measured thrust for the QPM (top) and GVDM (bottom) terms before and after detector acceptance has been taken into account.

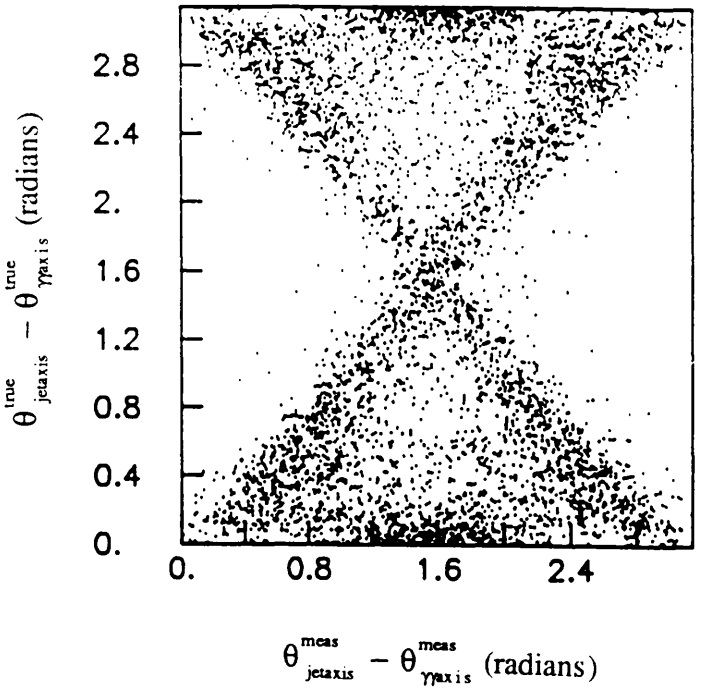

Fig 8.6 A correlation plot for the angle between the reconstructed jet axis and the $\gamma\gamma$ axis (in CMS) before and after detector acceptance has been taken into account for QPM events.

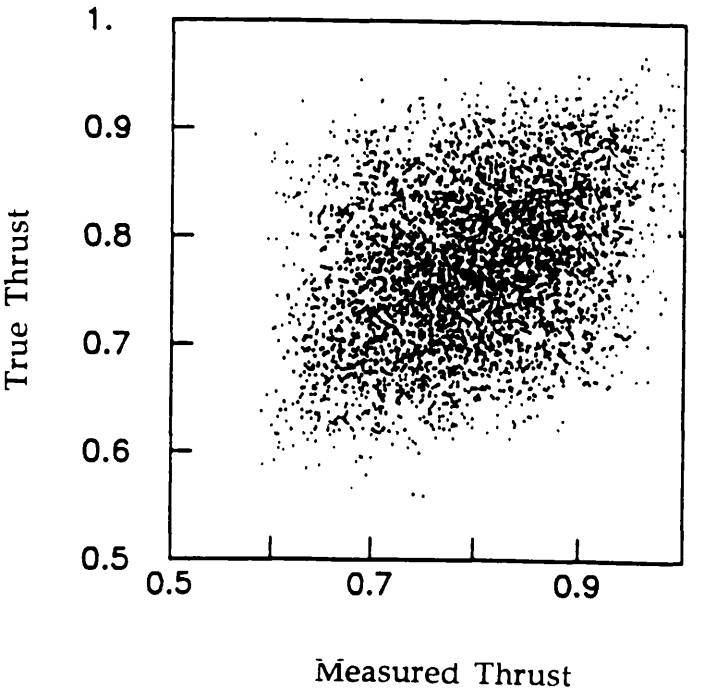

Fig 8.10 A correlation plot for the measured thrust of QPM events before and after detector acceptance has been taken into account.

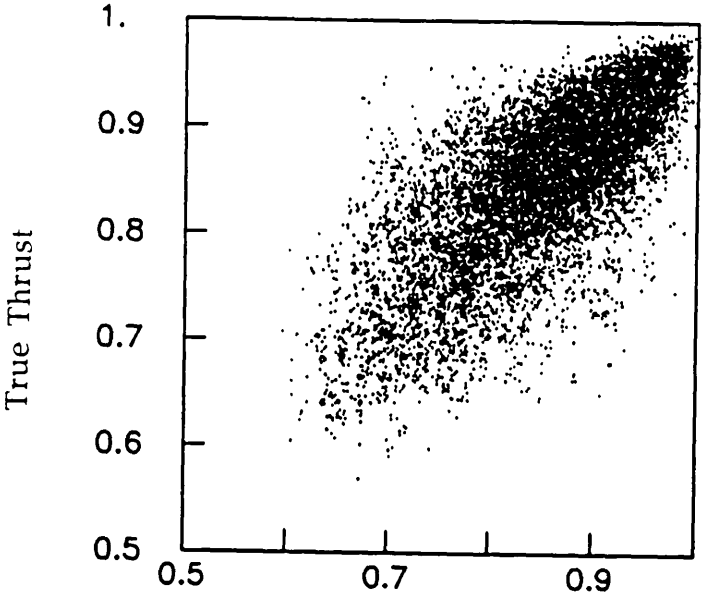

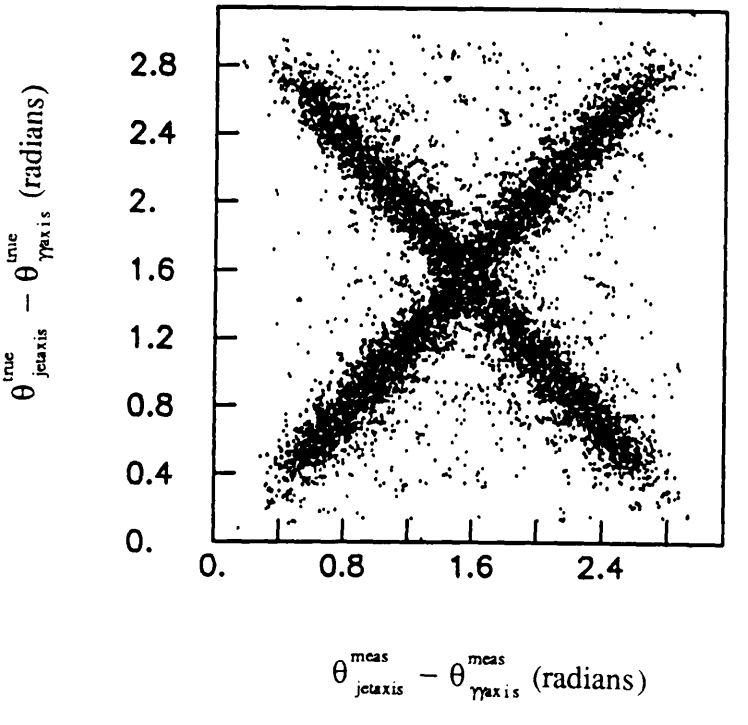

Fig 8.11 Correlation plots of reconstructed thrust and jet axis angle before and after detector acceptance effects have been taken into account for annihilation MC events.

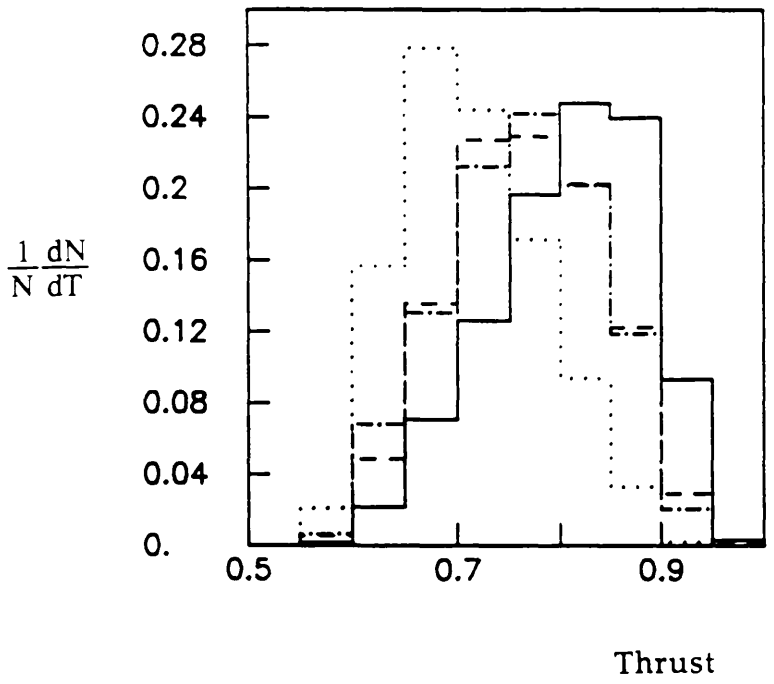

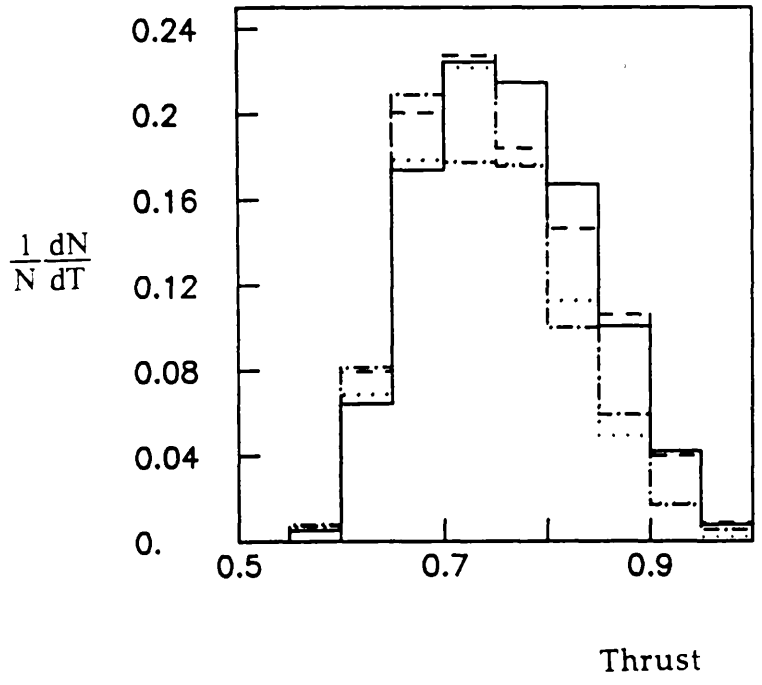

Fig 8.12 The thrust of 2-jet (solid), 3-jet (dashed), 4-jet (dash-dot) and phasespace models (dotted) before (top) and after (bottom) detector acceptance has been taken into account.

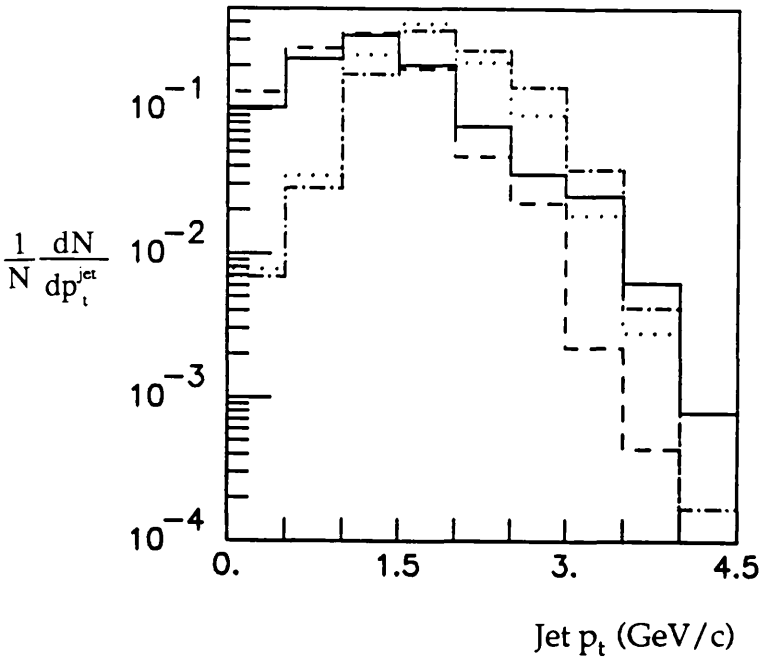

Fig 8.13 The reconstructed jet p_t for 3-jet (solid), 4-jet (dashed) and phasespace (flat in W, dash-dot and $1/W^2$, dotted) models after detector acceptance has been taken into account.

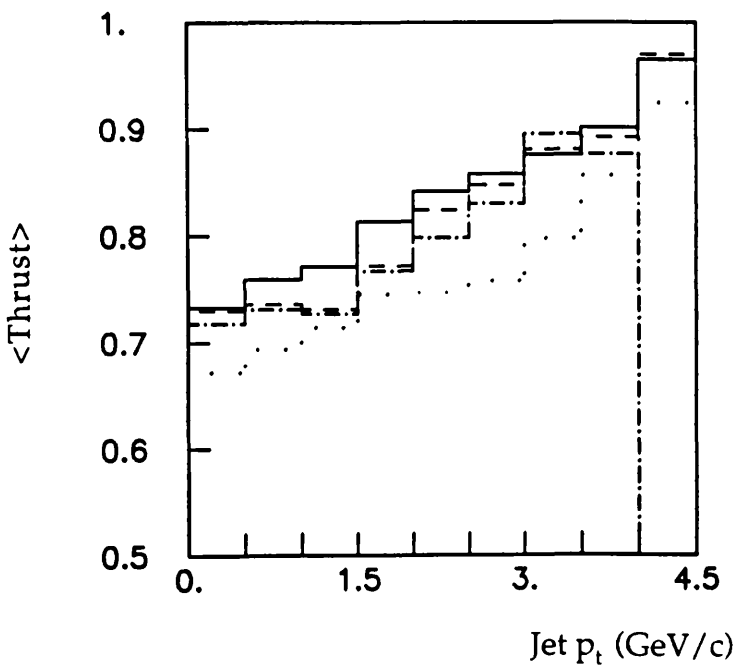

Fig 8.14 The mean thrust (after detector) as a function of jet p_t is shown for the two-jet model (solid), 3-jet (dashed), 4-jet (dash-dot) and phasespace (dotted).

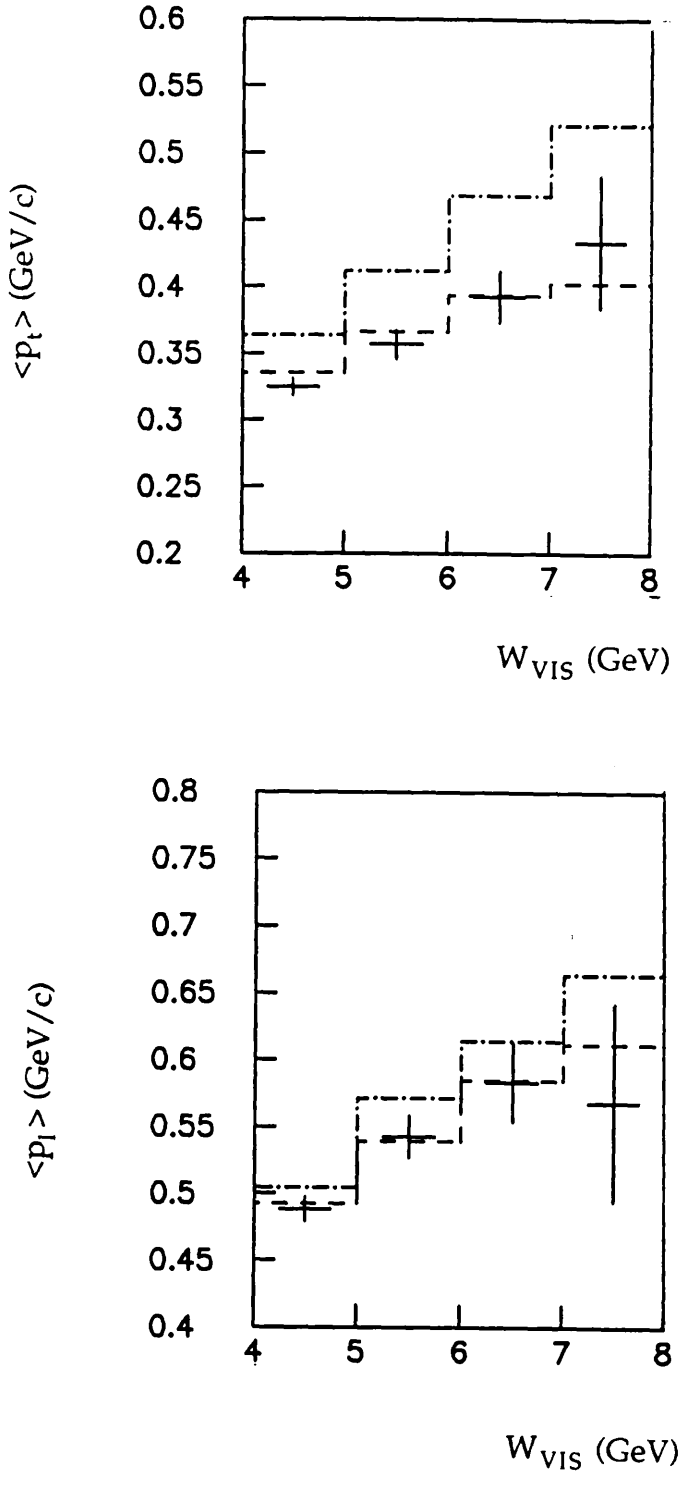

Fig 8.15 The mean transverse momentum component of all particles in a jet with respect to the jet axis, $\langle p_t \rangle$ and the mean longitudinal component, $\langle p_l \rangle$ as a function of the visible hadronic mass W_{VIS} are plotted for the untagged data and compared against the GVDM + QPM term (dashed) and phasespace (dash-dot).

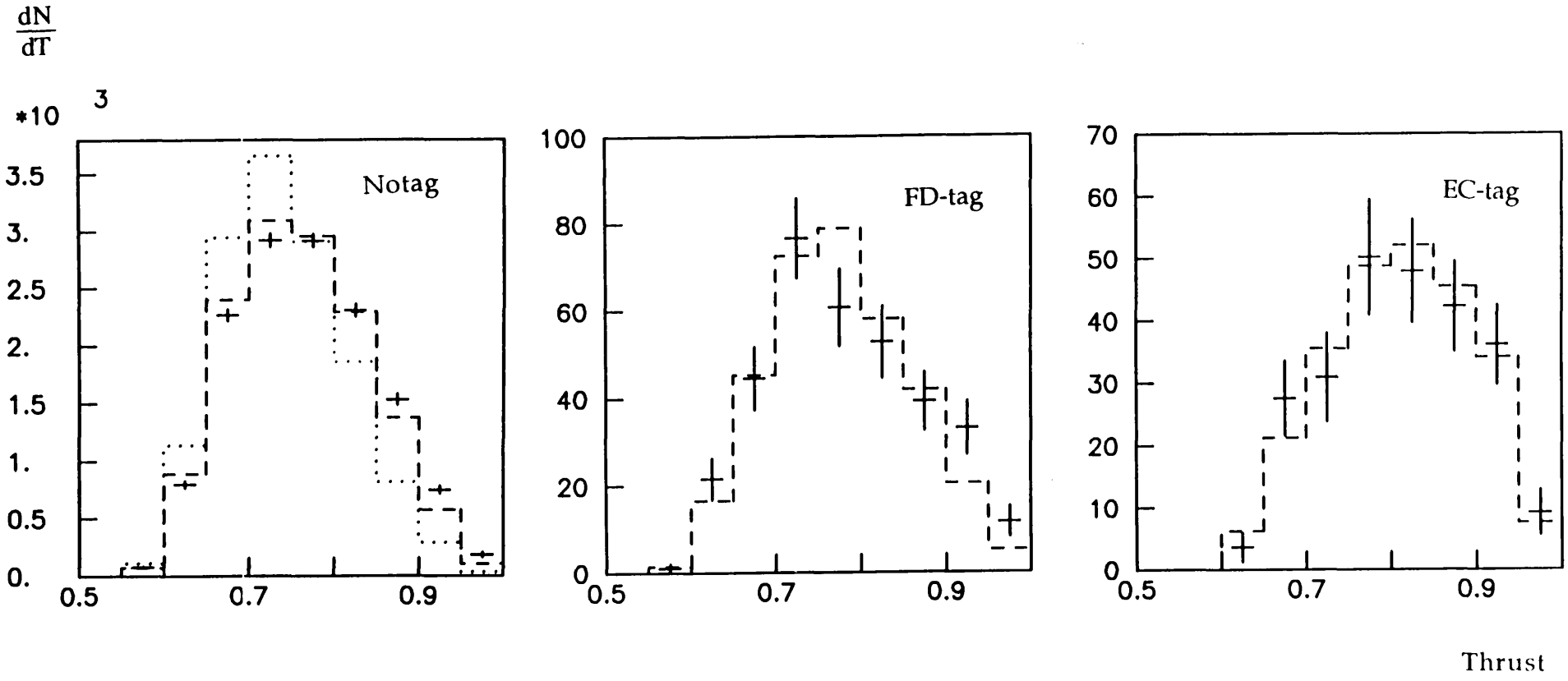

Fig 8.16 The thrust distributions for the three Q^2 regions are compared with GVDM + QPM (dashed) and also the phasespace model (untagged data only, dotted).

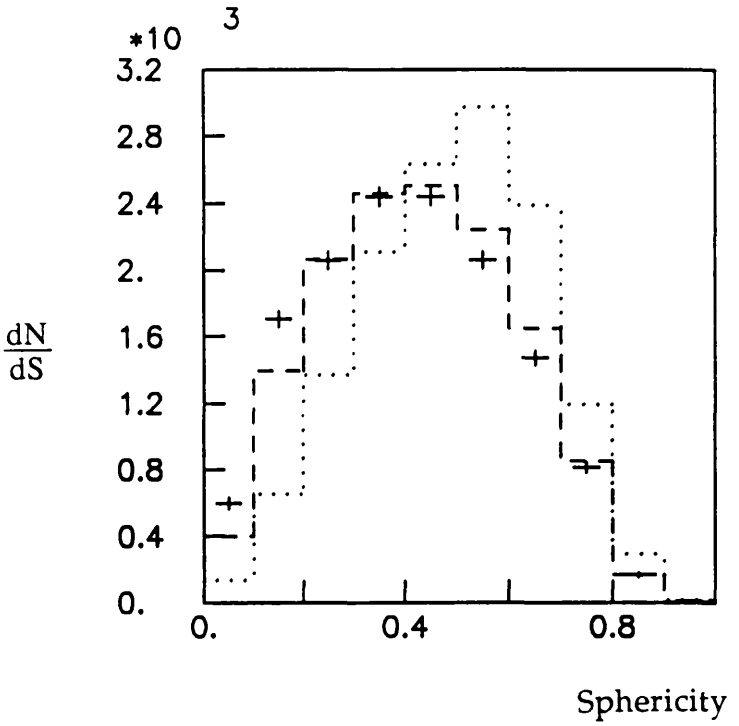

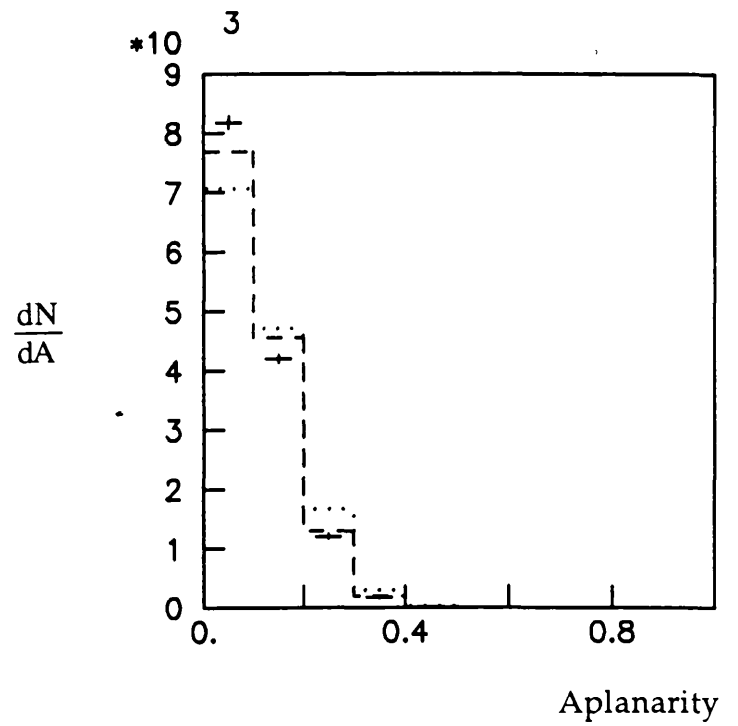

Fig 8.17a The untagged data distributions for sphericity and aplanarity are compared with GVDM + QPM (dashed) and phasespace (dotted).

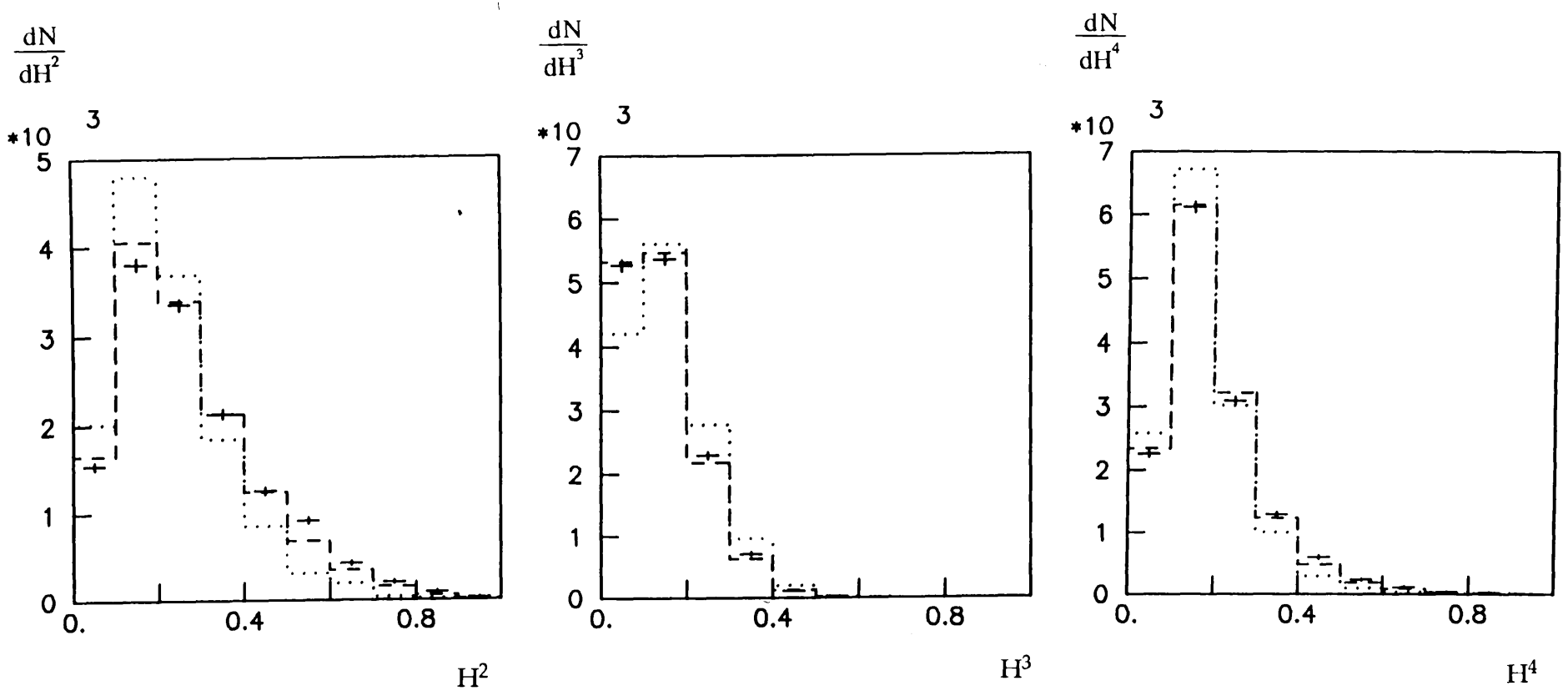

Fig 8.17b The untagged data distributions for the Fox-Wolfram moments are compared with GVDM + QPM (dashed) and phasespace (dotted).

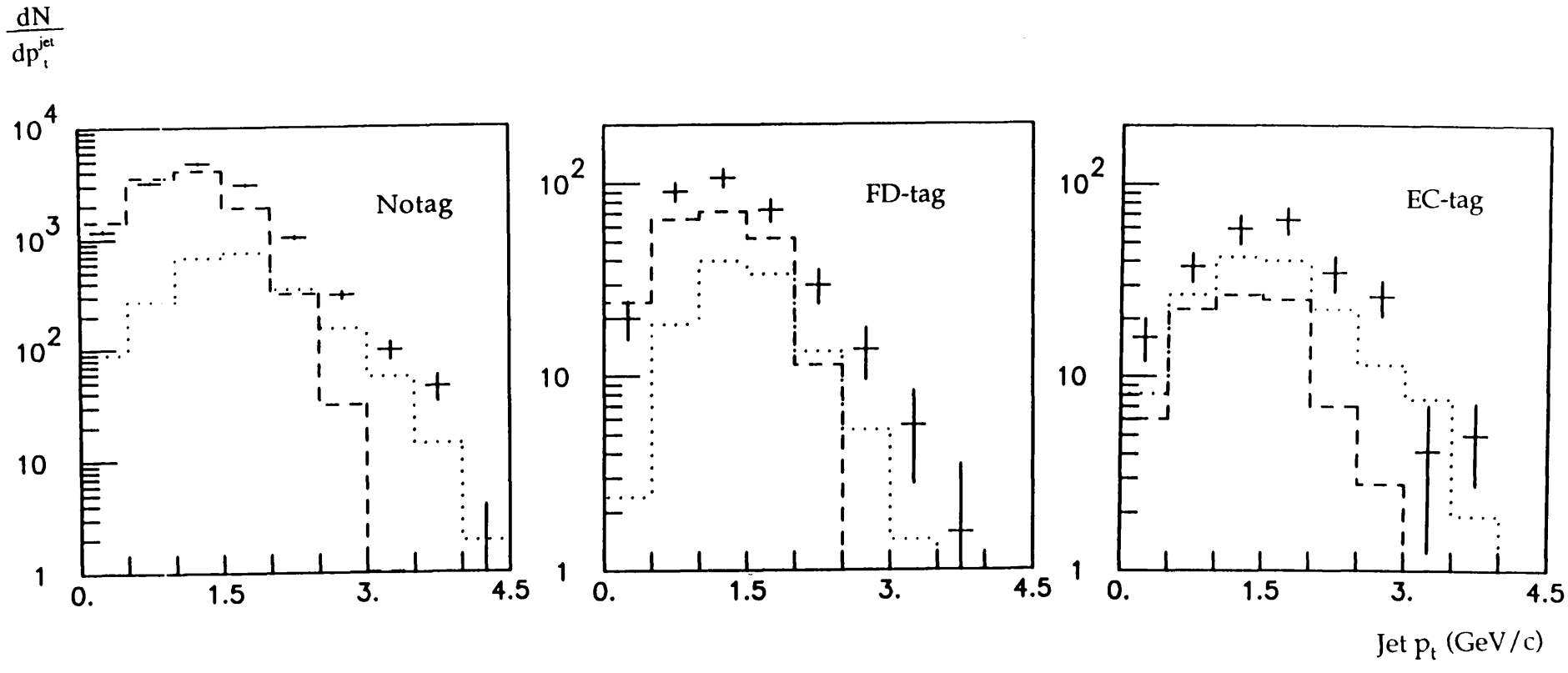

Fig 8.18 The jet p_t for each Q^2 region is compared to the GVDM (dashed) and QPM (dotted) terms separately.

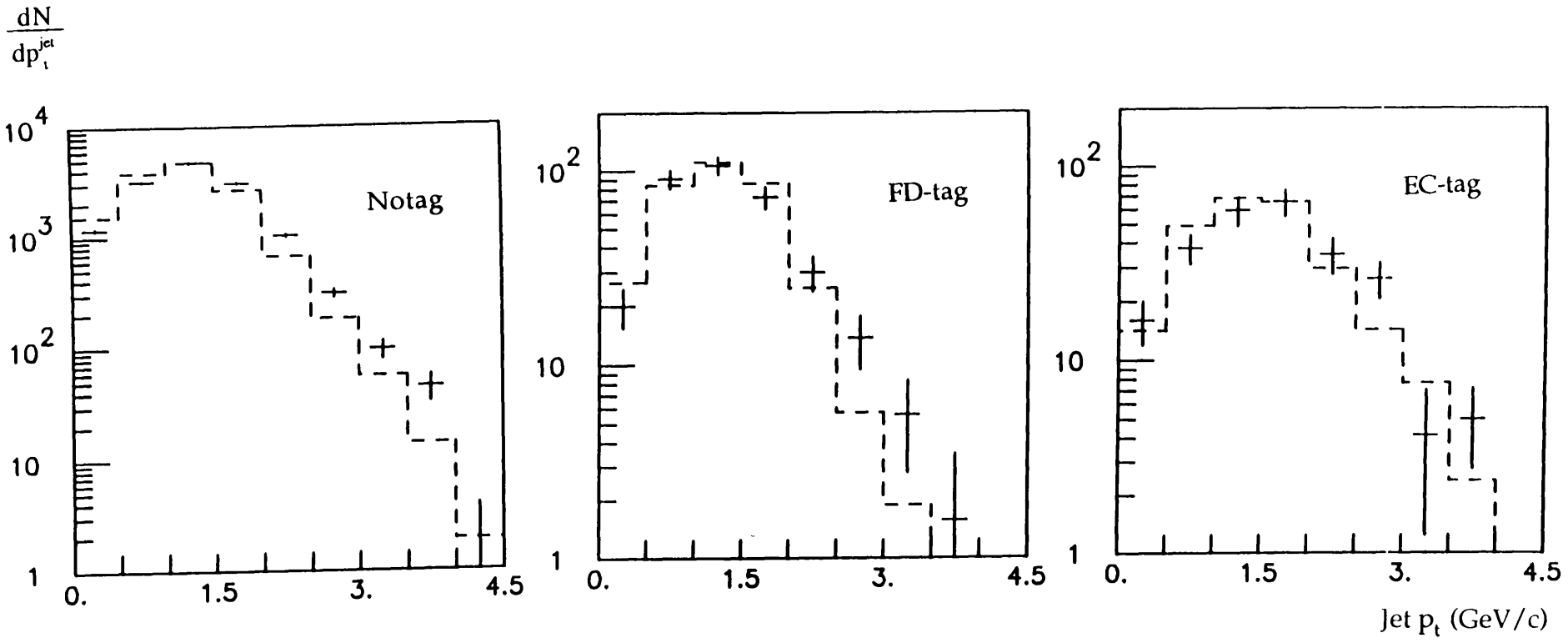

Fig 8.19 The jet p_t for each Q^2 region is compared to the GVDM + QPM term.

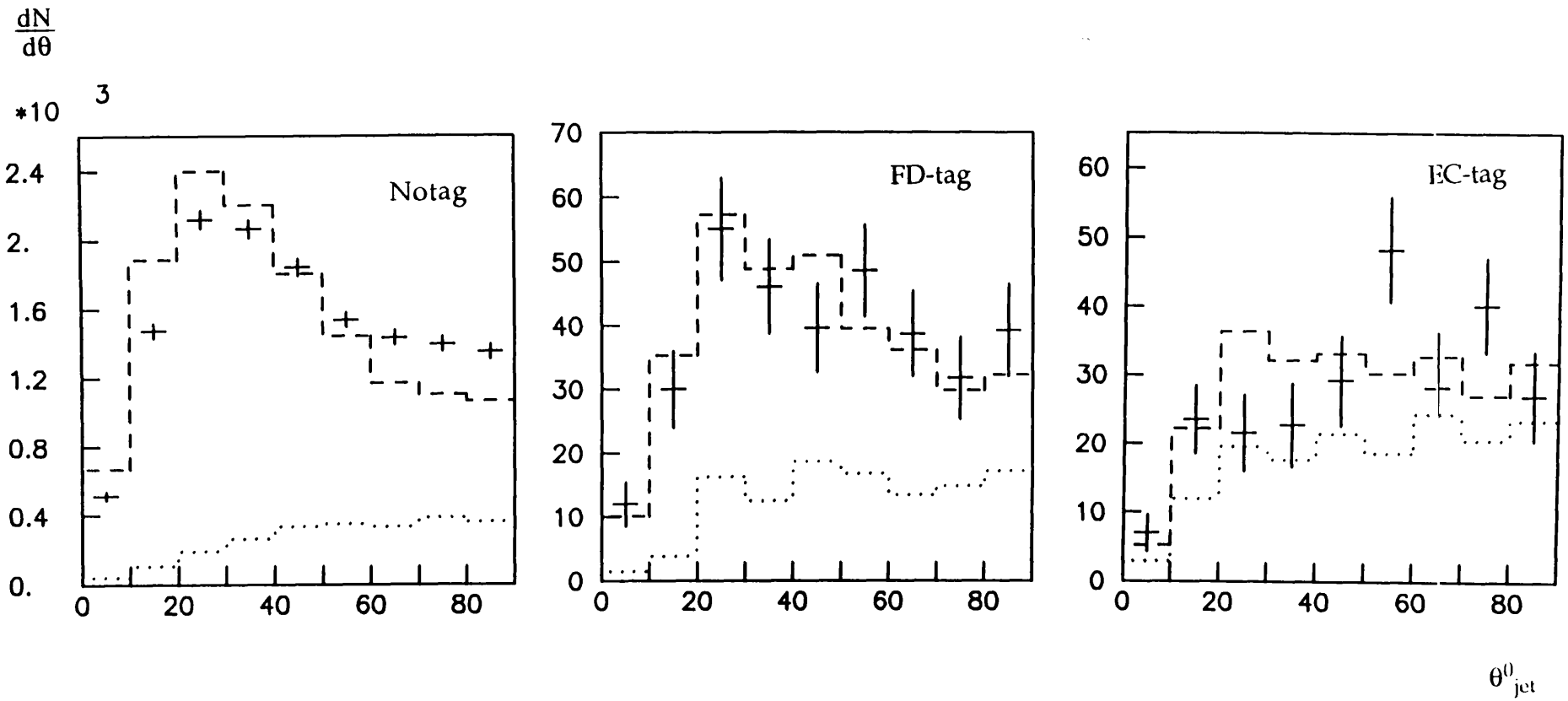

Fig 8.20 The angle between the reconstructed jet axis and the $\gamma\gamma$ axis (in the CMS) for each Q^2 region is compared with the GVDM + QPM term (solid) as well as the QPM term alone (dotted).

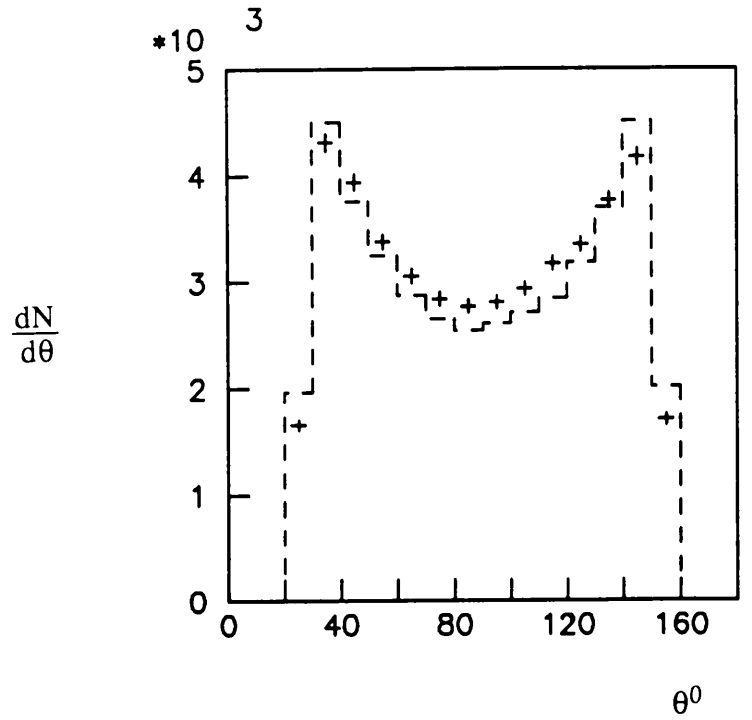

Fig 8.21 The angular distribution of charged tracks in the untagged data sample after tighter cuts were applied.

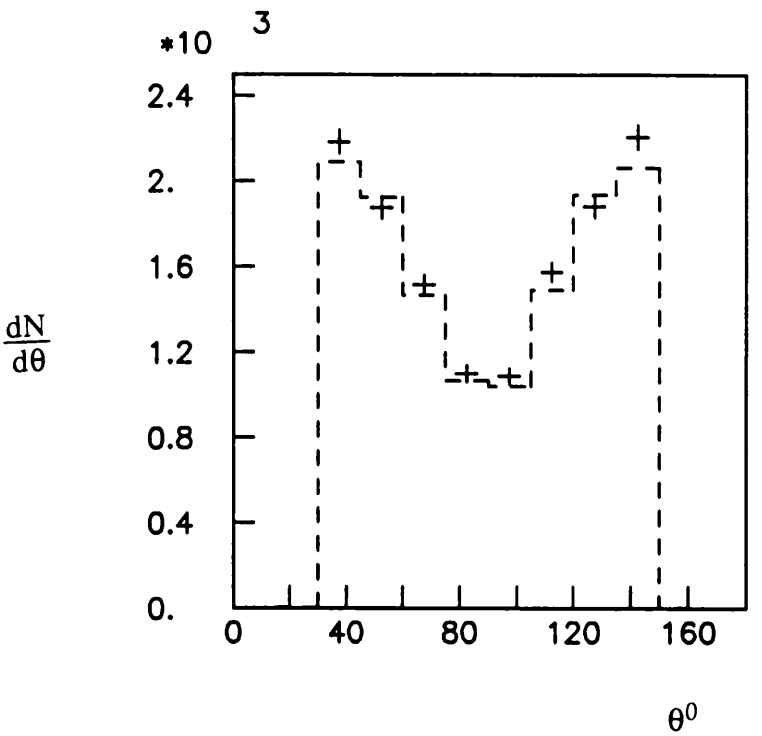

Fig 8.22 The angular distribution of neutral particles in the untagged data sample after tighter cuts were applied.

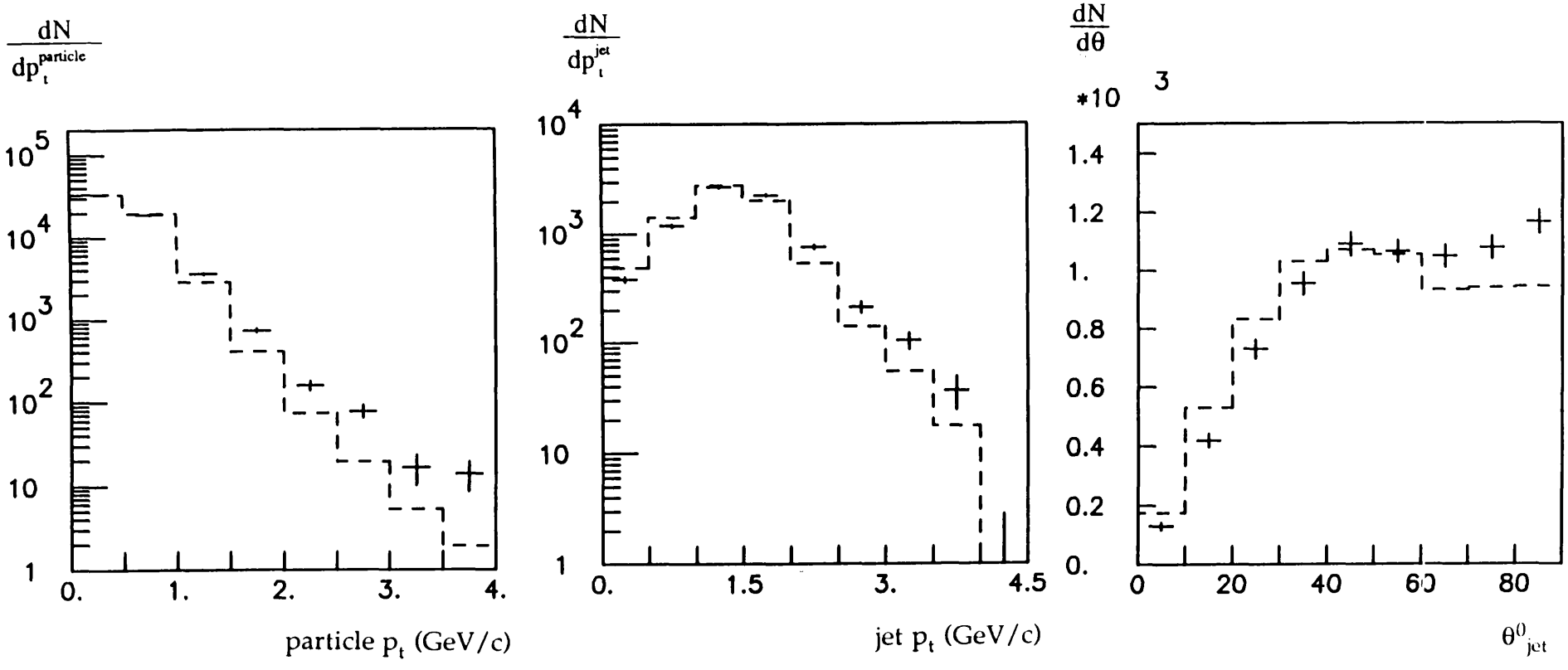

Fig 8.23 The particle p_t, jet p_t and jet angle distributions shown after tighter cuts were applied to the untagged data.

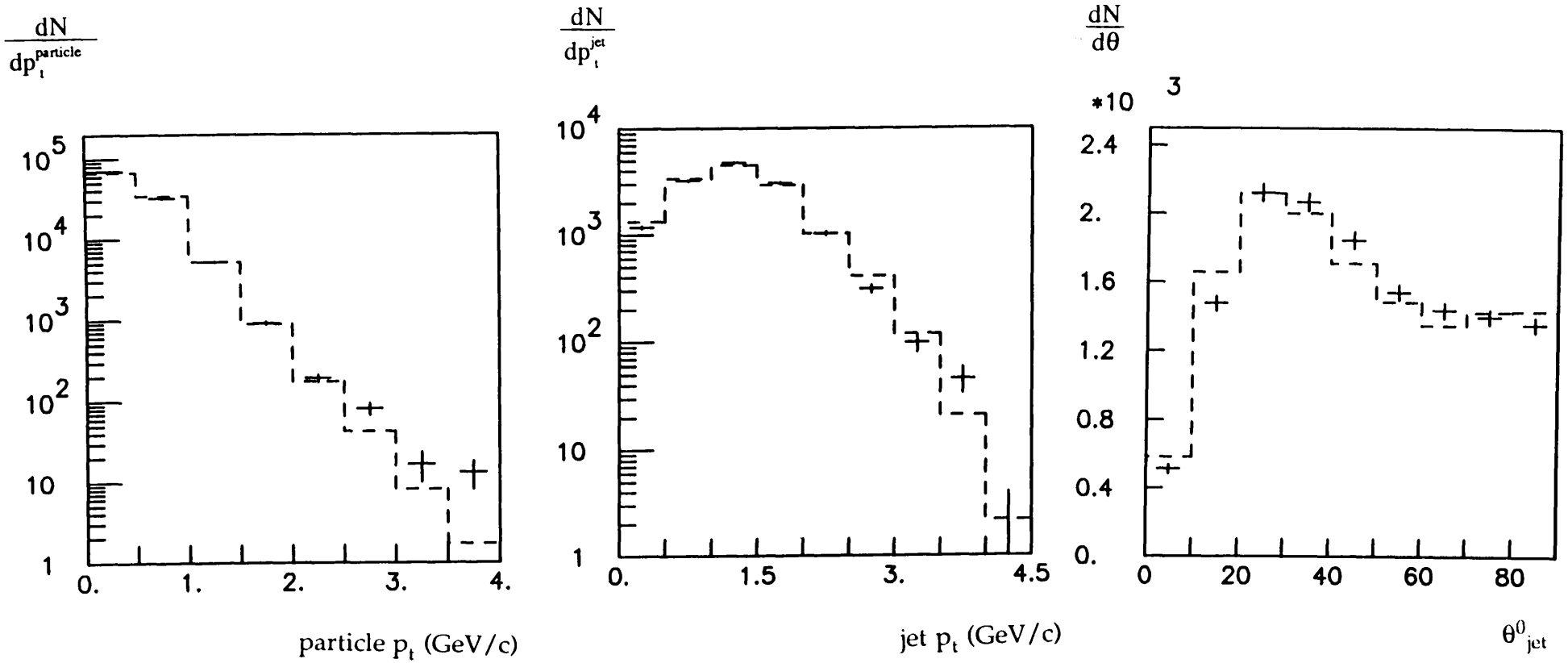

Fig 8.24 The particle p_t, jet p_t and jet angle distributions shown compared with the GVDM + QPM + phasespace ansatz.

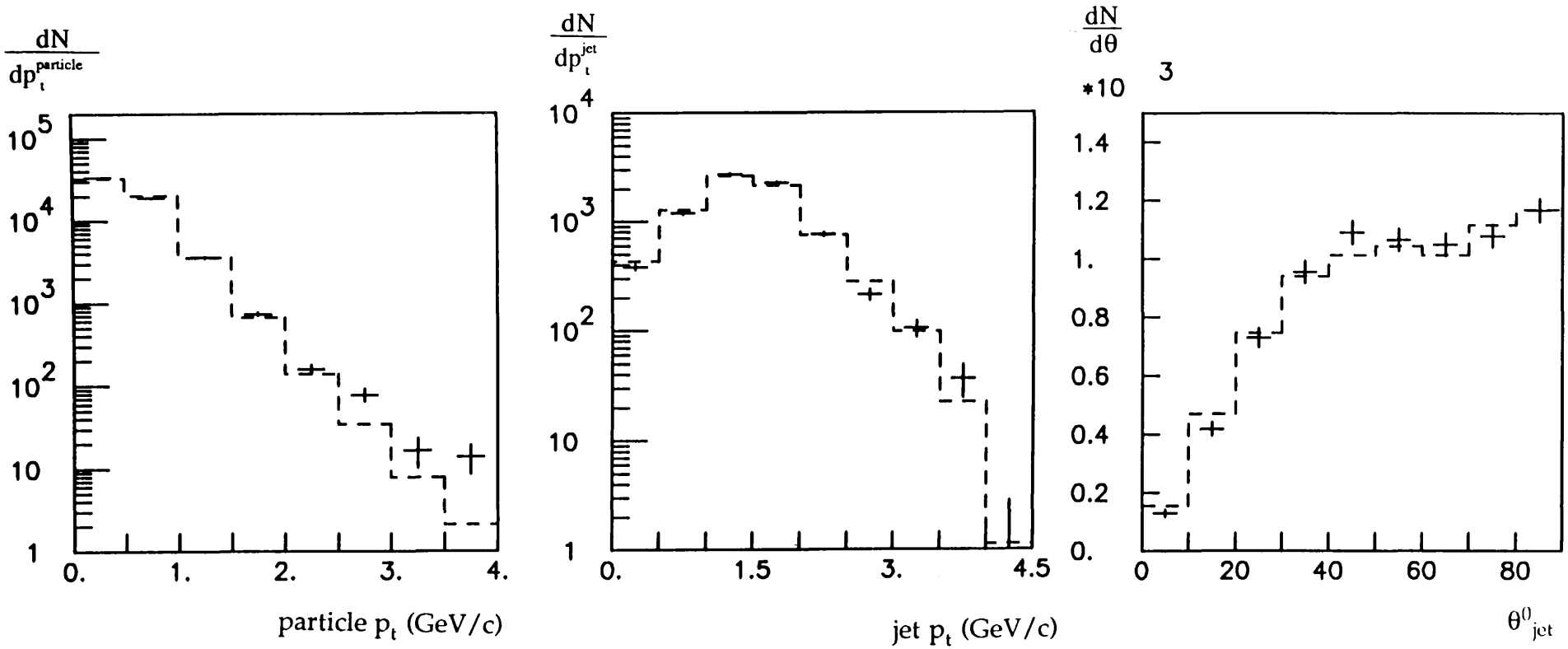

Fig 8.25 The particle p_t, jet p_t and jet angle distributions shown compared with the GVDM + QPM + phasespace ansatz with the tighter acceptance cuts.

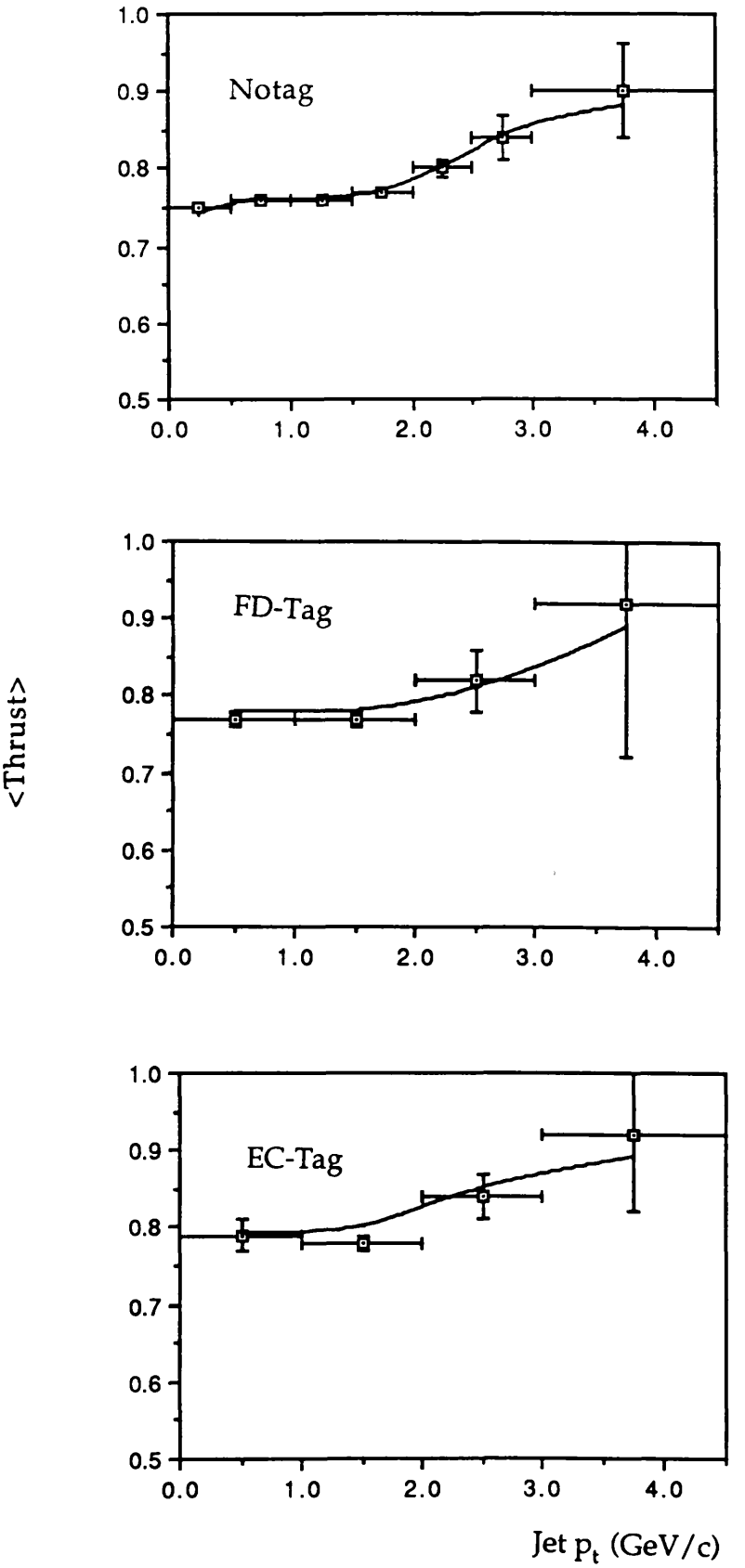

Fig 8.26 The mean thrust of events as a function of jet p_t compared with the GVDM + QPM ansatz in the three tagging regions. A line is drawn through the MC points to guide the eye.

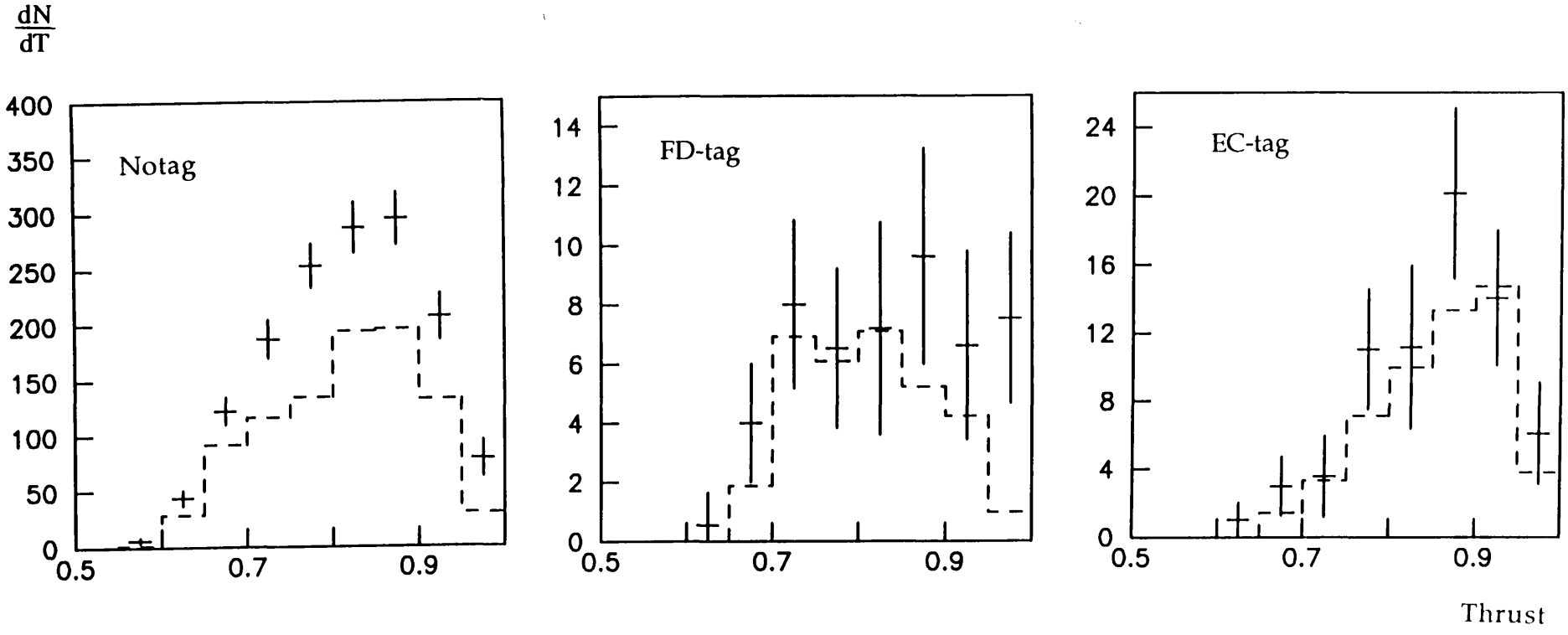

Fig 8.27 The thrust distribution of all events with jet $p_t \geq 2$ GeV/c compared with the GVDM + QPM ansatz in the three tagging regions.

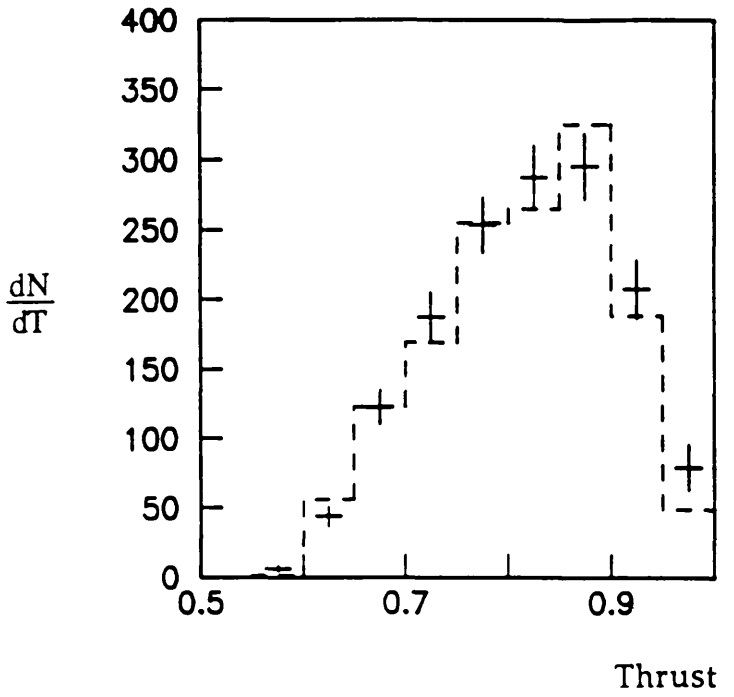

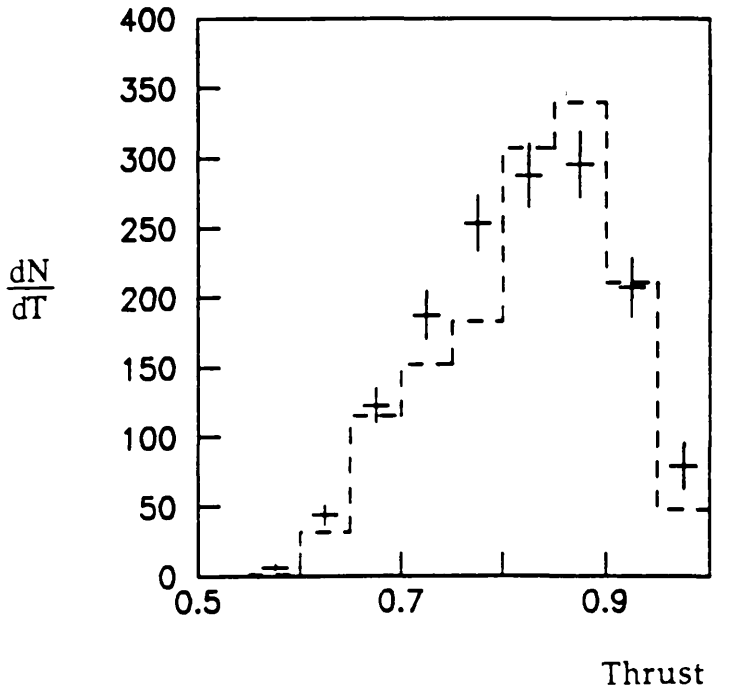

Fig 8.29 The thrust distribution of all events with jet $p_t \geq 2$ GeV/c in the untagged data compared with the QPM + GVDM plus an additional multijet term, 4-jet (top), 3-jet (bottom).

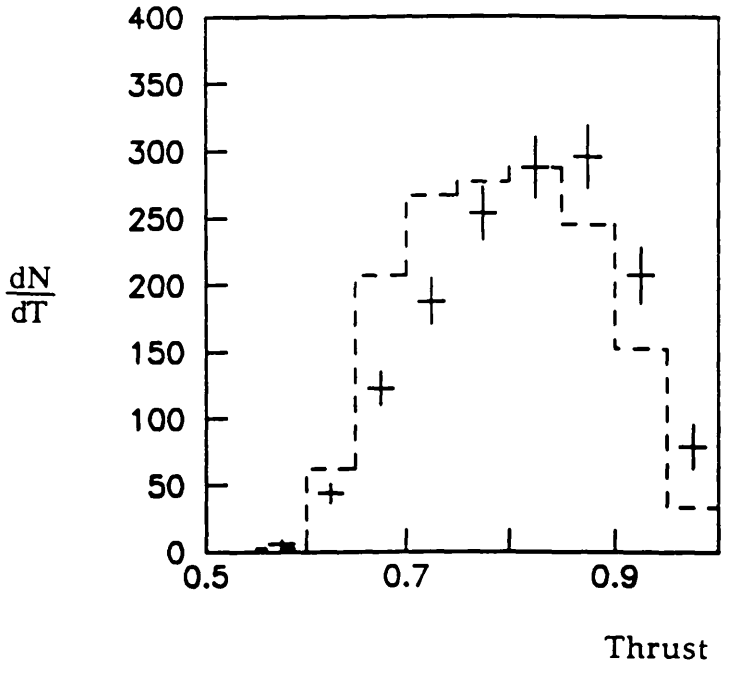

Fig 8.28 The thrust distribution of all events with jet $p_t \geq 2$ GeV/c in the untagged data compared with the GVDM + QPM + phasespace ansatz.

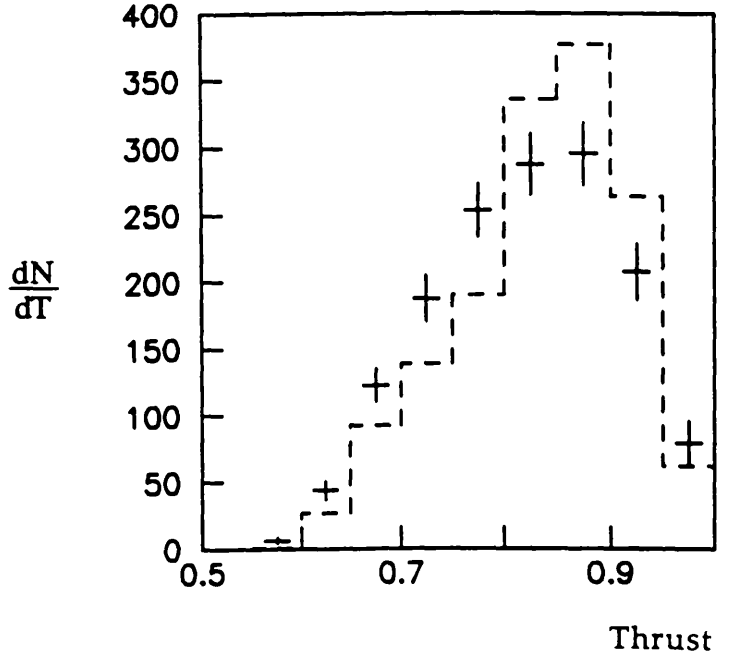

Fig 8.30 The thrust distribution of all events with jet $p_t \geq 2$ GeV/c in the untagged data compared with the GVDM + a renormalised quantity of QPM.

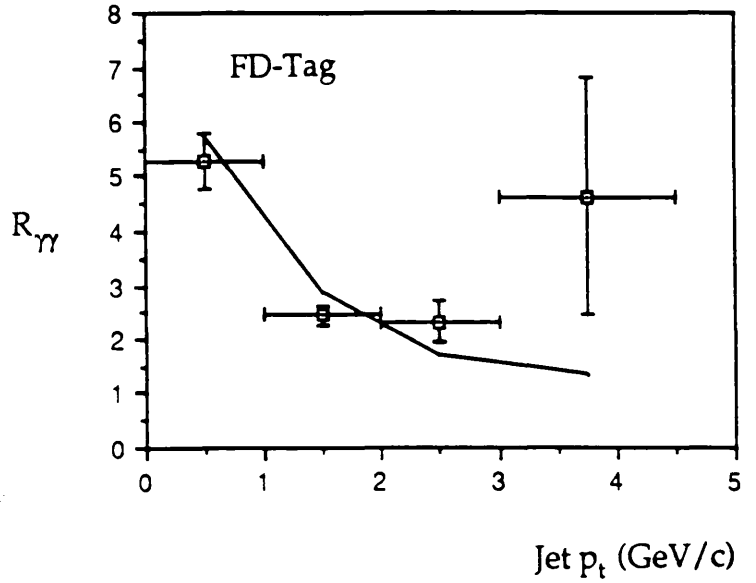

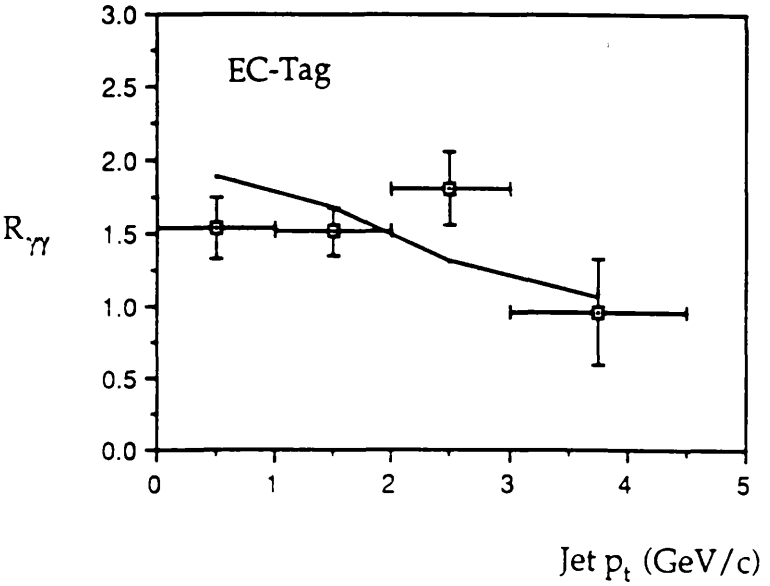

Fig 8.31 The $R_{\gamma\gamma}$ distribution of the forward and endcap tagged data is compared with GVDM + QPM. The MC points have been joined to help guide the eye.

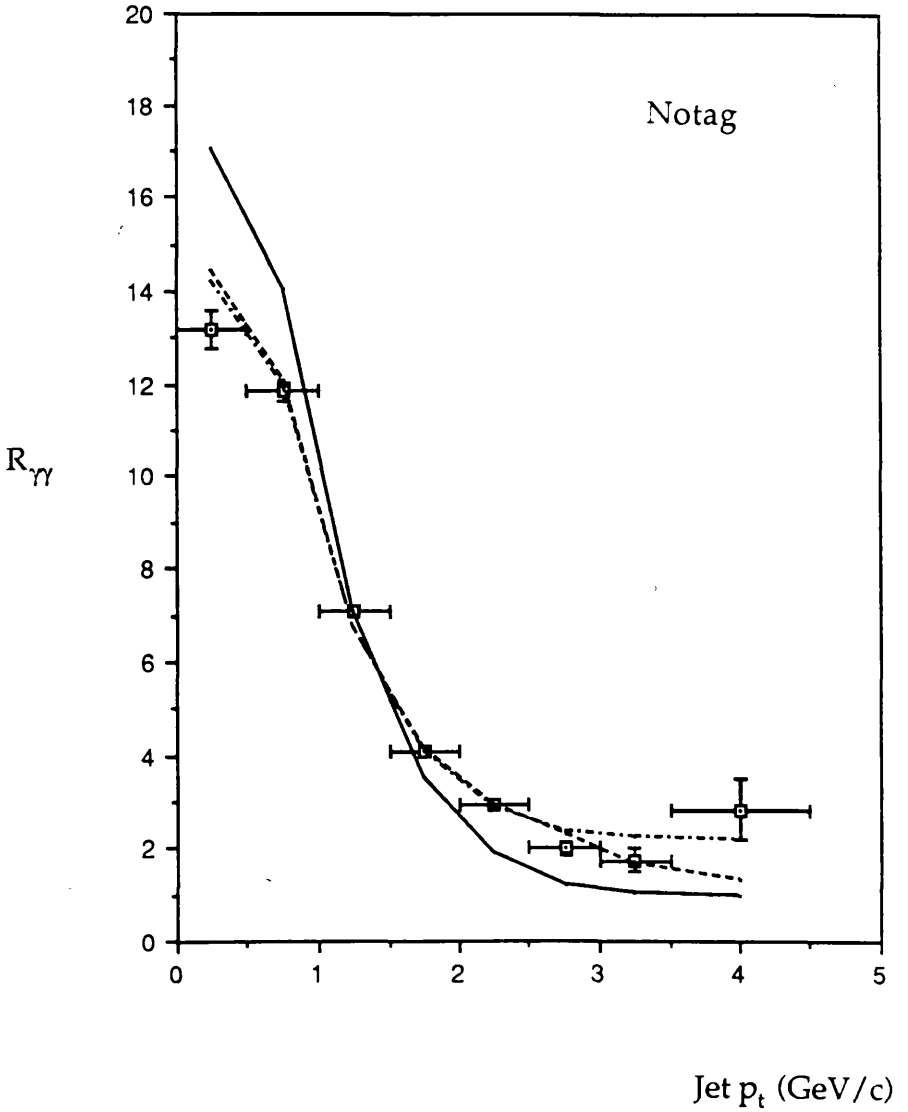

Fig 8.32 The $R_{\gamma\gamma}$ distribution of the untagged data is compared with GVDM + QPM (solid), GVDM+ QPM + phasespace ($1/W^2$, dashed) and GVDM + renormalised QPM terms (dot-dash). The MC points have been joined to help guide the eye.

Chapter 9

Summary and Conclusions

The principal aims of this thesis have been twofold. The first was to examine the general characteristics (ie W, Q^2) of the hadronic photon-photon data, and compare the data with a model consisting of a soft hadronic component plus a pointlike $\gamma\gamma \rightarrow qq$ component. The second aim was to study the excess of high p_t events at low Q^2 first observed by PLUTO (9.1), and examine their event topology.

The data used in this analysis were recorded during 1986 on the CELLO detector, which was sited on the PETRA e^+e^- accelerator at DESY, Hamburg. During this time PETRA ran with a beam energy of 17.5 GeV and the total integrated luminosity of data collected was $86pb^{-1}$.

The data studied was split into three Q^2 (where the Q^2 is the invariant mass of the virtual photon) regions in the range $0 < Q^2 < 30$ GeV^2 consisting of untagged events (with two undetected scattered beam leptons assumed to have been contained in the beam-pipe producing two nearly real photons) and single tagged events (where one beam lepton remains undetected producing a nearly real photon and one detected scattered beam lepton producing a highly virtual photon). Two tagging regions were used. Forward tags were detected in lead-glass scintillators close to the beam axis ($55 < \theta < 80$ mr) and endcap tags were detected in the lead-liquid argon endcaps ($150 < \theta < 360$ mr). The events were required to have ≥ 4 charged tracks and were constrained to the hadronic mass W_{VIS} region $4 \leq W_{VIS} \leq 9$ GeV. These selections produced three data samples, 15610 untagged events with $\langle Q^2 \rangle \sim 0.1$ GeV^2, 371 forward tagged events with $\langle Q^2 \rangle \sim 1.0$ GeV^2 and 302 endcap tagged events with $\langle Q^2 \rangle \sim 12.7$ GeV^2.

The data was first compared with an incoherent sum of a soft hadronic component, $\gamma\gamma \rightarrow \rho\rho$ and a pointlike component, $\gamma\gamma \rightarrow qq$.

The soft hadronic component was modelled using a vector meson dominance model. This was characterised by a limited p_t of the interacting mesons, with respect to the collision axis:

$$\frac{d\sigma}{dp_T^2} \approx e^{-5p_T^2}$$

The cross-section was assumed to be factorisable into W, Q^2 components for the VDM models , or a parameterised fit in the case of the GLM model. The cross-section for the process is large, being ~ 240nb independent of W, falling strongly with Q^2. The colliding mesons were fragmented into jets of hadrons (with specially fitted fragmentation parameters).

The pointlike hard scattering interaction, $\gamma\gamma \rightarrow qq$, was modelled using the quark parton model (QPM). This produces high p_t jets with:

$$\frac{dN}{dp_t^2} \propto \frac{1}{p_t^4}$$

This process has a smaller cross-section than VDM, ~ 10% at low Q^2, but a much flatter Q^2 dependence causing it to dominate at high Q^2. It also falls strongly as ~ $1/W^2$. The quark-antiquark pairs were fragmented into jets of hadrons using standard fragmentation packages.

At this stage of the analysis, the data was found to be best described by an incoherent sum of QPM + GVDM (using a flat W-independent cross-section of 252nb at $Q^2 = 0$ in the GVDM term). An incoherent sum of QPM + GLM also provided a good description of the data. A discrepancy in the inclusive particle p_t distribution at low Q^2 was observed. This has been observed in previous experiments (9.2).

A jet analysis of the data was then undertaken. A thrust analysis in the final state centre of mass provided a jet axis and a jet p_t for the event. The overall data was two-jet in nature. The tagged data was observed to be well described in thrust and jet p_t by the two-jet GVDM + QPM ansatz. However an excess in the number of medium and high jet p_t events was observed in the low Q^2 data. This has been observed by other experiments (9.1). Whereas PLUTO report a large excess of low thrust events in the low Q^2 data, this was not observed here. A possible explanation for this is that the limited angular acceptance of CELLO distorts the thrust of these events to higher values, making their identification difficult. MC studies support this conclusion.

An attempt was made to explain the observed excess of high jet p_t events by the inclusion of a third component. Three different models were used for this third component

1) Multijet terms modelling the processes $\gamma\gamma \rightarrow qqg$ and $\gamma\gamma \rightarrow qqqq$. These were generated with the same W, p_t dependences as QPM.

2) $\gamma\gamma \rightarrow$ hadrons, where the hadrons are produced with an isoptropic phasespace distribution. Both a flat W independent term and a $1/W^2$ term

were examined.

3) A rescaling of the QPM component.

It was observed that the jet p_t distribution could be well described by the inclusion of a phasespace component (with a $1/W^2$) dependence or by rescaling the QPM term. The multijet models did not provide a good description of the jet p_t distribution. Their jet p_t distributions are peaked at too low values. Since it has been shown that the excess favours a $1/W^2$ dependence and also produces high jet p_t events, it can be argued that the excess is pointlike in origin. The thrust of the high jet p_t events was described neither by the inclusion of a phasespace term (which underestimates the thrust), nor by scaling the QPM term (which overestimates the thrust). However, a good description of the thrust of high jet p_t events was provided by the addition of a multijet term to GVDM + QPM. Therefore it is concluded that the excess can be described by a pointlike interaction which produces high jet p_t events that have a multijet-like thrust distribution.

The CELLO Collaboration

H.-J. Behrend, L. Criegee, J. H. Field[1], GFranke, H. Jung[2],
J. Meyer, O. Podobrin, V. Schroder, G. G. Winter
Deutches Elektronen-Synchrotron, DESY, Hamburg, Germany

P. J. Bussey, A. J. Campbell, D. Hendry, S. J. Lumsdon, I. O. Skillicorn
University of Glasgow, United Kingdom

J. Ahme, V. Blobel, W. Brehm, M. Feindt, H. Fenner,
J. Harjes, J. H. Kohne, J. H. Peters, H. Spitzer
II. Institut fur Experimentalphysik, Universitat Hamburg, Germany

W.-D. Apel, J. Engler, G. Flugge[2], D. C. Fries, J. Fuster[3], P. Gabriel, K. Gamerdinger[4], P.Grosse-Wiesmann[5], M. Hahn, U. Hadinger, J. Hansmeyer, H. Kuster[6], H. Muller, K. H. Ranitzsch,
H. Schneider, R. Seufert
Kernforschungzentrum Karlsruhe und Universitat Karlsruhe, Germany

W. de Boer, G. Buschorn, G. Grindhammer[5],
B. Gunderson, Ch. Kiesling[7], R. Kotthaus, H. Kroha,
D. Luers, H. Oberlack, P. Schact, S. Scholz, W. Wiedenmann[8]
Max Planck-Institut fur Physik und Astrophysik, Munchen, Germany

M. Davier, J. F. Grivaz, J. Haissinski, V. Journe, D. W. Kim, F. Le Diberder, J.-J. Veillet
Laboratoire de l'Accelerateur Lineaire, Orsay, France

K. Blohm, R. George, M. Goldberg, O. Hamon, F. Kapusta, L. Poggioli, M. Rivoal
Laboratoire de Physique Nucleaire et des Hautes Energies,
Universite de Paris, France

G. d'Agostini, F. Ferrarotto, M. Iacovacci, G. Shooshtari, B. Stella
University of Rome and INFN, Italy

G. Cozzika, Y. Ducros,
Centre d'Etudes Nucleaires, Saclay, France

G. Alexander, A. Beck, G. Bella, J. Grunhaus, A. Klatchko, A. Levy, C. Milstene
Tel Aviv University, Israel

[1]Now at Universite de Geneve, Switzerland
[2]Now at RWTH, Aachen, Germany
[3]Now at Inst. de Fisica Corpuscular, Universidad de Valencia, Spain
[4]Now at MPI fur Physik und Astrophysik, Munchen, Germany
[5]Now at Stanford Linear Accelerator Center, USA
[6]Now at DESY, Hamburg, Germany
[7]Heisenberg Scholarship of Deutsche Forschungsgemeinschaft
[8]Now at CERN

References

Chapter 1

1.1 F. E. Low, Phys. Rev. 120 (1960) 582

1.2 S. J. Brodsky, T. Kinoshita, & H. Terazawa, Phys. Rev. 4D (1971) 1532

1.3 D. Bintinger et al, Phys. Rev. Lett. 54 (1985) 763

1.4 R. Brown & I. Muzinich, Phys. Rev. 4D (1971) 1496
C. E. Carlson & W. K. Tung, Phys. Rev. 4D (1971) 2873
V. M. Budnev et al, Phys. Rep. 15C (1975) 181

1.5 Ch. Berger & J. H. Field, Nucl. Phys. 187B (1981) 585

1.6 C. F. Weizacker, Z. Phys. 88 (1934) 315

1.7 R. Bhattacharya, J. Smith & G. Grammar, Phys. Rev. 15D (1977) 3267

1.8 J. J. Sakurai & D. Schildknecht, Phys. Lett. 40B (1972) 121

1.9 I. F. Ginzburg & V. G. Serbo, Phys. Lett. 109B (1982) 231

1.10 H. Aihara et al, Phys. Rev. 41D (1990) 2667

1.11 G. Giacomelli & M. Jacobs, Phys. Rep. 55 (1979) 1

1.12 T. F. Walsh & P. Zerwas, Phys. Lett. 44B (1973) 195
R. L. Kingsley, Nucl. Phys. 60B (1973) 45
R. P. Worden, Phys. Lett. 51B (1974) 57

1.13 S. J. Brodsky, T. A. DeGrand, J. F. Gunion & J. H. Weis,
Phys. Rev. 19D (1979) 1418

1.14 S. J. Brodsky & G. R. Farrar, Phys. Rev. Lett. 31 (1973) 1153
Phys. Rev. D11 (1975) 1309

1.15 K. Kajantie, 'Proceedings of the Fourth International Colloquium on Photon-Photon Interactions (Paris 1981)', edited by G. W. London p 255

1.16 W. J. Stirling, 'proceedings of the Fifth International Workshop on Photon-Photon Collisions (Aachen, 1983)', edited by Ch Berger, p 142

1.17 E. Gotsman, A. Levy & U. Maor, DESY Report, 87-102 (1987)

1.18 N. Arteaga-Romero et al, Z. Phys. 32C (1986) 105

Chapter 2

2.1 CELLO Collaboration, Phys. Lett. 126B (1983) 384
PLUTO Collaboration, Z. Phys. 27C (1985) 249

2.2 AMY, KEK Preprint 89-195, Submitted to Phys. Lett. B

2.3 J. H. Field, DESY Report, 81-037
J. Olsson, DESY Report, 87-136

2.4 C. Peterson, T. F. Walsh & P. Zerwas, Nucl. Phys. 174B (1980) 424
P. Zerwas, Phys. Rev. 10D (1974) 1485

2.5 PLUTO Collaboration, Phys. Lett. 142B (1984) 119

2.6 S. D. Drell & T. M. Yan, Phys. Rev. Lett. 25 (1970) 316

2.7 J. H. Field, 'Proceedings of the 8th International Workshop on Photon-Photon Collisions (Israel 1988)', edited by Uri Karshon, p 349
E. Gotsman, A. Levy, U. Maor, DESY Report, 87-102

2.8 T. F. Walsh and P. Zerwas, Phys. Lett. 44B (1973) 195
R. L. Kingsley, Nucl. Phys. 60B (1973) 45
R. P. Worden, Phys. Lett. 51B (1974) 57

2.9 E. Witten, Nucl. Phys. 120B (1977) 189

2.10 I. F. Ginzburg & V. G. Serbo, Phys. Lett. 109B (1982) 231

2.11 PLUTO Collaboration, Z. Phys. 26C (1984) 353
PLUTO Collaboration, Phys. Lett. 149B (1984) 421

2.12 TPC/2-γ Collaboration, Phys. Rev. 41D (1990) 2667

2.13 D. Bintinger et al, Phys. Rev. Lett. 54 (1985) 763

2.14 J. H. Field, F. Kapusta & L. Poggioli, Z. Phys. 36C (1987) 121

2.15 PLUTO Collaboration, Z. Phys. 26C (1984) 191

2.16 S. Maxfield, 'Proceedings of the 8th International Workshop on Photon-Photon Collisions (Israel 1988)', edited by Uri Karshon, p 172

2.17 PLUTO Collaboration, Z. Phys. 33C (1987) 351

2.18 TPC/2-γ Collaboration, $\gamma\gamma$ jet analysis paper, under preparation.

2.19 N. Arteaga-Romero et al, Z. Phys. 32C (1986) 105

Chapter 3

3.1 S. L. Wu, Phys. Rep. 107 (1984) 59

3.2 H. J. Berhend et al, Physica Scripta, 23 (1981) 610

3.3 B. Sack, Diploma Thesis, University of Hamburg, 1984

3.4 U. Binder, Diploma Thesis, University of Hamburg, 1984

3.5 W. De Boer et al, Nucl. Instr. & Meth. 176 (1980) 167

3.6 R. Aleksan et al, Nucl. Instr. & Meth. 185 (1981) 95

3.7 K. H. Blohm, CELLO note, unpublished

3.8 H. J. Berhend, Comp. Phys. Comm. 22 (1981) 365

Chapter 4

4.1 G. Franke, The CELLO Event Filter Program, CELLO note D035, 1985, unpublished

4.2 W. De Boer & I. Hildebrandt, CELLO note M159, unpublished
V. Blobel, Desy Report F14-79-02

4.3 M. Feindt, Criteria Applied in the 1986 DST Select Job, CELLO note D042, 1986, unpublished

4.4 VIOLA, A Program Package for Analysing CELLO data, a joint effort of the DESY-F14 group, unpublished

4.5 J. Harjes, Diploma Thesis, University of Hamburg, 1987

4.6 J. Ahme, Thesis, University of Hamburg, 1988

Chapter 5

5.1 W. De. Boer & M. Iacovacci, CELLO note, R02, 1988, unpublished

5.2 J. A. M. Vermaseren, Nucl. Phys. 229B (1983) 573

5.3 R. P. Feynman & R. D. Field, Nucl. Phys. 136B (1978) 1

5.4 F. H. Behrends, P. H. Daverveldt & R. Kleiss, Z. Phys. 22C (1984) 239

5.5 T. Sjostrand, & M. Bengsson, Comp. Phys. Comm. 43 (1987) 367

5.6 A. Tylka, Thesis, DESY Report, 85-04
J. M. Nye, Thesis, Lancaster University, 1986

5.7 G. Giacomelli & M. Jacobs, Phys. Rep. 55 (1979) 1

5.8 D. Hendry, Thesis, University of Glasgow, 1985

5.9 EGS: R. L. Ford & W. R. Nelson, SLAC-210, 1978
HETC: RISC Comp. Code Colection, Oak Ridge Nat. Lab. CCC-178

5.10 R. Brun et al, The GEANT3 Manual, CERN, DD/EE/84-1

5.11 K. H. Blohm, CELLO note, P045, 1987, unpublished

Chapter 6

6.1 PLUTO Collaboration, Phys. Lett. 94B (1980) 254
MARK II Collaboration, Phys. Lett. 105B (1981) 304

6.2 P. J. Bussey, Private Communications

6.3 A. Tylka, Thesis, DESY Report, 85-04
D. Hendry, Thesis, University of Glasgow, 1985

6.4 F. Kapusta, Private Communications

Chapter 7

7.1 W. de Boer & M. Iacovacci, CELLO Note R02, 1988, unpublished

7.2 PLUTO Collaboration, Z. Phys. 29C (1985) 499
TASSO Collaboration, Phys. Lett. 138B (1984) 219

Chapter 8

8.1 S. Brandt et al, Phys. Lett. 12 (1964) 57
E. Fahri et al, Phys. Rev. Lett. 39 (1977) 1587
A. de Rujula et al, Nucl. Phys. 138B (1978) 387

8.2 J. D. Bjorken & S. J. Brodsky, Phys. Rev. 1D (1970) 1416

8.3 G. C. Fox & S. Wolfram, Nucl. Phys. 149B (1979) 413

8.4 S. Cartwright, Thesis, University of Glasgow, 1983

8.5 Private communications, I. O. Skillicorn

8.6 N. Arteaga-Romero et al, Z. Phys. 32C (1986) 105

Chapter 9

9.1 PLUTO Collaboration, Z. Phys. 33C (1987) 351

9.2 PLUTO Collaboration, Z. Phys. 29C (1985) 499
TASSO Collaboration, Phys. Lett. 138B (1984) 219